Numerical modelling of shallow jet flows

A case study of Waterdunen

Y.B. (Yannick) Steenman

November 2020

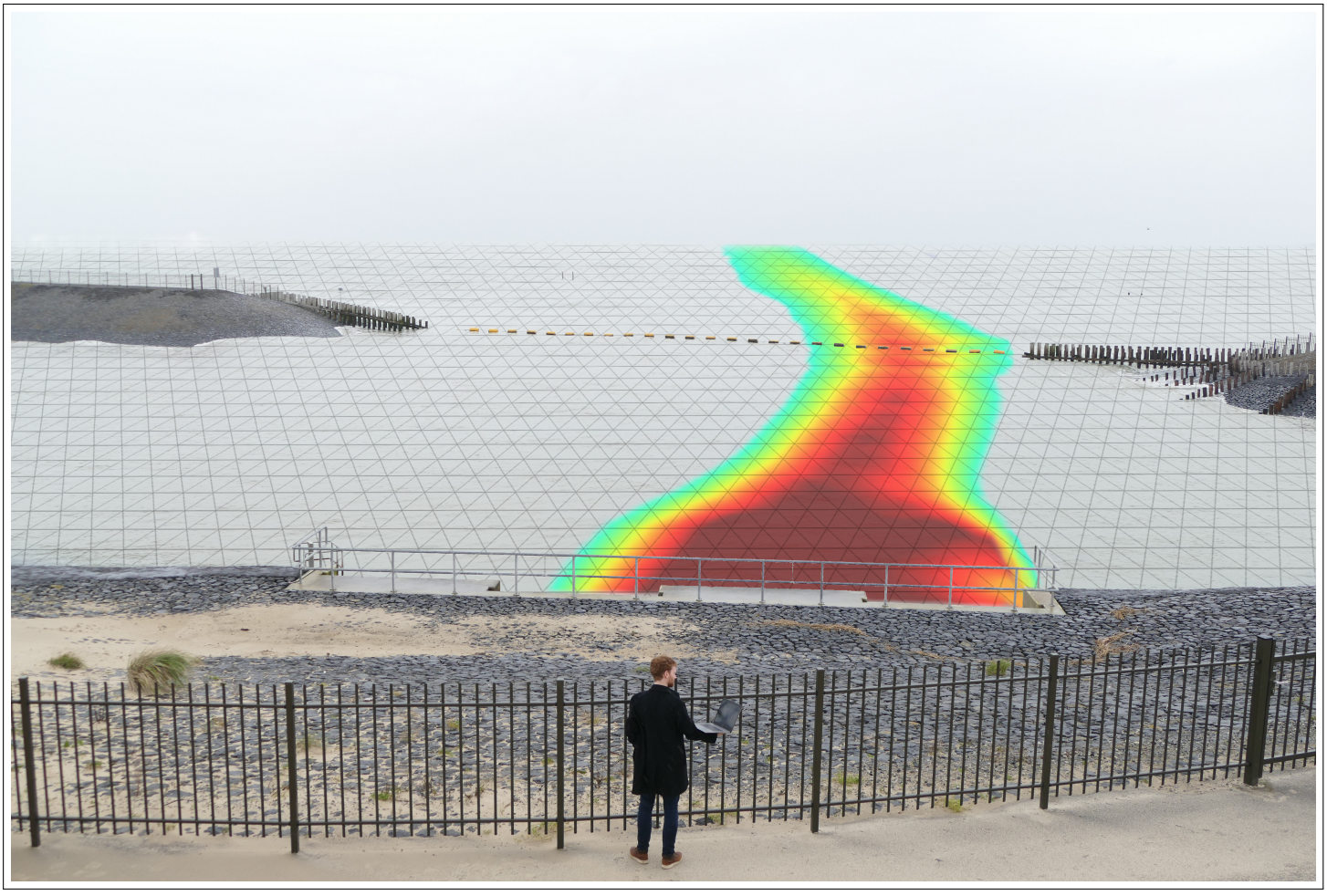

TU Delft

SVAŠEK HYDRAULICS

COASTAL, HARBOUR AND RIVER CONSULTANTS

Numerical modelling of shallow jet flows

A case study of Waterdunen

by

Y.B. Steenman

in partial fulfilment of the requirements for the degree of

Master of Science

in Civil Engineering

at the Delft University of Technology
to be defended publicly on 16th of November, 2020 at 13:30h.

Student number:	4381351	
Project duration:	February 2020 - November 2020	
Thesis committee:	Dr. ir. R.J. Labeur,	TU Delft, chairman
	Dr. ir. Y. B. Broekema,	TU Delft and Deltares
	Dr. ir. S. de Vries,	TU Delft
	Dr. ir. B.C. van Prooijen,	TU Delft
	Ir. Y. Attema,	Svašek Hydraulics Nederland

TU Delft

SVAŠEK HYDRAULICS
COASTAL, HARBOUR AND RIVER CONSULTANTS

Preface

The document you are reading is the final edition of my master's thesis on the numerical modelling of shallow jet flows. This thesis was the final hurdle I had to overcome to finalize my Master of Science in Hydraulic Engineering at the Delft University of Technology with the specialization directions Coastal Engineering and Environmental Fluid Mechanics.

This project originated from the design project of Svašek Hydraulics regarding the design of the bed protection at Waterdunen. With several unanswered questions remaining after the project and plenty of measurement data available, it was the ideal set-up for a master's thesis, which I gratefully took advantage of. My own goal regarding the thesis had always been to structurally dissect a numerical model and gain a complete understanding of how the model works. I am glad to say this goal has been reached tenfold.

First and foremost, I want to thank my graduation committee for their constructive criticism, enthusiasm and encouragement during the span of this work. Furthermore, I am grateful for the sense of realism the committee provided to this work, for without it I would probably still be working on the data analysis. I want to thank Robert Jan Labeur as the chairman of the committee for his constructive criticism on both the contents and the structure of the report. The large number of meetings we had together were always both insightful and fun. I want to thank Yorick Broekema for his assistance, primarily during the data-analysis. His enthusiasm regarding the subject always sparked over towards me, which helped during the tough times. I want to thank Bram van Prooijen for his cheerful and enthusiastic support during the meetings. Bram helped me keep an eye on the practical aspects of the thesis rather than solely focussing on the theoretical aspect. I want to thank Sierd de Vries for his assistance in the final stage of this thesis. Though we did not meet often, his insight helped me with the consistency of this work. Finally, I want to thank Ype Attema for his help throughout the entirety of the thesis. As my supervisor at Svašek Hydraulics, Ype immediately took me under his wing to help me realize not only a fulfilling thesis, but also my personal goals along the way. Together with the graduation committee, I want to thank Wim Uijttewaal for his valuable insight. Though regretfully he was not able to attend the full length of this work, his remarks in the early stages greatly helped steering the thesis in the correct direction.

Special thanks goes out to the employees at Svašek Hydraulics. Harmen, thank you for the extremely valuable discussions regarding the numerical software used in this work. Your lessons in FINEL were of great value to the quality of the numerical models set-up in this thesis. The knowledge you have regarding the fundamentals of hydrodynamics and numerical models is truly inspiring, and I hope to approach that same level one day. Sanne, thank you for the great help with the Wester Scheldt model. I appreciate the time you spent explaining the model and helping me include my own sections in the model. Finally, I want to thank the rest of the staff for the cheerful times in and outside of the office and the discussions which helped me improve the quality of this work.

I would like to thank my dad for the valuable discussions and the transportation service from and towards the office during the tough times. Our trip to Waterdunen was very fun, and the resulting front-page image looks great. Of course, I also want to thank my mom for looking after my health and making sure I do not stress too much during the final stages of my study in Delft.

Y.B. (Yannick) Steenman
Delft, November 2020

Abstract

Shallow jet flows are often coupled to high flow velocities and complex flow patterns. To properly ensure the stability of the barrier between both water bodies surrounding the jet, a scour analysis is often a necessity. Such analyses are inevitably coupled to the hydrodynamic processes occurring in jet flows, either in the form of loads on potential bed protections or equilibrium scour hole depths. Numerical models could assist in the design of bed protections by supplying accurate hydrodynamic input parameters for the design formulae or by predicting the hydrodynamic processes at play. Due to the limited computational power available, simplifications must be made within the numerical model to ensure reasonable computational costs. One of these simplifications is to resolve the flow in depth-averaged sense to create a 2DH model. To allow this simplification to be made, the performance of a 2DH model compared to a fully 3D model needs to be researched. By comparing simulations of a controlled environment and of a prototype scenario, insight in the predictive capabilities of the numerical models for possible other projects can be gained.

In literature, several hydrodynamic processes occurring in shallow jets are relatively well researched. It is known the jet can become asymmetrical due to a Coanda-like effect stimulated by either subtle pressure differences or asymmetric boundaries within the channel. Furthermore, recent research of Broekema et al. (2020) showed shallow jets over longitudinal slopes can remain attached depending on the slope steepness and horizontal non-uniformity of the flow. Both hydrodynamic processes can significantly alter the horizontal location and magnitude of high flow velocities in the channel. However, it has not yet been researched how well these processes can be captured by 2DH and 3D numerical models.

This work aims to research the performance of 2DH and 3D numerical models regarding the reproduction of the hydrodynamic processes in shallow jets. First, it was investigated which hydrodynamic processes thrive at a prototype shallow jet by analysing measurement data available at Waterdunen. Afterwards, we systematically determine the performance of both a 2DH and 3D numerical model by setting up FINEL models both for a laboratory experiment of a shallow jet and for the shallow jet at Waterdunen. Insight in the predictive capabilities of 2DH and 3D numerical models for shallow jets can contribute to future design problems surrounding shallow jets.

Information regarding the shallow jet at the seaside of the culvert at Waterdunen was obtained by Svašek Hydraulics, commissioned by the public government Waterschap Scheldestromen and the province of Zeeland, during a measurement campaign split into six individual measurement scenarios. Immediately at outflow from the culvert, the jet is subject to a 1:6 slope in streamwise direction. The geometry of the seaside channel is asymmetric, with 1:4 lateral slopes at either side of the channel. Furthermore, morphological changes as a result of the jet flow introduce an asymmetric topography in the channel.

Visual observations during the measurement campaign indicated the flow can be characterized by an horizontal contraction over the longitudinal slope and an asymmetric flow profile depending on which casings were active within the culvert. The analysis of the measurement data shows the jet concentrates on the eastern side of the channel during all six scenarios. As a result, the recirculation zones on either side of the jet can be characterized as a small, non-dominant recirculation zone on the east side of the jet and a large, dominant recirculation zone on the west side of the jet. The streamlines show a continuous horizontal contraction until the flow hits the eastern side of the channel. Over the longitudinal slope, the flow seems to remain attached to the bottom rather than separating. However, due to a relatively large clearance of the ADCP measurements with respect to the bottom, this cannot be proven directly.

It was decided to simulate the shallow jet of experiment 2.4.1 of van de Zande (2018) to investigate the performance of a 2DH and 3D numerical model for a laboratory simulation. In this experiment, the behaviour of an asymmetric shallow jet over a longitudinal slope at the point of the horizontal expansion was investigated. It was shown that both the 2DH and 3D numerical model were capable of reproducing the most dominant hydrodynamic processes within the jet. However, the accuracy with which the processes were reproduced differed significantly. The 2DH model reproduced too much curvature of the flow towards the lower wall of the flume compared to both the 3D model and the measurement data. As a result, the high flow velocities in the jet center were located further down in the channel. The flow velocities in the jet center were modelled with a maximum error of 12.4% in the 2DH model and 3.02% in the 3D model. The lower accuracy of the 2DH model is caused by the comparison between depth-averaged velocities and surface PIV velocities.

Due to the additional curvature the recirculating velocities in the non-dominant recirculation zone were modelled too high by the 2DH model, with an error of up to 56.6% relative to the jet center velocity. In the 3D model, this error decreased to 18.9%. However, it was remarked the recirculating flow velocities in the PIV data were subject to clumping of tracer particles. The horizontal streamline contraction was simulated in the 2DH model, but can only be directly related to the changes in water depth. In both the 3D model and the measurements, this horizontal streamline contraction was shown to continue further downstream of the slope. It was concluded the horizontal streamline contraction is directly related to the vertical velocity profile, which was observed to differ from the standard log-profile both on the slope and downstream thereof. The 3D model was capable of reproducing the vertical velocity profile with a maximum relative error of 10%.

In the numerical simulations at Waterdunen, both the 2DH and 3D models were shown to behave similarly. Both the 2DH and 3D numerical models were capable of reproducing the eastern concentration of the flow. However, the curvature of the jet further downstream was modelled more accurate in the 3D model. The better reproduction of the flow curvature in the 2DH model compared to the laboratory simulations is the result of the asymmetric inflow boundary, which allows the 2DH model to more easily resolve the flow curvature. Both models underestimate the flow velocities throughout the entire DOI. It was concluded this was caused by errors in the model input. Similar to the laboratory simulations, the 2DH model reproduced the horizontal streamline contraction over the slope but failed to reproduce the contraction further downstream. The 3D model was capable of reproducing the continuing streamline contraction. Furthermore, the 3D model reproduced vertical flow attachment over the slope, which complies well with the measurement data.

It was concluded that a 3D numerical model can better reproduce the flow curvature in case of asymmetrical flows. Furthermore, the recirculating flow is better reproduced by a 3D model compared to a 2DH model. Finally, a 3D model is capable of accurately reproducing the vertical velocity profile, which supplies additional information of accurate flow velocities at the bed. However, on a prototype scale the differences between a 2DH and 3D numerical model are small. In channels with symmetrical boundaries, it is suggested to use a 3D numerical model in case the flow is subject to the Coanda-like effect. However, if the inflow into the channel is already asymmetrical, a 2DH numerical model can be considered to save computational effort. Nevertheless, when employing a 2DH model one should be wary of geometric and topographic asymmetries, as the effect of both factors on the flow symmetry is still unclear.

Contents

List of Figures

List of Tables

Nomenclature

Abbravations

Abbravation	Description
$2DCS$	Two-Dimensional Coherent Structures
$2DH$	Two-Dimensional Horizontal
$2DV$	Two-dimensional Vertical
$3D$	Three-Dimensional
$ADCP$	Acoustic Doppler Current Profiler
ADV	Acoustic Doppler Velocimetry
AR	Aspect Ratio
BFS	Backwards Facing Step
CFD	Computational Fluid Dynamics
CG	Continuous Galerkin
DG	Discontinuous Galerkin
DNS	Direct Numerical Simulation
DOI	Domain Of Interest
ER	Expansion Ratio
$ES-SSB$	Eastern-Scheldt Storm Surge Barrier
FEM	Finite Element Method
$H-ADCP$	Horizontal Acoustic Doppler Current Profiler
LES	Large Eddy Simulation
PDE	Partial Differetial Equation
PIV	Particle Image Velocimetry
$RANS$	Reynolds-Averaged Navier-Stokes
STD	Standard Deviation
WCG	Weighted Center of Gravity
$ZOEF$	Zone Of Established Flow
$ZOFE$	Zone Of Flow Establishment

Greek Symbols

Symbol	Description	Units
Δ	Grid size	m
Δ_H	Horizontal grid size	m
Δ_{max}	Maximum grid size	m
Δ_{y0}	Horizontal grid size at the lateral wall	m
Δ_{z0}	Vertical grid size at the bottom	m
ϵ	Turbulent engery dissipation rate	$m^2 \cdot s^{-3}$
η	Kolmogorov length scale	m
κ	Von Kármán constant, $\kappa = 0.4$	–
ν_t	Turbulent viscosity	$m^2 \cdot s^{-1}$
σ_ϵ	Empirical coefficient for the $k-\epsilon$ model, $\sigma_\epsilon = 1.30$	–
σ_k	Empirical coefficient for the $k-\epsilon$ model, $\sigma_k = 1.00$	–
τ_w	Wall shear stress	$N \cdot m^{-2}$
θ	Implicity parameter	–
$\vec{\omega}$	Vorticity vector [ω_x, ω_y, ω_z	s^{-1}
δ	Mixing layer width	m
∇	Nabla operator	m^{-1}
ν	Kinematic molecular viscosity	$m^2 \cdot s^{-1}$
ω	Vorticity	s^{-1}
ω_x	Vorticity in streamwise direction	s^{-1}
ω_y	Vorticity in lateral direction	s^{-1}
ω_i	Vorticity in i direction	s^{-1}
ω_j	Vorticity in j direction	s^{-1}
ω_z	Vorticity in vertical direction	s^{-1}
ρ	Density	$kg \cdot m^{-3}$
$\tau_{x,y}$	Total horizontal shear stress	$N \cdot m^{-2}$
θ_T	Temperature	°

Roman Symbols

Symbol	Description	Units
$\vec{u}$	Velocity vector [u,v,w]	$m \cdot s^{-2}$
B	Channel width	m
b	Jet half-width	m
C_μ	Empirical coefficient for the $k-\epsilon$ model, $C_\mu = 0.09$	–
c_f	Hydraulic roughness	–
C_s	Smagorinsky coefficient	–
$C_{\epsilon 1}$	Empirical coefficient for the $k-\epsilon$ model, $C_{\epsilon 1} = 1.44$	–
$C_{\epsilon 2}$	Empirical coefficient for the $k-\epsilon$ model, $C_{\epsilon 2} = 1.92$	–
$c_{f,bed}$	Bed hydraulic roughness	–
$c_{f,wall}$	Wall hydraulic roughness	–
C_{lm}	Empirical coefficient for the mixing-length model, $C_{lm} = 0.16$	–
ER_c	Critical expansion ratio	–
Fr	Froude number	–
g	Gravitational acceleration, $g = 9.81$	$m \cdot s^{-2}$
H	Water depth	m
k	Turbulent kinetic energy	$m^2 \cdot s^{-2}$
K_r	Strouhal number	–
k_s	Nikuradse roughness height	m
L	Characteristic length scale	m
l_*	Characteristic wall length scale	m
l_m	Mixing length	m
L_t	Turbulence length scale	m
l_{max}	Maximum turbulence length scale	m
Q	Discharge	$m^3 \cdot s^{-1}$
Re	Reynolds number	–
S	Jet stability number	–
T	Timestep of time discretization at Waterdunen	–
t	Time	s
T_t	Tidal period	s
U	Characteristic velocity scale	$m \cdot s^{-1}$
U^+	Dimensionless flow velocity in streamwise direction (wall coordinate)	–

u_*	Bed shear velocity	$m \cdot s^{-1}$
u_i	Velocity in i direction	$m \cdot s^{-1}$
u_j	Velocity in j direction	$m \cdot s^{-1}$
u_n	Velocity in layer n	$m \cdot s^{-1}$
U_t	Maximum cross-sectionally averaged tidal velocity	ms^{-1}
u_x	Velocity in streamwise direction	$m \cdot s^{-1}$
u_y	Velocity in lateral direction	$m \cdot s^{-1}$
u_z	Velocity in vertical direction	$m \cdot s^{-1}$
W	Jet width	m
WCG	Weighted center of gravity	m
x	Streamwise coordinate	m
$\acute{x}$	Streamwise coordinate in rotated coordinate system	m
y	Lateral coordinate	m
$\acute{y}$	lateral coordinate in rotated coordinate system	m
y^+	Dimensionless coordinate in wall-normal direction (wall coordinate)	–
z	Vertical coordinate	m

1

Introduction

Closing off sections of the sea has become a world-wide famous trait of The Netherlands. Several large-scale dams and barriers have been constructed to protect the Dutch hinterland from flooding. Though this method is effective for flood protection, several unforeseen issues were noticed during and after the construction of the barriers. One of these issues lied in the water quality on the inland side of the impermeable barriers. An example lies in the closing of the Eastern-Scheldt, where during construction several environmental parties protested the ecological value of the inland lake would decrease drastically due to the closure.

The eventual compromise was found in the form of the Eastern-Scheldt Storm Surge Barrier (ES-SSB) as shown in figure 1.1. The ES-SSB is a closing structure which contains several gates to allow water to be exchanged between either side of the barrier in normal conditions. During storms, the gates can be closed off to protect the hinterland from flooding.

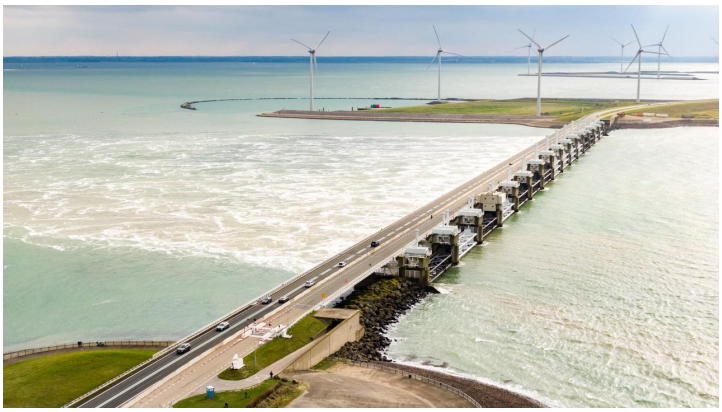

Figure 1.1: The Eastern-Scheldt Storm Surge Barrier. Source: https://www.nu.nl/binnenland/6029677/oosterscheldekering-gesloten-vanwege-hoge-waterstand.html.

Given the rise of building-with-nature solutions, this methodology of building partially closed off hydraulic structures has become the norm in The Netherlands. However, allowing free passage of water through the barrier does not come without consequences. The flow has to contract when moving through the barrier, increasing the flow velocity at the point of in- and outflow from the barrier. As a consequence, bottom erosion in the form of scour can become threatening to the stability of the closing hydraulic structure. To maintain a stable structure, scour protections are often a necessity.

For the design of scour protections knowledge of the hydrodynamic processes within the flow is required. For this purpose, research has been carried out regarding the flow through the closing hydraulic structures. More often than not, this flow can be characterized as shallow jet flow.

1.1. Introduction to shallow jets

The shallow jet is a particular type of flow where a strong, concentrated stream of water moves into a broad channel via an expansion. It is a flow-type that is not uncommon in The Netherlands, seeing practical application at for example the ES-SSB, Rammegors, and Waterdunen. In these applications, the driving force behind the jet is the tide. The complex hydrodynamic processes which characterize these flows are difficult to capture with design formulae, which makes the design of these scour protections difficult.

In order to better understand the hydrodynamics of shallow jet flows, physical and numerical studies have been carried out. Broekema et al. (2020) found that scour holes can exceed the calculated equilibrium depth due to a combination of horizontal flow convergence and vertical flow attachment. Additionally, Dewals et al. (2008) showed the horizontal distribution of streamwise velocity for jet flows is largely dependent on subtle instabilities within the system.

1.2. Numerical solutions

Due to the complexity of shallow jets, models are often required to gain predictive insight into the flow behavior during the design phase of hydraulic structures. These models can be separated into numerical or physical models. Computational Fluid Dynamics (CFD) has been a valuable tool in assisting the design of bed protections. The relatively low costs and little effort required to build a numerical model compared to a physical model make up most of this value. Nevertheless, the usage of numerical models does not come without risk. The current computational power available to most engineers is not sufficient for Direct Numerical Simulation (DNS) on large scales. For this reason, simplifications within numerical models are unavoidable. Knowledge of which simplifications can be made within a certain model can therefore largely influence the success of the simulation. For laboratory experiments, this can be managed due to the controlled environment. However, when considering specific prototype-scale issues which include a broad range of hydraulic processes, it becomes challenging to evaluate the effect of each simplification within the system.

The value of numerical models lies in the prediction of local and global hydraulic parameters on a significantly more accurate scale compared to design formulae which reduce the system to a more simple case. However, when considering systems of the size of the hydraulic structures as mentioned above, computational effort can quickly become unfeasible. Therefore, a popular simplification within numerical models is to resolve the flow field in a depth-averaged sense to create a two-dimensional horizontal numerical model (2DH). In such models, the flow is assumed to adhere to the standard logarithmic velocity profile over the vertical, whereas the horizontal flow profile is allowed to vary. The phenomenon of vertical flow attachment leads to the belief a 2DH model has the potential to resemble a more expensive three-dimensional (3D) model as the flow remains attached to the bed. Nevertheless, the importance of 3D effects within shallow jet flows remains unsure. This work aims to contribute to the aforementioned studies by comparing numerical representations of shallow jet flows for both a laboratory experiment and a prototype scenario at Waterdunen in a 2DH and 3D mode. Proper assessment of the capabilities of 2DH and 3D numerical models to reproduce shallow jet flows is valuable for the design of the necessary bed protections for such flows.

1.3. Problem definition

Shallow jet flows are coupled to high flow velocities and complex flow patterns. To properly ensure the stability of the barrier between both water bodies surrounding the jet, a scour analysis is often a necessity. Such analyses are inevitably coupled to the hydrodynamic processes occurring in shallow jet flows, either in the form of loads on potential bed protections or equilibrium scour hole depths. Most design formulae for the determination of either parameter tend to generalize towards simple, uniform flows, either neglecting the complex structure of jet-like flows or representing complexity in the form of simplified parameters. Numerical models could assist in the design of bed protections by supplying accurate hydrodynamic input parameters for the design formulae or by predicting the hydrodynamic processes at play. Due to the limited computational power available, simplifications must be made within the numerical model to ensure reasonable computational costs. One of these simplifications is

to resolve the flow in a depth-averaged sense to create a 2DH model. The usage of a 2DH model could be justified by the found absence of vertical flow separation at the ES-SSB. To allow this simplification to be made, the importance of 3D effects on the hydrodynamic processes within shallow jet flows should be researched. The comparison between a 2DH and 3D numerical model supplies insight in the consequences of additional simplifications within the models, both for the capability of the models to reproduce the hydrodynamic processes as for the accuracy of the resolved flow field. By comparing simulations of a controlled environment and of a prototype scenario, insight in the predictive capabilities of the numerical models for possible other projects can be gained.

1.4. Objective and research questions

1.4.1. Research objective

The main aim of this work is to assess the required numerical tools to reproduce the hydrodynamics of shallow jet flows in a complex topography in a case study at Waterdunen. A better understanding of the required numerics to reproduce such flows can improve both the accuracy and efficiency of the used numerical models in scour analyses. Both a 2DH and 3D numerical model will be set-up for both a laboratory experiment and for Waterdunen to assess the influence of the simplifications made between both models. The essence of the objective can be captured in the following sentence:

Assessing the capability of two- and three-dimensional numerical models to reproduce the hydrodynamic processes of shallow jet flows over complex topographies both in a controlled environment and a prototype scenario.

1.4.2. Research questions

The main research question of this master thesis is based on the research objective:

> *Which hydrodynamic processes can be identified in the shallow jet at Waterdunen and what are the additional benefits of using a 3D numerical model compared to a 2DH numerical model for the reproduction of these processes?*

The following sub-questions are formulated to answer the research question:

1. Which hydrodynamic processes can be observed to be important in the shallow jet flow at Waterdunen?
2. Which of these hydrodynamic processes can be reproduced by 2DH and 3D numerical models of a laboratory experiment of a shallow jet?
3. Which of these hydrodynamic processes can be reproduced by 2DH and 3D numerical models of the shallow jet at Waterdunen?

1.5. Methodology

To properly answer the research questions an analysis of the current knowledge of jet flows over complex topographies is carried out in the form of a literature study in chapter 2. The literature study aims to make *a priori* estimations of which processes will be important in the case study at Waterdunen, which will be sought after in the analysis of the obtained field data in chapter 3. With the obtained knowledge, requirements for a numerical model can be set-up and a numerical software package can be chosen.

After the software and used parametrizations are determined, both a 2DH and 3D numerical model will be set-up for a laboratory experiment of van de Zande (2018) in chapter 4. The 3D model will contain an identical discretization compared to the 2DH model to solely assess the importance of the added dimension and to not introduce further numerical differences. For both models it will be assessed whether they accurately reproduce the hydrodynamic processes as observed during the experiment and why (not). This way, the model results can be compared to accurate and complete measurement sets in a controlled environment.

After the performance of the model in a controlled environment has been verified, both a 2DH and

3D numerical model will be set-up for Waterdunen in chapter 5. The importance of the observed inaccuracies of the models during the simulations of the laboratory experiment will be sought after, which will indicate the importance of each process in the field. By comparing the model results to the results of the measurement campaign, it can be assessed whether either model can reproduce the flow field at Waterdunen in a satisfactory manner and what the observed differences are.

The results of both the laboratory simulations and the Waterdunen simulations will be discussed in chapter 6, after which the sub-questions and research question will be answered in chapter 7.

2

Literature study

The literature study aims to investigate the known hydrodynamic processes which occur in shallow tidal jets. Furthermore, the knowledge obtained from the literature study is used to investigate the measurement data obtained at Waterdunen and to estimate which numerical tools are required for the reproduction of such flows. First, the hydrodynamic processes in shallow jets are explained in section 2.1. Afterwards, asymmetric jet flows are discussed in section 2.2, followed by an introduction to boundary layers in section 2.3. The effect of vertical flow separation and vertical flow attachment is investigated in section 2.4, while the effect of horizontal flow separation is investigated in section 2.5. Finally, an experiment of van de Zande (2018) in which most of the named processes are found is explained in section 2.6. This chapter is concluded in section 2.7.

2.1. Shallow jets

As stated in the introduction, the considered flow cases in this master's thesis are identified as shallow jet flows. Jets are characterized by a fluid injection from an opening into a stagnant ambient fluid (Uijttewaal, 2018). The high-velocity jet flow exchanges momentum with the stationary ambient fluid, accelerating the ambient fluid while decelerating the jet. Depending on the jet type and configuration, the momentum exchange can happen in the horizontal plane, vertical plane, or both. In large field applications, the jet flow can often be simplified as shallow jet flow, in which the dominant momentum exchange occurs in the horizontal plane. The assumption of shallow jets indicates 2D horizontal turbulence dominates over the 3D turbulence. The other end of the spectrum is fully 3D turbulent flow, where the flow is not restricted in the vertical by the water depth.

2.1.1. Definition

Jirka and Uijttewaal (2004) defined shallow flow to be a type of flow for which the transverse length scale is much larger than the vertical length scale. The result is that turbulent length scales and turbulent time scales in the horizontal plane are of a larger magnitude than in the vertical plane due to the confinement of the flow in the vertical direction. Figure 2.1 shows an example of a shallow jet. As the jet flows into the stationary ambient fluid, a shear layer develops on either side of the jet, separating the stationary fluid from the jet and generating momentum exchange. Initially, this shear layer also develops towards the center of the jet. The point where both inward developing shear layers meet determines the end of the Zone of Flow Establishment (ZOFE). Both inward shear layers span the potential core wherein the flow velocity is equal to the flow velocity at the jet exit (Cohen, 2012). The ZOFE is followed by the Zone of Established Flow (ZOEF), in which the center-line flow velocity falls below the flow velocity at the jet exit. Only two shear layers remain on either side of the jet. Both these shear layers span the mixing layer. Due to the momentum exchange, the shear layers curve into the ambient fluid, increasing the width of the mixing layer when moving in downstream direction. Figure 2.1 also shows the velocity profiles of the developing jet. When neglecting wall friction, a block-shaped velocity profile enters the channel at $x = 0$ in figure 2.1. When moving in downstream direction, the velocity profile deforms and is well represented by a Gaussian profile (Uijttewaal, 2018).

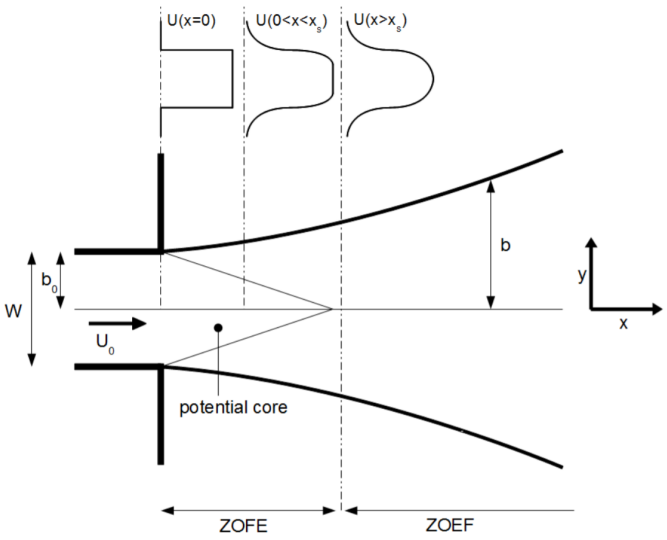

Figure 2.1: Example of a horizontal shallow jet showing the velocity profile (top) and mixing layer development in streamwise direction (Cohen, 2012).

2.1.2. Influence of shallowness

In definition, turbulence is a 3D phenomenon due to the important role of vorticity (Talstra, 2011). Vorticity is the tendency of a fluid to rotate and is defined in equation 2.1 (Pietrzak, 2013).

$$\vec{\omega} \equiv \nabla \times \vec{u} \tag{2.1}$$

In 3D turbulent flows, vortices are unstable and break up into smaller vortices, transferring energy from the large-scale turbulent structures to the small-scale turbulent structures. This process is called the energy cascade and continues to the smallest scale, which is defined as the Kolmogorov scale (Uijttewaal, 2018). The role of vorticity in the energy cascade is highlighted in the vorticity equation as shown in equation 2.2, which is the curl of 3D Navier-Stokes equations.

$$\frac{D\omega_i}{Dt} = \omega_j \frac{\partial u_i}{\partial x_j} + \nu \frac{\partial^2 \omega_i}{\partial x_j^2} \tag{2.2}$$

Where: i, j = Dimension (x,y,z)
ω_i = Vorticity in direction of coordinate (equation 2.1)
ν = Kinematic molecular viscosity ($10^{-6}\ m^2/s$ if temperature is $20°$)

The first term on the right-hand side of equation 2.2 is the vortex stretching term which indicates the interaction between vorticity and the velocity field. It shows that if the vortices are elongated perpendicular to the vorticity plane, the vorticity in that same direction will increase. An important property of shallow jet flow is the limiting effect of vortex stretching due to the relatively small water depth. In an ideal 2D fluid the vortex stretching term will eliminate from equation 2.2 and vorticity would be a conserved quantity. It can be shown that this conservation of vorticity would give rise to an inverse energy cascade of energy transport from the small-scale turbulent motion to the large-scale turbulent motion. This results in stable large-scale turbulent structures rather than the constant vortex shredding as in 3D flows. In reality, vortex stretching is merely hindered and the inverse energy cascade is not dominant. However, in shallow flows, the large-scale horizontal turbulent structures called two-dimensional coherent structures (2DCS) tend to be quite stable (Talstra, 2011). From this, we can deduce that the dominant turbulence in shallow tidal jets are found in the form of stable 2DCS in the horizontal plane, whereas the vertical turbulence has relatively little influence.

2.1.3. Shallow jet stability

To further investigate the behaviour of shallow jets, we investigate the jet stability. In the jet, the horizontal mixing layer is bounded by two shear layers. Cohen (2012) states that the vortices of two shear layers are counter-rotating and often non-symmetrical over the jet axis. The latter means that the vortices are miss-aligned and cause a meandering of the jet. An example of this meandering behaviour in a wake is shown in figure 2.2.

Figure 2.2: Example of the meandering motion of fluid: the wake of an inclined flat plate under an angle of attack at 45°. Source: An Album of Fluid Motion (1981).

Van Prooijen and Uijttewaal (2002) have observed that the 2DCS causing this meandering behaviour can have a much larger impact on the flow structure than the 3D turbulence, as the latter contributes little to the growth of the mixing layer. Ho and Huerre (1984) state that these 2DCS are formed by rolling-up of small waves and vortices, which grow exponentially with streamwise distance. Whether or not this unstable system occurs depends on the jet stability number, as defined in equation 2.3 (Canestrelli et al., 2014). From the equation, it is visible that the bottom friction is the stabilizing factor.

$$S = \frac{0.881 c_f b}{H} \tag{2.3}$$

Where: c_f = Bottom friction coefficient
b = Half-width of the jet
H = Water depth

This stability parameter is inversely related to the Aspect ratio (AR), defined as the water depth divided by the jet width. Linear stability theory and experiments found a large range of critical values for which jets become unstable, ranging from 0.06 to 0.12 according to van Prooijen and Uijttewaal (2002) and from 0.06 to 0.6 according to Canestrelli et al. (2014). For example, at Waterdunen, a first estimation of c_f can be set to be 0.01. With b = 2 m for the jet half-width and H = 3 m for one individual jet, one finds $S \approx 0.006$. For the confluence of three jets out of all individual casings, one finds $S \approx 0.018$. Therefore the expectation would be a stable jet, which is important for the data-analysis in chapter 3. It can be concluded that there is a difference between stable and unstable jets, indicating 2DCS on either side of the mixing layer can cause a meandering behaviour of the jet.

2.1.4. Shallow tidal jets

In this work, the driving force causing the jet is often the tide. Tidal jets differ from non-tidal jets in the non-stationary behaviour induced by the tide. Rather than short-term variations introduced by turbulence, tidal flows also contain a long-term varying trend. Depending on the considered culvert, this can result in a reversion of the flow direction. Each time the flow is reversed, the jet has to 'start up' and a vortex dipole is generated (Afanasyev, 2006). A vortex dipole is characterized by two counter-rotating large vortices flowing symmetrical on either side of the center-line axis of the jet. A well-defined vortex dipole in air is shown in figure 2.3. Vortex dipoles propagate with a speed proportional to the total

vorticity in each vortex (Wells and van Heijst, 2003). If this speed is lower than the tidal flow velocity during reverse tide (sink flow velocity), the dipole is sucked back through the jet opening and interacts on the other side during outflow. The ratio between dipole velocity and sink flow velocity is captured in the Strouhal number, as defined in equation 2.4 (Nicolau del Roure et al., 2009).

$$K_W = \frac{W}{U_t T_t} \tag{2.4}$$

Where: W = Jet width
U_t = Maximum cross-sectionally averaged tidal velocity
T_t = Tidal period

Figure 2.3: Practical example of a vortex dipole. Image source: The New York Times, The Inevitability of Bumps (https://www.nytimes.com/2007/06/12/business/12turbulence.html)

Wells and van Heijst (2003) and Nicolau del Roure et al. (2009) both distinguish one critical Strouhal number for which the transition for different dipole interactions occurs.

- K_W < 0.13: The vortex dipole escapes the channel and flows away before the next tidal cycle.
- K_W = 0.13: The vortex dipole remains stationary during reverse tide.
- K_W > 0.13: The vortex dipole is trapped in the channel and is sucked back during reverse tide.

As an example, the Western Scheldt is subject to an M2 tide with a corresponding tidal period of 44700 s. Considering a maximum flow velocity in the order of 10 m/s and a jet width of 12 meters, the Strouhal number can be shown to be $K_w \approx 2.7 \cdot 10^{-5} << 0.13$. Therefore the vortex dipole is able to escape the channel long before the tide reverses and no interaction is expected, which is important information for the simulations at Waterdunen. It can be concluded that the flow reversal due to the tide can influence the jet behaviour if the tidal period is small.

2.2. Asymmetric jet flow

Numerous physical experiments described in literature have observed flow through a sudden expansion becomes asymmetric under certain conditions (e.g. Kantoush et al. (2008)). The asymmetry in the flow field is attributed to a Coanda-like effect. The Coanda effect is the tendency of a fluid or gas to remain attached to solid surfaces. Many people have experienced the Coanda effect when pouring liquid out of a glass, as shown in figure 2.4. The driving force behind the effect is pressure, with the pressure along the solid surface often being lower compared to the other side. Considering the asymmetric set-up in Panitz and Wasan (1972), it was suggested vortices rotating towards the solid surface draw the primary jet stream towards it. Considering symmetrical set-ups, subtle instabilities such as a small pressure difference can lead to higher flow velocities on one side of the jet. This in turn decreases the pressure on that side, steering the jet towards an asymmetrical configuration (Sobey and Drazin, 1986).

Fearn et al. (1990) found that at a certain Reynolds number the unique symmetrical flow configuration is no longer stable and the flow solution bifurcates at a pitchfork point, enhancing either one of two stable asymmetrical solutions. The Reynolds number is defined in equation 2.5, indicating the ratio

Figure 2.4: Practical example of the Coanda effect. Source: Coanda Effect: Why Is It So Hard To Pour Liquid From Mugs? (https://www.scienceabc.com/pure-sciences/coanda-effect-why-is-it-so-hard-to-pour-liquid-from-mugs.html)

between the inertial forces and the viscous forces. Various researchers made the effort to pinpoint a critical Reynolds number for which the flow tends to become asymmetric. However, in the turbulent flow regime it was shown by Ghidaoui and Kolyshkin (1999) the Reynolds number has a limited effect on the flow stability for $Re > 1000$.

$$Re = \frac{UL}{\nu} \tag{2.5}$$

For highly turbulent flows Dewals et al. (2008) found the ratio between the expanded channel length and width largely influences symmetry of the flow, with asymmetric configurations found for longer, more narrow channels and symmetric configurations for shorter, more wide channels. Furthermore, it was shown by Graber (2006) the expansion ratio (ER), defined as the expansion width divided by the jet width, also influences the flow symmetry based on the Froude number. The Froude number is defined as the ratio between inertial forces and gravity as shown in equation 2.6. For $Fr < 0.2$ it was observed the critical expansion ratio equals $ER_c = 1.5$, above which the flow becomes unstable and therewith asymmetric. For increasing Froude numbers this critical expansion ratio decreases to $ER_c = 1.2$ for critical flows.

$$Fr = \frac{U}{\sqrt{gH}} \tag{2.6}$$

Dewals et al. (2008) employed a parameter called the non-dimensional moment to represent the asymmetry in the channel. In this work, a similar parameter is employed, being the weighted center of gravity (WCG) of the flow. Contrary to the non-dimensional moment, the WCG accounts for changes in the width and depth of the channel. Furthermore, the WCG supplies a weighted lateral coordinate in the local coordinate system where most momentum is transported in streamwise direction. The definition of the WCG of the flow is shown in equation 2.7.

$$WCG = \frac{\int_{-B/2}^{B/2} u_x y dy}{\int_{-B/s}^{B/2} |u_x| dy} \tag{2.7}$$

In equation 2.7, u_x is the velocity in streamwise direction and y is the lateral coordinate. With the origin of the coordinate system located at the center-line of the channel the WCG only becomes nonzero if the lateral flow profile in the channel is asymmetric. The reason why the absolute value is taken in the denominator is explained in chapter 3.

Figure 2.5a shows an example of an asymmetric flow pattern. Between figure 2.5a and 2.5b it is evident the form of the recirculation zones changes as a result of the flow asymmetry. The recirculation zone on the side of the channel the jet concentrates on is shortened and is coined the non-dominant recirculation zone, whereas the recirculation zone on the other side of the channel is broadened and

coined the dominant recirculation zone.

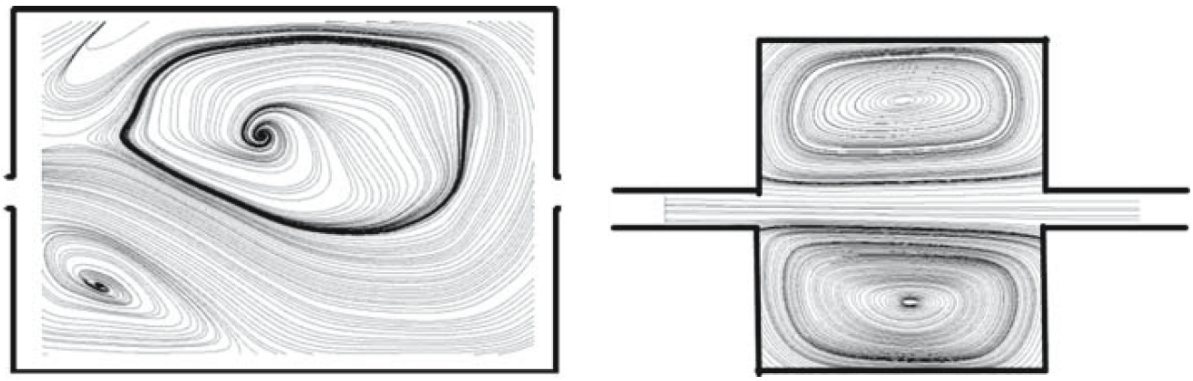

(a) Asymmetric flow field observed for geometry no. 1 in (Dewals et al., 2008).

(b) Symmetric flow field observed for geometry no. 4 in Dewals et al. (2008).

Figure 2.5: Experimentally observed flow field and streamlines for geometries no. 1 (a) and no. 4 (b) in Dewals et al. (2008).

As an example, at Waterdunen the length of the channel is approximately 200 m. With a width of approximately 40 meters, one finds an AR of 5. Assuming all three cases are active, the effective jet width is 12 m. Therefore, the ER is approximately 3.3. According to the research of Graber (2006), the AR is large enough to enforce asymmetric flow. This is further enhanced by the asymmetrical inflow and geometry at Waterdunen, which will be explained in chapter 3. It can be concluded shallow jets can either be symmetrical or asymmetrical depending on the inflow boundary condition, channel geometry, and channel topography. Whether the jet remains symmetric or becomes asymmetric influences the shape and size of the adjacent recirculation zones.

2.3. An introduction to boundary layers

The transition from hydrodynamics to morphodynamics and therefore sediment transport can often be found in the flow boundary layers. Furthermore, boundary layers can be difficult to capture within numerical models (Andersson et al., 2011). Flow near a solid wall is characterized by large velocity differences. At the wall the fluid will have zero velocity relative to the wall, meaning at a stationary wall the velocity of the fluid is equal to zero. This is called the no-slip condition. The no-slip condition gives rise to a large velocity gradient in the flow as the zero velocity at the wall quickly increases to the free-stream velocity. The height in the water column spanned by this velocity gradient is called the boundary layer. Properties such as the bed shear stress are largely dependent on the boundary layer, indicating the importance of boundary layers for sediment transport.

Boundary layers can either be turbulent or laminar depending on the Reynolds number. Water starts to show turbulent processes at $Re > 1000$ (Uijttewaal, 2018). As an example, at Waterdunen the stream-wise velocity U is in the order of 3 m/s and the water depth in the order of 3 m, meaning the vertical Reynolds number can be estimated to be in the order of 10^7. This means the boundary layer can be characterized as being turbulent. Turbulent boundary layers consist of four sections, as portrayed in the schematization shown in figure 2.6 (Uijttewaal, 2018).

The wall region spans around 20% of the total boundary layer height while the core region spans the other 80%. Within the wall region, the separation of the viscous sub-layer, buffer layer, and inner layer is made based on the dominating terms in the definition of the total horizontal shear stress shown in equation 2.8. The first term in the equation indicates the shear stress induced by viscous forces while the second term is called the horizontal Reynolds stress which is a turbulent shear stress (Andersson et al., 2011).

$$\tau_{xy} = \rho\nu\frac{d\langle\vec{u}\rangle}{dy} - \rho\langle u_x u_y\rangle \tag{2.8}$$

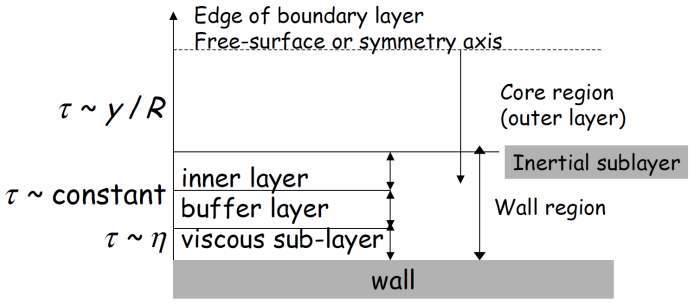

Figure 2.6: Schematization of the bottom boundary layer (Uijttewaal, 2018).

- In the viscous sub-layer, the first term dominates and the shear stress is primarily determined by viscous forces. This can be explained due to the no-slip condition, stating that the horizontal flow velocities should reach zero at the wall. Therefore at the wall itself, the horizontal shear is solely determined by viscosity.
- Further up in the water column the flow velocities start to increase and as a result, the Reynolds stresses increase in magnitude. The region where the viscous stresses and Reynolds stresses are of near-equal magnitude is called the buffer layer.
- When the turbulent stresses start to dominate the inner layer or the fully turbulent sub-layer is reached. In the fully turbulent sub-layer, the flow velocity is nearly equal to the free stream velocity.

Empirical data captures these transitions using wall parameters. The wall parameters are captured in the set of equations 2.9 (Andersson et al., 2011).

$$\begin{aligned} u_* &= \sqrt{\tau_w/\rho} \\ l_* &= \nu/u_* \\ U^+ &= U/u_* \\ y^+ &= y/l_* \end{aligned} \tag{2.9}$$

In this set of equations, u_* is a shear velocity and l_* a wall-length scale where viscosity dominates. y^+, therefore, defines the ratio between the actual height in the water column and the height largely dominated by viscous forces. This ratio can be used to define boundaries for each layer:

- $0 < y^+ < 5$: Viscous sub-layer
- $5 < y^+ < 30$: Buffer layer
- $30 < y^+ < 400$: Fully turbulent sub-layer

Using this characterization, one can visualize the contributions of the two terms in equation 2.8 for the specific regions. This is made visible in figure 2.7. The figure shows the ratio between the total shear stress to the relative terms in equation 2.8. Initially, the first term dominates but sharply diminishes with increasing y^+. Somewhere within the buffer layer, the second term starts to dominate and eventually, the contribution of the viscous stresses is negligible somewhere in the fully turbulent sub-layer. It should be noted that the total shear stress remains approximately constant over the entire wall region, as is shown by the top function. In this section, it was shown the no-slip condition introduced at solid walls creates a layer of high-velocity gradients wherein sediment transport takes place. Furthermore, the size of this boundary layer can be approximated with empirical formulae. When the flow is subject to a horizontal or vertical expansion, boundary layer separation may occur. Both horizontal and vertical flow separation will be discussed in the subsequent sections.

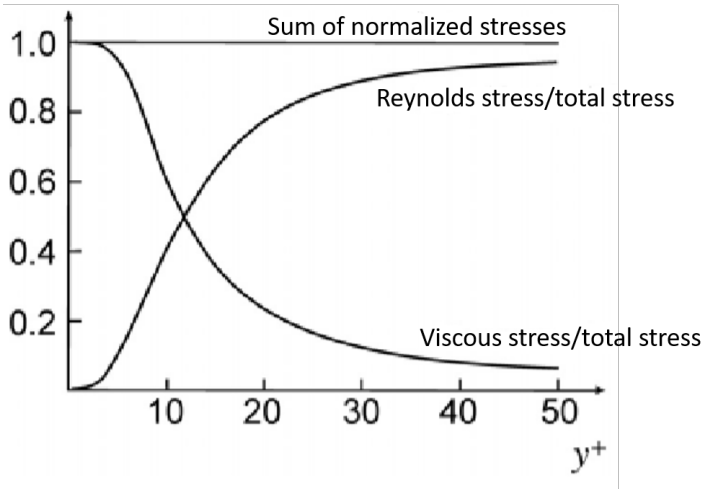

Figure 2.7: Near-wall stresses in the inner region of the turbulent boundary layer (Andersson et al., 2011).

2.4. Vertical boundary layer separation and attachment

In non-uniform channels, the behaviour of the boundary layers can change as a result of geometric or topographic changes. Vertical flow separation is a well-studied subject which is known to introduce complex hydrodynamic processes into the system. However, recent research by Broekema et al. (2020) has shown the flow may remain attached under certain conditions. This section discusses both possibilities.

2.4.1. Vertical flow separation

Vertical flow separation occurs when the vertical boundary layer loses contact with the bed. The cause for flow separation is often an adverse pressure gradient. The adverse pressure gradient works in the direction of the bed shear stress, diminishing the equilibrium of forces held by a stable boundary layer (Simpson, 1996). A possible cause for the adverse pressure gradient is a deceleration of the flow near a deepening of the channel. The process of vertical flow separation is shown in figure 2.8. Figure 2.8a shows an initially stable boundary layer with the pressure force and wall shear stress in equilibrium and opposite of sign. With a sudden sign change of the pressure in figure 2.8b the forces can no longer be in equilibrium, creating an unstable scenario.

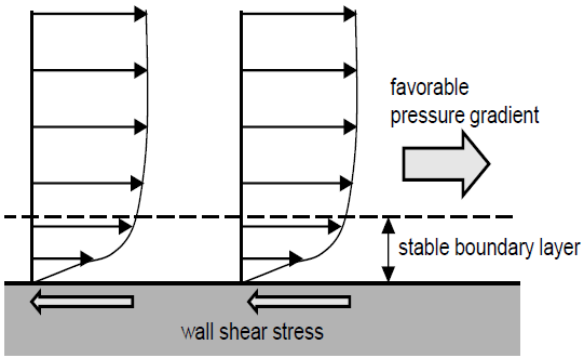

(a) Favourable pressure gradient in the direction of the flow.

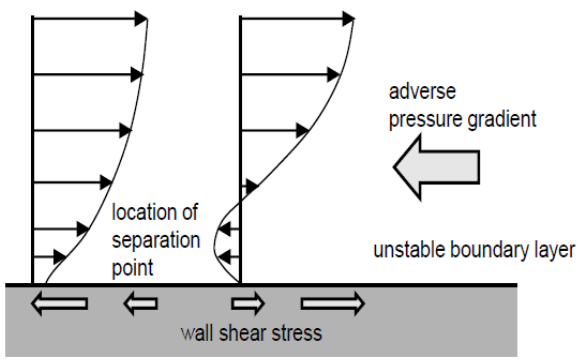

(b) Adverse pressure gradient separating the boundary layer.

Figure 2.8: Illustration of flow separation showing the impact of a pressure gradient on the boundary layer equilibrium Talstra (2011).

A well-studied case of vertical flow separation occurs at the backward-facing step (BFS), as shown in figure 2.9. The hydrodynamic processes occurring at a BFS are similar to flow separation over sloping bottoms such as present in scour holes. A summary of the hydrodynamic processes thriving at the BFS is given by Chen et al. (2018). The flow field generally consists of four regions, being the separated

shear layer, the recirculation region, the reattachment region and the attached/recovery region (Chen et al., 2018).

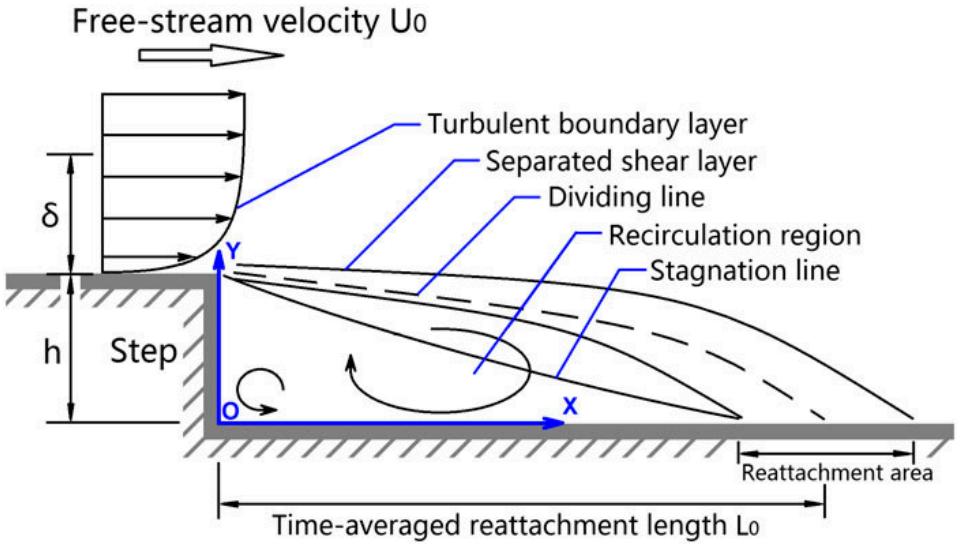

Figure 2.9: Schematic of turbulent backward-facing step flow (Ma and Schröder, 2017).

2.4.1.1 Reattachment region

The reattachment region reaches from the expansion to the reattachment point, which is the location where the turbulent shear layer collides with the solid wall. Furthermore, it marks the end of the recirculation region. The point of reattachment can be considered to be the location where the highest bed shear stresses occur on the bed due to the combination of high mean flow velocities and large turbulent fluctuations (Schiereck, 2017). The location of the reattachment point is fluctuating in time within a certain range. For the case of the BFS, the distance between the step and the reattachment point is dependent on the step expansion ratio, which is the difference between surface-level heights up- and downstream of the step (Simpson, 1996). Flow separation over a curved bottom is more complex as the point of separation varies with flow characteristics like the Reynolds number (Razi et al., 2017). The linearly sloping bed considered in the case of Waterdunen lies in between both boundaries and can be compared to flow separation over a scour hole. Hoffmans and Booij (1993) states that for flow separation over scour holes, the reattachment length varies between 5 and 8 times the maximum scour hole depth. At the reattachment point, the flow is separated into two streams, one towards the recirculation zone and one in streamwise direction. Bradshaw and Wong (1972) state that this causes the large eddies in the shear layer to be torn in two, resulting in a rapid decrease of turbulent shear stress.

2.4.1.2 Shear layers

Bradshaw and Wong (1972) state that two shear layers exist after separation. Within the first shear layer, the fluid is relatively unaffected by the step, but follows the side effects of the separation like the curvature of the streamlines. This shear layer is referred to as the original shear layer. The new shear layer, indicated by separated shear layer in figure 2.9, is well-represented by a Gaussian velocity profile and contains large eddies. These eddies grow by entraining fluid from the recirculation zone and the original shear layer. The shear layer is the result of the velocity difference between the original shear layer and the recirculation zone. The dividing line falls within the shear layer as shown in figure 2.9. This line indicates the point in the water column where the integrated velocity from the wall upwards changes sign from negative to positive (Adrian et al., 1998).

2.4.1.3 Recirculation region

If the adverse pressure is large enough, the flow near the wall can redirect to be opposite to the depth-averaged longitudinal flow, giving rise to a recirculation zone. The flow velocity in the recirculation

zone is around 30% of the main-stream velocity (Uijttewaal, 2018). For a sloping bed, Broekema et al. (2020) showed that it is the vertical recirculation region that dissipates most of the kinetic energy in the flow. The stagnation line indicated in figure 2.9 spans the area where the time-averaged velocity equals zero.

2.4.1.4 Attached region

As stated above, after flow reattachment the shear stress reduces significantly. A new boundary starts developing from the surface downstream of the reattachment point in which the logarithmic velocity profile holds well. However, Bradshaw and Wong (1972) states it takes around 30 times the mixing layer width at the point of reattachment to fully develop this new boundary layer.

2.4.2. Vertical flow attachment

Observations near the ES-SSB showed a contraction of the streamlines at the water surface after the jet exit rather than the expected flow divergence as observed in the standard jet profile in figure 2.1. Furthermore, the scour hole found downstream of the jet was observed to reach depths deeper than the expected equilibrium scour depth. This case was researched by Broekema et al. (2018), who observed that a vertically uniform velocity profile persisted in the scour hole. This means flow separation had not occurred and the flow remained attached, leading to high flow velocities near the bed. Broekema et al. (2018) showed this phenomenon called vertical flow attachment was partly the result of the conservation of potential vorticity. The conservation of potential vorticity states that the ratio between vorticity and water depth remains constant. If the water column elongates due to an increase in water depth, the vorticity of the column needs to increase to conserve angular momentum and therefore potential vorticity. This conservation law is shown in figure 2.10, where in the case of flow attachment the bulk of the flow is redistributed in the vertical plane (2.10a) while in the case of flow detachment the bulk of the flow is redistributed in the horizontal plane (2.10b). With the extra assumptions of small lateral velocities and lateral slip boundaries, Broekema et al. (2018) showed that due to this conservation of potential vorticity, flow over an expansion may experience additional streamwise accelerations, which can reduce the deceleration due to the expansion and therewith result in flow attachment.

This theory led to several follow-up experiments. Van de Zande (2018) conducted physical model tests for shallow jets aiming to find the relation between horizontal flow contraction and vertical flow attachment, as will be explained in section 2.6. Üşenti (2019) researched the development of scour holes for jet flows to investigate the effect of the horizontal non-uniform flow field behind a lateral expansion. He also found higher near-bed velocities compared to the horizontal uniform flow case. Furthermore, he found an uniform vertical velocity profile, which is in-line with van de Zande (2018) and Broekema et al. (2018). He also noted that convergence of the surface flow does not necessarily indicate vertical flow attachment.

Broekema et al. (2020) conducted similar physical experiments considering horizontal non-uniform flow over a longitudinal linear slope. They found that the transition from vertical flow attachment to vertical flow separation occurred for milder lateral gradients in streamwise velocity. By investigating the lateral velocity gradient and the mixing layer width, they concluded that the phenomenon of flow attachment could not exclusively be related to the conservation of potential vorticity. However, the vertical stretching and horizontal compression of the conveying flow as in figure 2.10 could be observed in the experiments.

By comparing the separated and attached flow cases, it was concluded that flow separation and the corresponding recirculation zone are far more dissipative compared to a flow that remains attached. A lot more potential energy is lost, which is why the pressure decreases over the slope. Therefore, no connection between the pressure gradient and the transition between flow states could be determined. As the streamwise pressure gradient was observed to be highly uniform throughout the domain, it was hypothesized that there is a difference between the global and local flow behaviour.

A second rising hypothesis was that the transition between flow states may originate from the extra turbulence induced by the horizontal non-uniformity and the longitudinal slope. It was concluded that high lateral velocity gradients positively stimulate flow attachment. High lateral velocity gradients are

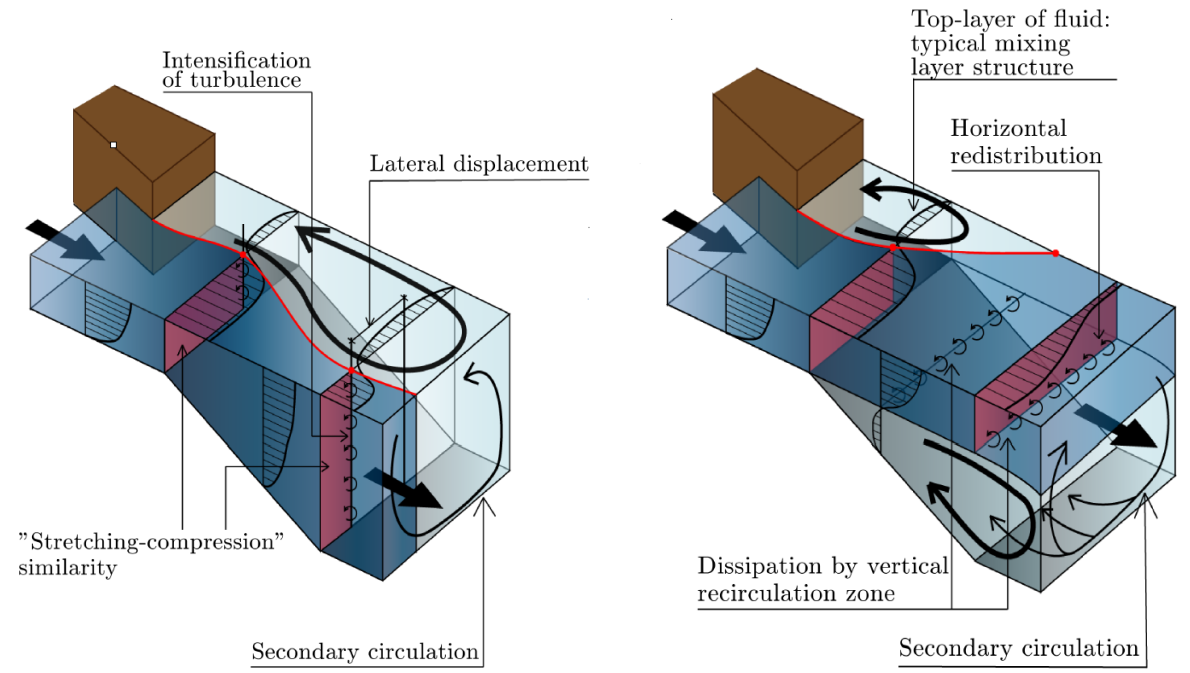

Figure 2.10: Conceptual visualization of the two different observed flow structures in the flume experiment carried out by Broekema et al. (2020). (a) a flow that stays attached to the bed and converges in the horizontal plane; (b) a flow that separates from the bed and diverges in the horizontal plane. In both cases, the velocity averaged over the flume cross-section reduces proportionally to the increase in cross-section, but in (a) the bulk of the flow (Red cross-section) is redistributed over the vertical whereas in (b) the bulk of the flow is redistributed over the horizontal. The red line denotes the interface between the main flow and the horizontal recirculation zone (Broekema et al., 2020).

paired with high turbulence intensities and instabilities. The slope was shown to intensify the turbulence. Therefore, it is possible that the horizontal mixing layer grows larger due to the increased turbulence and compresses the flow conveying channel, stimulating flow attachment.

This section showed that if the flow is subject to an adverse pressure gradient, either the flow can remain attached to the bed or the flow can separate. In the case of the latter, more kinetic energy is dissipated in the system due to the vertical recirculation zone. In the case of flow attachment, the flow velocities at the bed are higher, increasing the risk of scour.

2.5. Horizontal flow separation

Considering flow subject to a horizontal expansion, horizontal flow separation might occur. Flow separation in the horizontal plane contains many similarities with flow separation in the vertical plane, where this time the horizontal boundary layer loses contact with a lateral wall. An illustration of the different terminologies used in horizontal boundary layer separation is shown in figure 2.11 in the form of flow past a single rectangular groyne. Due to separation, a lateral velocity gradient occurs over the separation area, which causes a lateral transfer of streamwise momentum in the form of a shear layer as visible in figure 2.11(c) and (d). Similar to vertical flow separation, the momentum transfer creates a zone of recirculating flow. Talstra (2011) indicates that such a recirculation is often steady for shallow flows with solid walls, and is indicated as the primary gyre in figure 2.11(b) and (c). The recirculation zone spans the reattachment length, after which the lateral boundary layer restores. Castro and Epik (1996) found it takes around 2.5 times the reattachment length before the boundary layer is fully restored. Furthermore, the shear stress was found to fall below the standard value for boundary layers after the initial increase at the reattachment point.

The primary gyre can in turn give rise to an adverse pressure gradient, allowing it to separate from the wall. This can result in a secondary gyre, indicated in figure 2.11(b) and (c). Whether a secondary

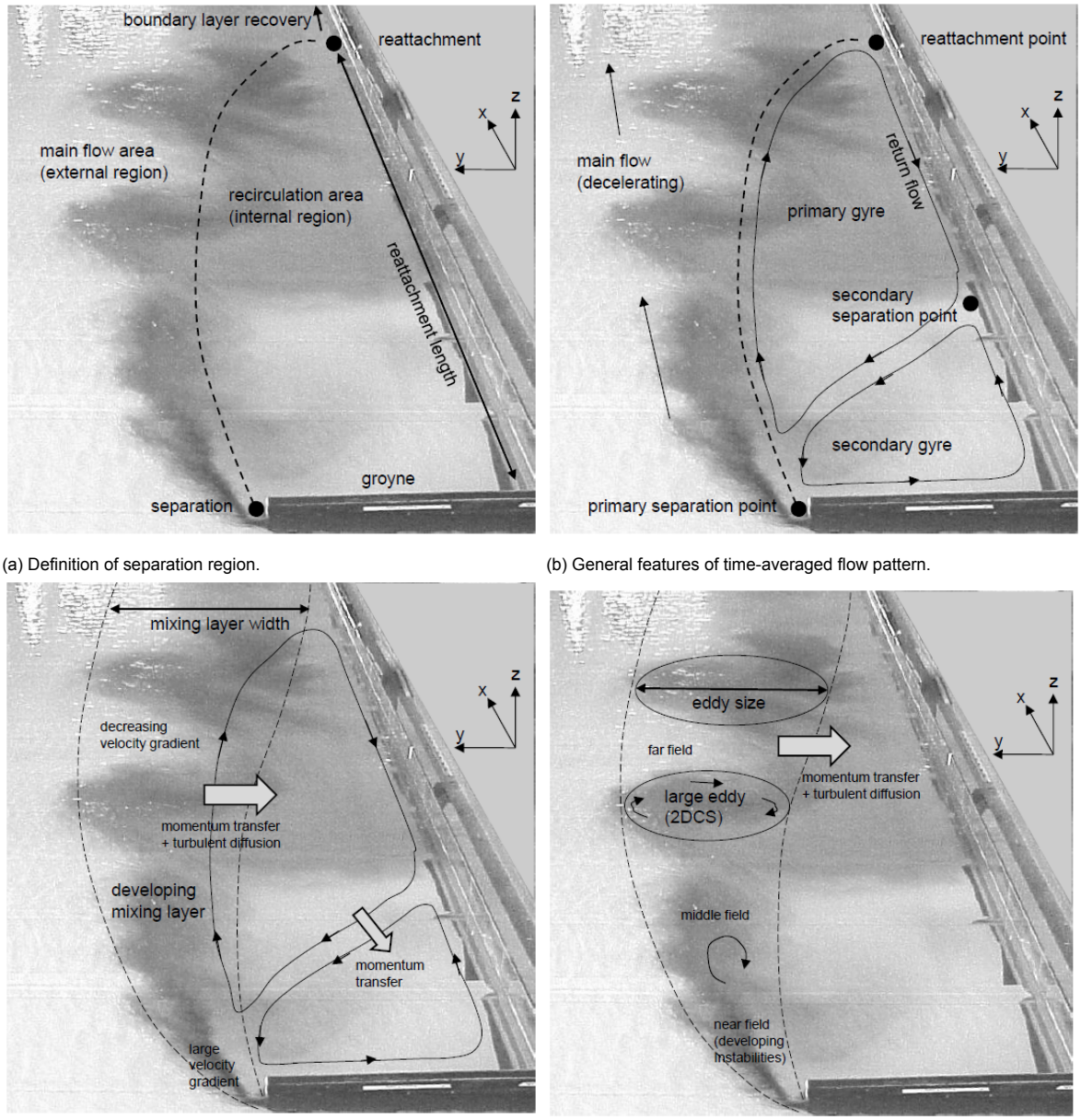

(a) Definition of separation region.

(b) General features of time-averaged flow pattern.

(c) Mixing layer development, velocity gradients, momentum transfer and turbulent diffusion.

(d) Large eddy development (vortex shedding).

Figure 2.11: Explanation of general terminology for shallow separation events (example: shallow flow past single groyne, laboratory experiments by van Prooijen (2004)). Turbulent flow details are visualized by dye which has been injected in the neighborhood of the groyne tip (Talstra, 2011).

gyre forms depends on the local geometry (Talstra, 2011). It was found that when such a secondary gyre is observed, its location is more variable than the stable primary gyre. A secondary gyre can also be observed in vertical flow separation, as shown in the upstream corner in figure 2.9.

Within the shear layer, multiple 2DCS can be observed. Within the groyne field, these 2DCS can either develop along with the mixing layer or develop stationary just downstream of the groyne tip. In the case of the latter, the gyre detaches from the groyne tip and propagates downstream once it has sufficiently grown in size and energy, often merging with the primary gyre. The growth of the 2DCS in the mixing layer occurs roughly proportional to the mixing layer width. Talstra (2011) found that the occurrence of these 2DCS is dependent on the formation of the secondary gyre rather than flow separation or the primary gyre alone. Therefore, they do not originate solely from topographic forcing, but

rather from the gyre configuration. The 2DCS sustain the primary gyre by feeding it momentum and energy, which is a typical 2DH effect. Furthermore, within the numerical analysis of Talstra (2011), it was found that regardless of the 2DH structure of the flow, the 2DCS cause vertical recirculation zones which are said to originate from the centrifugal forces.

2.6. Experiment of van de Zande (2018)

Most of the aforementioned hydrodynamic processes in shallow jet flows can be observed in the laboratory experiments of van de Zande (2018). The laboratory experiments were set-up to investigate the influence of both a lateral velocity gradient and grid turbulence on flow separation over a longitudinal slope in shallow water flow as a part of an ongoing study of the flow near the ES-SSB. A schematization of the experimental set-up is shown in figure 2.12.

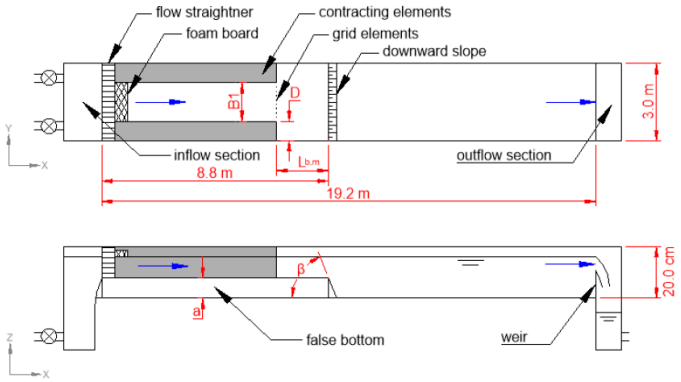

Figure 2.12: Top and side view of the experimental layout including the main dimensions of the shallow water flume. The variables indicate the upstream flow width B_1, the width of a single contracting element D, the distance between the lateral expansion and the upstream end of the downward slope $L_{b,m}$, the height of the false bottom a and the upstream scour slope β The blue arrows indicate the flow direction (van de Zande, 2018).

Particle Image Velocimetry (PIV) was used to visualize the surface flow field, whereas Acoustic Doppler Velocimetry (ADV) was employed to measure flow velocities at various locations in the water column. For experiment 2.4.1, the results are discussed below. The reader is referred to van de Zande (2018) for more information regarding the experiment.

2.6.1. PIV measurements

Three cameras were used for the PIV measurements, ranging from $x = 6.15$ m to $x = 10.96$ m, with the expansion located at $x = 8.8$ m. The entire width of the flume was monitored. The time-averaged flow profile of all three cameras is shown in figure 2.13. Note that the cameras solely measure the surface flow velocities due to the usage of PIV. The black dots indicate the location of the ADV measurements, whereas the dotted lines indicate the range of the longitudinal slope. In figure 2.13 a lateral contraction of the streamlines is clearly visible, starting at the beginning of the longitudinal slope. Furthermore, the jet can be observed to move towards the eastern side of the channel, indicating an asymmetric flow profile.

The streamlines in figure 2.13 show the existence of four separate recirculation zones. Two upstream corner eddies can be observed on either upstream corner of the expanded section of the flume. Furthermore, the dominant and non-dominant recirculation zone can be observed adjacent to the jet on either side of the flume.

2.6.2. ADV measurements

Contrary to the PIV measurements, ADV measurements are limited to one location at a time. In total 24 unique locations have been measured during the experiment, in which the x, y, and z locations differ. In streamwise direction measurements were carried out just in front of the slope ($x = 8.7$ m), on the slope ($x = 9.04$ m) and just after the slope ($x = 9.38$ m). The horizontal variation in the measurements

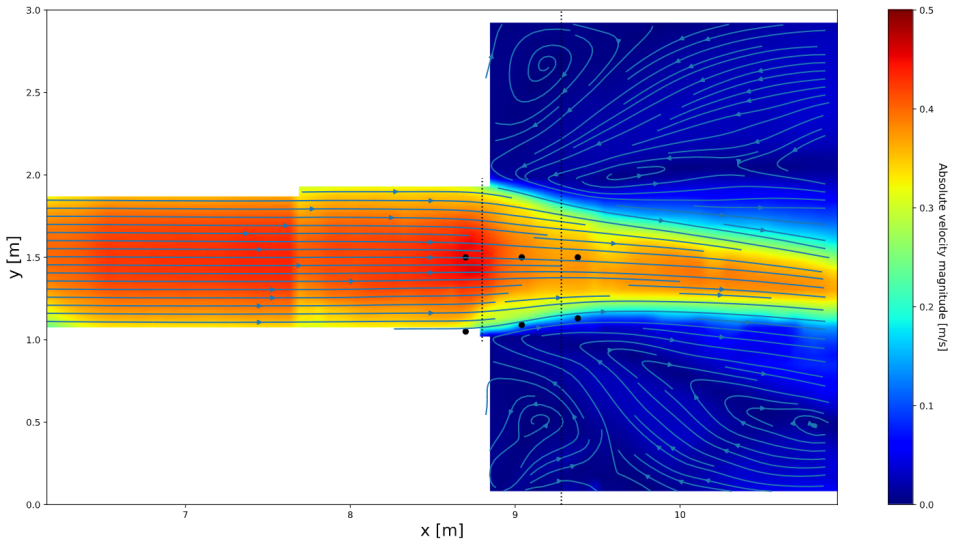

Figure 2.13: Time-averaged surface flow profile of all three cameras used in the PIV analysis of experiment 2.4.1 in van de Zande (2018). The black dots indicate the ADV measurement locations.

is shown as the black dots in figure 2.13. The variation over depth of the ADV measurements is shown in figure 2.14 at the locations with $y = 1.5$ m. This depth variation is identical for the other measurement location for the same x.

Figure 2.14 clearly shows the absence of flow separation over the slope. Nevertheless, it can be seen that the adverse pressure gradient does slow down the flow velocities close to the bed. This phenomenon causes the velocity profile to deviate from a standard logarithmic velocity profile on the slope and further downstream, whereas the upstream velocity profile seems to adhere to the logarithmic velocity profile.

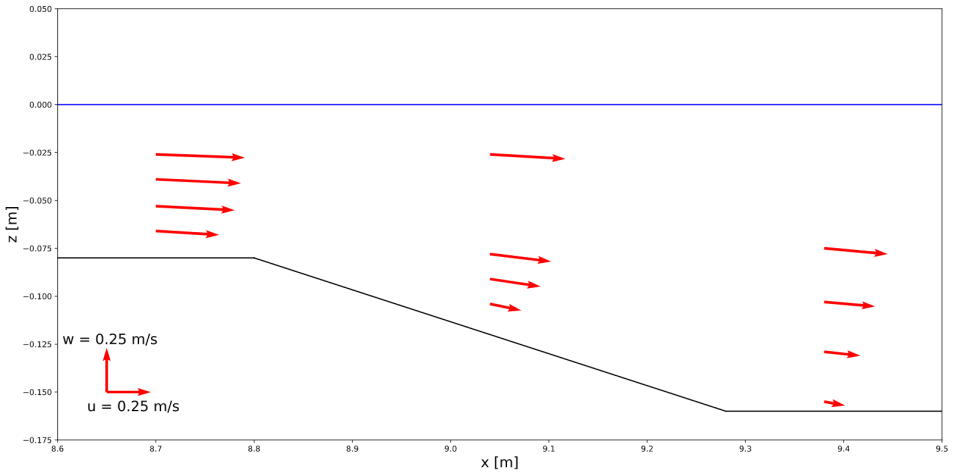

Figure 2.14: Time-averaged ADV measurements at $y = 1.5$ m during experiment 2.4.1 in van de Zande (2018).

2.7. Conclusion

In this chapter, the behaviour of shallow jets as known in literature has been discussed. Shallow jets are characterized by a transverse length scale which is significantly larger compared to the vertical length scale, allowing large-scale horizontal turbulent structures to dominate over the vertical turbulence. After the lateral expansion, the jet starts exchanging momentum with the stationary ambient fluid, altering the horizontal velocity profile and curving the shear layers into the ambient fluid. On either side of the jet, a recirculation zone can be identified.

It was observed that this classical jet profile is not always adhered to. It was shown by Dewals et al. (2008) that a symmetrical jet configuration is highly unstable for turbulent flows with high expansion ratios and aspect ratios. The stable asymmetrical configuration favours either side of the channel and introduces a dominant and non-dominant recirculation zone, which can differ both in shape and size from their symmetrical counterparts.

When the jet is subject to a streamwise decrease in bed level, vertical flow separation might occur. The adverse pressure gradient created by the higher water-depth works together with the bed shear stress to decelerate the flow and can reverse the flow direction. This process is similar to horizontal flow separation, which often occurs if the expansion of the jet is sudden. Both types of flow separation create a zone of recirculating flow which contains a stable primary gyre and sometimes a less stable secondary gyre. If the strength of the adverse pressure gradient is reduced, as for example at a gradual deepening of the channel, the flow might remain attached. It was observed this phenomenon of flow attachment is related to a horizontal contraction of the jet and depends on the lateral non-uniformity of the flow (Broekema et al., 2020).

This chapter showed that several hydrodynamic processes in shallow jets have been studied using laboratory experiments. However, it is still unclear how well numerical models are capable of capturing these processes. In the upcoming analysis of the measurement data at Waterdunen, these hydrodynamic processes will be sought after. Identifying the hydrodynamic processes at Waterdunen helps both to understand the flow and to set-up requirements for numerical models to reproduce the flow.

3

Data analysis Waterdunen

This chapter explains the case study of Waterdunen and the corresponding measurement campaign that was carried out. After an introduction to Waterdunen in section 3.1, the set-up of the measurement campaign is explained in section 3.2. Afterwards, the data obtained during the measurement campaign is processed in section 3.3. The data is analysed from a depth-averaged perspective in section 3.4 and from a vertically varying perspective along transects in section 3.5. The purpose of both analyses is to discover which hydrodynamic processes thrive at the considered channel at Waterdunen. Finally, the main findings are concluded in section 3.6.

3.1. Introduction

Waterdunen is a newly built recreational area aimed to increase the ecological, economical, and cultural value of West-Zeeuws-Vlaanderen, The Netherlands. It consists of an inland lake connected to the Western Scheldt with a tidal culvert (Dutch: *Getijdenduiker*). The culvert serves to translate the tidal motion of the Western Scheldt to Waterdunen in a controlled fashion. By partially closing off the culvert, a damped tidal motion is created in Waterdunen. The culvert outflow can be characterized as a shallow tidal jet and induces high flow velocities on either side of the culvert. To prevent the undermining of the overlaying dikes due to scour, a bed protection was designed to keep potential scour holes away from the culvert. The executor of this design project was Svašek Hydraulics commissioned by the public government Waterschap Scheldestromen and the province of Zeeland. At the seaside of the culvert, this bed protection was designed based on a depth-averaged numerical model. However, a lot of uncertainty persisted in the determination of the maximum magnitude of the flow velocity at the seaside of the culvert. Therefore, a measurement campaign was carried out to properly determine the behaviour of the flow and to validate a subsequent three-dimensional numerical model. During the campaign, the flow velocities were observed to be higher than originally anticipated and it was shown a three-dimensional numerical model rendered more accurate flow velocities over the channel length.

The tidal culvert at Waterdunen consists of four separate casings, each having a width of four meters and a height of three meters through which water can pass. Figure 3.2 shows a detailed overview of the seaside channel. Three out of the four casings serve to create the damped tidal motion in Waterdunen while the most western case in figure 3.2 serves to drain water from the nearby polder. Figure 3.1 shows an overview of the area. The culvert is constructed inside the dikes which protect the hinterland from the Western Scheldt. Two automatic slides are serially placed within each casing to regulate the amount of water allowed to pass through the culvert, creating a similar scenario as a sublate (Dutch: *onderspuier*) if one of the slides is in use.

Throughout the remainder of this work, the two channels on each side of the culvert will be called the seaside, which refers to the Western Scheldt side. Whereas the channel that connects the Western Scheldt side to the inland lake of Waterdunen will be called the inland side. The presented study will focus on the former of the two. It can be seen in figure 3.2 that the outflow of the culvert flows into a varying topography in the longitudinal and transverse sense with a downward slope in the longitudinal

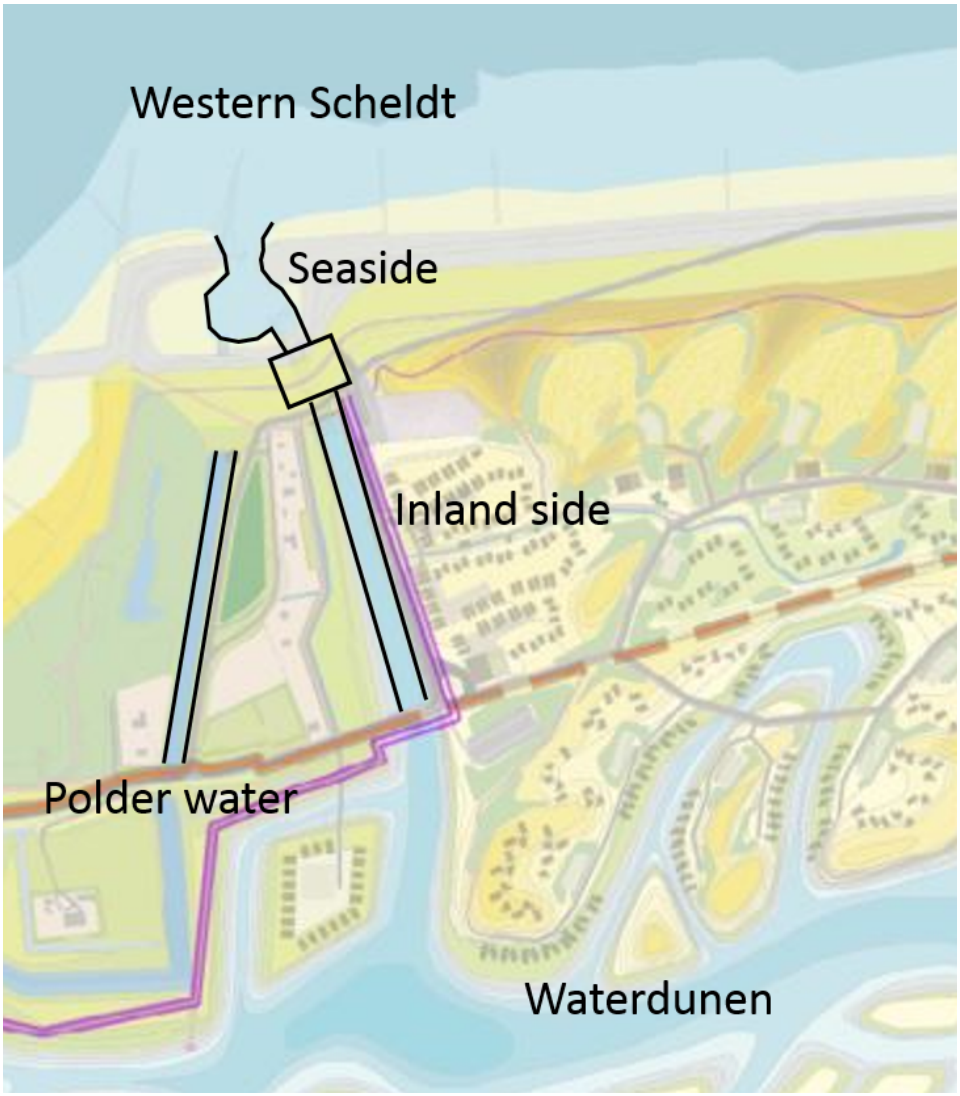

Figure 3.1: Overview of the recreational area Waterdunen showing the tidal culvert connecting the Western Scheldt to the inland lake. Source: http://magazine.waterdunen.com/.

direction directly at the outflow point and 2 slopes in transverse direction throughout the cross-section. A typical plot of the bed levels inside the channel is shown in figure 3.3 (rotated), whereas figure 3.4 shows a side-view of the culvert.

3.2. Measurement campaign

The measurement campaign near Waterdunen consisted of 13 measurement scenarios, of which 7 were carried out at the inland side and 6 were carried out at the seaside of Waterdunen. Detailed information regarding each individual scenario is given in appendix A.1. Four different measurement techniques were used in the campaign, which are summed up in table 3.1. However, the primary source of data used in this thesis are the sailed ADCP measurements.

The regular ADCP (Workhorse Rio Grande) was attached to a vessel that sailed over a variety of transects throughout the channel. The center-line of the channel was considered the priority transect, which was sailed multiple times. However, the vessel often deviated slightly from the straight transect due to the high velocities in the channel. The resulting transects are therefore often curved along the middle of the channel. The ADCP measured the horizontal flow velocities and flow direction in various locations in the water column with a spatial interval of Δz = 0.25 m in the vertical direction and a starting

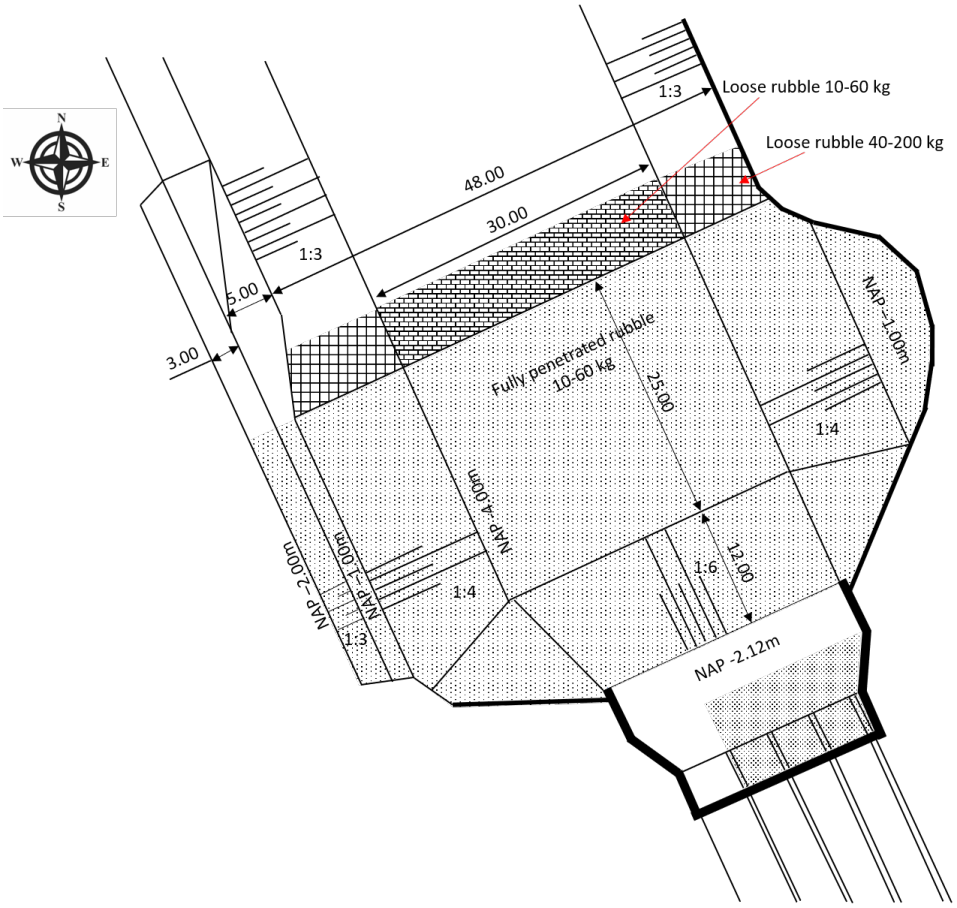

Figure 3.2: Overview of the bathymetry at the seaside of the culvert at Waterdunen.

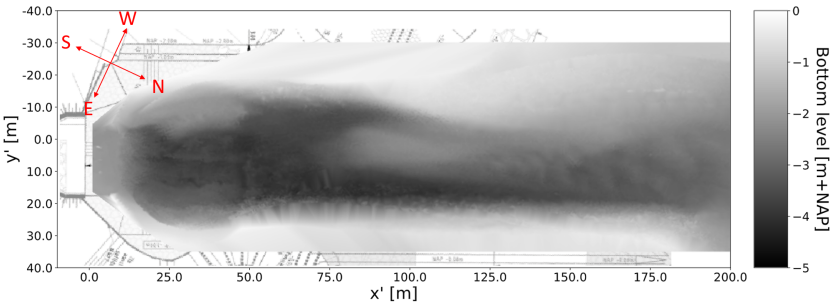

Figure 3.3: Typical bed levels in the seaside channel at Waterdunen.

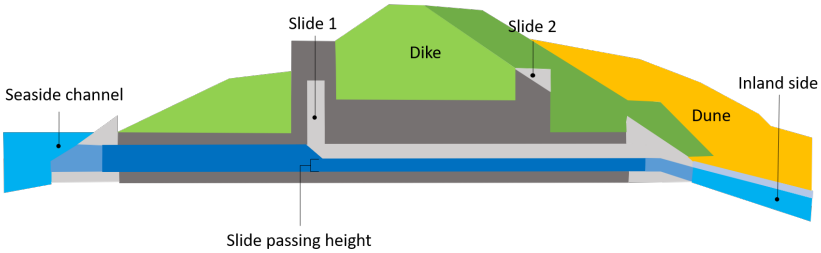

Figure 3.4: Side view of the culvert at Waterdunen.

depth of 1.04 m from the water surface. The water depth along the transect was also measured by the ADCP. The ADCP measured with a frequency of 1.43 Hz or with one full-depth measurement every

Table 3.1: Overview of the measurement techniques used in the measurement campaign. ADCP = Acoustic Doppler Current Profiler and H-ADCP = Horizontal Acoustic Doppler Current Profiler.

Technique	Description	Result
ADCP	Sailing measurements	Horizontal flow profile over depth and water depth
H-ADCP	Stationary measurements	Horizontal flow flow profile over lateral cross-section
Valeport	Sailing measurements	Flow velocity and direction at set depth
Pressure sensor	Stationary measurements	Surface level elevation

0.7 seconds. As the length of each transect varied, the sailing time and therefore the amount of output data varied per transect.

Pressure sensors were placed at pre-determined, stationary locations within the system. On the inland side, two pressure sensors were placed within the lake combined with one pressure sensor at the most eastern casing of the culvert. Inside the culvert, one pressure sensor was placed at the location of the slides. At the seaside two pressure sensors at the most eastern and most western casing of the culvert were placed. Additionally, tidal data obtained from a nearby station at Vlissingen with a time lag and amplitude correction factor was used to simulate the water depths at the seaside of the culvert. The used time lag was 8 minutes and 27 seconds, with an amplitude correction factor of 0.9854.

The velocity measurements obtained using the (H-)ADCP measurements were rendered inaccurate at certain locations close to the culvert due to high air entrapment in the flow. Therefore, measurements of the velocity magnitude obtained using a valeport were used to validate the (H-)ADCP data. A valeport is a propeller attached to a boat to obtain a simple measurement of the velocity magnitude and direction at a set depth, which was around 0.5 m relative to the water surface for the measurement campaign. The valeport was placed on the opposite side of the boat relative to the ADCP, meaning the measurement locations of the two devices varies around 1 meter in longitudinal and 1 meter in lateral direction. The measurement frequency of the valeport was 0.2 Hz or 1 measurement every 5 seconds. The output value is the average of the impeller counts during this time interval.

The slide configuration varied between scenarios but was kept at a constant level during each individual scenario. One of the two slides within each casing was always fully open, while the other slide varied in height. During the first measurement scenario, the slide configuration allowed for a passing water height of 0.4 meters, which increased to the full 3 meters at measurement scenario 5. The definition of the passing height is shown in figure 3.4.

During the measurement campaign, it was observed that sedimentation occurred at the seaside during the time the culvert was not in use. It was expected that the excess sediment would influence the obtained flow profile, which would then deviate from the expected profile obtained when the culvert would be used fully. After the third measurement scenario, it was therefore decided to flush the channel to erode the excess sediment away.

3.2.1. Visual observations

The schematization in figure 3.2 shows that the outflow in the seaside channel is asymmetrical as only three out of the four cases are used to transport water between Waterdunen and the Western Scheldt. During the measurement campaign the following important characteristics were observed (Svasek Hydraulics, 2020):

- The flow strongly concentrates on the eastern side of the channel directly after outflow from the culvert, which is also the location where the highest flow velocities were measured.
- The surface streamlines were observed to contract rather than diverge over the slope.
- The flow is variable and shows meandering properties, meaning the jet flow displaces in transverse direction, dislocating the point of the highest flow velocities to sometimes occur at the main channel and sometimes at the eastern transverse slope. Therefore the flow is observed to be non-stationary, even under relatively constant discharges and water levels.

- Whether the flow concentrates on the eastern slope is dependent on the case configuration. In some scenarios with only the 2 west-most cases active, the flow could concentrate on the western slope.
- The location most vulnerable to high flow velocities is the transition from penetrated rubble to loose rubble at around 37 meters from the culvert indicated in figure 3.2.

A typical flow pattern at the seaside of the culvert is shown in figure 3.5. The initial flow is super-critical coming from the culvert (point A). At the interface between sub- and super-critical flow an hydraulic jump is present just in front of the slope (point B). At the longitudinal slope, the jet visibly contracts, which leads to higher flow velocities (point C). Furthermore, the flow can be seen to move towards the eastern side of the channel. At point D the flow hits the bank and a clear recirculation zone can be distinguished towards the east, indicated by point E. The jet moves further north and starts to expand in lateral sense (point F). This marks the end of another recirculation zone towards the west of the channel indicated (point G).

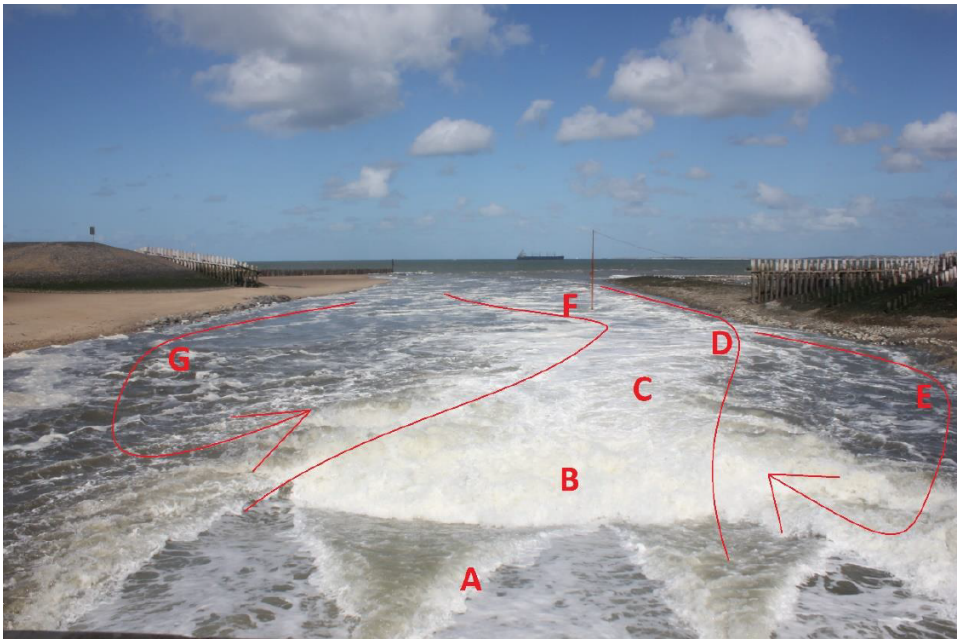

Figure 3.5: Typical flow scenario at the seaside of the culvert (Svasek Hydraulics, 2020).

3.3. Data processing

The data sets available for each measurement scenario contains the ADCP measurements of all the transects sailed during the scenario, the H-ADCP measurements during the scenario, the water levels at the inland side and the seaside as measured by the pressure sensors, the slide configurations during the time span of the scenario and the modified seaside water level as computed using the Vlissingen data. Scenario 4 to 6 contain the additional valeport data, of which scenario 6 consists solely of valeport data. Table 3.2 summarizes the conditions for each measurement scenario. All six measurement scenarios fall within the transition from high water to low water, meaning the downstream water level is dropping during the scenario. The increasing slide passing height causes a variable discharge over the scenarios, with a higher passing height resulting in a higher discharge in most cases.

The primary reason for concern regarding the accuracy of the data comes from the air entrapment in the flow, especially at high flow velocities near the culvert. In scenarios 4 and 5, the ADCP measurements close to the culvert can be validated using the valeport data, as the valeport is unaffected by air entrapment. This enables a direct comparison between the results to evaluate the accuracy of the ADCP. During this comparison, it should be taken into account that the resolution of the valeport is significantly lower than of the ADCP and averages out small timescale turbulence. Therefore it can

Table 3.2: Overview of the six measurement scenarios at the seaside of Waterdunen.

Scenario	Date	Begin time	End time	Transects sailed	Slide passing height [m]
1	17/09/2019	07:50:00	11:51:10	43	0.39
2	20/09/2019	09:38:56	12:56:21	46	0.69
3	25/09/2019	14:38:10	18:27:19	66	0.90
4	07/11/2019	13:10:30	16:13:19	51	1.62
5	04/12/2019	09:49:37	12:17:51	47	2.97
6	20/12/2019	12:30:47	14:32:57	19	1.00

be preemptively said that the ADCP data will fluctuate more and should solely be discarded based on average values.

Additionally, the data was evaluated using a Hampel filter with a threshold value of 7 times the STD and a window size of 9. Details of the Hampel filter are explained in appendix A.2. To ensure enough data points were available for interpolation, the data was replaced using linear interpolation over the window rather than removing the data points.

For the analysis of the data the system is translated to a local, rotated coordinate system (x', y', z), with x' in the streamwise direction towards the Western Scheldt, y' towards the east and z points in the vertical direction. This process is explained in appendix A.3.

3.4. 2DH analysis

For the 2DH analysis, the data was first evaluated using a moving average filter of 3 subsequent data points. The moving average filters out small-scale turbulence to obtain a better view of the mean flow structure during the considered timestep. Afterwards, the data was linearly interpolated to a (x', y', t) grid with $\Delta x' = 2$ m, $\Delta y' = 1$ m and $\Delta t = 10$ min. This results in a 60×100 horizontal grid. The value for Δt was sometimes lower when data sets were removed due to inaccuracies. Using a time-average of 10 minutes ensures multiple transects are sailed during the timesteps, allowing for better coverage throughout the timesteps. Furthermore, the time-averaging ensures the 10-minute-mean flow properties are shown, meaning turbulent fluctuations are not present in the data.

The spatial coordinate system is shown in figure 3.6, showing the origin of the system lies at the outflow point of the culvert in x' direction and along the channel center-line in y' direction. Furthermore, the cardinal directions are added to the figure. Due to the rotation, the eastern direction is on the bottom side of the images, whereas the streamwise direction roughly corresponds to the north direction. In the analysis, these directions are often referred to (e.g. west side of the channel referring to the upper section of the images).

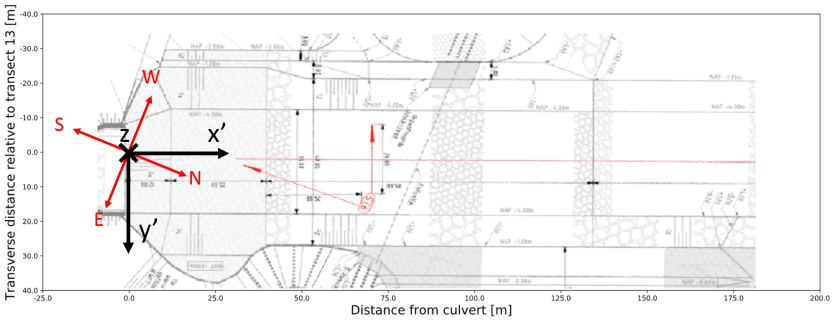

Figure 3.6: Used coordinate system in the data-analysis with x' in streamwise direction, y' in transverse direction and z in vertical direction, together with the cardinal directions.

The measurement scenarios were not carried out to obtain full coverage of the channel, but rather

to focus on the points of interest for the validation of the bed protection. In order to investigate the accuracy of the interpolation, the resolved discharges along lateral cross-sections were compared to the discharges through the culvert based on the water level difference inside Waterdunen. The performance of the interpolation is measured using the relative discharge per transverse cross-section, which is defined as the discharge through a transverse cross-section divided by the actual discharge through the culvert. This process is explained in detail in appendix A.4.

The 2DH analysis of each measurement scenario is given in appendix A.5. This section presents the most important conclusions. During the analysis, it was observed that scenarios 4 and 5 have the most amount of data throughout the channel as transverse cross-sections were sailed during these scenarios. This allows for better spatial interpolation, of which the accuracy can be evaluated using the relative discharge. Scenario 6 solely consists of valeport data, which cannot be transformed into depth-averaged values. Therefore, the scope of the 2DH analysis lies in scenarios 1 to 5. The flow patterns were analysed based on the computed streamlines and absolute velocity magnitudes. The streamlines were projected on a topography map showing the local water depths, which resulted from a topographic survey carried out at the beginning of each measurement scenario. The time interpolation resulted in multiple timesteps T on which data was interpolated. Depending on the scenario, different timesteps contain better or worse measurement coverage throughout the channel. Therefore, the timesteps which are analysed are not equal between scenarios. The current analysis primarily focuses on scenario 5, in which T = 2 (09:59 to 10:06) and T = 6 (10:41 - 10:51) contained the best data quality.

3.4.1. Asymmetry

In all five measurement scenarios, the flow was observed to move towards the eastern side of the channel. It is unsure where the flow starts to curve towards the eastern slope, yet some observations in scenario 3 indicate this process might start at the foot of the longitudinal slope. It was observed that the jet hits the eastern slope at approximately $x' = 45$ m. After the jet hits the eastern slope, the flow either sticks to the eastern side of the channel until most of the energy is dissipated as observed in scenario 3, or the flow curves towards the middle at a distance of around 75 m from the culvert. In the case of the latter, the flow does not seem to move towards the western slope but tends to remain in the middle of the channel. However, a symmetric configuration was not found. A typical flow profile in the channel is shown in figure 3.7. In both figure 3.7a and 3.7b, the eastern concentration of the jet flow is evident. This asymmetric configuration is similar to the asymmetric flow as observed by van de Zande (2018) and Kantoush et al. (2008) and can therefore be attributed to a Coanda-like effect. The cause of the Coanda-like effect was hypothesized to be the asymmetrical inflow and the asymmetrical channel geometry and topography. The important effect of the former has been confirmed by visual observations during the measurement campaign, as for certain outflow configurations with only the two west-most cases active the flow becomes asymmetric along the west side of the channel.

The asymmetry of the flow was captured for measurement scenario 5 using the WCG as explained in the literature study. The unit of the WCG is $[m]$, indicating the weighted lateral coordinate y' where most momentum is transported in the channel. It should be noted that in the definition of the WCG, the negative recirculating velocities on the western side of the channel also contribute to a more eastern position of the WCG in the nominator of equation 2.7. However, the negative recirculating velocities also contribute to a lower value of the denominator. For this reason, the absolute value was taken in the denominator. This way, the recirculating velocities on the west side are not accounted for twice. This works well if it is assumed all velocities on the western side of the channel are negative and all velocities on the eastern side are positive, which is mostly true at Waterdunen. However, caution should be taken when this parameter is employed in different situations.

It can be seen the location of the WCG in streamwise direction varied in time, mostly due to the differences in channel coverage between timesteps. The resulting locations of the WCG at T = 2 during scenario 5 is shown in figure 3.8. Per definition, the location of the WCG is $y' = 0$ for symmetrical flow. Due to the lack of measurements at the outflow from the culvert, the initial locations of the WCG are unavailable. However, directly at the first calculated location of the WCG, the bulk of flow transport is located on the eastern side of the channel. The peak asymmetry, which corresponds to the highest value for the WCG, was measured around $x' = 60$ m from the culvert. However, as was said before,

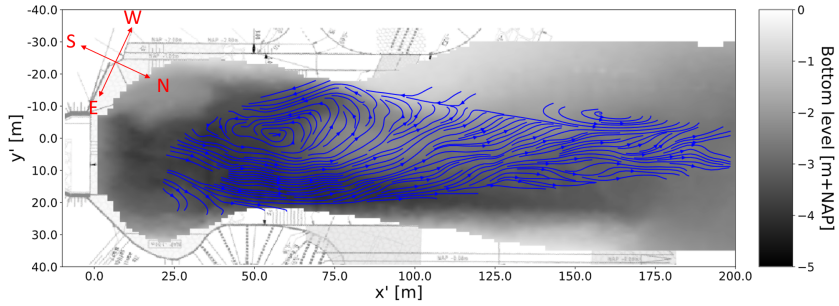

(a) Streamlines for T = 2.

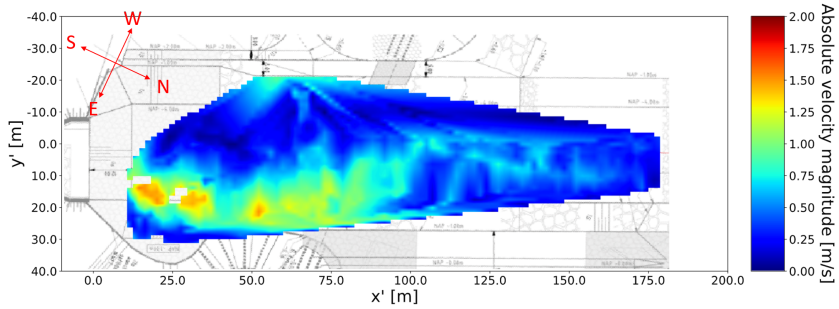

(b) Absolute velocity magnitude for T = 2.

Figure 3.7: Typical flow profile at Waterdunen as collected from the measurement campaign. Data taken from T = 2 (09:59 - 10:06) for scenario 5, which corresponds to Q = 46.6 m^3/s and Δh = 0.4 m. (a) shows the streamlines, indicating the eastern concentration of the flow. (b) shows the absolute velocity magnitude.

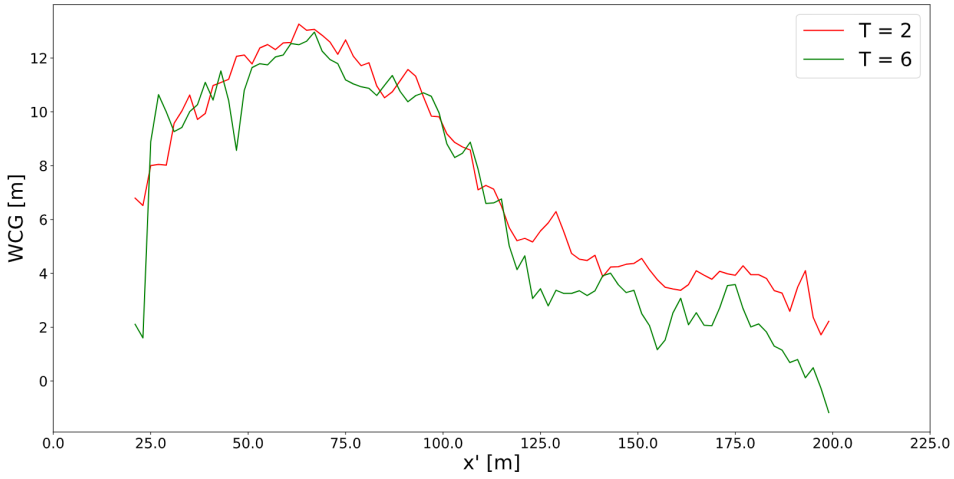

Figure 3.8: Location of the weighted center of gravity for T = 2 and T = 6 during scenario 5.

recirculating velocities on the west side of the channel also contribute to a positive lateral coordinate of the WCG, indicating this location is not necessarily the most eastern location of the jet. However, the lateral position of the WCG seems to comply with the movement of the jet in figure 3.7, which shows the flow remains attached to the eastern slope between $50 < x' < 75$ m. Further downstream, the position of the WCG slowly moves towards the west and approaches $y' = 0$ at $x' = 200$ m from the culvert. The latter indicates the jet spreads out relatively evenly throughout the channel. However, for this purpose, it should be noted a large portion of the western side of the channel is not mapped for $x' > 75$ m.

Between T = 2 and T = 6, it can be seen the maximum lateral position of the WCG changes relatively little. The most notable change occurs at $x' > 110$ m, where the flow tends to become more symmetric at T = 6 compared to T = 2. However, considering the flow profile at T = 6 in figure A.8, this

might be the result of interpolation errors on the east side of the channel.

3.4.2. Recirculation zones

The strength of the recirculating velocities and the size of the recirculation zones were analyzed throughout each measurement scenario. The visual observations stated two recirculation zones are present, one on each side of the jet. Due to the asymmetric flow pattern, the recirculation zones are also asymmetric with the dominant recirculation zone on the western side of the channel and the non-dominant recirculation zone on the eastern side of the channel. Very few transects actually crossed the non-dominant recirculation zone, meaning its existence could not be proven with the data. The dominant recirculation zone can be mapped more accurately. The vertical vorticity defined in equation 3.1 is usually a useful tool to investigate the size of recirculation zones. However, vorticity in definition favours small-scale fluctuations. These small-scale fluctuations are prone to measurement inaccuracies and interpolated values, as a gradient is resolved. After resolving the vertical vorticity field, it was determined the measurement was not accurate enough to provide an accurate estimate of the vertical vorticity. No clear zero-vorticity region could be observed, as would be expected in the center of the jet, and the distinction between dominant and non-dominant recirculation zones is small.

$$\omega_z = \frac{\partial u_{y'}}{\partial x'} - \frac{\partial u_{x'}}{\partial y'} \tag{3.1}$$

Where: ω_z = Vertical vorticity
$u_{y'}$ = Velocity in streamwise direction
$u_{x'}$ = Velocity in lateral direction

For this reason, it was decided to evaluate the width of the dominant recirculation zone by fitting a polynomial through the streamwise velocity component over a lateral cross-section for the entire channel. An example is visible in figure 3.9. The lateral location where the streamwise velocity component becomes negative for the fitted curve was used as an indicator of the width of the recirculating area. Using this approach, no clear variation in the width of the recirculating area could be observed during all scenarios. Even for scenario 4, where the discharge ramps up from low to high values (figure A.12), no clear difference was observed.

The dominant recirculation zone ends where the flow detaches from the eastern side of the channel and spreads out across the channel, blocking the dominant recirculation zone. From the data of scenario 5 in figure 3.7, it can clearly be seen this happens at approximately $y' = 100$ m.

Regarding the strength of the recirculation zone, only for scenario 5 a clear increase in recirculating velocities was observed for increasing discharges. For other scenarios, this increase was either too small to be observed or the data coverage over the recirculation zone was not broad enough to visualize the high velocities. For scenario 5, it was observed the recirculating velocities sometimes exceeded the flow velocity in the primary jet stream. It was discussed in the literature study that the recirculating velocities can be approximated to be 30% of the main stream velocity, which is significantly lower compared to the measured recirculating velocities. This high-velocity recirculating flow is located on the western lateral slope of the channel. As the ADCP device was attached to a boat, measuring along the lateral slope was difficult due to the low water depth. It is hypothesized the ADCP interacted with the water which was displaced by the vessel's propeller, as additional thrust was required to prevent the vessel from running ashore.

3.4.3. Lateral velocity profiles

During the analysis of the recirculation zones, multiple velocity profiles were fitted through lateral cross-sections. For scenarios 4 and 5, the jet appears to have a nice parabolic shape. An example is shown in figure 3.9. The flow shows a clear maximum point on the eastern side of the channel which decreases towards the eastern boundary and towards the middle of the channel, where the flow eventually becomes negative at the start of the recirculation zone. The recirculation zone shows a clear minimum velocity, after which the velocity increases and seems to reach zero at the western boundary.

During scenario 3, a more linear lateral profile was observed. The flow seems to reach its maximum

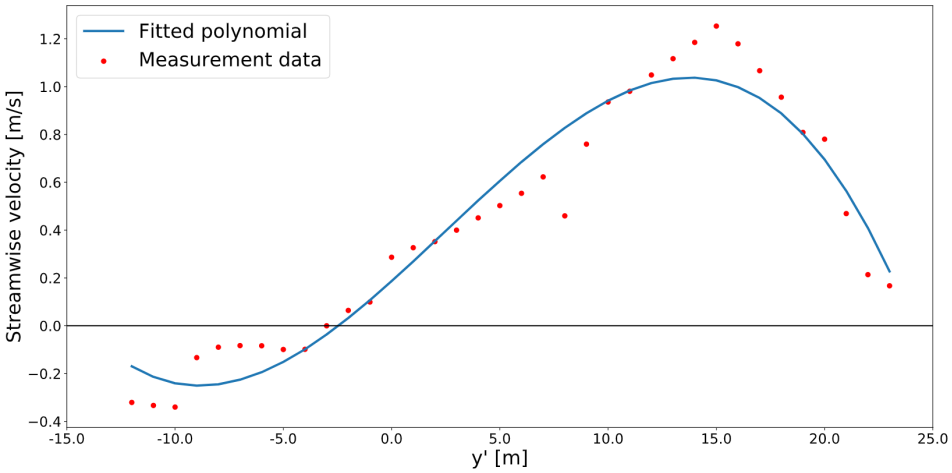

Figure 3.9: Example of polynomial fit through the lateral data points for a lateral cross-section 40 m from the culvert during T = 6 in measurement scenario 5.

very close to the eastern wall, where supposedly a very steep velocity gradient requires the flow to comply with the no-slip condition at the solid wall. However, this gradient was not measured. An example is shown in figure A.21. As the flow velocity becomes negative to indicate the start of the recirculation zone, no clear minimum was observed. However, this was hypothesized to be caused by the lack of data on the west side of the channel.

It was hypothesized the stronger eastern concentration observed during scenario 3 compared to scenarios 4 and 5 was a result of the topographic changes caused by the flushing campaign after scenario 3. However, the stronger concentration was not observed during scenarios 1 and 2 which contain a near-equal topography compared to scenario 3. Therefore no clear cause for the strong eastern concentration was found.

3.4.4. Depth-averaged streamline contraction

It was explained in the literature study in chapter 2 that in standard jet flow the streamlines diverge into the stationary ambient fluid as shown in figure 2.1. Visual observations at Waterdunen showed the surface streamlines contract in horizontal direction rather than the standard divergent behaviour. Due to the little measurements close to the jet, this cannot be confirmed using the data. However, the behaviour of the streamlines further downstream can be analysed.

Considering the streamline plot in figure 3.7 a slight contraction of the streamlines can be noticed when the jet hits the eastern slope. This is slightly visible in figure 3.7a, but is better visible at T = 4 (10:21 - 10:31) shown in figure 3.10. It was hypothesized the better visibility was caused by the higher discharge at the later timestep. The streamlines seem to contract slightly until the jet reaches the eastern side of the channel. After the jet remains attached to the east for approximately 30 meters, the streamlines seems to diverge again.

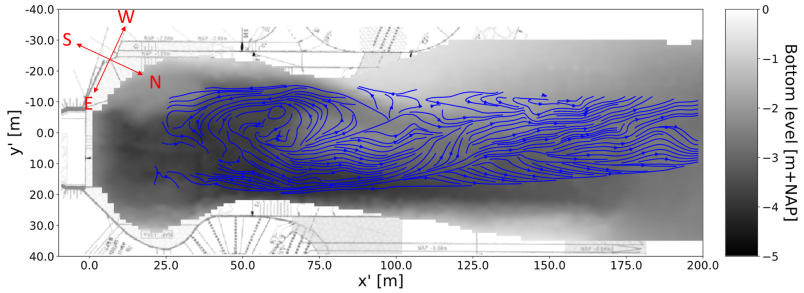

Figure 3.10: Depth-averaged streamline plot for T = 4 during scenario 5.

3.4.5. Surface streamline contraction

When considering the surface streamlines, the contraction of the streamlines can be observed more clearly. This is shown in figure 3.11, showing the surface streamlines for T = 4 during scenario 5. It can be seen the streamlines contract until the eastern slope is hit and diverge again further downstream. Note that the first measurement of the ADCP is at a depth of around 1 m. The lower visibility of the contraction during the depth-averaged analysis might be caused by the lower quality of the data at depth.

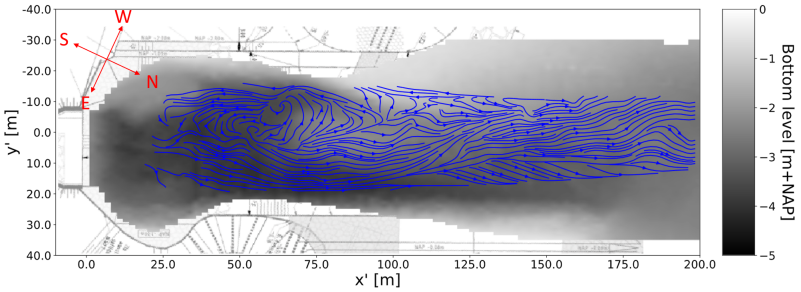

Figure 3.11: Surface streamline plot for T = 4 during scenario 5.

3.4.6. Topography

The flushing campaign carried out after scenario 3 allows the flow behaviour to be tracked for multiple topographic configurations. Figure 3.12 shows three topographic maps for scenario 3, 4 and 5 respectively. The result of the flushing campaign is evident comparing figure 3.12a and 3.12b, where the shallow sand bar in the middle of the channel has been flushed away. However, a clear separation between a shallower middle and a deeper eastern section persists in the channel.

Comparing figures 3.12b and 3.12c the development of the channel in time can be seen. The shallow section in the south-west corner of the channel seems to be subject to erosion, deepening the western side. However, further downstream the western section seems to be subject to sedimentation. Considering the deep channel on the east side, a clear alternating bar pattern seems to develop between both scenarios around 100 m from the culvert, moving towards the middle of the channel. Though these topographic changes can serve as a proxy for the averaged flow phenomena in the channel, a lot more information is required to draw clear conclusions.

3.5. 2DV analysis

In the 2DH analysis, the flow velocities were averaged over the depth to obtain the horizontal velocity profile. For the 2DV analysis, the variation over depth of the flow velocity was analysed to determine which vertical hydrodynamic processes are apparent in the flow near Waterdunen. For the determination of the vertical flow profile only the ADCP measurements were suitable, as it is the only measurement device that measured over depth.

The 2DV analysis was carried out per transect, meaning the data was not interpolated in time. Longitudinal transects were projected as if they were straight, removing the lateral coordinate and solely observing the (x', z) plane. The data points were averaged with a moving average filter of three subsequent velocity measurements to smoothen the profile, resulting in a total average time of around 2.1 seconds. Afterwards, the averaged data points were interpolated to a 200×20 grid spanning 200 m in streamwise direction with $\Delta x' = 1$ m and 5 m over the depth with $\Delta z = 0.25$ m. The large amount of turbulence in the stream close to the jet influences the accuracy of the measurements and therewith the number of data points available. The data was analysed in 2 sections, one section within the first 75 m downstream of the culvert and one section covering the full length of the transect.

3.5.1. Flow attachment

The primary focus of the 2DV analysis was to investigate whether flow separation occurs in the channel. Even though flow separation would most likely occur at the longitudinal slope, it is also possible the flow

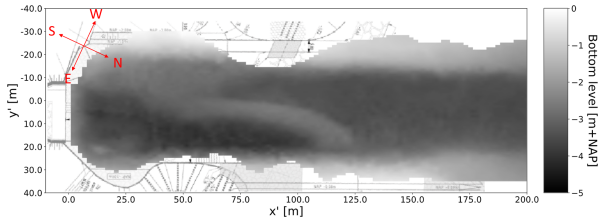

(a) Scenario 3.

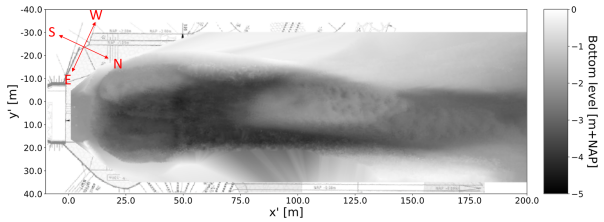

(b) Scenario 4.

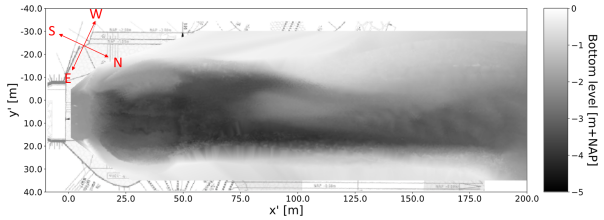

(c) Scenario 5.

Figure 3.12: Topographic maps for scenario 3 (a), scenario 4 (b) and scenario 5 (c).

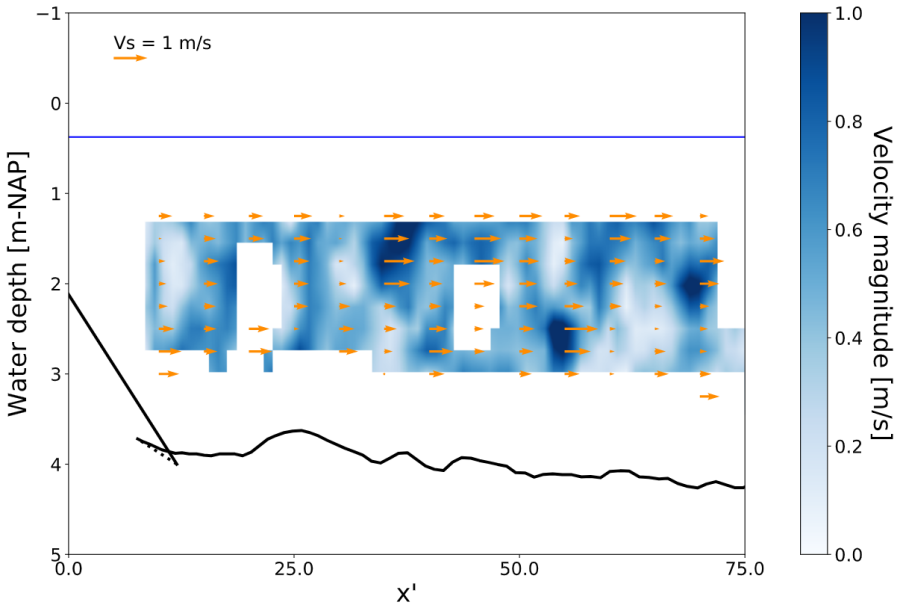

(a) Velocity profile over depth for the initial 75 m from the culvert.

(b) Sailed transect.

Figure 3.13: Vertical variation of the streamwise velocity component (arrows) along the initial 75 m from the culvert for transect 5 of scenario 3 ($Q = 21\ m^3/s$) projected on the vertical variation of the absolute flow velocity along the same transect.

separates elsewhere in the channel due to the varying topography. During the analysis it was observed that the ADCP left a relatively large space between the bottom and the deepest measurement, leaving a large blank space when investigating the vertical velocity profile as can be seen in figure 3.13. For low discharges, the initial 75 m from the culvert are largely non-uniform both over the vertical and in the streamwise direction during all scenarios. With higher discharges, the flow profile seems to become

more uniform over depth. In none of the scenarios, a clear recirculating pattern underneath the primary jet stream has been observed. However, during scenario 2, a strong recirculating current at depth has been observed slightly towards the west of the primary jet stream. Though this phenomenon has been sought after during other scenarios, it was not observed again.

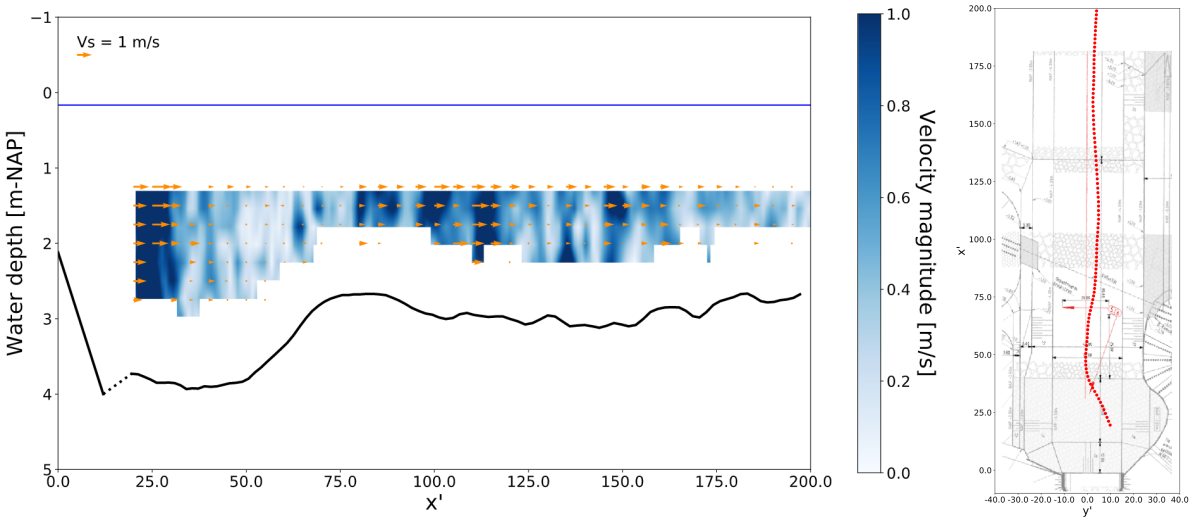

(a) Velocity profile over depth for entire transect.

(b) Sailed transect.

Figure 3.14: Vertical variation of the streamwise velocity component (arrows) along the entire transect for transect 1 of scenario 5 ($Q = 45\ m^3/s$) projected on the vertical variation of the absolute flow velocity along the same transect.

During scenarios 1, 4, and 5 the flow can be observed to move over the shallower section in the middle of the channel when the flow velocities in the jet are still high. Figure 3.14 shows the jet pattern over the shallow middle section for scenario 5. It can be observed the high flow velocities in the jet move over the shallow section, yet no clear vertical flow processes such as flow separation can be observed. As a result of the shallower water depth in the middle, a slight acceleration can be observed where the jet stream moves over the shallow middle section.

Though no clear flow separation can be observed, the flow does not seem to be uniform over the vertical for the low discharges. For high discharges, the flow seems to be a lot more uniform over depth, as is visible in figure 3.15. Furthermore, looking at a full transect along the primary flow-conveying channel as in figure 3.16, the jet seems to be relatively uniform in streamwise direction with only the expected dissipation as variation starting around 100 m from the culvert.

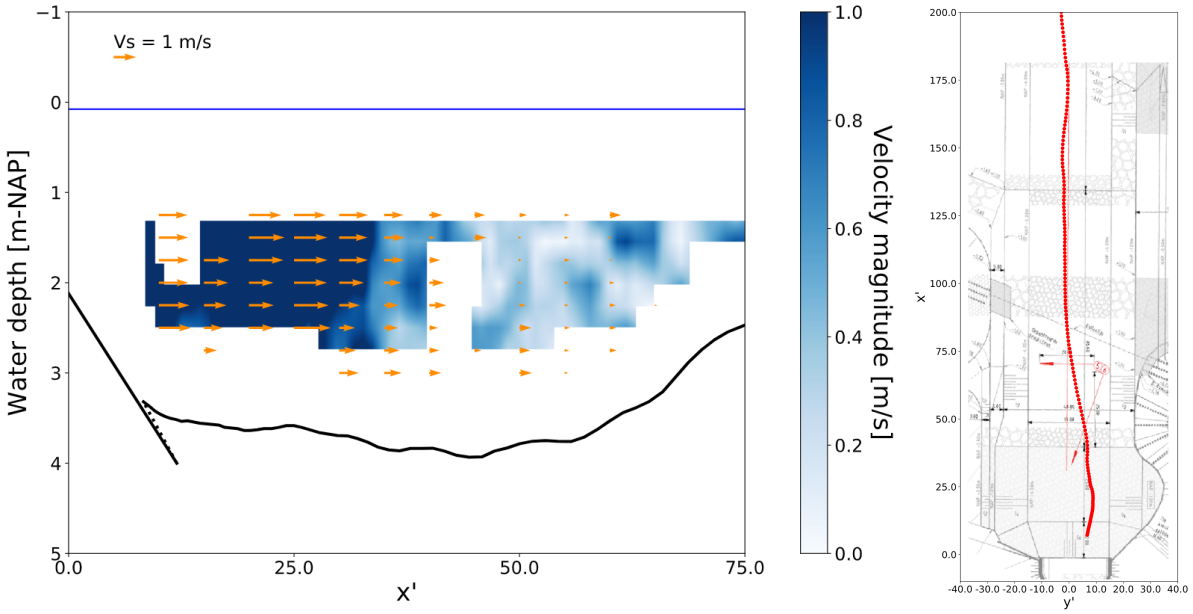

(a) Velocity profile over depth for the initial 75 m from the culvert.

(b) Sailed transect.

Figure 3.15: Vertical variation of the streamwise velocity component (arrows) along the initial 75 m from the culvert for transect 17 of scenario 4 ($Q = 37\ m^3/s$) projected on the vertical variation of the absolute flow velocity along the same transect.

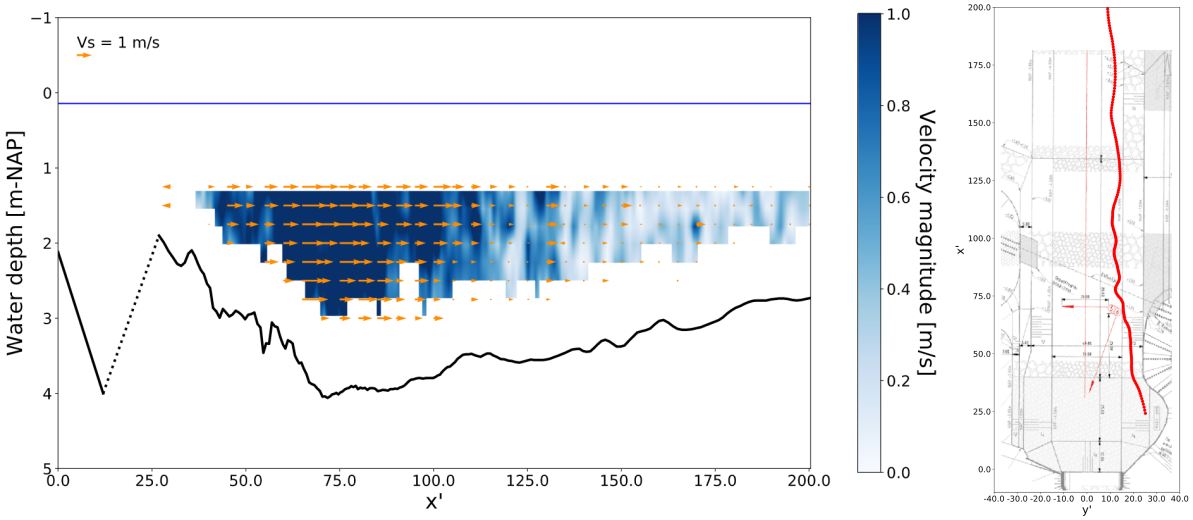

(a) Velocity profile over depth for entire transect.

(b) Sailed transect.

Figure 3.16: Vertical variation of the streamwise velocity component (arrows) along the entire transect for transect 2 of scenario 5 ($Q = 44\ m^3/s$) projected on the vertical variation of the absolute flow velocity along the same transect.

3.6. Conclusion

In the previous sections, the hydraulic phenomena thriving at Waterdunen have been highlighted. Below, a summary concludes the observations.

- In all measurement scenarios, the flow concentrates on the eastern side of the channel. This creates an asymmetric flow pattern as was expected from the literature study in chapter 2. It was discussed this asymmetric flow pattern is the result of a Coanda-like effect. The jet seems to reach the eastern slope at a streamwise distance of around 40 to 50 meter. No relationship between these distances and the discharge or water level has been found.
- Corresponding to the asymmetric flow pattern, a dominant and non-dominant recirculation zone can be distinguished. The dominant recirculation zone is located on the western side of the channel and spans approximately 100 m downstream from the culvert. The non-dominant recirculation zone is located on the east side of the channel and spans the initial 30 m from the culvert.
- A horizontal contraction of the streamlines was observed rather than the diverging behaviour which is expected for jet flows. This contraction was better visible for the surface streamlines compared to the depth-averaged streamlines. Furthermore, visual observations showed this contraction starts approximately at the start of the longitudinal slope up until the jet hits the eastern side of the channel. As discussed in the literature study in chapter 2, this indicates the bulk of the flow is redistributed over the vertical plane rather than the horizontal plane, indicating the flow might remain attached to the slope.
- It appears two flow configurations exist: one where the flow moves towards the center of the channel and spreads out and one where the flow remains attached to the eastern side of the channel. In the former flow state, the jet appears to meander across the channel. It was discussed in the literature study that this is unlikely to be the result of an unstable jet. Rather, it can be expected the meandering property is related to the Coanda-like effect.
- The bathymetry of the channel coincides with the flow patterns found, with a deep topographic channel in front of the eastern transverse slope. After measurement scenario 3 a flushing campaign was carried-out to flush out a sand bar that was present along the middle of the channel.
- From the 2DV analysis, it was concluded that no clear recirculating area can be observed, though little data was available in the lower sections of the water column. From the data, it seems likely the flow remains attached to the bottom throughout the channel. This is further justified by the observation of the horizontal streamline contraction. It was discussed in the literature study in chapter 2 that the phenomenon of flow attachment introduces higher flow velocities near the bed compared to flow separation.

The aim of this work is to investigate whether a 2DH and a 3D numerical model can replicate the above observations. In this chapter, several conclusions were drawn regarding the hydrodynamic processes thriving at Waterdunen. It can, however, be concluded that even though a lot of data is available, the data is not ideal to investigate all hydrodynamic processes. Close to the culvert, nearly no accurate measurements are available and the flow fields contain plenty of interpolated values and missing data points. This might pose problems when comparing the numerical results to the measurement results, as certain sections of the reproduced flow field cannot be validated and an interpolation error is already present within the measurements. For this reason, it was decided to first validate the numerical models with a laboratory data set which complies with the hydrodynamic processes observed above. The chosen laboratory experiment was experiment 2.4.1 of van de Zande (2018). The reasoning behind this choice is given in appendix B.1.

4

Validation of the 2DH and 3D numerical flow models

To answer the primary research question of this work, insight into the performance of numerical models regarding the hydrodynamic processes named in the previous chapter is required. To obtain this knowledge, the chosen model software is first validated using experiment 2.4.1 of van de Zande (2018). The model software package which is used in this thesis is FINEL. The reasoning behind this choice is explained in appendix B.2. FINEL is the in-house model of Svašek Hydraulics which can run in a 3D and 2DH mode using identical numerical discretization. An introduction to FINEL is given in section 4.1, after which the model set-up is explained in section 4.2. Afterwards, the results of the 2DH model are discussed in section 4.3 and the results of the 3D model in section 4.4. Section 4.5 explains the concluding remarks on the model performances.

4.1. Introduction to FINEL

FINEL (FINite ELements) is a computational model software developed by Svašek Hydraulics based on the Finete Elements Method (FEM). The model can run in different modes depending on the requirements of the user. Two different software packages are available, being the FINEL-Explicit package and the FINEL-Implicit. Of the two, the latter is more flexible. A 2DH model created in the FINEL-Implicit software can be expanded to a 3D model by adding layers in the vertical direction with the same grid and discretization methods used. Therefore, a comparison between the two configurations of the model is strictly based on the addition of the third dimension, rather than the numerical artifacts caused by the different schemes or numerical grids. In a FINEL-Explicit model, the model can only run in a 2DH mode. Therefore, the FINEL-Implicit software package will be used in this model.

4.1.1. Practical application

The FINEL software package can be used in a 1DV, 1DH, 2DV, 2DH and 3D modes and employs a co-located grid. In case a 1DH or 2DH mode is used, the depth-averaged Shallow-Water Equations (SWE) are solved, rather than the non-hydrostatic Navier-Stokes equations. Depending on which mode is used, the elements are either line segments (1D), triangles (2D), or tetrahedrons (3D). The discretization of the continuity and momentum equation is second-order accurate, with time-stepping done using the theta-method to achieve either first- or second-order accuracy. It should be noted that supercritical flow cannot be simulated using the FINEL software.

4.1.2. Mathematical basis

A full description of the mathematics on which FINEL is based is given in Labeur (2009), with a summary given in this section. An advantage of the Finite Element Method concerning the Finite Difference Method is the flexibility of the grid to be unstructured, allowing the reconstruction of complex geometries. Compared to a Finite Volume Method the Finite Element Method is superior based on the ease of acquiring higher orders of accuracy due to the implementation of the integral form of the Partial Differential Equations (PDE) (Wendt, 2008).

For the weak formulation of the advection-diffusion equations a mixture of Continuous and Discontinuous Galerkin (CG and DG) is used to optimize favourable characteristics of both methods. A DG method, though in essence more accurate than its CG counterpart, contains substantially more degrees of freedom due to the discontinuities present on each of the element interfaces. This is made visible in figure 4.1 from Labeur (2009). From a computational point of view, the DG methods are therefore restricted to explicit problems, as implicit methods require the inversion of a global matrix containing significantly more entries due to the extra degrees of freedom.

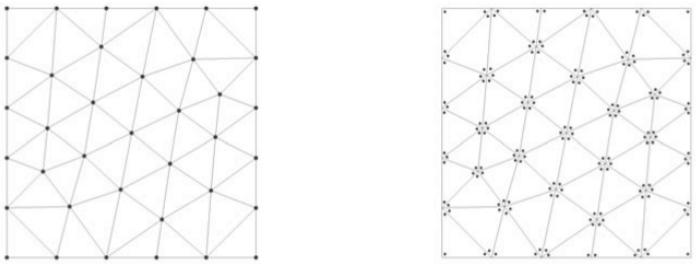

Figure 4.1: Nodal degrees of freedom for the linear CG method (a) and the DG method (b) Labeur (2009).

One of the issues with CG concerns the preservation of monotonicity if the Péclet number becomes larger than one. The Péclet number can be seen as a local Reynolds number within an element, indicating the importance of advection within the flow. Therefore CG methods require a stabilization method that can either be difficult to implement for complex flows or induce undesired numerical diffusion.

The Galerkin Interface Stabilization method developed in (Labeur, 2009) therefore exploits a combination of both DG and CG. A global continuity constraint is set for the local interface flux, coupling the local interface flux to a global interface variable with unique values defined on interfaces. This process allows the local discontinuous functions to be expressed in terms of the global interface variable. These local expressions can be used to construct the global system to determine the global interface variable, which in turn can be used to determine the local discontinuous function via back substitution. This effectively reduces the global system of equations to be of the same structure as a comparable CG system while using local discontinuous functions to maintain system stability.

4.1.3. Turbulence closure models

FINEL contains a broad range of available turbulence closure models. As the software has both a 2D and 3D mode, horizontal and vertical turbulence closure models are separated. This subsection briefly explains the physical basis of both turbulence closure models used in this work.

4.1.3.1 Vertical turbulence closure model

The standard $k-\epsilon$ turbulence model is used to simulate turbulence in the vertical plane. This model is therefore only used by the 3D model. It was shown in Bardina et al. (1997) that the $k-\epsilon$ model performs relatively poor when considering separating flows. Nevertheless, it was hypothesized the lack of visible vertical flow separation both at Waterdunen and in the laboratory experiment was sufficient to allow the usage of the $k-\epsilon$ model.

The $k-\epsilon$ turbulence closure model makes use of Reynolds averaging to introduce the Reynolds stresses into the Reynolds-Averaged Navier Stokes (RANS) Equations. By employing the Boussinesq approximation the Reynolds stresses are described in terms of the mean velocity gradients analogously to molecular viscosity. The remaining issue lies in the determination of the turbulent viscosity ν_t. In the standard $k-\epsilon$ model the turbulent viscosity is determined using the turbulent kinetic energy k and the turbulent energy dissipation rate ϵ. Both parameters are determined using simplified transport equations which are explained in appendix B.3. As the turbulent viscosity is a function of a length scale and

a velocity scale, $\nu_t \propto k^2\epsilon^{-1}$ as $\epsilon \propto k^{3/2}l^{-1}$ and $k \propto u^2$. This relation is often prescribed with a constant C_μ, with the complete formulation shown in equation 4.1.

$$\nu_t = c_\mu \frac{k^2}{\epsilon} \tag{4.1}$$

It should be noted that the turbulent viscosity is not bounded for every value of ϵ or k. This can result in large errors near the bottom, where both k and ϵ reach a maximum. Within the model, the turbulent viscosity is therefore bounded to a maximum with the turning point at $k^{3/2} = \epsilon l_{max}$. This system is shown in equation 4.2. l_{max} is a maximum turbulence length scale, which is set as the water depth.

$$\nu_t = \begin{cases} c_\mu \frac{k^2}{\epsilon} & \text{if } k^{3/2} < \epsilon l_{max} \\ \max\left(\mu, l_{max}k^{1/2}\right) & \text{if } k^{3/2} \geq \epsilon l_{max} \end{cases} \tag{4.2}$$

4.1.3.2 Horizontal turbulence closure model

In the horizontal plane, a mixing-length model turbulence closure model is employed. Specifically for the mixing-length model, the turbulent fluctuations are assumed to be a function of a length scale l_m over which mixing and transport of momentum takes place (Uijttewaal, 2018). The resolved turbulent viscosity is therefore related to l_m^2 and the local velocity gradient.

Two methods of the mixing-length model are available in FINEL. The Smagorinsky model does not use Reynolds averaging and calculates the mixing length by multiplying the horizontal grid size Δ_h with the Smagorinsky coefficient C_s. Similar to a LES, turbulent fluctuations larger than the grid size Δ_h are resolved for. Therefore, the Smagorinsky model is also suitable as a sub-grid scale model for LES.

The second method relates the mixing length to an user-supplied length scale for turbulence L_T. This length scale can then be related to the mixing length using a constant C_{lm}. L_T can be approximated to be around $0.5 - 1$ times the mixing layer width. The constant C_{lm} can be calculated by re-writing equation 4.1. $C_{lm} = C_\mu^{3/4} = 0.16$ follows when using the standard value for C_μ.

4.1.4. Friction

Every solid boundary in FINEL is considered to be hydraulically rough. Bottom and wall friction in FINEL can be defined using four different roughness parameters. Each parameter is rewritten to the Nikuradse Roughness height k_s by the software. Using k_s, the hydraulic roughness c_f is calculated by the model. The derivation of this relation is given in appendix B.4. The reasoning behind this choice lies in the physical basis of the parameters, as k_s is a property of the boundary whereas c_f is a property of the flow. This internal calculation can be bypassed by defining c_f directly in the input.

It is explained in appendix B.4 that the hydraulic roughness at the bed $c_{f,bed}$ is a function of k_s, the Von Kárman constant κ, and the vertical grid resolution Δz_0 at the bottom in a 3D model. The used equation within the software is given in equation 4.3. In a 2DH model the vertical grid resolution is replaced with the water depth H as shown in equation 4.4. Both definitions were determined to comply with one another, meaning the depth-averaged velocities in the 3D model should comply with the 2DH velocities if friction is the only influence on the flow.

$$c_{wall,3D} = \left(\frac{1}{\kappa}\ln\frac{\Delta z_0}{k_s/30} - \frac{2}{\kappa}\right)^{-2} \tag{4.3}$$

$$c_{f,2D} = \left(\frac{1}{\kappa}\ln\frac{H}{k_s/30} - \frac{1}{\kappa}\right)^{-2} \tag{4.4}$$

The definition of the hydraulic roughness at lateral walls $c_{f,wall}$ in a 3D model is nearly identical to the definition of $c_{f,bed}$, using solely k_s and the horizontal grid resolution next to the wall Δy_0. However, in a 2DH model $c_{f,wall}$ is not simulated in FINEL.

4.2. Model set-up

Both a 2DH and a 3D numerical model were set-up to analyse the shallow jet flow in experiment 2.4.1 of van de Zande (2018). This section aims to explain the set-up of both models.

4.2.1. Turbulence closure models

For the vertical $k-\epsilon$ model, the standard values for the model constants were used as was suggested by Andersson et al. (2011). This results in:

- $C_\mu = 0.09$
- $C_{\epsilon 1} = 1.44$
- $C_{\epsilon 2} = 1.92$
- $\sigma_k = 1.00$
- $\sigma_\epsilon = 1.30$

The horizontal Smagorinsky mixing length model was used. C_s = 0.1 was used as suggested in Talstra (2011). As the Smagorinsky model was employed as a mixing length model rather than a sub-grid scale model for LES, the resolved turbulent viscosity in the simulations was low compared to a more standard mixing length model (as $\Delta_h << L_T$).

4.2.2. Numerical grid

Compared to rectangular grid cells, triangles have a certain orientation concerning the local coordinate system. Due to the extremely unstable nature of the symmetric flow configuration, it was hypothesized this grid orientation might influence the stable asymmetric flow solution. For this reason, it was decided to use a grid generator which randomly fits triangles throughout the numerical domain. This reduced the influence of the grid orientation on the numerical solution.

The total length of the flume spanned 19.2 meters. However, both the PIV measurements and the ADV measurements were only carried out on the interval $6.16 < x < 11$ m. Therefore, this domain can be considered the domain of interest (DOI). Outside of the DOI, the horizontal grid resolution was set at $\Delta_h = 0.1$ m to use approximately 10 grid cells over the width of the contracted channel. Moving into the DOI, the resolution becomes higher with $\Delta_h = 0.045$ m to ensure approximately 10 grid cells over the length of the longitudinal slope. A figure of the total horizontal grid is shown in figure 4.2.

For the 3D simulation, a sensitivity analysis was performed to determine both the vertical grid resolution at the bottom and the required amount of layers. These analyses are displayed in appendix B.7. The result shows that an equidistant vertical grid with $\Delta z = 0.01$ m yielded the most accurate results. This translates to 8 grid cells in the upstream channel and 16 grid cells in the expaned section of the flume.

4.2.3. Friction

In appendix B.5 it is hypothesized the negligence of wall friction can influence the accuracy of the model based on preliminary 2DH simulations which showed high velocities at the walls. For this reason, it was decided to prescribe c_f directly as input in the 2DH model and to adjust the value for c_f at the lateral walls. As an identical horizontal grid is used in the 2DH and the 3D simulations, the value for Δy_0 remains equal.

During the experiment, wooden contracting elements were used together with smooth HPL plates on the bottom. $k_s = 0.001$ m is used as an estimation of the roughness height for both materials. Furthermore, the standard value for the Von Kármán constant $\kappa = 0.4$ was used as is recommended in Uijttewaal (2018). Using these parameters, the bottom hydraulic roughness was calculated in equation 4.4 to lie between $0.0029 < c_{f,2D,bot} < 0.0038$ depending on the local water depth. Furthermore, the wall hydraulic roughness was calculated in equation B.18 to be $c_{f,2D,wall} = 0.0059$ as would be simulated by a 3D model. In the 3D model, a global value $k_s = 0.001$ m was used, combined with $\kappa = 0.4$.

4.2.4. Numerical parameters

4.2.4.1 Flux limiter

The flux limiters available in FINEL are explained in appendix B.6. In the preliminary simulations in appendix B.5 it was noticed the additional accuracy gained by neglecting the flux limiter was substantial. When using the flux limiter, additional accuracy could be gained by increasing the grid resolution and therewith the computational effort. It was decided to neglect the flux limiter to preserve computational effort and maintain stability. This decision had two consequences.

First, the model was observed to become unstable at the downstream water level boundary when neglecting the flux limiter. It was therefore decided to replace the water level boundary with a Riemann boundary condition as will be explained in subsection 4.2.5. Though this yielded stable results, the Riemann boundary condition was not optimized. It was hypothesized the Riemann boundary was too reflective, which yielded inaccuracies in the model. This will be explained in further detail in section 4.3.

Second, the neglect of the flux limiter created wiggles around steep gradients, most notably at both lateral sides of the jet.

4.2.4.2 Time-stepping

As the horizontal Smagorinsky model was used, it was possible to perform a LES if the grid resolution is high enough. Therefore, in the preliminary simulations presented in appendix B.5 a sensitivity analysis was carried out to determine the influence of a variety of values for θ on the accuracy of the resolved turbulent fluctuations. It was concluded the influence of θ was small as the used numerical grid is too coarse to accurately resolve the turbulent fluctuations in the system. According to Pope (2001), a grid resolution with $\Delta_{max} = O(10^{-4})$ is required to perform an accurate LES of the current experiment. The required computational effort makes such a simulation unfeasible. Nevertheless, as only the time-averaged flow field are investigated, the consequence of the lower accuracy is minimal for the current study. It was therefore chosen to maintain $\theta = 1$ to yield more stability and use the Smagorinsky model as a mixing-length model.

4.2.5. Boundary conditions

At the upstream boundary, a constant discharge of $Q = 30$ l/s was used, complying with the experimental settings. It was explained in subsection 4.2.4 that a Riemann boundary condition was necessary at the downstream boundary to maintain stability. The corresponding water level for the Riemann invariant was set at $H = 0.16$ m to comply with the experimental settings. The velocity for the Riemann invariant was calculated based on the average velocity through the boundary, meaning $u = Q/BH = 0.0625$ m/s. However, it can be argued that due to the lateral non-uniformity of the flow this velocity value should be varying along the boundary. Nevertheless, no information regarding the outflow velocities during the experiment was available. It was therefore decided to keep the imperfect Riemann boundary condition as the influence within the DOI was expected to be small. Furthermore, the Riemann boundary condition would not be used in the Waterdunen model, meaning optimization of the boundary has little value considering the purpose of this work.

4.2.6. Sinks

In the literature study, it was explained an unstable symmetric flow configuration bifurcates at a pitchfork point and eventually settles at either one of two stable asymmetrical configurations. This was also noticed in the laboratory experiments of van de Zande (2018), where the jet would either concentrate on the upper or lower lateral wall. In the laboratory experiments, the asymmetry was enforced on the lower wall by placing a small brick at the upper contracting element at the point of the expansion. In the numerical models, the asymmetry towards the lower wall was enforced by modelling a discharge sink of 10% of the total discharge on the lower half of the flume just after the expansion. This ensured the jet would always concentrate on the lower wall.

4.2.7. Summary

The final model settings are summarized in table 4.1. Furthermore, an image of the horizontal grid and the boundary conditions is shown in figure 4.2.

Table 4.1: Final model settings for the simulations of laboratory experiment 2.4.1 of van de Zande (2018).

Run	$\Delta x_{min} - \Delta x_{max}$ **[m]**	$\Delta y_{min} - \Delta y_{max}$ **[m]**	Δz **[m]**	Δt **[s]**	c_f	κ	**lim u**	θ	C_s
Final	0.045 - 0.1	0.045 - 0.1	0.01	0.11	VAR	0.4	OFF	1	0.1

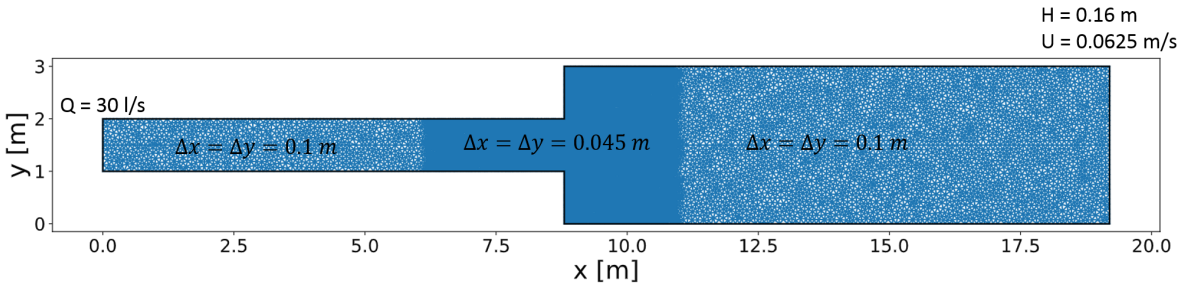

Figure 4.2: Horizontal grid with boundary conditions as employed in the model validation.

4.3. 2DH model results

The experiments of van de Zande (2018) have been explained in the literature in section 2.6. The purpose of this chapter is to obtain information regarding the performance of a 2DH and 3D FINEL model regarding the reproduction of the hydrodynamic processes researched in section 2 and recognized in section 3. Therefore, the primary aim of the model analyses is to assess the capabilities of the model to reproduce the asymmetric flow field, the recirculation zones, the horizontal streamline contraction, and the vertical flow attachment. Aside from these processes, the accuracy of the models will be assessed as well in the form of lateral and vertical velocity profiles.

The modelled flow field is shown in figure 4.3a, together with the contour lines for $|\vec{u}| = 0.35$ m/s (inner) and $|\vec{u}| = 0.2$ m/s (outer) of the PIV data. The PIV data from van de Zande (2018) is repeated in figure 4.3b.

4.3.1. Asymmetry

From figure 4.3a, it is evident the modelled flow curves towards the lower side of the flume to form an asymmetric flow pattern throughout the flume. The jet hits the lower wall at $x = 13$ m, 4 m downstream from the expansion. Nevertheless, it can be observed the curvature of the modelled flow is significantly higher compared to the curvature in the measured flow field.

To better quantify the error made by the 2DH model, the WCG was used. To calculate the position of the WCG, the coordinate system is displaced to define $y = 0$ at the center-line of the channel, being positive towards the upper section of the channel as shown in figure 4.4. The resulting positions of the WCG are therefore negative if the jet flow moves towards the lower section of the channel and positive if the flow moves towards the upper section of the channel. Figure 4.5 shows the lateral positions of the WCG along the x-axis for both the 2DH model and the PIV measurements.

The model shows the WCG is located on the upper side of the channel until $x = 10$ m. This indicates the dominance of the bottom-side recirculating velocities over the asymmetric flow. These bottom flow velocities are negative at a positive y location, resulting in a shift of the WCG towards the upper side of the flume. The PIV measurements show a movement of the WCG towards the bottom section of the flume, indicating the lack of high-velocity recirculating flow on the bottom side of the channel.

At $x = 9.3$ m, the WCG resolved in the model can be seen to move towards the bottom section of the channel. The initial curvature starts slow but gradually increases. At $x = 10.3$ m the WCG in the model passes the WCG in the experiment. From figure 4.5 it is evident the 2DH model hits the lower wall further upstream compared to the PIV data.

Figure 4.6 shows the magnitude of the lateral velocity component throughout the channel as repro-

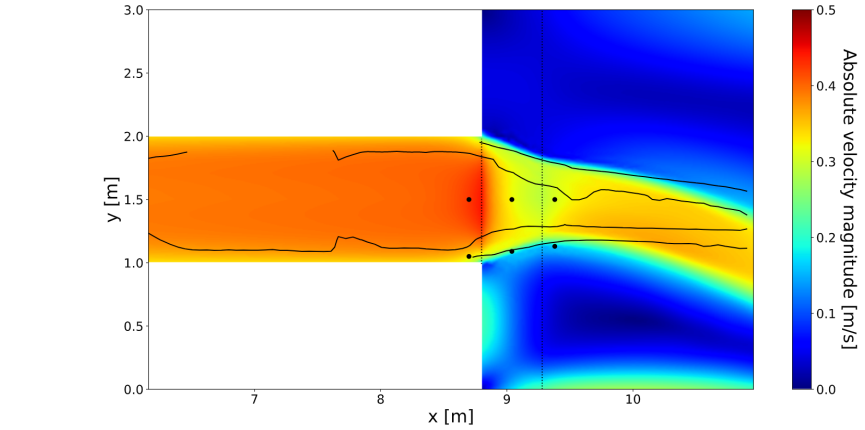

(a) 2DH model.

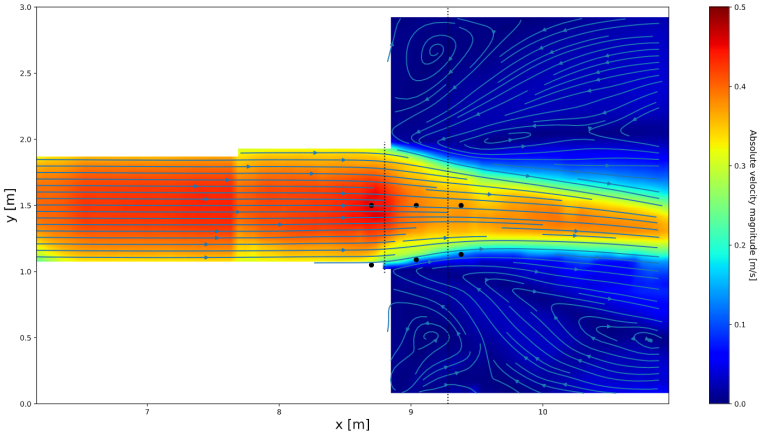

(b) PIV data of van de Zande (2018).

Figure 4.3: Reproduced flow profile of the 2DH model within the DOI with the contour lines for $|\vec{u}| = 0.1$ m/s and $|\vec{u}| = 0.35$ m/s of the PIV measurements (black lines) and the locations of the ADV measurements (black dots) (a) and a repeat of the PIV data of van de Zande (2018) (b).

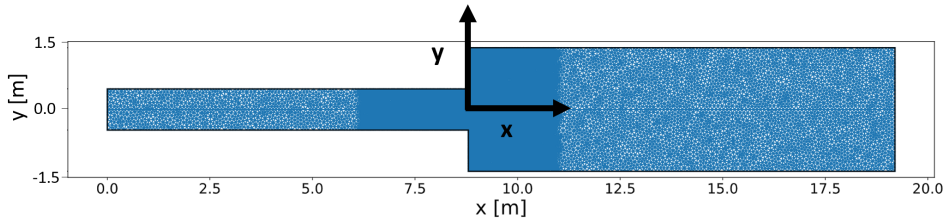

Figure 4.4: Coordinate system used for the determination of the WCG.

duced by the 2DH model (4.6a) and as measured using the PIV data (4.6b). On $y \geq 1.5$ m, the model reproduces relatively large negative velocities originating from the dominant recirculation zone 'press down' on the jet stream. Along the expanding wall at $x = 8.8$ m, high positive velocities are present. However, further downstream, these upwards facing velocities are absent. As a result, the jet moves towards the lower section of the flume. In the PIV data in figure 4.6b, these high negative lateral velocities in the dominant recirculation zone are absent. Later in this section, it will be shown this is caused by a differently shaped dominant recirculation zone. In the PIV data, the dominant recirculation zone is contracted by the upstream corner eddy, which changes the orientation of the streamlines concerning the jet. Therefore, the lateral velocity component pushing the jet down is smaller compared to the 2DH model results.

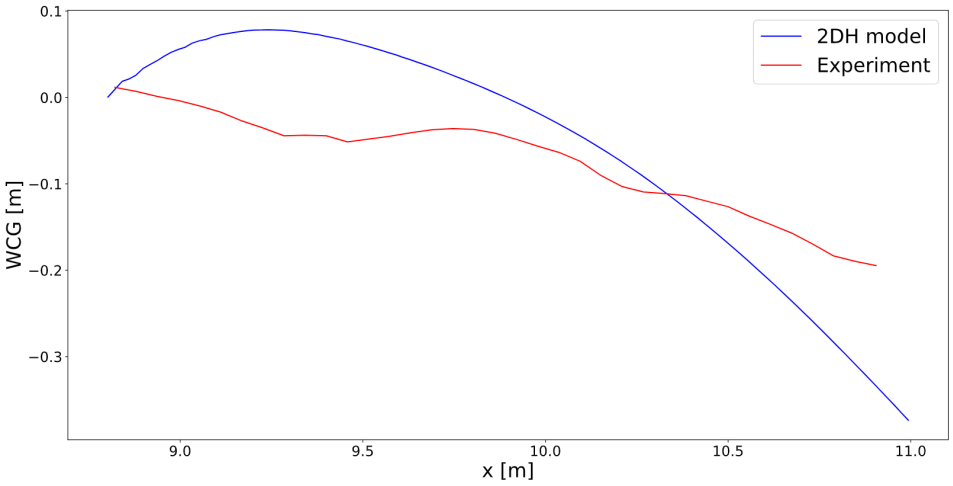

Figure 4.5: Lateral coordinate of the WCG within the DOI for both the 2DH model and the PIV data.

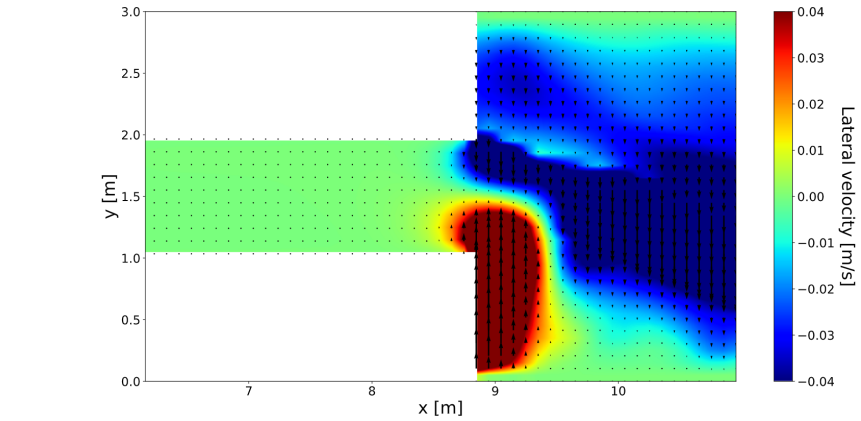

(a) 2DH model.

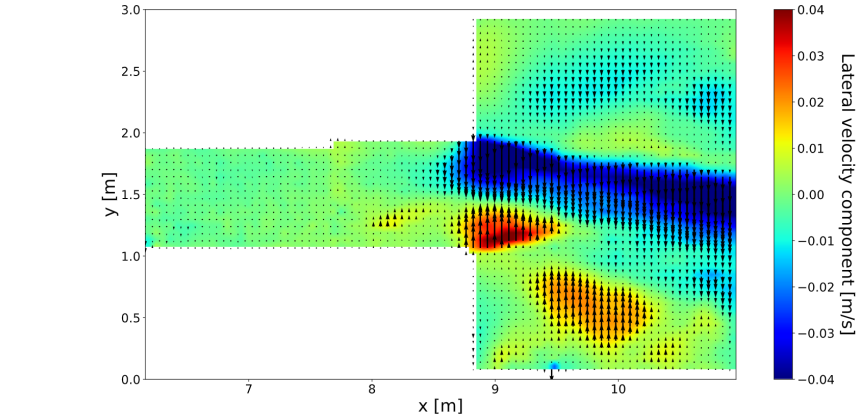

(b) PIV data of van de Zande (2018).

Figure 4.6: Reproduced lateral flow velocities by the 2DH model (a) and the measured lateral flow velocities using the PIV (b).

4.3.2. Recirculation zones

Both the streamlines and vertical vorticity distribution of both the 2DH model and PIV measurements are shown in figure 4.7. The unexpected sign change of the vorticity which is visible on both outskirts of the jet is attributed to the absence of a flux limiter. This causes the velocity to slightly wiggle around steep gradients, which is also visible in figure 4.9. They are therefore likely to be the result of a numerical cause rather than a physical one, which is why they will be ignored in the analysis.

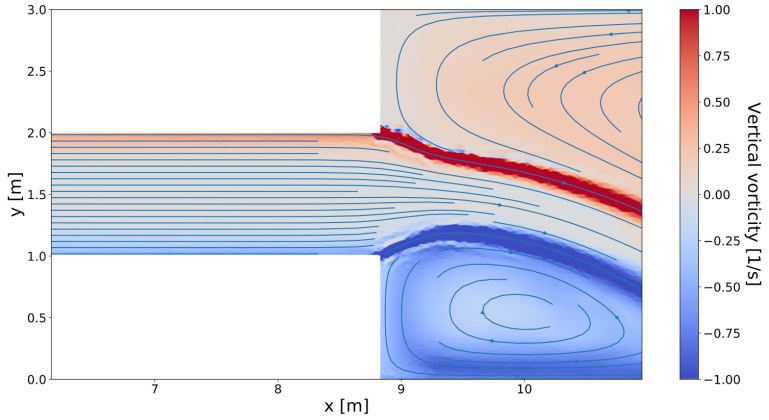

(a) 2DH model.

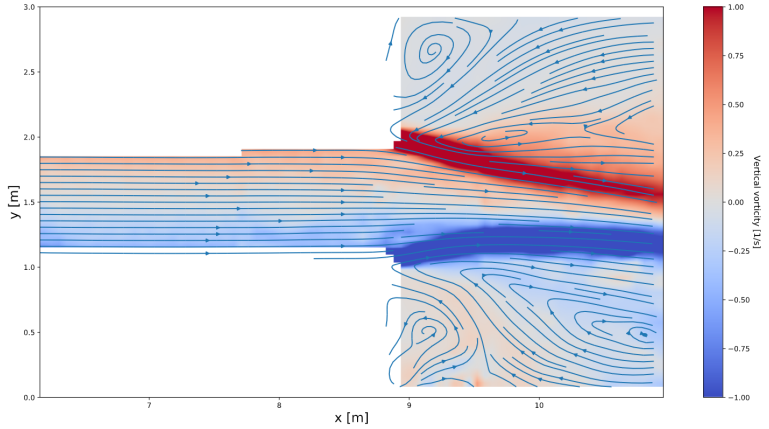

(b) PIV data of van de Zande (2018).

Figure 4.7: Modelled streamlines and vertical vorticity distribution for the 2DH simulation and the PIV data of experiment 2.4.1 of van de Zande (2018).

Two recirculation zones can be observed in the measured streamlines in figure 2.13, with the dominant recirculation zone with positive vertical vorticity on the top side of the flume and the non-dominant recirculation zone with negative vertical vorticity on the bottom side of the flume. The corner eddies which were observed from the PIV measurements in figure 4.7b are absent. Dewals et al. (2008) suggested wall friction plays a pivotal role in the modelling of the upstream corner eddies. In a standard 2DH FINEL model, wall friction is neglected. For this reason, it was expected that the upstream corner eddies would not be simulated. Considering the streamlines, the high lateral velocities as were discussed above can clearly be observed. The additional width of the dominant recirculation zone allows the negative lateral velocities to span a broader section of the DOI compared to the positive lateral velocities in the non-dominant recirculation zone. It is theorized this partly causes the higher curvature in the 2DH model.

In the model set-up in section 4.2, it was explained it was attempted to simulate wall friction in the 2DH model by increasing the bed hydraulic roughness at the lateral walls in the input parameters. Though this parameterization increased the accuracy of the model, as is explained in appendix B.5, it is likely the parameterization does not yield the same results as an actual inclusion of wall friction would. In a 3D FINEL model, wall friction is attributed to vertical grid elements placed on the boundary, affecting the flow from the side. In the 2DH parameterization, the larger bed friction affects the flow from the bottom. The effect can therefore be expected to differ, as will also be shown in the lateral velocity profiles in section 4.3.4. For this reason, the absence of the upstream corner eddies is attributed to an incorrect parameterization of the wall friction in the 2DH model.

Aside from the absence of the corner eddies, a sudden increase in flow velocity along the bottom wall can be observed. In the measurement data, these high recirculating velocities were not found. These higher recirculating velocities are partly caused by the more upstream located attachment point of the jet to the lower wall. This compresses the non-dominant recirculation zone and therefore increases the recirculating velocities. Furthermore, the absence of a correct inclusion of wall friction likely increased the recirculating flow velocities next to the wall.

Another argument for the discontinuity between the modelled recirculating velocities and the measured recirculating velocities lies in the possibility of measurement errors in the recirculation zones. It was stressed in van de Zande (2018) that the tracer particle distribution could contribute to measurement inaccuracies. In the video data of the experiment it was observed that few tracers were present in the upstream-upper section of the flume. Regarding the upstream-lower section of the flume, large clumps of tracer particles can be observed rather than individual particles. As clumps of tracers are less representative for the actual flow velocity, this might have influenced the extremely low recirculating velocities which were measured.

From the above, it was concluded that the recirculation zones are not modelled correctly. The upstream corner eddies are not modelled, which can pose problems when investigating, for example, the sediment recirculation inside the flume. Furthermore, the upstream corner eddies contract the dominant recirculation zone and might reduce the increased curvature observed in the 2DH model. Finally, the recirculating flow velocities are modelled too high in both the dominant and non-dominant recirculation zone. Though this might be attributed to measurement errors, it is likely the incorrect parameterization of wall friction and the increased curvature of the jet affected the result.

4.3.3. Horizontal streamline contraction

To quantify the streamline contraction, the jet width was determined using the maximum and minimum vertical vorticity ω_z within each lateral cross-section. The second term in the definition of the vertical vorticity in equation 3.1 will be dominant in the lateral non-uniform jet flow. The development of the second term can be evaluated as the second derivative of the lateral velocity profile, $\frac{\partial u^2}{\partial^2 y}$. This derivative has a local maximum between the non-dominant recirculation zone and the jet center and a local minimum between the dominant recirculation zone and the jet center. When neglecting the contribution of the first term in equation 3.1, this roughly corresponds to the maximum and minimum vorticity within the lateral profile respectively. The distance between the maximum and minimum vorticity in a lateral cross-section was therefore used to define the contraction of the jet and therewith the contraction of the streamlines. Due to turbulent diffusion and the corresponding streamline divergence as visible in figure 2.1, this approach is not fully accurate, yet can still serve as an indicator of the streamline contraction.

Figure 4.8 shows the development of the approximated jet width for $x \geq 8.8$ m for both the model and the PIV measurements. It should be noted that the initial jet width of the PIV measurements is inaccurate as a certain clearing for the wall is required in the PIV measurements, which is why the initial jet width is smaller than 1 m.

From figure 4.8 it was observed the decrease in jet width for both the model and the PIV measurements follow a similar path over the length of the slope. However, at the end of the slope, the 2DH model simulates a slightly stronger contraction. Assuming the width of both jets start at $b_0 = 1$ m, it was calculated the contraction of the jet over the slope is around 0.3 m for the measurements and 0.37 m for the 2DH model. At the end of the slope ($x = 9.28$ m), it was observed the modelled jet width stops decreasing and remains relatively constant over the remaining length of the DOI, showing a slight increase of the jet width at the end. Contrary to that, the PIV measurements were observed to show a continuing decrease of the jet width over the entire length of the DOI. From these observations, it was concluded the model properly simulated the horizontal contraction of the jet over the slope, but failed to simulate the continuing contraction further downstream and the correct magnitude of the contraction.

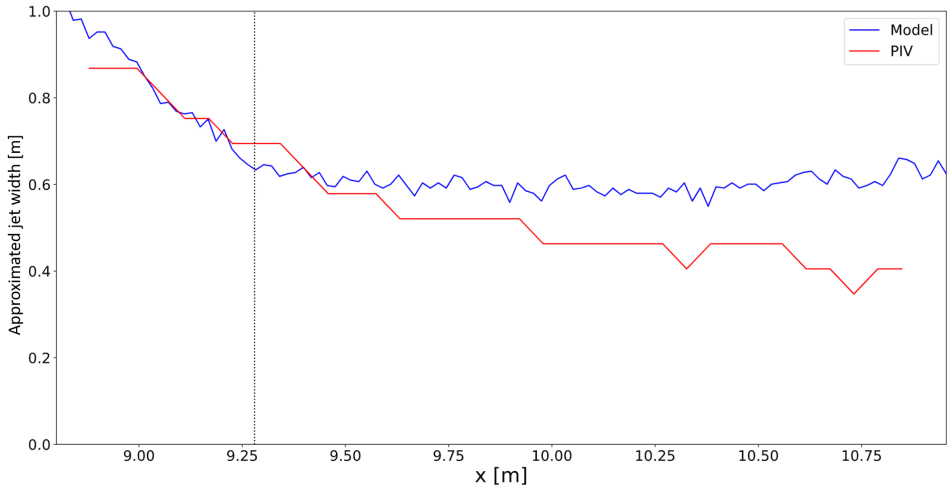

Figure 4.8: Approximated jet width development for $8.8 \leq x \leq 11$ m for both the PIV measurements (red) and the 2DH modelled jet (blue).

4.3.4. Lateral velocity profiles

Figure 4.9 shows three lateral velocity profiles at $x = 8.7$ m, $x = 9.04$ m and $x = 9.38$ m corresponding with the ADV measurement locations. Note that at $x = 9.38$ m, the ADV data is not shown as the measurements were carried out at depth (figure 2.14) meaning they neither represent the surface velocity nor the depth-averaged velocity. For the other two ADV measurement locations it is assumed the top velocity properly represents the surface velocity and that the depth-varying measurements are sufficient to represent the depth-averaged velocities.

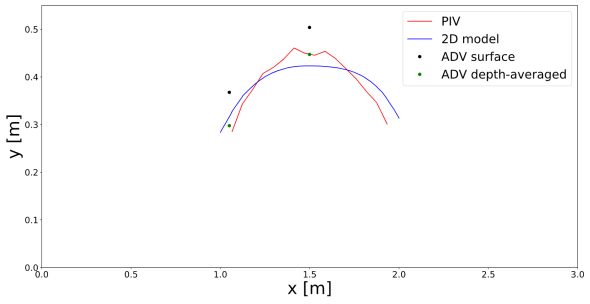

(a) x = 8.70 m.

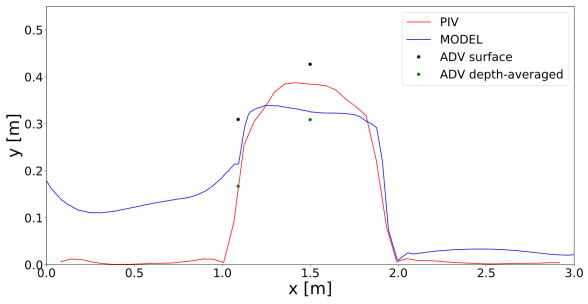

(b) x = 9.04 m.

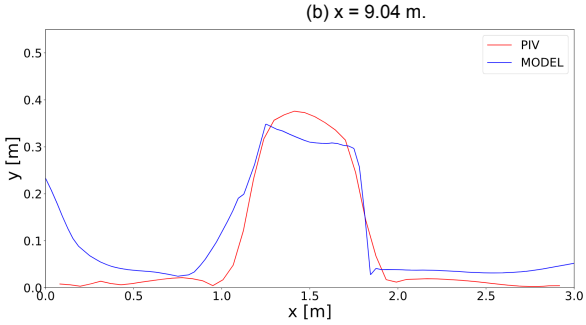

(c) x = 9.38.

Figure 4.9: Lateral distribution of the total horizontal velocity for three lateral cross sections through the flume.

From figure 4.9a it can be seen the modelled upstream velocity profile underestimates the jet centerline velocity compared to both the depth-averaged ADV measurements and the PIV measurements. Furthermore, the flow velocities next to the lateral walls are overestimated in the model. This suggests the parameterization of wall friction was indeed incorrect. Table 4.2 shows the maximum error made by

the 2DH model relative to the jet center-line velocity from the PIV data at the locations of the ADV data. As mentioned above, the error made in the non-dominant recirculation zone is especially significant.

Table 4.2: Error made by the 2DH model with respect to the PIV-measured flow velocity in the jet center. The considered values are in the non-dominant recirculation zone ($0 \leq y < 1$), within the jet ($1 \leq y \leq 2$), and in the dominant recirculation zone ($2 < y \leq 3$).

	Error with respect to the jet center-velocity [%]		
x [m]	$0 \leq y < 1$	$1 \leq y \leq 2$	$2 < y \leq 3$
8.7	-	8.16	-
9.04	43.1	12.4	7.13
9.4	56.6	7.35	9.17

Considering figure 4.9b, it was observed that the velocity profile with $1 \leq y \leq 2$ is reproduced relatively accurately in the 2DH model. Compared to the PIV measurements, the velocities are slightly underestimated, though this is to be expected when comparing surface velocities with depth-averaged velocities. Compared to the depth-averaged ADV measurements, the flow velocity in the center and towards $y = 1$ m is modelled with a small error. However, figure 2.14 shows the ADV measurements which were carried out favoured the bottom section of the water column, indicating the depth-averaged velocity profile might be an underestimation of actual depth-averaged velocity.

When approaching the side walls at $y = 0$ and $y = 3$, the flow velocity is higher compared to the measurements. The increase towards $y = 3$ m in the upper section of the flume is hypothesized to be the result of the incorrectly modelled Riemann boundary condition. A better-defined velocity distribution for the Riemann invariant along the boundary was thought to be less reflective and therefore more accurate for the representation of the jet. However, due to the lack of measurements at the outflow boundary, the velocity distribution at outflow would simply be an estimation. Furthermore, the Riemann boundary condition will not be used in the Waterdunen models as the downstream boundary conditions will be further away from the DOI. For these reasons, the optimization of the Riemann boundary condition was not further explored in this research.

Towards $y = 0$ m the flow velocity was observed to again increase within the recirculation zones in figures 4.9b and 4.9c, which was not observed during the experiment. The reasoning behind the higher recirculating velocities was given in section 4.3.2.

4.3.5. Conclusion

It can be concluded the 2DH model is capable of reproducing the horizontal contraction of the streamlines over the lateral slope and the asymmetric flow pattern. Furthermore, in definition, the 2DH model reproduces the vertical flow attachment. However, the recirculation zones were not modelled properly and the accuracy with which the other processes are reproduced is doubtful.

The lateral velocity profiles in figure 4.3a indicate the parametrization of wall friction in the 2DH model was incorrect. Furthermore, the flow velocities in both the dominant and non-dominant recirculation zones were overestimated by the model. The higher recirculating velocities in the dominant recirculation zone were attributed to be the result of the imperfect Riemann boundary condition which was used. The higher recirculating velocities in the non-dominant recirculation zone are the result of the increased curvature of the flow and the incorrect parameterization of the wall friction. However, it is likely the measurement underestimated the recirculating velocities due to clumping of tracer particles during the experiment. The initial contraction of the jet over the longitudinal slope is reproduced in a satisfactory manner, yet the continuation of this contraction in the deeper section of the flume is not simulated.

Considering these results, it was concluded a better definition of the wall friction in the model would increase the accuracy of the model. However, this is arduous to do due to the lack of vertical discretization, meaning wall friction cannot be placed on vertical grid elements. It was also concluded the horizontal streamline contraction is directly related to the changing water depth in the 2DH model. This is a discontinuity compared to the measurement data, where the streamlines were observed to

continue contracting past the longitudinal slope. As the vertical velocity profile in the 2DH model is also directly related to the water depth, this might indicate a discontinuity between the assumed log-profile in the 2DH model and the actual vertical velocity profile. This will be investigated in the subsequent 3D analysis.

4.4. 3D model results

In the previous section the 2DH model results were discussed. It was concluded the 2DH model reproduced most of the hydrodynamic processes observed in the laboratory experiment, though with low accuracy. The resulting flow profile therefore deviated from the measured flow profile. This section discusses the 3D model results, which is set-up in a similar fashion to the previous section. The additional vertical discretization allows for a proper inclusion of wall friction in the model. Furthermore, it can be investigated whether the vertical velocity profile is correctly simulated.

The modelled surface flow field is shown in figure 4.10, together with the contour lines for $|\vec{u}| = 0.35$ m/s (inner) and $|\vec{u}| = 0.1$ m/s (outer) of the PIV data. Note that the surface flow field is now used instead of the depth-averaged flow field of the 2D simulation in figure 4.3a. The PIV data is repeated in figure 4.10b.

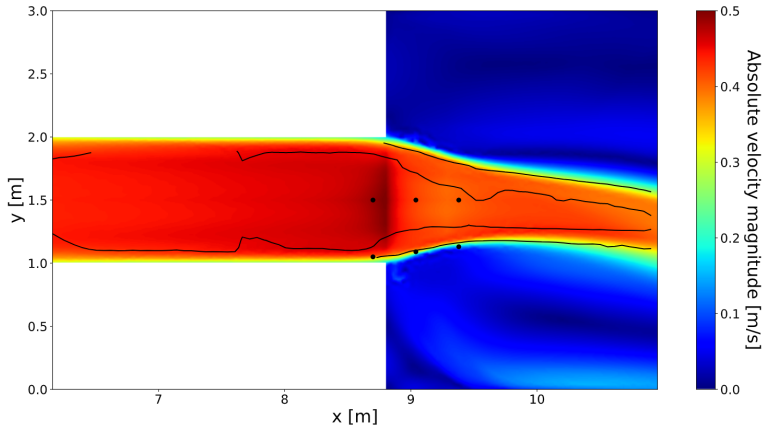

(a) 3D model.

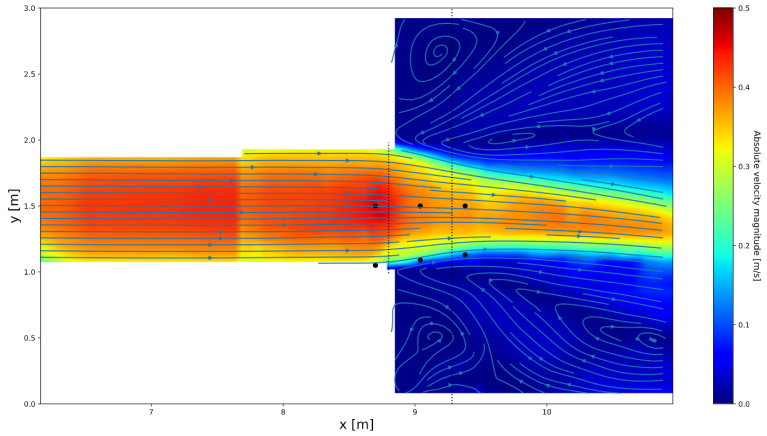

(b) PIV data of van de Zande (2018).

Figure 4.10: Reproduced flow profile within the DOI using the 3D model with the contour lines for $\vec{u} = 0.1$ m/s and $\vec{u} = 0.35$ m/s of the PIV measurements (black lines) and the locations of the ADV measurements (black dots) (a) and a repeat of the PIV data of van de Zande (2018) (b).

4.4.1. Asymmetry

Figure 4.10 shows the asymmetric pattern of the jet towards the lower side of the basin corresponds nicely with the PIV measurements. To better identify the accuracy of the model, the position of the

WCG is used in the same fashion as in the 2DH analysis. The positions of the WCG for the 3D model is compared with the PIV data and the 2DH model in figure 4.11.

In the figure, it can be observed that the recirculating velocities are still modelled incorrectly from the initial shift of the WCG towards the upper section of the flume. At $x = 9.5$ m the position of the WCG in the 3D model moves towards the lower section of the flume nearly parallel with the observed PIV measurements. Due to the discontinuity of the recirculating velocities between the PIV data and the 3D model, the position of the WCG will remain unequal throughout the entire domain. However, the near-parallel shift of the WCG towards the lower section of the flume indicates the curvature of the flow is of near-equal magnitude.

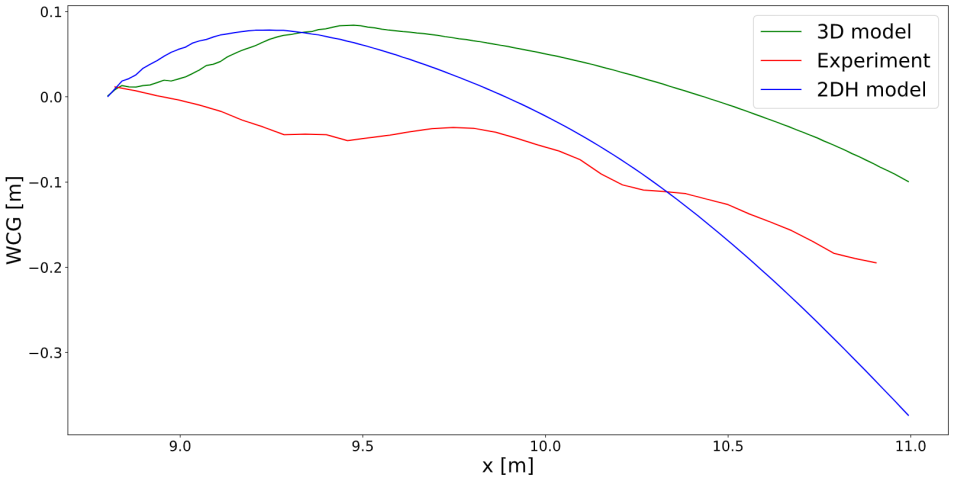

Figure 4.11: Lateral coordinate of the WCG within the DOI for the 3D model, the 2DH model and the PIV data.

Comparing the results of the 3D model to the 2DH model, it was observed both the initial upward shift and the following downward shift of the WCG happen more gradually in the 3D model. Comparing the point of attachment to the lower wall, the 3D model simulates that the jet hits the flow at a distance of $x = 14$ m, which is 5.2 m from the expansion and 1.2 m further downstream compared to the 2DH model. The better reproduced curvature of the flow in the 3D model suggests the downstream location of the attachment to the lower wall is more accurate in the 3D model.

To identify the cause of the better reproduced recirculating velocities, the magnitude of the lateral velocity component throughout the DOI is shown in figure 4.12. The high positive and negative lateral velocities direction at the expansion are similar to the results of the 2DH model. However, further downstream, the high negative lateral velocities in the dominant reciculation zone at $y \geq 1.5$ m cannot be observed in the 3D model. The positive lateral velocities in the non-dominant recirculation zone are still present. As a result, the jet is better maintained in the center of the channel and curves less towards the lower section of the flume. This is caused by a change in the dominant recirculation zone, which will be discussed in the subsequent subsection. Compared to the PIV measurements, the reproduction of the lateral velocity component in the 3D model complies significantly better compared to the 2DH model results. This attributes to the better reproduced curvature in the 3D model.

It was concluded the 3D model accurately simulates the asymmetric flow pattern within the DOI. Unfortunately, no statement could be made regarding the further development of the asymmetric pattern in the flume due to the lack of PIV data further downstream.

4.4.2. Recirculation zones

Figure 4.13 shows the vertical vorticity ω_z distribution within the DOI, combined with the streamlines for both the 3D model and the PIV measurements. Again, the unexpected sign changes of the vorticity surrounding the jet are attributed to the wiggly behaviour of the model due to the absence of a flux

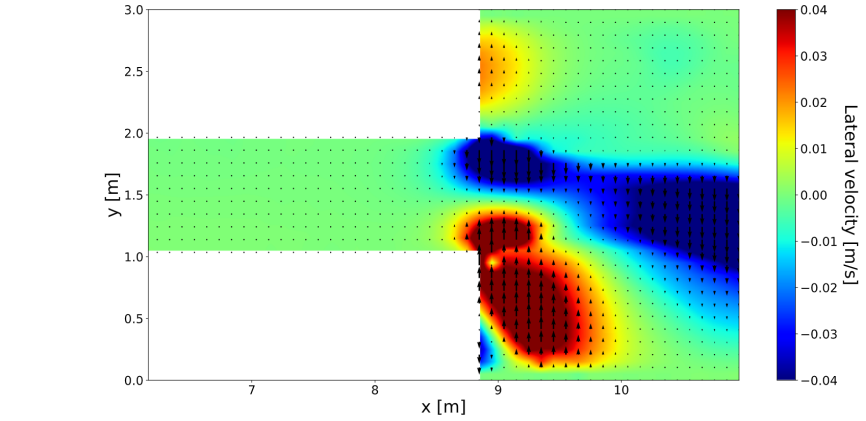

(a) 3D model.

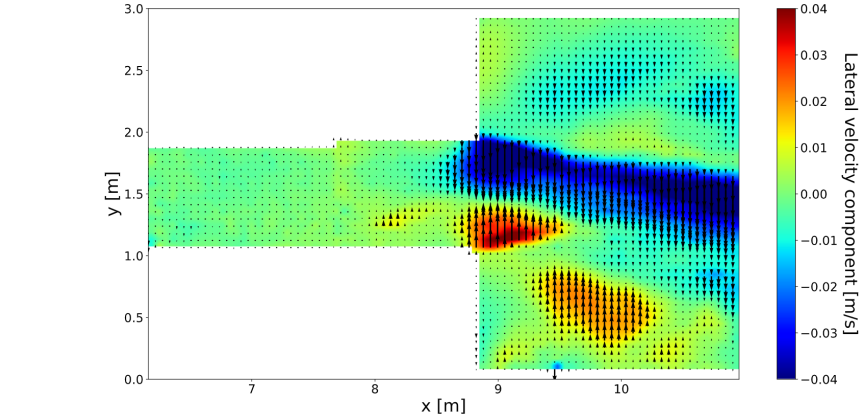

(b) PIV data of van de Zande (2018).

Figure 4.12: Reproduced lateral flow velocities by the 3D model (a) and the measured lateral flow velocities using the PIV (b).

limiter. Note that, contrary to the 2DH simulations, now only the surface velocities are used for the determination of ω_z rather than the depth-averaged velocities to comply with the PIV data.

Four recirculation zones can be identified within figure 4.13, two on either side of the jet. In the bottom section of the flume the non-dominant recirculation zone is clearly visible as the large clock-wise rotating eddy. Furthermore, in the upstream corner in the bottom section of the flume a corner eddy can be identified to rotate counter-clockwise. Next to the lower wall of the flume the sudden vorticity increase shows the presence of the wall boundary layer. In the upper section of the flume the dominant recirculation zone is less present as it is largely overruled by the upstream-upper corner eddy. This change in the shape of the dominant recirculation zone decreases the lateral flow velocities in the dominant recirculation zone. It can be seen in figure 4.13a that the streamlines in the dominant recirculation zone approach the jet at a small angle, whereas in the 2DH model results the streamlines in the dominant recirculation zone were nearly perpendicular to the jet.

Comparing figure 4.13 to the experimental data in figure 4.13b it was observed all four recirculation zones were reproduced by the 3D model, contrary to only the dominant and non-dominant recirculation zone in the 2DH simulation. This justifies the suggestion by Dewals et al. (2008) indicating the importance of wall friction for the reproduction of corner eddies. Furthermore, the inclusion of the corner eddies in the 3D model alter the shape of the dominant recirculation zone and therewith improve the modelled curvature of the jet.

Though discontinuities between the vertical vorticity distribution and the streamlines between the PIV data and the 3D model are evident, inaccuracies in the PIV data should be taken into account. It was stressed in van de Zande (2018) that the tracer particle distribution could contribute to measurement

inaccuracies. In the video data of the experiment it was observed very few traces were present in the upstream-upper section of the flume. Therefore, it is difficult to draw conclusions from the observed and modelled recirculation zones in the upper section of the flume. It was readily explained in the 2DH analysis that in the lower section of the flume the tracer particles were clumped, which could have influenced the accuracy of the data. These effects make it difficult to draw conclusions on the differences between the 3D simulation and the PIV data. For the purpose of this work, it was concluded the recirculation zones were correctly reproduced by the 3D simulation as all four recirculating areas are captured, without making a statement regarding the shape or size of the individual recirculation zones.

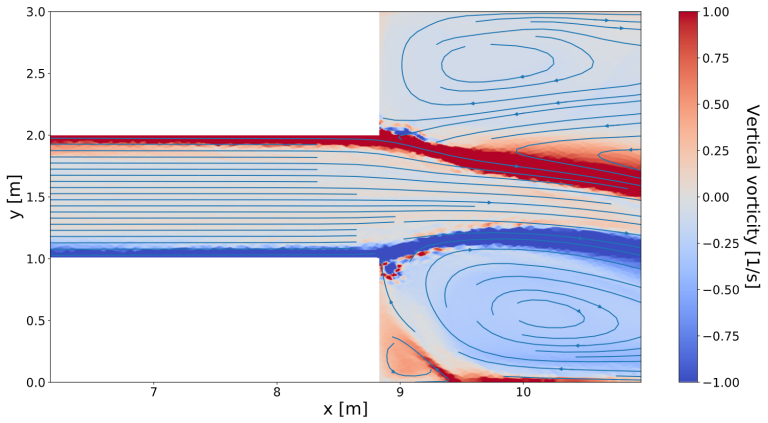

(a) 3D model.

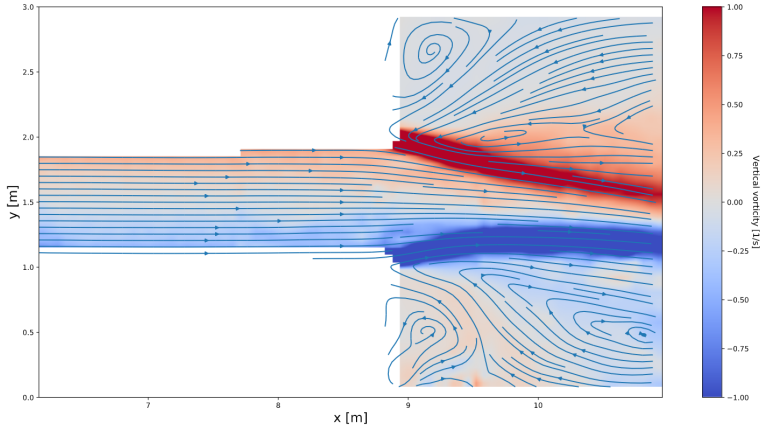

(b) PIV data of van de Zande (2018).

Figure 4.13: Modelled streamlines and vertical vorticity distribution for the 2DH simulation and the PIV data of experiment 2.4.1 of van de Zande (2018).

4.4.3. Horizontal streamline contraction

Already from figure 4.10 it can be seen the horizontal surface streamline contraction is more gradual compared to the 2DH simulation in figure 4.3a, which complies better with the PIV data in figure 2.13.

Again, the jet width as determined using the maximum and minimum vorticity in each lateral cross-section was used to determine the jet contraction as explained in section 4.3. Both the surface values and the depth-averaged values were considered in this analysis. The result is shown in figure 4.14, which shows the comparison of the PIV measurements with the 3D and 2DH model. Even though the jet width on the slope does not comply directly with the PIV measurements, the contraction of the jet is simulated along a nearly equal slope. It was calculated that the surface streamline contraction of the 3D model over the slope equals 0.28 m, which slightly underestimates the contraction according to the PIV data.

Furthermore, contrary to the 2DH model, the jet width in the 3D model can be seen to continue de-

creasing after the slope, both for the depth-averaged and surface streamline contraction. This also complies with the PIV data. Due to the differences between the 3D modelled depth-averaged streamline contraction and the 2DH modelled streamline contraction, it was concluded that the 3D model reproduces the streamline contraction differently compared to the 2DH model, rather than just supplying additional information regarding the surface contraction.

Considering the difference in jet width b between the PIV data and the 3D model, it was observed the difference remains relatively constant throughout the DOI with around 0.06 m, which is an error of around 6% compared to the starting jet width of 1 m. It was concluded the 3D model properly reproduces the streamline contraction throughout the entire DOI.

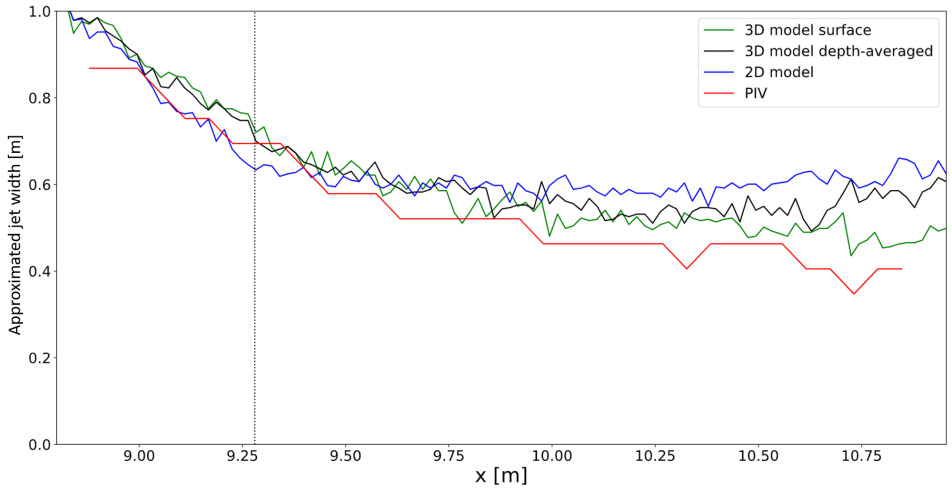

Figure 4.14: Approximated jet width development for $8.8 < x < 11$ m for both the PIV measurements (red), the 2DH modelled jet (blue) and the 3D modelled jet (green and black).

4.4.4. Lateral velocity profiles

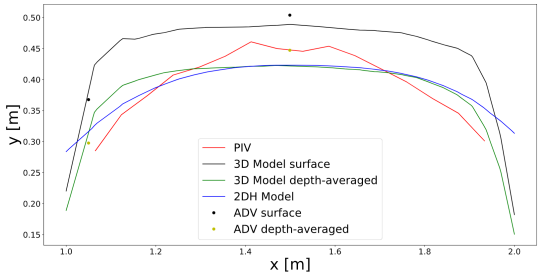

(a) x = 8.70 m.

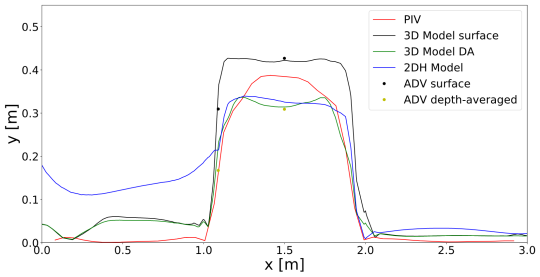

(b) x = 9.04 m.

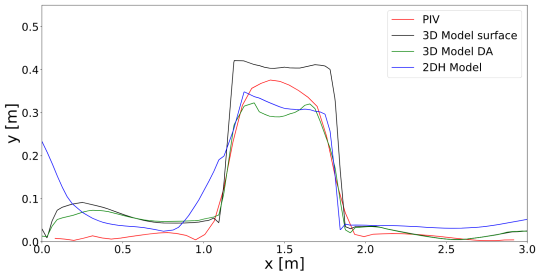

(c) x = 9.38.

Figure 4.15: Comparison of lateral distribution of the total horizontal velocity for three lateral cross sections through the flume for the 3D simulations and the experimental data.

Figure 4.15 shows the lateral velocity profiles for each ADV measurement location, comparing the PIV,

ADV, 3D model surface velocities, 3D model depth-averaged velocities and the 2DH model velocities. Comparing the depth-averaged velocities of the 3D model to the velocities of the 2DH model in figure 4.15a, it can be seen the velocities in the flume center are nearly equal, but vary largely towards either confining wall. At the location of both lateral walls the velocities are largely overestimated by the 2DH model compared to the 3D model. Table 4.3 shows the error made by the 3D model relative to the PIV flow velocity in the jet center for the non-dominant recirculation zone, the jet center, and the dominant recirculation zone. Especially in the non-dominant recirculation zone, a significant decrease of the error compared to the 2DH model can be seen. It was concluded that the proposed parameterization of the wall friction in the 2DH does not comply with the 3D model. Furthermore, table 4.3 shows the error made by the 3D model in the jet center is significant. Figure 4.15 shows the error the result of an overestimation of the flow velocity in the jet center. However, compared to the ADV measurements, the reproduced flow velocities comply well.

Table 4.3: Error made by the 3D model with respect to the PIV-measured flow velocity in the jet center in the non-dominant recirculation zone ($0 \leq y < 1$), within the jet ($1 \leq y \leq 2$), and in the dominant recirculation zone ($2 < y \leq 3$).

	Error with respect to the jet center-velocity [%]		
x [m]	$0 \leq y < 1$	$1 \leq y \leq 2$	$2 < y \leq 3$
8.7	-	6.1	-
9.04	12.4	10.2	3.66
9.4	18.9	12.0	2.02

Figures 4.15b and 4.15c show the velocities in the upper recirculating area are simulated better compared to the 2DH model, as the velocities are nearly zero. However, inaccuracies still persist as the velocities are still non-zero. Considering the lower-section recirculation zone a more significant decrease in recirculating velocities can be observed. It was hypothesized in section 4.3 that the high recirculating velocities simulated by the 2DH model were the result of the lack of proper parameterization of the wall friction and the more upstream located reattachment point. The more complying curvature of the flow and the inclusion of wall friction in the 3D model lead to believe both these issues no longer hold, which is consistent with the observed decrease in recirculating velocities. Nevertheless, a maximum error of 18.9% persists in the 3D model. Though it can be speculated this is the result of an imperfect inclusion of wall friction or a curvature located further upstream compared to the measurement data, the discontinuity between the measurements and the model might also be caused by the named measurement inaccuracies.

Comparing the 2DH velocities and the 3D depth-averaged velocities, it can be observed the simulation of the jet is similar. Due to the higher curvature in the 2DH model, figure 4.15c shows higher velocities towards the bottom side of the flume. Nevertheless, between $1 < y < 2$ both models are similar. Large differences between both models can be noticed at either recirculation zone, as discussed above.

It was observed that the surface velocities of the 3D model are significantly higher than the PIV measurements in all three cross-sections. However, the surface ADV data and the modelled surface velocities comply well. Table 4.4 shows the error made at four of the six horizontal locations of the ADV measurements relative to the ADV measurements. The ADV measurements downstream of the slope are not considered as no measurement close to the surface was made. It can be seen at $x = 8.70$ m that both the wall and center-line measurement are simulated accurately with only a small error. At $x = 9.04$, the center-line velocity is simulated accurately as well, yet the measurement towards the side of the jet is simulated with an error > 10%. However, the velocity gradient at $y = 1.09$ m is very steep, as can be observed in figure 4.15b, meaning a very small deviation in jet width already results in a significant velocity decrease. The accuracy at $x = 8.70$ m indicates the wall friction as modelled by the 3D model yields accurate results.

It was concluded the 3D model simulated the velocity profiles in the jet correctly. In the center-line of the jet, the maximum error made was around 3% compared to the ADV data. The parametrization of the wall friction appeared correct in the approach channel, though a small overestimation of the jet width resulted in a large error at the jet side. Though the error made in the dominant recirculation zone

is high at 18.9% of the center-line velocity, it is thought the recirculating flow velocities in the PIV data are underestimated due to clumping of tracer particles.

Table 4.4: Absolute error made when comparing the 3D surface velocities to the ADV measurements of experiment 2.4.1 of van de Zande (2018).

x [m]	y [m]	Absolute error [%]
8.70	1.50	3.02
8.70	1.05	1.97
9.04	1.50	1.69
9.04	1.09	12.6

4.4.5. Vertical velocity profiles

With the additional vertical discretization, the vertical velocity profiles simulated by the 3D model can be compared with the ADV data as shown in figure 4.16. Additionally, the logarithmic velocity profile as reproduced by the 2DH model is shown using the depth-averaged velocity values from the 2DH model. The error made by both models is quantified using the relative error. The results are shown in table 4.5. The relative error was defined as the average error made when comparing the individual ADV measurements with the modelled velocities at equal height. For this purpose, the 3D modelled velocities are interpolated linearly to the location of the ADV measurements. The interpolation error made was assumed small due to the large amount of layers in the model.

It can be observed from figure 4.16 that at $x = 8.70$ m both the 3D and 2DH model simulate a logarithmic velocity profile which only creates a small error with respect to the ADV measurements. Further downstream, the adverse pressure gradient on the slope slows down the water in the lower section of the water column compared to the standard log profile. This process is captured by the 3D numerical model.

On the slope and downstream thereof, the velocities in the lower half of the water column are lower for the measurements and the 3D model compared to the standard log-profile. This indicates the adverse pressure gradient on the slope slows down the water in the lower section of the water column. In the 2DH model, this effect is partly counter-acted by lower velocities simulated by the log profile in the upper section of the water column, resulting in similar depth-averaged flow velocities. Nevertheless, it is evident the standard log profile as employed by the 2DH model does not comply with the vertical velocity profile on and downstream of the slope.

Though on the slope the error made by the 3D model is still relatively large with 10.1%, the error made by the standard log-profile in the 2DH model is significantly higher at 21.8%. Downstream of the slope, the error made by the 2DH model is even larger at 32.5% whereas the error made by the 3D model decreases to 7.4%. From these errors, it can be concluded the 3D model is capable of capturing the effect of the adverse pressure gradient on the vertical velocity profile.

The adaptation of the vertical log-profile to the adverse pressure gradient is sudden in the 2DH model. This means that at the position of the changed water depth, the log-profile is assumed to immediately adapt towards a new equilibrium log-profile. In the measurements and the 3D model results, it is evident this adaptation is not sudden as the vertical velocity profiles do not comply with the vertical log-profile. From this, an hypothesis was made for the differences in modelled horizontal streamline contraction between the 2DH and 3D model.

Broekema et al. (2018) has shown the relationship between horizontal streamline contractions and vertical velocity profiles, where the bulk of the flow is redistributed over the vertical rather than the horizontal over longitudinal slopes when considering vertical flow attachment. Considering the 2DH model, this redistribution is sudden as the vertical velocity profile immediately adapts to a new equilibrium. Therefore, the horizontal streamline contraction is a function of the water depth changes. Considering the 3D model and the measurements, this redistribution is not sudden and continues further

downstream, corresponding to the continuing streamline contraction downstream of the slope.

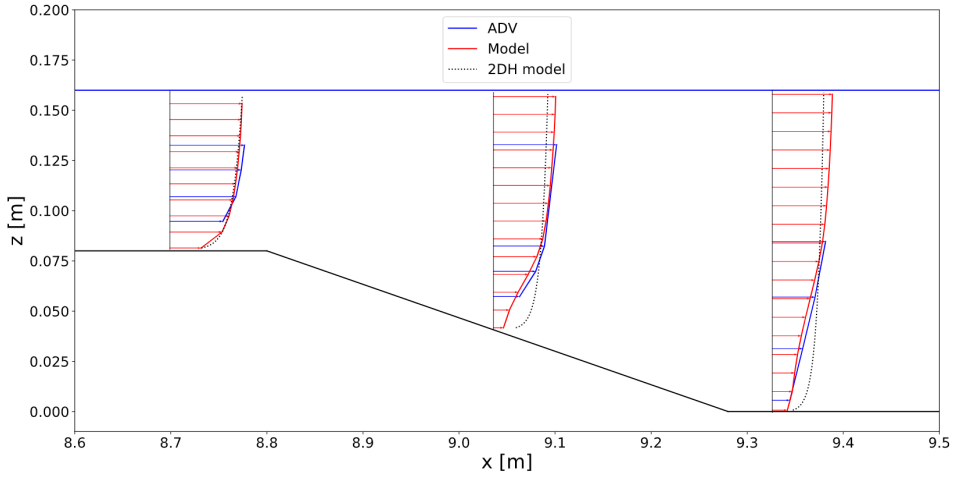

Figure 4.16: Comparison of vertical velocity profile simulated by the ADV data, the 3D model and the standard log-profile used in the 2DH model at $y = 1.5$ m.

Table 4.5: Relative error made comparing the 3D vertical velocity profile to the individual ADV measurements at y = 1.5 m.

x [m]	Relative error 3D [%]	Relative error 2DH [%]
8.70	5.73	6.81
9.04	10.1	21.82
9.38	7.4	32.47

4.5. Conclusion

To conclude, it was observed that both the 2DH model and the 3D model were capable of reproducing most of the hydrodynamic processes researched by van de Zande (2018). Both models correctly simulated a concentration of flow along the bottom wall of the flume. Nevertheless, based on the position of the WCG, it was concluded that the 2DH model simulated too much curvature, meaning the flow reached the bottom wall too far upstream compared to the PIV measurements. It was suggested that this at least partially caused the higher recirculating velocities which were observed in the non-dominant recirculation zone in the 2DH simulation. This is stimulated by the lower recirculating velocities found in the 3D model in which the curvature was simulated more accurately. The more accurate reproduction of the flow curvature in the 3D model is the result of lower negative lateral velocities in the upper section of the flume compared to the 2DH model. This discontinuity in the magnitude of the lateral velocities between both models is an alteration of the shape of the dominant recirculation zone.

The discontinuity in the lateral position of the WCG between the PIV measurements and the 3D model simulations were the result of the higher recirculating velocities which were modelled in the non-dominant recirculation zone. Possible causes for these higher velocities were speculated to be a more upstream reattachment point, an incorrect parameterization of wall friction or possible measurement errors in the PIV data due to clumping of tracer particles which was observed in the video measurements.

Dewals et al. (2008) suggested the upstream corner eddies which were observed in asymmetric flow could only be simulated by a numerical model containing wall friction. The simulations carried out in this work confirm this, where the 2DH simulation without wall friction solely reproduced the dominant and non-dominant recirculation zone and the 3D simulation reproduced all four recirculating gyres. The latter also complies with the PIV measurements. Furthermore, the inclusion of the corner eddies altered the shape of the dominant recirculation zone, which in turn decreased the curvature towards the east in the 3D model. Nevertheless, discontinuities between recirculating areas observed in the PIV data and the 3D simulation were evident. It was observed that the upper corner eddy was modelled too large, whereas the bottom corner eddy was modelled too small. However, due to the possibility of errors in the PIV data regarding the recirculating areas as stressed in van de Zande (2018) and as observed in the video measurements it could not be said whether the model was incorrect.

Regarding the vertical velocity profiles it was observed that the 3D model correctly simulated the vertical flow attachment on the slope and downstream of the slope. The deviation from the standard logarithmic velocity profile on both locations was also simulated correctly, showing lower velocities in the lower section of the water column due to the adverse pressure gradient. The vertical velocity distribution in the 2DH model is therefore incorrect over both the slope and downstream thereof, resulting in an maximum relative error of 32.5%. Nevertheless, the 3D model contained relative errors of up to 10% in the vertical velocity profiles. The 3D model was especially erroneous on the slope.

Both the 2DH and the 3D model rightfully simulated a streamline contraction over the longitudinal slope directly at the expansion. The jet contracted more in the 2DH model compared to the 3D model and the PIV measurements. However, at the end of the longitudinal slope the jet in the 2DH model stopped contracting and remained relatively constant throughout the rest of the DOI. This does not comply with the PIV measurements, where the jet was observed to continue contracting after the slope. The 3D model did simulate this continuous contraction after the slope, though the initial jet contraction was observed to be lower compared to the PIV measurements.

It was concluded the horizontal streamline contraction is related to the vertical velocity profile. The relation between horizontal streamline contractions and vertical flow profiles has already been shown in Broekema et al. (2020), where it was explained the bulk of the flow is redistributed in the vertical plane in the case of vertical flow attachment. In the 2DH model, the relation between the changes in water depth and the streamline contraction was thought to be the result of changes in the vertical log-profile due to the changes in water depth. In the 3D model, the vertical velocity profile can be seen to differ from the vertical log-profile on the slope. Further downstream, the profile still deviates from a standard log-profile. Downstream of the slope, the vertical profile will move towards an equilibrium log-profile as simulated in the 2DH model. As the redistribution of the bulk of the flow happens gradually in the

3D model and abrupt in the 2DH model, it is likely the corresponding horizontal streamline contraction behaves in a similar fashion.

The lateral velocity profiles showed that the parameterization of wall friction in the 2DH model was incorrect. Comparing the surface velocities of the model, the ADV and the PIV, it was concluded that the PIV measurements underestimated the surface velocity. It was concluded that the 3D simulated surface velocities complied well with the surface ADV measurements.

5

2DH and 3D model application at Waterdunen

In the previous chapter, knowledge was gained regarding the performance of 2DH and 3D FINEL models for the reproduction of shallow jet flows. With the obtained knowledge, the models for Waterdunen can be set-up. The flow at the seaside of Waterdunen had already been investigated using numerical models in Svasek Hydraulics (2020). They used both a FINEL2D-Explicit and a TUDFLOW3D as model to investigate the flow. Their model results are discussed in appendix C.1.

This chapter will explain the FINEL models set-up to analyse the flow at Waterdunen and compare their results with the measurements from the measurement campaign. It was chosen to simulate measurement scenario 5 since the data quality was high during this scenario. Furthermore, the slide was not used in scenario 5, which saves complexity within the numerical model. Both a 2DH and a 3D model were set-up to assess the performance of either model. First, the model set-up is discussed in section 5.1. Afterwards, the results of the 2DH simulation are discussed in section 5.2, and the results of the 3D simulation are discussed in section 5.3. The simulations are concluded in section 5.4.

5.1. Model set-up

Similar to the previous chapter, identical numerical and physical settings were used for the 2DH model and the 3D model save for the vertical discretization, and corresponding turbulence closure model. This ensures the differences between the results of either model are only caused by the inclusion of the third dimension in the 3D model.

Instead of simulating only the seaside channel at Waterdunen, a large Western Scheldt model was used to minimize the effect of the tidal boundary conditions. This Western Scheldt model required a spin-up time of 3 days before the start of the discharge through the culvert to remove the effect of the initial conditions.

5.1.1. Western Scheldt model

It was noticed in the validation in chapter 4 that the simulations of the experiment of van de Zande (2018) became unstable at the downstream boundary condition if no flux limiter was employed. To counteract this effect in the laboratory simulations, a Riemann boundary condition was set-up at the downstream boundary, which was hypothesized to cause small errors within the DOI. To bypass this effect in the Waterdunen models, the downstream boundary conditions were placed far away from the DOI. Instead of a single downstream boundary condition, three tidal boundary conditions were placed in the North Sea containing multiple tidal constituents. This model was created and calibrated by Svašek Hydraulics. An overview of the numerical domain is shown in figure 5.1.

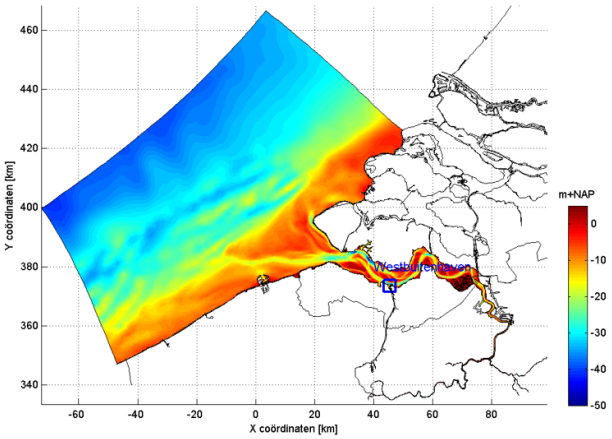

Figure 5.1: Overview of the overlaying Western Scheldt model used to simulate the downstream boundary conditions for the Waterdunen model.

5.1.2. Domain of interest

The domain of interest spans the measured section of the seaside channel of Waterdunen as was analysed in the data analysis in chapter 3. This area spans around 200 m downstream of the culvert and approximately 10 m upstream from the culvert. Nevertheless, the most important hydraulic processes, such as the asymmetry and the contraction of the jet, are visible in the initial 100 m downstream from the culvert. It was therefore decided to refine the grid on this interval.

5.1.3. Numerical grid

Within the Western Scheldt model, the grid size ranges from $\Delta_H = 2120$ m in the North Sea to $\Delta_H = 137$ m in the Western Scheldt. Moving towards Waterdunen, the grid gradually refines to $\Delta_H = 7$ m just outside of Waterdunen.

Inside the DOI, the horizontal grid size equals $\Delta_H = 0.7$ m. This size roughly corresponds to the separating walls between the casings inside the culvert. Therefore, one grid cell separates the individual outflow streams. Just outside of the DOI, from 100 to 200 m downstream from the culvert, the horizontal grid resolution was doubled to $\Delta_H = 1.4$ m to preserve computational power.

The entire length of the culvert including the inflow point was modelled using the fine grid of $\Delta_H = 0.7$ m. Again, this size was chosen to resemble the width of the separating walls between casings. Furthermore, approximately 6 grid cells span each casing, leaving room for the effect of wall friction in the 3D model. This fine grid was extended 20 m upstream from the inflow point of the culvert.

A small section of the inland side of Waterdunen was also modelled to circumvent the effect of instabilities of the upstream boundary on the inflow into the culvert. Therefore, the upstream boundary condition was located approximately 100 m upstream from the point of inflow into the culvert. The horizontal grid size from the boundary towards the refinement close to the culvert was set at $\Delta_H = 2.8$ m as this was estimated to be sufficiently fine for the approach flow. A close-up of the grid surrounding Waterdunen is shown in figure 5.2.

Considering the vertical discretization in the 3D model, the vertical grid size inside the DOI was set to roughly comply with the horizontal grid size. With an average water depth of 4 meters, 8 layers were used inside the DOI, resulting in $\Delta z = 0.5$ m. This ensures $\Delta z \approx \Delta_H$. Outside the DOI either 2 or 3 layers were used depending on the local water depth.

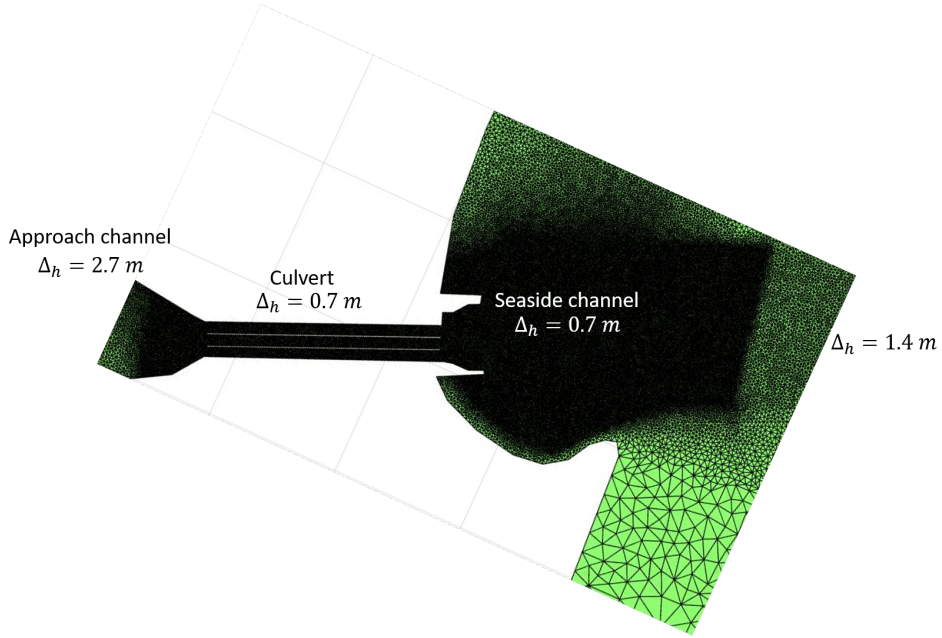

Figure 5.2: Close-up of the numerical grid surrounding the DOI at Waterdunen.

5.1.4. Roughness

The Nikuradse roughness height was set to vary within the model. A value of $k_s = 0.035$ m was calibrated by Svašek Hydraulics to most accurately represent the bedforms in the North Sea and Western Scheldt within the model. At Waterdunen the roughness was set to vary depending on the bottom type. Inside the culvert, the Nikuradse roughness was approximated to be $k_s = 0.001$ m. The inside of the culvert was expected to be relatively smooth, indicating a low Nikuradse roughness could be used.

Outside of the culvert, the loose rock of the bed protection was assigned a Nikuradse roughness height of $k_s = 2d_{n,50}$ as suggested in Schiereck (2017). However, it should be noted this approximation for k_s is largely variable, for relations such as $k_s = 6d_{n,50}$ are also noted in Schiereck (2017).

For the penetrated rock in the initial 30 m downstream from the culvert, the Nikuradse roughness was estimated to be around $k_s = 0.1$ m as no clear guidelines could be found. This value roughly corresponds to half the nominal diameter of the stones.

Contrary to the simulations of the laboratory experiment, no effort was made to simulate wall friction in the 2DH model. The results from the previous section pointed out used parameterization of wall friction in the 2DH model did not comply with the measurement data or the 3D model results. This means both the physical and numerical basis of the parameterization was doubtful, even though the 2DH model results did improve.

5.1.5. Groynes

Waterdunen lies within a groyne system in the Western Scheldt. These groynes create wakes on their downstream side where the flow is relatively unaffected by the tidal movement. During the simulations, it was noticed this affected the curvature of the jet flow in the seaside channel. It was therefore decided to include several groynes into the model to ensure the flow follows the correct path. This included three groynes on the east side of Waterdunen and one groyne on the west side of Waterdunen. The individual groynes were simulated as weirs within the model with a set crest height at 0.5 m+NAP and equal slopes of 1:8 towards either side of the crest. Considering the water levels in the channel, this indicates the crests are never submerged during the simulations.

5.1.6. Salinity
Salinity transport was completely neglected within the models as no data regarding the salinity concentrations was available. Salinity differences could cause density differences between the inland lake and the seaside channel at Waterdunen, which in turn could affect the outflow from the culvert. However, the imposed density differences were expected to be small. It was therefore assumed the neglect of salinity had little effect on the model results.

5.1.7. Turbulence closure models
In the preliminary simulations at Waterdunen explained in appendix C.2, the same horizontal Smagorinsky mixing length model was used as in the validation in chapter 4. It was observed the model resolved a plethora of instantaneous vortices around the jet, which would grow and shred from the primary jet stream. These vortices create a relatively blurred time-averaged flow profile that did not comply with the results of the data analysis in chapter 3. The Smagorinsky model allows these vortices to be resolved if they are larger than the horizontal grid size Δ_H.

To simulate a more accurate flow field, it was decided to resolve the mixing-length by prescribing a turbulent length scale L_t to the model rather than using Δ_H. As a result, all turbulent fluctuations are neglected and only the mean flow profile is resolved. L_t was approximated to be 6 m, which corresponds to half the jet width of all three casings combined. Using the constant $C_{lm} = 0.16$ explained in chapter 4, the resulting mixing length equals $l_m = 1$ m. Compared to the Smagorinsky model, this mixing length is approximately 14 times larger. Therefore, the resolved turbulent viscosity is significantly larger compared to the previous simulations, which is likely to dampen the resolved vortices. However, this also introduces more turbulent diffusion into the system, which affects the hydrodynamic processes. Though the effect of different turbulence closure models on the resolved flow field is not investigated in this work, this should be kept in mind during the analysis.

The laboratory simulations showed the $k-\epsilon$ model reproduced accurate vertical velocity profiles with a maximum relative error of 10%. This was deemed adequate for the Waterdunen simulations, meaning the same $k-\epsilon$ model was used as prescribed in chapter 4.

5.1.8. Numerical parameters
Complying with the laboratory simulations, no flux limiter was used within the model to ensure second-order accuracy. Furthermore, the implicity factor θ was set at 1 as no instantaneous turbulent fluctuations are resolved using the current mixing-length turbulence closure model. The depth-averaged analysis of the measurement data partook on a time-averaged, interpolated grid with $\Delta t = 10$ minutes, meaning the instantaneous turbulent fluctuations would have little additional value. However, the neglect of turbulent fluctuations should be kept in mind when comparing instantaneous transects sailed during the measurement campaign to the model results.

5.1.9. Boundary conditions
Three tidal boundary conditions were imposed on the edges of the numerical domain inside the North Sea. During the simulations, it was noticed the 2DH and 3D numerical model simulated different downstream water levels at equal times. This discontinuity was likely caused by the neglect of salinity transport in the models, which primarily affected the 3D model simulations. For the purpose of this work, the downstream water levels of the 2DH and 3D numerical models were matched as accurately as possible by altering the simulation times. The reproduced water levels are compared to the measured water levels in figure 5.3.

Figure 5.3 shows both models overestimate the downstream water level compared to the measurements. Furthermore, the water levels simulated by the individual models are not equal, with the 3D model being slightly more accurate compared to the 2DH model. It can be seen the 2DH model is slightly further in the tidal cycle compared to the 3D model and the measurements based on the rate of change of the downstream water level.

Though it is difficult to quantify the effect of the discontinuity in the downstream water level, it can be said the flow velocities can be expected to be slightly lower in the models. This again affects the repro-

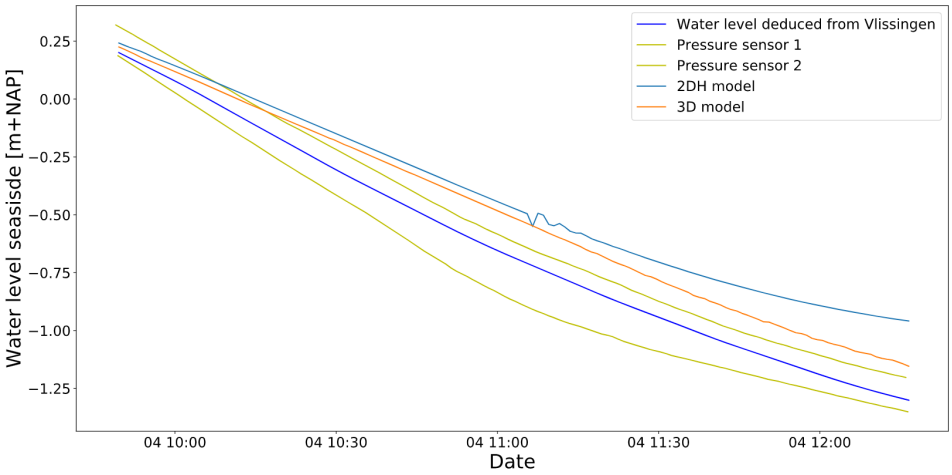

Figure 5.3: Comparison of the water levels downstream of the culvert as simulated by the 2DH and 3D model and as measured during the measurement campaign.

duction of the hydrodynamic processes. This should be kept in mind when analysing the model results.

On the inland side of Waterdunen, a discharge boundary condition was imposed around 100 m upstream from the culvert. The discharge values were calculated based on the volume of water inside Waterdunen as was also done in chapter 3. The process is explained in detail in appendix A.4. It should be noted that this is an approximation of the discharge through the culvert. This approximation is sensitive to surface disturbances in Waterdunen such as surface waves and wind set-up. Therefore, a small error in the discharge can be expected.

The discharge through the culvert started well before the measurement campaign to reach the desired water level difference and discharge during the campaign. It was noticed that the calculated discharge was oscillatory. It was therefore decided to smoothen the discharge curve, as is shown in figure 5.4. The oscillatory movement is likely caused by surface disturbances inside the lake, such as wind set-up and surface waves.

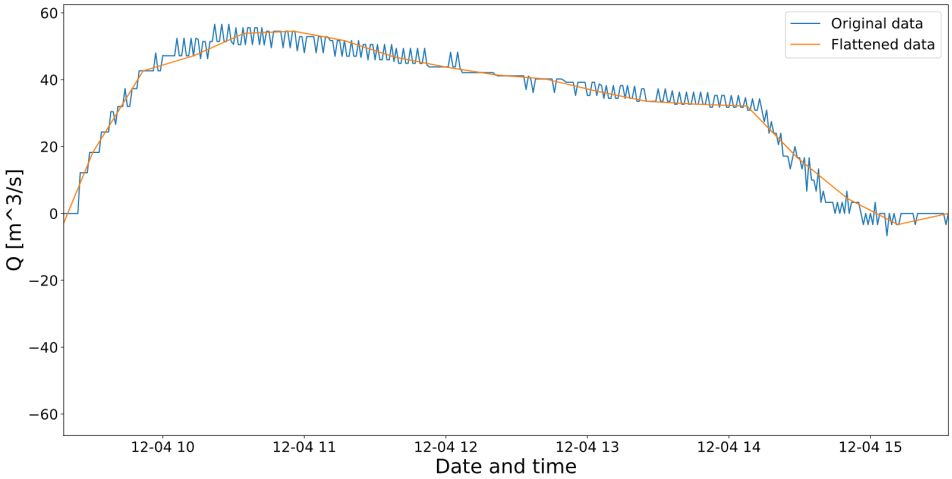

Figure 5.4: Varying discharge as calculated using the volume of water inside Waterdunen (blue) and the flattened discharge input in the numerical models (orange).

5.1.10. Analysed timesteps

During the data analysis in chapter 3, the data was interpolated on timesteps with $\Delta t = 10$ min. Therefore, several points in time were created where the flow could be analysed. The data analysis in

appendix A showed that for scenario 5 timesteps T = 2 and T = 6 yielded the most complete flow profiles. Furthermore, between T = 2 and T = 6 the water level in the channel was dropping due to the tide and the discharge slightly increased. Therefore, a comparison between either timestep allows for an analysis of the effect of both a decreasing H and an increasing Q. Finally, the flow remains sub-critical during both timesteps. The relevant parameters at T = 2 and T = 6 during scenario 5 are shown in table 5.1.

Table 5.1: Time steps used in the analysis of the data.

Time step	Begin time	End time	Discharge [m3/s]	Downstream water level [m + NAP]
T = 2	09:59	10:06	45.0	0.03
T = 6	10:41	10:51	54.2	-0.49

5.2. 2DH model results

This section will portray the 2DH model results. The methodology as used in the previous chapter will be used here as well, in which each hydrodynamic process will be investigated individually. However, certain phenomena cannot be directly compared to the measurement data. The obtained knowledge from the previous chapter can be used to suggest differences and inaccuracies between the models and the measurement data. Furthermore, the development of the flow at lower H and higher Q will be investigated by comparing flow profiles between T = 2 and T = 6.

The absolute velocity magnitudes for T = 2 and T = 6 are shown in figure 5.5a and 5.5c. The most important parameters corresponding to both timesteps are explained in table 5.1. For comparison purposes, the interpolated flow fields from the measurement data at both timesteps are included in figures 5.5b and 5.5d. In the caption of the figures, the discharge and downstream water levels are included to interpret the error made by the 2DH model concerning the water level in the channel. It shows that the water levels reproduced by the 2DH model are higher compared to the measurement data. In general, this results in lower flow velocities in the model compared to the measurement data. This is visible when comparing the model results to the measured data in figure 5.5. The 2DH model underestimates the flow velocity throughout the DOI for both timesteps. Furthermore, the width of the jet is smaller in the 2DH model compared to the measurements. However, this is likely the result of the performed interpolation.

5.2.1. Asymmetry

The model results in figures 5.5a and 5.5c clearly portray the eastern concentration of the flow as was also observed from the measurement data in figures 5.5b and 5.5d. The movement towards the east starts directly when the streams from the three individual casings merge. In the model, the flow stops curving towards the east at the end of the eastern cove at $x' = 45$ m and detaches from the eastern side of the channel at $x' = 55$ m. Both values can be seen to vary slightly with time. Comparing figure 5.5a to figure 5.5b and the streamlines in figure 5.7, it was concluded the location of attachment is correctly simulated by the 2DH model. However, the position of detachment is located further downstream for the measurement data.

The WCG as defined in equation 2.7 was used to identify the asymmetry of the flow. In order to properly compare the 2DH model results to the measurements, the data was interpolated to the same 101×61 grid as the measurement data. Furthermore, grid cells without measurements in the measurement data are also neglected in the grid of the model results to make a fair comparison. The WCG indicates the weighted lateral coordinate y' where the bulk of the flow is located and therefore serves as an indicator for the asymmetry of the flow. Figure 5.6 shows the variation of the location of the WCG in streamwise direction for both the measurements and the 2DH model for T = 2 and T = 6.

Directly at the first measurement of the position of the WCG, the model shows a more eastern position of the WCG compared to the measurements. Considering figure 5.5, this is the result of the broader jet visualized in the measurement campaign due to the interpolation. As the east side of the jet is not measured during the campaign, this interpolation favours the west side and therewith more

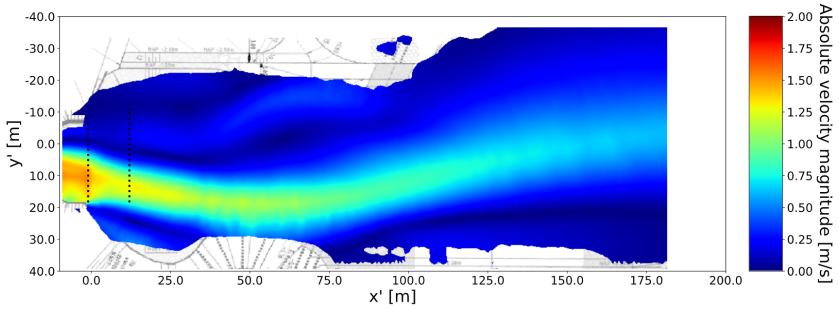

(a) 2DH modelled absolute velocity magnitudes for T = 2 ($Q = 45\ m^3/s$, $H = 0.11$ m+NAP).

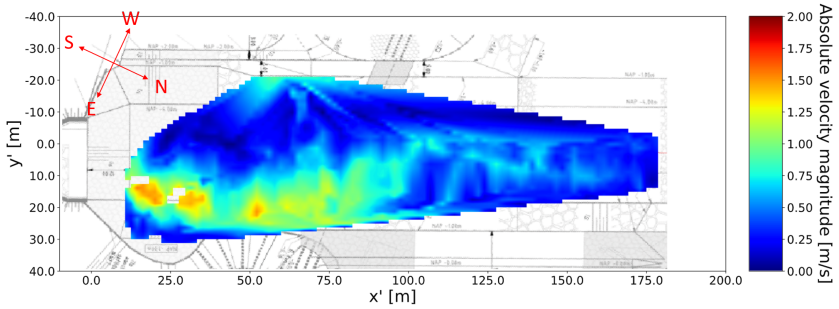

(b) Interpolated flow field for T = 2 ($Q = 45\ m^3/s$, $H = 0.03$ m+NAP).

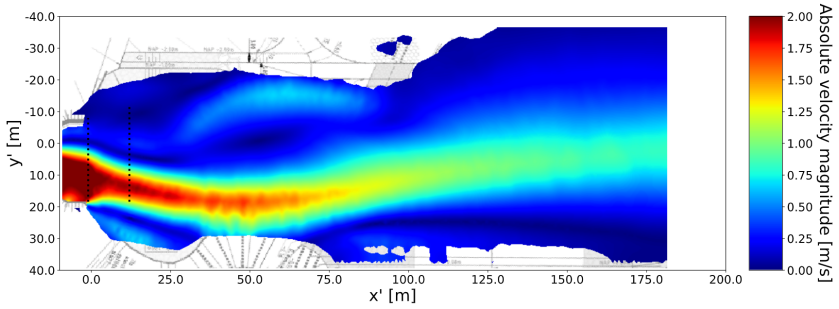

(c) 2DH modelled absolute velocity magnitudes for T = 6 ($Q = 54\ m^3/s$, $H = -0.31$ m+NAP).

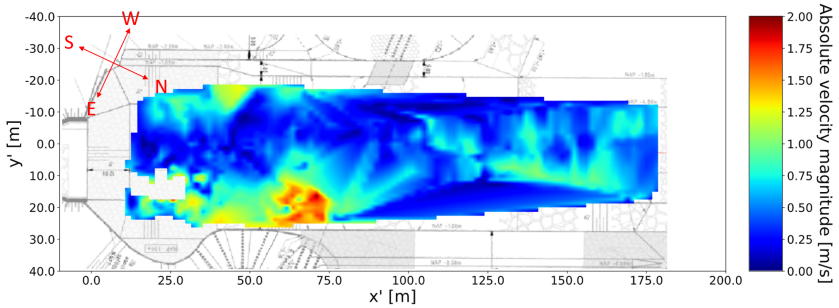

(d) Interpolated flow field for T = 6 ($Q = 54\ m^3/s$, $H = -0.5$ m+NAP).

Figure 5.5: Absolute velocity magnitude as modelled using the 2DH model at T = 2 and T = 6 of scenario 5.

western locations of the WCG. For $25 \leq x' \leq 55$, the position of the WCG in the model displaces slightly towards the east corresponding to the eastern movement of the jet. The measurements show a relatively steep eastern shift of the WCG. This is the result of the lateral transects sailed on the critical position at $x' = 30$ m, which contract the jet due to the absence of lateral interpolation.

At $x' \geq 55$ the position of the WCG moves towards the west in the model due to the detachment of the flow. Figure 5.5a shows the simulated jet at T = 2 moves all the way to the west side of the channel in a meandering-like fashion, whereas figure 5.5c shows the simulated jet at T = 6 in moves towards a symmetrical configuration. The WCG does not shift towards the west at T = 2 as the data on

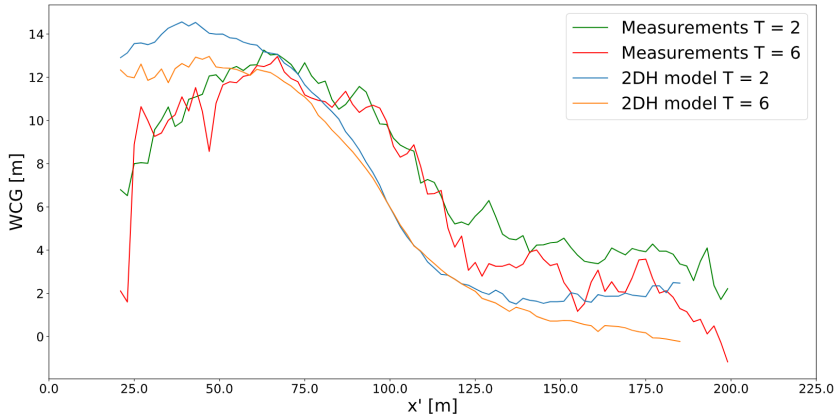

Figure 5.6: Lateral position of the weighted center of gravity in streamwise direction for T = 2 and T = 6 for both the 2DH model and the measurements.

the west side of the channel is neglected for $x' \geq 125$ to ensure a fair comparison with the measurement data (see figure 5.5b). However, without neglecting the data on the west side of the channel, the modelled WCG at T = 2 clearly moves towards the west side of the channel.

In the measurement data, the shift towards the west happens approximately 30 m further downstream compared to the 2DH model. On $50 \leq x' \leq 75$ m the WCG still moves toward the east due to the inclusion of the recirculating velocities at $x' \geq 50$ m. These recirculating velocities are already mapped further upstream in the 2DH model. The curvature of the flow towards the west is relatively equal between the 2DH model and the measurement data. However, the measurement data show the jet remains further towards the east at the end of the DOI compared to the 2DH model.

It can be concluded the general outline of the positions of the WCG is similar. Both the 2DH model and the measurements show an asymmetrical flow pattern towards the eastern section of the channel, where the flow curvature stops at approximately $x' = 45$ m. Considering the critical point in the bed protection, this indicates the position of the high flow velocities is modelled correctly. However, further downstream, the curvature of the flow is modelled incorrectly. The 2DH model shows the jet detaches from the east side of the channel and either meanders across the channel or spreads out into a symmetrical configuration. The measurements show the jet remains on the east side of the channel.

5.2.2. Recirculation zones

Figure 5.7 shows the streamlines for the 2DH model and the measurement data at T = 2 and T = 6. Furthermore, the vertical vorticity across the channel is shown for the 2DH model. As confirmed by the visual observations, the 2DH model shows a small recirculation zone is present in the cove east of the jet. This recirculation zone can be considered the non-dominant recirculating zone and is indicated with number 1 in figure 5.7. West of the jet, the dominant recirculation zone is indicated with number 2.1 in figure 5.7. The dominant recirculation zone starts directly at outflow and spans around 100 m in downstream direction, which complies with the measurements.

Remarkably, a secondary eddy is present in the upstream-west corner of the dominant recirculation zone, indicated by number 2.2 in figure 5.7. It was noted that the existence of this secondary eddy depends on the turbulence settings, as the eddy is absent when using a mixing length of $l_m = 2$ m (which complies with $L_t = 12$ m). In the measurements, this secondary eddy cannot be observed. The measurements at T = 6 in figure 5.7d show straight streamlines in the west side of the channel where the reproduced streamlines in figure 5.7c are curved due to the secondary eddy.

Aside from the dominant and non-dominant recirculation zones, another recirculation zone can be observed where the jet loses contact with the solid wall, indicated by number 3 in figure 5.7. It is this recirculation zone that pushes the primary jet stream away from the eastern side of the channel and causes the flow to spread out across the channel. Between figure 5.7a and 5.7c, it can be seen this

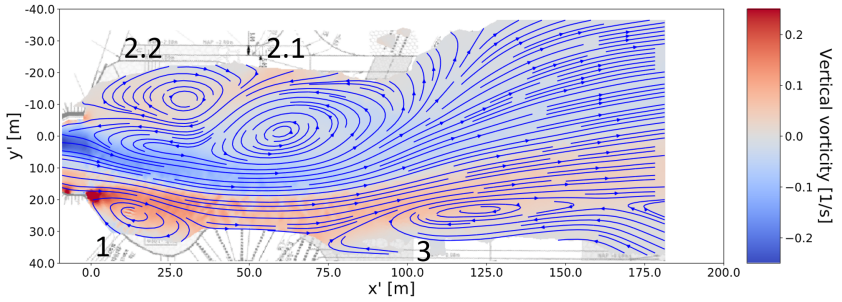

(a) Streamlines and vertical vorticity for the 2DH model at T = 2.

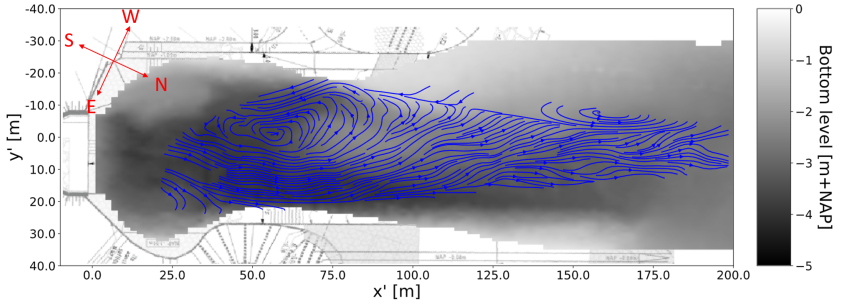

(b) Streamlines calculated using the measurement data at T = 2.

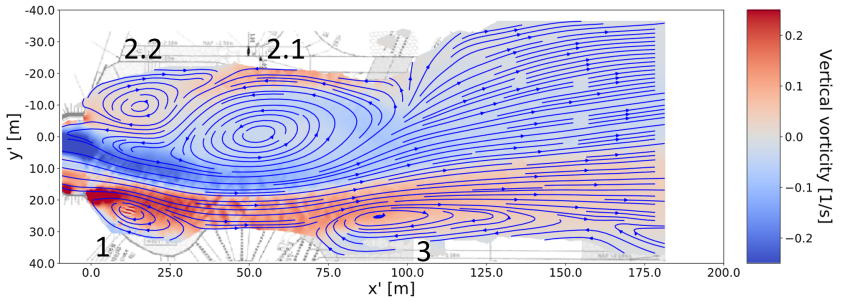

(c) Streamlines and vertical vorticity for the 2DH model at T = 6.

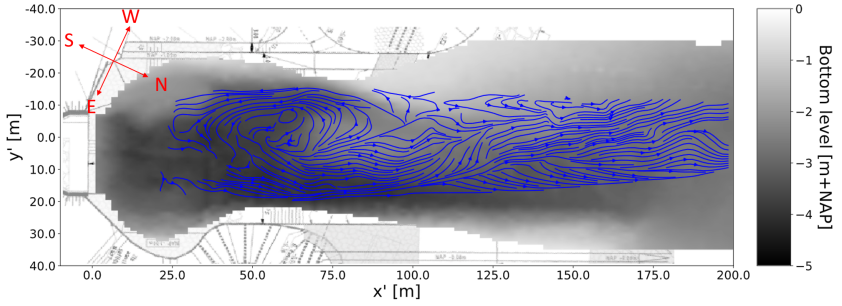

(d) Streamlines calculated using the measurement data at T = 6.

Figure 5.7: Streamlines through the channel as reproduced by the 2DH model and as calculated from the measurement data, combined with the vertical vorticity distribution for the 2DH model.

recirculation zone moves further upstream, likely due to the lower water level. As a result, the jet detachment from the eastern side of the channel is positioned further upstream, as was noticed earlier in this section.

Comparing figures 5.7a and 5.7c, it can be seen that the recirculation zones 2 and 3 vary slightly between the timesteps. The non-dominant recirculation zone remains stationary between T = 2 and T = 6. In the western section of the channel, it can be seen that the dominant recirculation zone pushes the secondary gyre further upstream. The result is a wider primary gyre and a smaller secondary gyre. The size of the dominant recirculation zone remains equal between T = 2 and T = 6. Recirculation zone

3 displaces further upstream in T = 6 compared to T = 2. As a result, the flow detaches from the east side of the channel further downstream at T = 6 compared to T = 2.

In the measurements, the dominant recirculation zone was observed to vary little between timesteps, which complies well with the model observations. The recirculation zones indicated by numbers 1 and 3 in figure 5.7 are not present in the measurement data. Recirculation zone 3 pushes the jet more towards the middle of the channel at approximately $x' = 75$ m. The existence of this third recirculation zone is sensitive to both the groyne settings in the model and the modelled water level in the channel. The recirculation zone is adjacent to the first groyne on the east side of the channel, indicating the local water depth at the location of the recirculation zone is dependent on both the crest height and slope of the groyne. Furthermore, as the recirculation zone is located on a slope, its position is dependent on the water depth. As the parameters used to construct the groynes in the model are estimated and the water levels in the channel were shown to deviate from the measurements, it cannot be said whether this recirculation zone is likely to exist in the channel.

Figure 5.5 shows the recirculating velocities on the west side of the channel are underestimated in the 2DH model compared to the measurement data. This is especially visible between figures 5.5c and 5.5d. In the measurements, the recirculating velocities can become $1.25\ m/s$ or higher, whereas in the model the recirculating velocities remain well below $1\ m/s$. Furthermore, the position of the high-recirculating velocities is different for the model compared to the measurement data. In the model, the recirculating velocities in the dominant recirculation zone curve towards the middle of the channel due to the presence of the secondary gyre, whereas the recirculating velocities in the measurement data remain on the far-west side of the channel. These lower recirculating velocities will be investigated later in this section.

5.2.3. Streamline contraction

Due to the lack of measurement data close to the jet, the contraction of the jet over the longitudinal slope cannot be determined from the measurement data. Furthermore, the vorticity plot for the measurement data does not show feasible results as explained in chapter 3. For this reason, the modelled streamline contraction could not be compared to the measurement data.

Whether the horizontal streamlines contract is further investigated using the maximum and minimum vertical vorticity as explained in chapter 4. As the jet width as determined using this method is oscillatory, the data was processed using a moving average filter of 15 values, which corresponds to approximately 3 meters in downstream direction.

Figure 5.8 shows the jet width b_{jet} estimated with the distance between the maximum and minimum vorticity for each lateral cross-section for T = 2 and T = 6 in the initial 40 m downstream from the culvert. Furthermore, the bed level is shown in figure 5.8b to indicate the length of the slope and magnitude of the topography changes in downstream direction. It can be seen that the jet width in both time-steps behaves similarly. The jet width first increases when the outflow from the individual casings merge. When the jet moves over the slope, the jet visibly contracts in all the scenarios, with the stronger contraction at T = 6. When the topographic changes due to the slope are lower, the jet contraction slows down as well and b_{jet} remains approximately equal. This process is very similar to the 2DH model behaviour observed in the laboratory simulations in chapter 4, where the flow contraction is solely determined by the topographic changes. This does not comply with the measurements, in which a continuation of the contraction further downstream from the slope was observed.

5.2.4. Lateral velocity profiles

The model results were compared to all 13 lateral transects sailed during the measurement scenario. An example is shown in figure 5.9. The relative error was used to determine the differences between the modelled transects and the measured transects. The average relative error across all transects is 18%. This relatively high error is explained by two things. First, as shown in figure 5.9, the measured flow velocities are largely oscillating. This might be caused by the turbulent fluctuations within the jet. The oscillating flow velocities result in a relatively high error concerning the smooth model data. Second, considering all lateral transects sailed, it was concluded the 2DH model consistently simulated

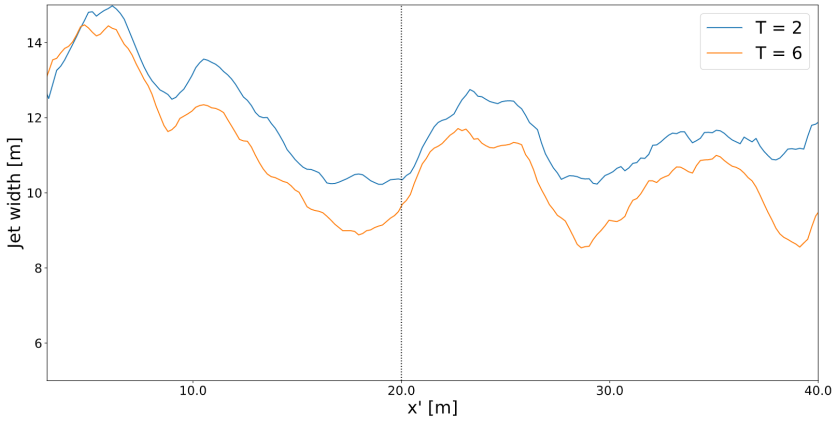

(a) Estimated jet widths for T = 2 and T = 6 in the initial 40 m downstream from the culvert.

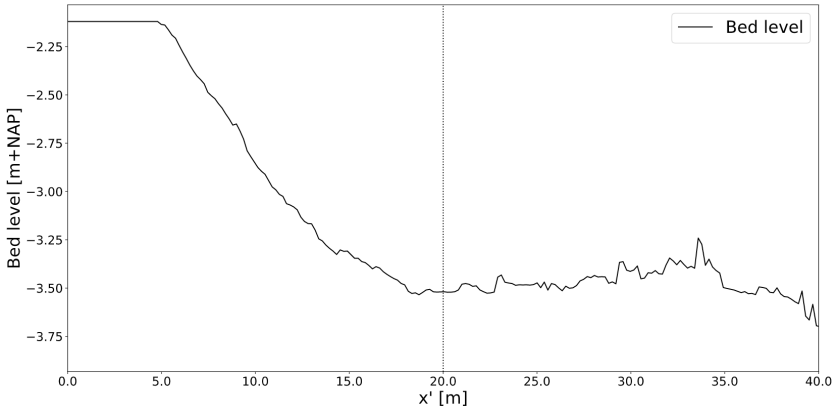

(b) Bed level in the initial 40 m downstream from the culvert.

Figure 5.8: Estimated jet widths for T = 2 and T = 6 and bed level in the initial 40 m downstream from the culvert.

lower flow velocities throughout the entire transect compared to the measurement data. This is also visible in figure 5.9.

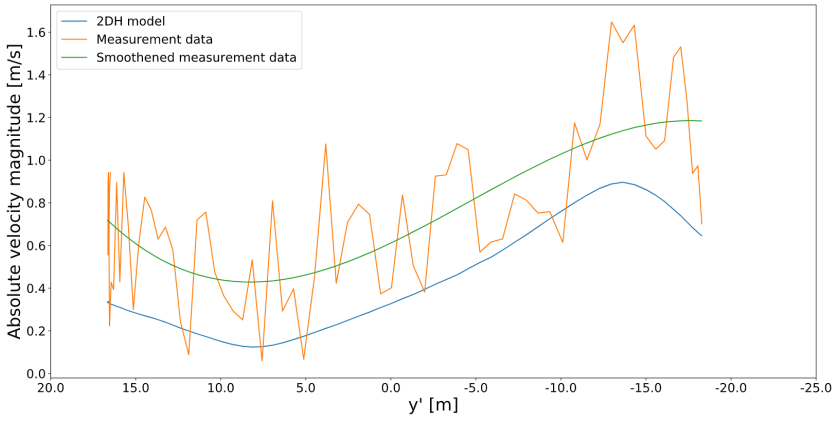

Figure 5.9: Flow velocities along a lateral transect for both the 2DH model and the measurement data.

The lower flow velocities can be caused by multiple factors. The higher water level in the seaside channel that is reproduced by the 2DH model certainly contribute to the lower velocities. Another possible factor is a miscalculation of the discharge. It is possible either the pressure sensor data in the inland lake at Waterdunen or the measured storage changes in Waterdunen are erroneous, which would result

in wrong discharges throughout the simulation. One final factor could be an incorrect reproduction of the recirculating velocities. Higher recirculating velocities would require higher velocities in the primary jet stream to maintain an equal discharge. Furthermore, considering the lateral transects such as figure 5.9, the model is especially erroneous in the dominant recirculation zone, reproducing significantly lower flow velocities. However, it was hypothesized in the data analysis in chapter 3.1 that the high recirculating velocities measured by the ADCP were influenced by the propeller of the vessel, as the measured recirculating velocities were abnormally high. Therefore, this final theory is unlikely.

It can be concluded the 2DH model reproduces flow velocities which are too low, both in the dominant recirculation zone and in the primary jet stream. Nevertheless, the shape of the lateral velocity profile is correct when comparing the 2DH model results with the measurement data. This makes it plausible the lower flow velocities are a result of incorrect model settings rather than an incorrect reproduction of hydrodynamic processes.

5.2.5. Conclusion

This section portrayed the 2DH results of the simulations at Waterdunen. It was shown the 2DH model shows a strong flow concentration on the east side of the channel, complying with the measurements. The location where the streamlines stop curving towards the east was shown to be equal to $x' = 45$ m. Considering the streamlines and the WCG, this location corresponds to the location found in the data analysis in chapter 3. The flow was shown to detach from the eastern side of the channel due to the formation of a recirculation zone adjacent to the eastern groyne. The existence of this recirculation zone depends largely on the reproduced water level and the groyne settings. At T = 2, the modelled jet meanders towards the western side of the channel. This was not observed in the measurement data. At T = 6, the jet spread out across the channel and approaches a symmetrical configuration. This complies better with the measurement data. From these observations, it was concluded the 2DH model reproduced the eastern movement caused by the Coanda-like effect correctly, but the movement of the jet further downstream incorrectly. The latter of the two might be caused by an incorrect reproduction of the downstream water level or incorrect groyne parameters.

Three recirculation zones were observed in the model results. The existence of the non-dominant recirculation zone from the visual observations was confirmed. Furthermore, the dominant recirculation zone was observed to be split in a primary and secondary reciculating gyre. Based on the measurement data at T = 6, he existence of the secondary gyre is unlikely. A third recirculation zone can be observed where the flow detaches from the eastern side of the channel, of which the existence could not be verified with the measurement data. At higher discharges, the primary gyre in the dominant recirculation zone was observed to widen at the expense of the width of the secondary gyre. The size and shape of the recirculation zones was shown to vary little with increasing discharge or decreasing water level, which was also concluded in the data analysis in chapter 3. Furthermore, the size of the dominant recirculation zone was reproduced correctly in the 2DH model.

The horizontal streamlines were shown to contract over the longitudinal slope directly at the outflow from the culvert. This contraction was observed to increase with increasing discharge and lower downstream water level. Similarly to the observations in chapter 4, the contraction is solely determined by topographic changes. Downstream of the slope, the horizontal streamline contraction stops. This is contrary to the observations in the data analysis in chapter 3, where the horizontal streamlines were shown to contract further downstream.

The 2DH model was incapable of accurately reproducing the magnitude of the flow velocities throughout the channel. Both in the primary jet stream and in the dominant recirculation zone, the magnitude of the flow velocities was too low in the 2DH model. As the shape of the lateral velocity profiles of the 2DH model was correct, it was concluded this discontinuity in the velocity magnitude was the result of incorrect model inputs, such as the water level in the channel and the discharge.

5.3. 3D model results

This section will show and explain the 3D model results in similar to the previous section. From the previous section, it can readily be concluded that it is difficult to draw clear conclusions from comparisons between the model and the measurement data due to a lack of data in crucial sections in the channel and inaccuracies due to the required interpolation of the measurement data. Therefore, certain hydrodynamic processes will solely be analysed based on the 2DH and 3D numerical results. With the addition of the knowledge gained from the model validation in chapter 4, suggestions can be made regarding the accuracy of both numerical models.

Figure 5.10 shows the absolute velocity magnitudes for both the 3D model and the measurement data at T = 2 and T = 6, together with the countour lines for $|\vec{u}| = 1$ m/s (inner) and $|\vec{u}| = 0.5$ m/s (outer) for the 2DH model. The captions include the water levels which were modelled and measured. It can be seen the water levels in the 3D model are higher compared to the measurement data, as was discussed in section 5.1. However, the discontinuity is smaller compared to the 2DH model.

Comparing the contour lines in figure 5.10a to the 3D flow field it can be seen the 3D model simulates slightly less curvature towards the east and slightly lower flow velocities in the jet. However, most notably, the flow in the 3D model remains on the east side of the channel after the eastern attachment, whereas the 2DH jet moves towards the west side of the channel. In figure 5.10c, it can be seen that the eastern movement of the jet is equal for both the 2DH model and the 3D model. Furthermore, the non-dominant recirculation zone is modelled equally as well. However, the position of high flow velocities in the dominant recirculation zone is more towards the west for the 3D model compared to the 2DH model. Comparing the model results to the measurement data, the 3D model underestimates the flow velocities throughout the entire DOI, similar to the 2DH model.

5.3.1. Asymmetry

Similar to the 2DH model, the 3D model also shows the eastern concentration of the flow. The jet hits the east wall of the channel at approximately $x' = 45$ m and detaches from the eastern side of the channel at $x' = 55$ m, similar to the 2DH model. However, further downstream, the flow remains on the east side of the channel in the 3D model, which complies better with the measurements.

The WCG was used to better capture the asymmetry of the flow. Similar to the 2DH analysis, the data points were interpolated to the same grid as employed in the data analysis in chapter 3. Furthermore, any grid cells without measurement data are neglected in the model results for a fair comparison. The lateral position of the WCG throughout the channel for both the 2DH and 3D model and for the measurements are shown in figure 5.11. Comparing the 2DH and 3D model results in figure 5.11, it can be concluded the position of the WCG is similar between both models and both timesteps for $x' \leq 75$ m. However, further downstream, discontinuities between the model results are present.

Similar to the 2DH model results, the initial eastern shift of the WCG is evident in the 3D model from the first measurement point onward. However, the position of the WCG is consistently further east for the 2DH model compared to the 3D model. This can also be seen in figure 5.10, where the 3D model shows slightly less curvature compared to the 2DH model. The peak eastern positions of the WCG for the 3D model comply well with the measurements, though the streamwise location of the peak is shifted. Similar to the 2DH model, the eastern movement of the WCG found in the measurements up to $x' = 75$ m cannot be found in the model data as the recirculating velocities are already present further upstream.

The largest discontinuity between the 2DH and 3D model is found at $x' \geq 75$ m. In the 2DH model, the jet moves towards the east in a meander-like fashion at T = 2, and toward a symmetrical flow configuration at T = 6. In the 3D model, the jet remains on the east side of the channel for both timesteps. This complies better with the measurement data compared to the 2DH model. Apparently, the 3D model is capable of better reproducing the curvature of the flow after the eastern attachment. However, between T = 2 and T = 6, it can be seen the curvature of the flow is dependent on both the discharge and the downstream water level. Therefore, the lower water level in the 3D model might affect the

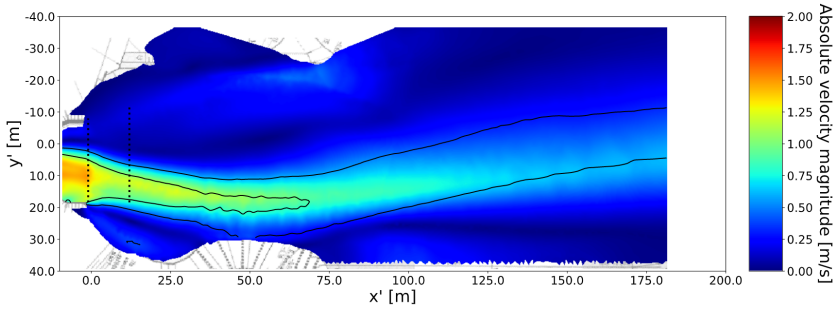

(a) 3D modelled absolute velocity magnitudes for T = 2 ($Q = 45\ m^3/s$, $H = 0.085$ m+NAP.)

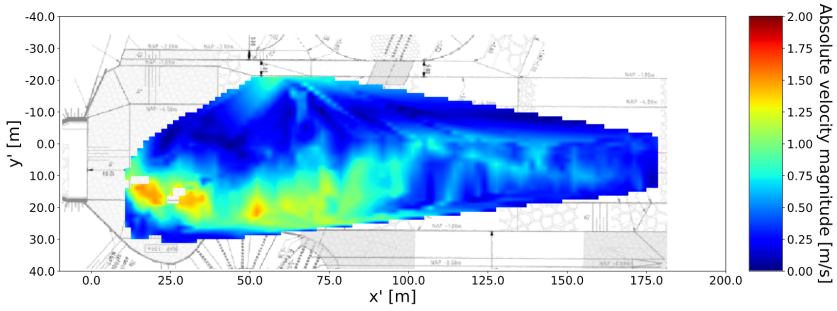

(b) Interpolated flow field for T = 2 ($Q = 45\ m^3/s$, $H = 0.03$ m+NAP.)

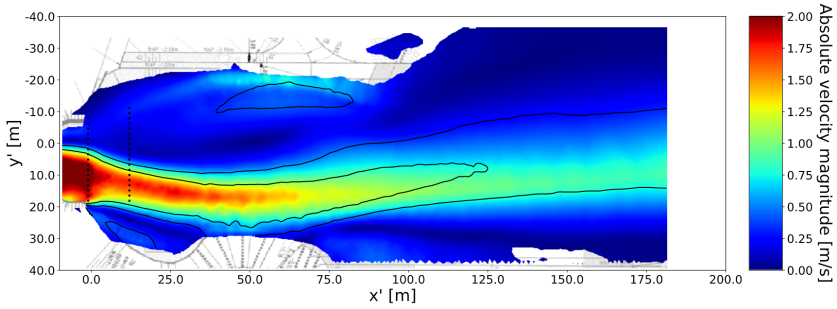

(c) 3D modelled absolute velocity magnitudes for T = 6 ($Q = 54\ m^3/s$, $H = -0.35$ m+NAP.)

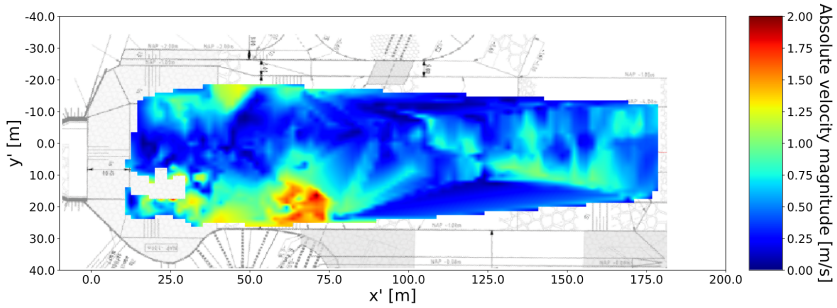

(d) Interpolated flow field for T = 6 ($Q = 54\ m^3/s$, $H = -0.5$ m+NAP)

Figure 5.10: Absolute velocity magnitude as modelled using the 3D model at T = 2 and T = 6 of scenario 5.

results. Nevertheless, it can be concluded the 3D model is capable of reproducing the flow curvature throughout the DOI. This was also concluded in the model validation in chapter 4. There, the better curvature was attributed to a better reproduction of the dominant recirculation zone. This makes it likely the better curvature reproduced by the 3D model is the result of a more accurate reproduction of the recirculation zone adjacent to the eastern groyne.

5.3.2. Recirculation zones

Figure 5.12 shows the vertical vorticity field and the streamlines for T = 2 and T = 6. In both figures, the dominant and non-dominant recirculation zone are clearly visible, indicated by numbers 1 and 2

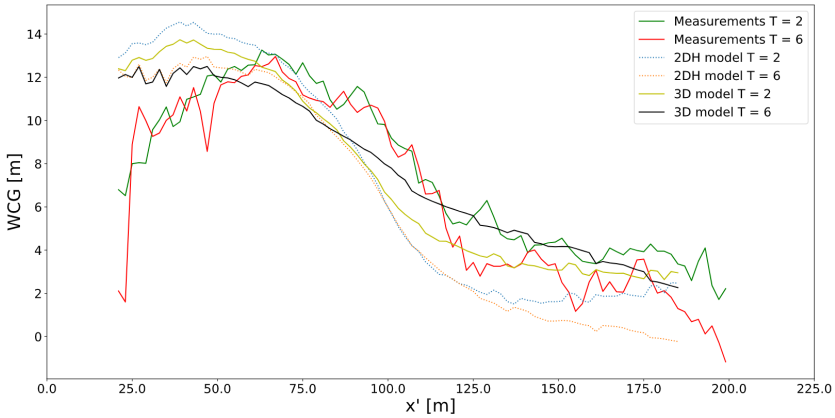

Figure 5.11: Lateral position of the weighted center of gravity in streamwise direction for T = 2 and T = 6 for the 3D model, the 2DH model and the measurements.

in figure 5.12. Contrary to the 2DH model, no secondary gyre is present in the dominant recirculation zone. Therefore, the dominant recirculation zone spans the entire west side of the jet without another counter-rotating gyre present. Comparing figures 5.12c and figure 5.12d, it can be seen the absence of the secondary gyre complies better with the measurements. In the 2DH model, the secondary gyre contracts the primary gyre in the initial 40 m from the culvert. As a result, the high recirculating velocities in figure 5.5 are curved towards the east. As this secondary eddy is not present in the 3DH model, the recirculating velocities remain on the west side of the channel. This explains the discontinuity in the position of the high recirculating velocities in figure 5.10c. The more western location of the high recirculating velocities in the 3D model comply better with the measurement data.

It should be noted that the existence of this secondary eddy is largely dependent on the employed turbulence closure model and the corresponding parameters. A 3D simulation with a lower turbulent viscosity does portray the secondary gyre in the dominant recirculation zone. The addition of the vertical $k-\epsilon$ increases the total turbulent viscosity in the channel. As a higher turbulent viscosity dampens vortices, it is expected the additional turbulent viscosity in the 3D model added by the vertical turbulence closure model is the cause for the neglect of the secondary eddy.

Aside from the dominant and non-dominant recirculation zone, a third recirculation zone is present at $x' = 75$ m on the east side of the jet. In the 2DH model, this recirculation zone was shown to push the jet stream more towards the center of the channel. In the 3D model, this third recirculation zone has a lower impact. Especially at T = 2, the length of the recirculation zone is significantly smaller in the 3D model compared to the 2DH model. When analysing the model results later than T = 6, it can be seen this third recirculation zone disappears due to the decreasing downstream water level. Therefore, the discontinuity between the 2DH and 3D model regarding the third recirculation zone is attributed to the lower water level in the 3D model compared to the 2DH model, as explained in section 5.1. Based on the results from the model validation in chapter 4, the better reproduction of this third recirculation zone results in the better curvature downstream of the eastern attachment of the jet.

Figure 5.10 shows the magnitude of the recirculating velocities is lower for the 3D model compared to the measurements. This was also observed in the 2DH model. Compared to the 2DH model, the recirculating velocities are of near-equal magnitude. In the previous section, multiple reasons were given for the lower flow velocities. The lower flow velocities are further investigated later in this section.

5.3.3. Streamline contraction

The distance between the maximum and minimum vertical vorticity is used as a proxy for the horizontal streamline contraction. In the data analysis in chapter 3, it was observed the horizontal streamline contraction is better visible when considering the surface streamlines compared to the depth-averaged streamlines. This was investigated using the 3D model. However, the found differences between the contraction of the surface streamlines and depth-averaged streamlines were minimal. Therefore, it was

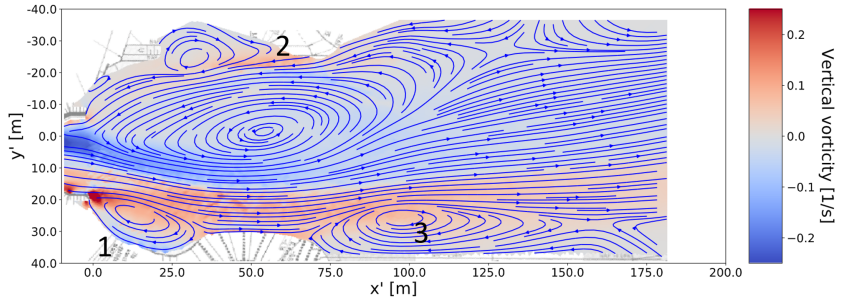

(a) Streamlines and vertical vorticity for the 3D model at T = 2.

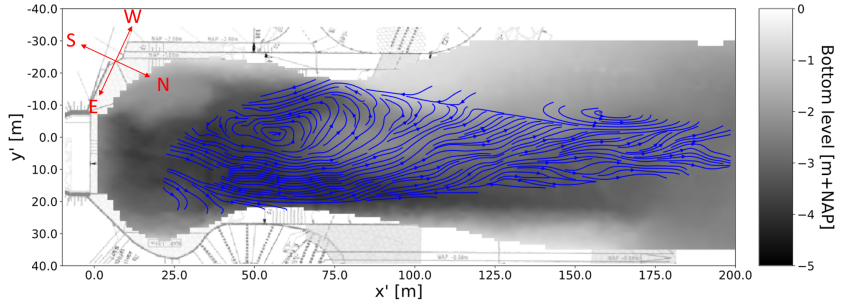

(b) Streamlines calculated using the measurement data at T = 2.

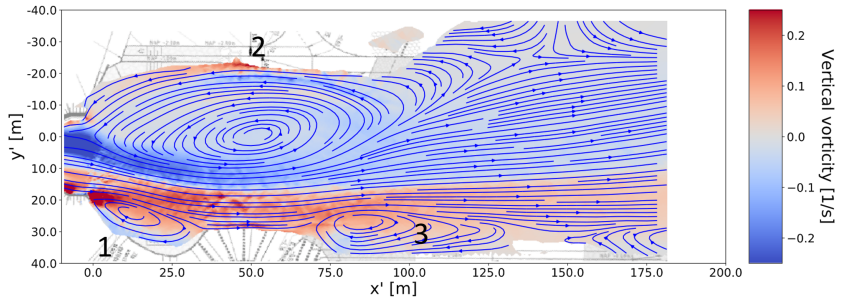

(c) Streamlines and vertical vorticity for the 3D model at T = 6.

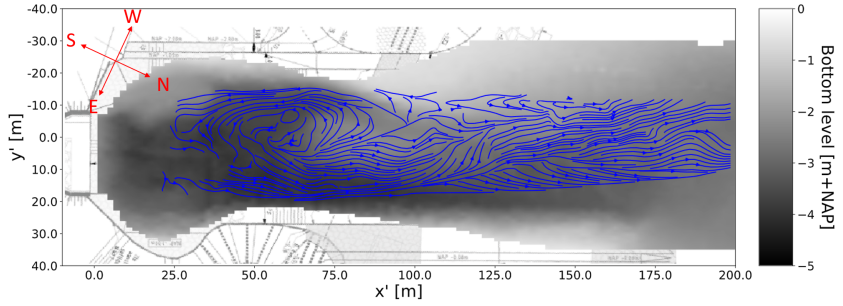

(d) Streamlines calculated using the measurement data at T = 6.

Figure 5.12: Streamlines through the channel as reproduced by the 3D model and as calculated from the measurement data, combined with the vertical vorticity distribution for the 3D model.

concluded the better visibility of the streamline contraction in chapter 3 is the result of the lower quality of the data at depth compared to the surface measurements.

Figure 5.13 shows the approximated jet width in each lateral transect for both the 2DH model and the 3D model. The streamline contraction for the 3D model was calculated using the depth-averaged vertical vorticity. As no measurement data is available close to the culvert and the vertical vorticity field of the measurement data was inaccurate due to the required interpolation, the model results are not compared to the measurement data.

In figure 5.13 it can be seen the jet width in the 3D model is decreasing, indicating a contraction of the horizontal streamlines. Similar to the 2DH model, this contraction is more significant at T = 6 compared to T = 2, indicating the dependence of the streamline contraction on the discharge and water level. Over the slope, it can be seen the jet in the 3D model contracts less compared to the 2DH model. However, the jet in the 3D model continues contracting downstream of the slope, though with a lesser magnitude. This is especially visible at T = 6. This complies with the conclusions of the model validation in chapter 4, where the same discontinuity between the 2DH and 3D streamline contraction was observed. The continuing contraction of the streamlines in the 3D model is the result of the continuing redistribution of the bulk of the flow over the vertical and indicates vertical flow attachment. In the 2DH model, this redistribution is instantaneous and therefore directly dependent on the water level changes. As soon as the water level stops changing, the contraction also stops, which is visible in figure 5.13.

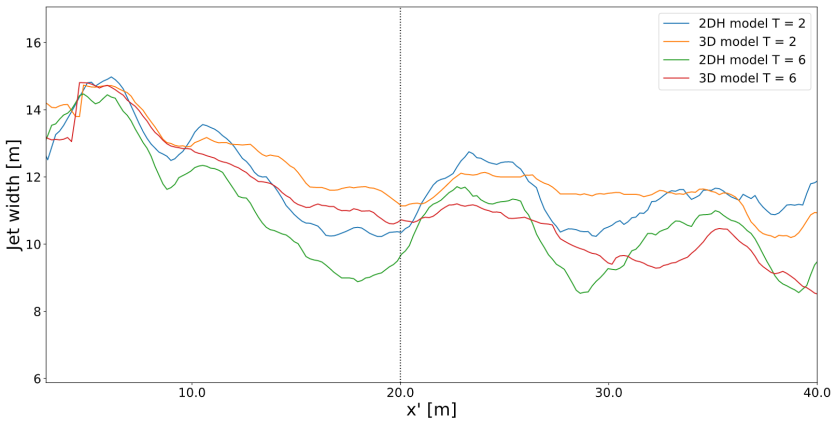

Figure 5.13: Approximated jet width along the initial 40 m downstream from the culvert for both T = 2 and T = 6 using the surface vertical vorticity and the depth-averaged vertical vorticity.

5.3.4. Lateral velocity profiles

The model results were compared to all 13 lateral transects sailed during the measurement scenario. An example is shown in figure 5.9. The relative error was used to determine the differences between the modelled transects and the measured transects. The definition of this error is explained in section 4.4. The average relative error across all transects was 18.75 %. Surprisingly, the error made by the 3D model is higher compared to the 2DH model. When analysing all transects, it can be seen the flow velocities in the 3D model are slightly lower compared to the 2DH model and as a consequence slightly more erroneous compared to the ADCP data.

Figure 5.14 compares the ADCP data to the 2DH model results and the 3D model results for one transect. Similar to the 2DH model, it can be observed the flow velocities are consistently too low for the 3D model compared to the ADCP measurements. Comparing the 2DH model results to the 3D model results, it is evident the same shape of the lateral velocity profile is obtained. This similarity is consistent throughout all lateral transects. This justifies the assumption that the lower flow velocities are a result of model input errors rather than errors in the reproduction of the hydrodynamic processes.

It is also seen in figure 5.14 that the 3D model shows lower flow velocities compared to the 2DH model. This is especially visible in the dominant recirculation zone. It was shown in the previous section that the dominant recirculation zone in the 2DH model is contracted due to the presence of a secondary eddy. As a result, the recirculating flow velocities are expected to increase. Due to the absence of this secondary eddy in the 3D model, the recirculating flow velocities are slightly lower. As the momentum from the recirculation zone gets re-integrated into the primary jet stream, this also results in a slightly lower flow velocity in the jet.

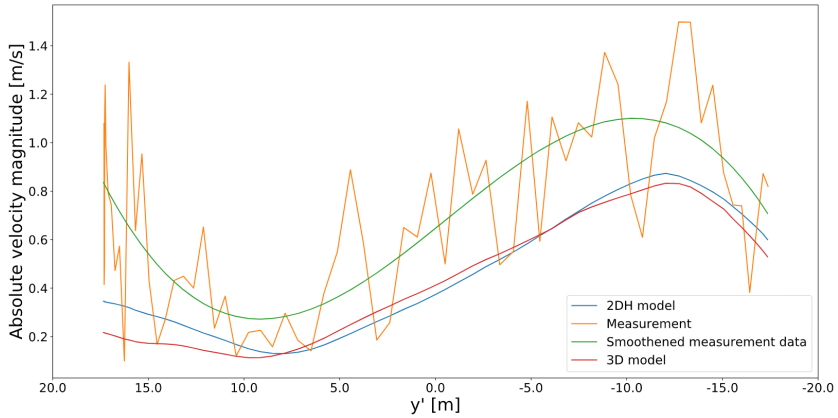

Figure 5.14: Flow velocities along a lateral transect for the 3D model, the 2DH model and the measurement data.

5.3.5. Vertical velocity profiles

It was assessed whether the vertical velocity profiles modelled in the 3D model are accurate with respect to the measurement data. For this purpose, longitudinal transect 1 of scenario 5 was investigated similarly to figure 3.14. The result is shown in figure 5.15. Comparing figure 5.15 to figure 3.14, it can observed the outline of the flow is similar. Close to the jet, the flow velocities are high. As the jet moves towards the east, the transect no longer crosses the primary jet stream and the flow velocities decrease. Over the shallow section of the channel, the flow velocities increase again. A discontinuity between the measurements and the modelled flow field lies in the consistent high flow velocities past $x' = 75m$ in the model. Though some high flow velocities were measured, the measured flow velocities are generally lower compared to the modelled velocities. Figure 5.15 nicely portrays the logarithmic velocity profiles which are generated by FINEL.

The reproduced outflow from the culvert was investigated by creating transects along with the model data following the primary jet stream. Figure 5.16 shows the vertical velocity profiles along $-15 < x' < 30$ m. It can be observed that upstream of the slope the velocity profile complies with the standard logarithmic velocity profile. On the slope, the velocities in the lower half of the water column decrease due to the adverse pressure gradient. However, it can be observed the flow remains attached to the bottom. Moving further downstream the velocities in the lower half of the water column remain low. However, a new equilibrium logarithmic velocity profile can be seen to develop.

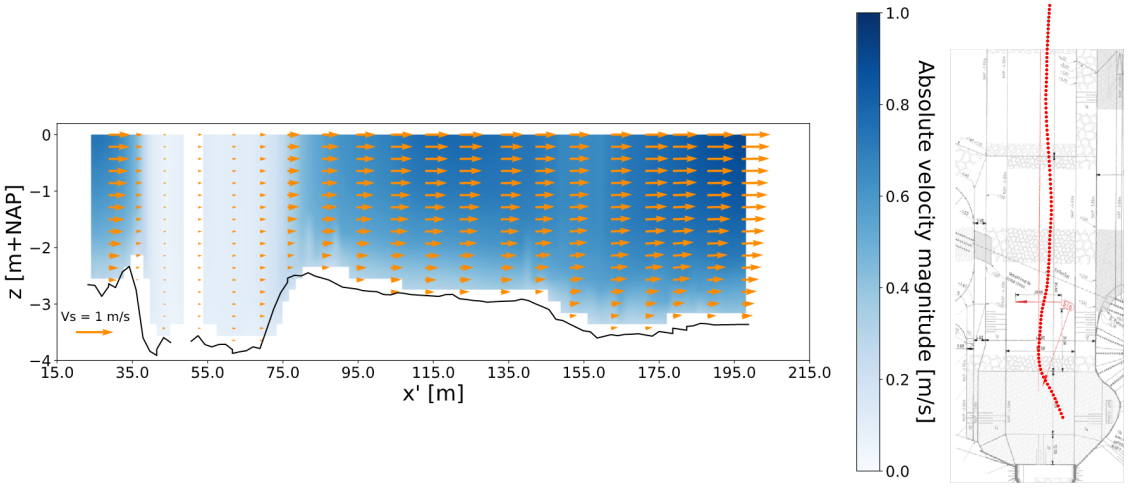

(a) Modelled flow velocities along transect.

(b) Sailed transect.

Figure 5.15: 3D modelled vertical velocity profiles along transect 1.

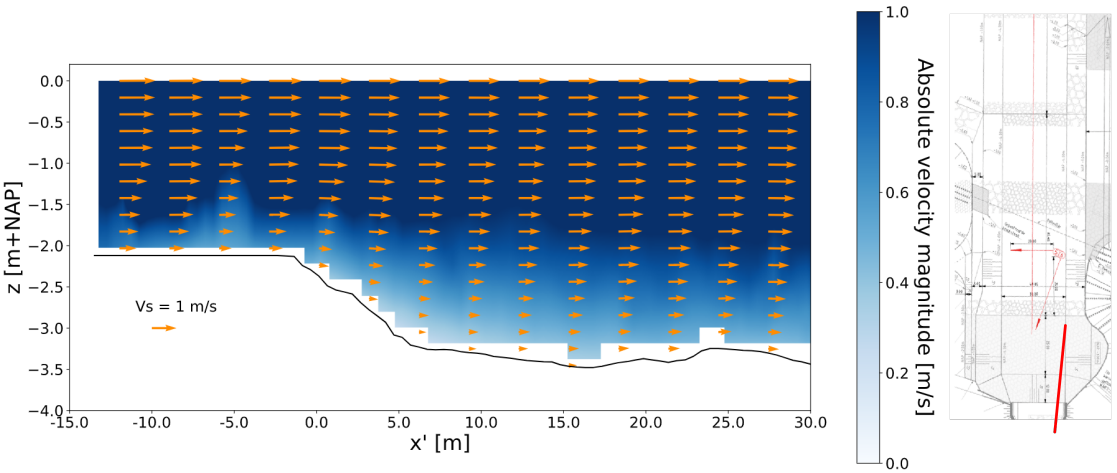

(a) Modelled flow over the longitudinal slope at outflow.

(b) Considered transect

Figure 5.16: 3D modelled vertical velocity profiles at outflow from the culvert.

5.4. Conclusion

From the simulations of the seaside of Waterdunen it was concluded both the 2DH and 3D model reproduced similar flow fields. The horizontal flow contraction, the eastern flow concentration and the dominant, and non-dominant recirculation zone were modelled by both models. The flow curves towards the eastern side of the channel and stops curving towards the east after 45 m, which was also observed in the data analysis in chapter 3. Further downstream, the jet detaches from the east side of the channel due to a recirculation zone which forms adjacent to the groyne on the east side of the channel. This recirculation zone pushes the jet towards the center of the channel. However, the strength of the recirculation zone was shown to be dependent both on discharge and water level. The jet in the 2DH and 3D model remained on the eastern side of the channel at T = 6, whereas the jet in the 2DH model at T = 2 can be observed to cross the channel in a meander-like fashion and attach to the western side of the channel. The latter did not comply with the measurement data. Based on the WCG, it was shown the 2DH model was capable of reproducing the initial curvature towards the east but was unable to simulate the proper path of the jet after the attachment. The 3D model was capable of correctly reproducing the curvature throughout the entire DOI.

Though the conclusion that the 3D model simulates the curvature more accurately compared to the 2DH model complies with the conclusions from the model validation in chapter 4, the accurate reproduction of the eastern concentration of the 2DH model was not expected based on the validation. This indicates the large effect of the asymmetric inflow in the channel on the flow symmetry. Furthermore, as the visual observations state a western concentration of the flow was found when using only the middle two casings, the effect of the asymmetric geometry is overruled by the asymmetric inflow.

In both the 2DH and 3D models, a contraction of the jet can be observed over the longitudinal slope directly at the outflow from the culvert. This contraction of the jet serves as a proxy for the horizontal streamline contraction. The gradient of the slope was measured to gradually decrease in downstream direction rather than the linear slope as was modelled in the model validation. In the 2DH simulation, the contraction of the jet is clearly visible where the slope is steep. However, when the slope becomes more gentle, the contraction stops and the jet width remains approximately constant. The contraction was observed to be of slightly higher magnitude for higher discharges and lower downstream water levels. In the 3D simulation, the contraction of the jet was observed to continue downstream of the slope. On the steeper section of the slope, the jet contraction is rapid and gradually slows further downstream. The continuation of the jet contraction was also observed in the measurement data in chapter 3, indicating the 3D model better reproduces the jet contraction. This was also concluded in the model validation in chapter 4. For higher discharges and lower downstream water levels, the simulated streamline contraction in the 3D model was severely higher.

Both a dominant and non-dominant recirculation zone can be observed in either model. The existence of both recirculation zones was also the conclusion of the data analysis in chapter 3. Remarkably, in the 2DH model the dominant recirculation zone consists of a primary and secondary gyre, whereas in the 3D model only one stable gyre can be observed. However, the existence of this secondary gyre is largely dependent on the used turbulence model and turbulence parameters. As no measurements are available at the modelled location of the secondary gyre, it cannot be said which model complies best with the measurements. However, the streamlines of the measurement data at T = 6 indicate the secondary gyre might not exist. The size of the dominant recirculation zone is simulated correctly by both models. Regarding the strength of the dominant recirculation zone, both models underestimated the recirculating flow velocities compared to the measurement data. However, it was noticed in the data analysis in chapter 3 that the measured recirculating velocities were abnormally high and likely influenced by the propeller of the vessel.

The magnitude of the flow velocities is significantly lower in both models compared to the measurements throughout the entire DOI. This resulted in an average relative error of 18% for the 2DH model and 18.75% for the 3D model. When comparing the flow profiles reproduced by the 2DH and 3D model to the measured data, the shapes of the profiles are similar. Furthermore, the velocity profiles reproduced by the 2DH and 3D model are nearly identical for most transects. Therefore, it is thought the reproduced flow velocities are the result of input errors, such as errors in the determination of the dis-

charge.

The 3D model simulates vertical flow attachment over the longitudinal slope. This complies with the hypothesis drawn from the data analysis in chapter 3. Upstream from the slope, the vertical velocity profile complies with the standard logarithmic velocity profile. On the slope, this profile is disturbed by the adverse pressure gradient. As a result, the flow velocities in the lower half of the water column are lower compared to a standard log-profile. The vertical flow attachment, the horizontal streamline contraction, and the deviation from the standard log-profile comply with the conclusions from the model validation in chapter 4. A direct comparison between measurements along a longitudinal transect showed the modelled velocity profiles roughly comply with the measurements, indicating high flow velocities at similar locations.

The differences between the 2DH and 3D models were observed to be less impacting at Waterdunen compared to the laboratory experiment. The lesser difference is the direct result of the correctly simulated curvature towards the east of the 2DH model. In the model validation, the incorrect curvature resulted in higher recirculating velocities in the non-dominant recirculation zone and therewith an incorrect reproduction of the lateral flow fields. In the laboratory experiment, this asymmetry was hypothesized to be the result of subtle instabilities occurring during the experiment. At Waterdunen, both the inflow into the channel and the channel geometry are already asymmetrical. Apparently, this makes it easier for models to correctly simulate pressure differences in transverse direction and hence the flow asymmetry.

6

Discussion

The main aim of this work was to get a better understanding of the numerical modelling of shallow jet flows. This was achieved by analysing 2DH and 3D numerical reproductions of shallow jet flows for both a laboratory experiment and a prototype scenario. This chapter aims to place the found results in context by explaining the authors' interpretation of the results. The asymmetric flow profile, recirculation zones, and the horizontal streamline contraction are discussed individually to discuss the drawn conclusions and their practical application. The discussion is concluded with a final comparison between 2DH and 3D numerical models regarding shallow jet flows.

6.1. Asymmetrical flow profile

One of the dominant hydrodynamic processes analysed in this work is the Coanda-like effect which causes the asymmetrical flow. Similar to the Coanda effect, the driving force for the asymmetric configuration is pressure. However, the Coanda effect states that the considered moving entity follows the contour of a solid surface it is attached to. It is a change in geometry of the solid surface which enforces the pressure difference. The considered process in this work is different whereas the flow initially loses contact with a laterally confined wall and eventually reattaches.

Though it is known this Coanda-like effect is enforced by subtle pressure differences caused by asymmetries in the geometry, topography, or inflow boundary conditions, the process is not well understood. Furthermore, in this work, it has been observed that dissipative processes such as bottom and wall friction also play a pivotal role in the proper reproduction of the flow asymmetry. From the laboratory simulations, it was concluded the inclusion of wall friction in the 3D model lead to the better reproduction of the flow curvature compared to the 2DH model. Due to wall friction, the upstream corner eddy in the dominant recirculation zone was reproduced, which contracted the dominant recirculation zone and lowered the negative lateral velocities on the jet. However, this is a chicken and egg dilemma, where the recirculation zones influence the asymmetry of the jet, and the asymmetry of the jet influence the shape and size of the recirculation zones. This problem was not solved in the current study.

Preliminary 2DH laboratory simulations with high bed friction coefficients (e.g. $c_f = 0.1$) close to the lateral walls showed a significantly better curvature compared to more realistic wall friction parameterizations. An extreme was shown when high bed friction coefficients were modelled throughout the entire flume, which led to a completely symmetrical flow profile.

One factor which was not investigated in this work is the effect of different turbulence closure models on the model results. Considering the laboratory experiments, the used Smagorinsky mixing-length model resolved a small horizontal turbulent viscosity as it is usually employed as a sub-grid scale model. The effect of a higher turbulent viscosity was analysed by increasing the mixing-length to 0.08 m in both the 2DH model and the 3D model. In the 2DH model, the effect on the curvature was limited. However, in the 3D model, the curvature towards the east was significantly increased and more closely resembled the 2DH model results due to a more contracted upstream corner eddy in the dominant recirculation

zone. This indicates the employed turbulence closure model can have a significant effect on the flow curvature and therewith the performance of the model. This limits the results of this work to the employed Smagorinsky mixing-length model in the laboratory simulations and the standard mixing-length model in the simulations at Waterdunen.

From the results of the laboratory simulations, it seems that the inclusion of wall friction improves the modelled curvature of the flow. However, the above statements show that dissipative processes in general can have a large influence on the flow curvature. For this reason, it cannot be excluded that more dissipation added to the system diminishes the effect of one of the driving processes for the flow curvature. However, this was not further analysed in this work.

Considering the Waterdunen models, it was shown the differences in curvature between the 2DH and 3D models are less evident. This proves the importance of the asymmetric inflow and geometry at Waterdunen. Apparently, when the pressure instabilities are no longer subtle, the neglect of wall friction has a severely lower impact on the flow curvature. This is further justified by the fact that different casing configurations allowed the flow to concentrate on the western side of the channel. This was one of the conclusions of the visual observations, where it was seen that when only the two middle casings were in use the flow moved towards the west rather than the east.

6.2. Recirculation zones

In the laboratory simulations, the differences in the reproduction of the recirculating zones were attributed to the neglect of wall friction in the 2DH model. This complies with the findings of Dewals et al. (2008), who stated wall friction plays a pivotal role in the reproduction of the corner eddies.

When considering the dominant and non-dominant recirculation zone, relatively high errors were made by both models in the reproduction of the recirculating flow velocities. Nevertheless, it was also observed that the PIV measurements likely underestimated the recirculating flow velocities due to the clumping of tracer particles. However, parameters such as the turbulent viscosity also influence the recirculating velocities. When using a larger mixing-length in the laboratory simulations, lower recirculating flow velocities were reproduced by the 2DH model, decreasing the relative error. This indicates a more accurate turbulence closure model might result in a better comparison between the 2DH and 3D numerical models.

The practical application of the recirculation zones is closely related to sediment transport. This work has indicated the close relationship between the recirculation zones and the symmetry of the jet. In the laboratory simulations, it was shown the wrongly simulated curvature of the flow had a significant impact on the recirculating velocities in the non-dominant recirculation zone. Furthermore, the shape and size of the recirculation zones is dependent on the flow symmetry. When considering sediment transport, this could affect the position where suspended sediment is deposited. For the Waterdunen simulations, the absence or presence of the secondary eddy could alter sediment transport throughout the channel.

6.3. Horizontal streamline contraction

It was repeatedly shown in this work that the modelled horizontal streamline contraction in a 2DH model is a function of the water depth. Broekema et al. (2020) has shown the relation between the horizontal streamline contraction and the vertical flow profile. It was stated that two flow configurations exist, one where the flow diverges horizontally and separates vertically, and one where the flow converges horizontally and remains attached vertically. Between either configuration, the bulk of the flow redistributes over the vertical plane or the horizontal plane respectively. In a 2DH model, this vertical redistribution of the flow happens instantaneously, where a change in water depth immediately changes the vertical flow profile towards a new equilibrium log-profile. This explains the direct relationship between the modelled horizontal flow contraction and the water depth changes in the 2DH model.

In the 3D models, the horizontal contraction happened more gradually. This complies with the slower redistribution of the flow over the vertical in the 3D model. Considering the vertical velocity profiles in

the 3D model, it can be observed the vertical velocity profile on the slope and downstream thereof do not comply with the standard log-profile. Therefore, the redistribution of the bulk flow does not happen instantaneously but gradually. Further downstream of the slope, the flow will slowly move towards an equilibrium log-profile again.

When considering the jet contractions for both the laboratory simulations and for the Waterdunen simulations, it was concluded the contraction was stronger in the 3D model compared to the 2DH model. Using the above theory, the stronger contraction might be necessary as the redistribution of the flow is an energy-consuming process in the 3D model. However, this was not further investigated in this work.

In this work, the horizontal streamline contraction was approximated by estimating the jet width based on the maximum and minimum vertical vorticity in lateral cross-sections. Though this was proven to work reasonably well, the vertical vorticity was shown to be oscillatory throughout the channel and thus might not be the best indicator for the jet width. It is suggested the streamline contraction could better be captured using the lateral velocity component for symmetrical flows. Due to the asymmetry of the flows considered in this work, the lateral velocity component is largely influenced by the curvature of the flow. When considering symmetrical flows, the lateral velocity component would be a better indicator for the horizontal streamline contraction.

6.4. 2DH vs 3D models

This work has shown the differences between 2DH and 3D numerical models regarding the reproduction of shallow jets. The most important difference lies in the reproduction of the flow curvature in the case of asymmetrical flow. An important consequence of the wrongly reproduced flow curvature in the 2DH model lies in the predictive capabilities of the model regarding future projects. If parameters such as the ER or the AR indicate the flow might become asymmetrical, it was shown a 2DH model might predict an incorrect location of the high flow velocities. When considering the design of bed protections, this means the predicted position of high bed shear stresses can be wrong. Therefore, it is advised to use a 3D numerical model for design purposes, as a 3D model was shown to be capable of replicating the flow curvature in a correct manner.

However, if the inflow into the channel is already asymmetrical, a 2DH numerical model can be considered to save computational effort. Nevertheless, when employing a 2DH model one should be wary of geometric and topographic asymmetries, as the effect of both factors on the flow symmetry is still unclear.

The additional vertical discretization in a 3D numerical model can be valuable when considering the coupling between hydrodynamics and morphodynamics. Using a 2DH numerical model, the user is limited to using depth-averaged flow velocities when calculating parameters such as the bed shear stress. This work has shown a 3D model can predict the vertical velocity profile well, indicating the flow velocities near the bed can be used to calculate the bed shear stresses. Though the coupling between morphodynamics and hydrodynamics are always dependent on roughness parameters, this additional information can increase the accuracy of the resolved bed shear stress.

It should be noted the numerical models which were used in this work were set-up using the large amount of available data from both the laboratory experiment and the measurement campaign. Even with the available data, it was concluded from the Waterdunen models that the flow velocities throughout the lateral transects were modelled too low due to erroneous input data. This error affected the 3D model more compared to the 2DH model. Considering the average design project, this much detailed data will not be available. The additional complexity of a 3D model has the potential to reproduce the flow more accurately, but it is also significantly more sensitive to errors in the input compared to a 2DH model. It is therefore stressed to use 3D models with caution and to do proper research regarding the model input.

7

Conclusion and recommendations

In this chapter, the conclusions and recommendations regarding this research will be explained. First, the research objective will be re-evaluated and the research questions will be answered in section 7.1. Afterwards, recommendations for further research or improvement of the current work will be described in section 7.2.

7.1. Conclusions

7.1.1. Research objective

As formulated in the introduction in chapter 1, the objective of this research can be captured with the following sentence:

> *Assessing the capability of two- and three-dimensional numerical models to reproduce the hydrodynamic processes of shallow jet flows over complex topographies both in a controlled environment and a prototype scenario.*

The numerical software package FINEL was employed to achieve this objective, using the software in both a 2DH and 3D mode to analyse the shallow jet experiment 2.4.1 of van de Zande (2018) and the seaside outflow of the tidal culvert at Waterdunen. It was shown in the simulations of the laboratory experiment that both a 2DH model and a 3D model are capable of reproducing the driving hydrodynamic processes occurring in shallow jet flows. Nevertheless, the accuracy with which the processes were reproduced differs significantly, favouring the 3D model.

The differences found in the model validation were sought after in the prototype scale model simulations at Waterdunen. It was found the differences between the 2DH and 3D model were less impactful on a prototype scale compared to the laboratory scale, with the 2DH and 3D model reproducing the flow with similar accuracy.

7.1.2. Subquestions

In the introduction in chapter 1, several sub-questions were formulated to help answer the research question. These sub-questions will be answered in this section.

1. ***Which hydrodynamic processes can be observed to be important in the shallow jet flow at Waterdunen?***

   The jet flow at Waterdunen was observed to be subject to a Coanda-like effect, resulting in an asymmetric flow profile which concentrates the flow on the eastern side of the channel. As a result, the recirculation zones were asymmetric as well with a dominant recirculation zone on the west side and a non-dominant recirculation zone on the east side of the channel.

   A contraction of the surface streamlines was observed rather than the expected divergence. From

the measurement data, it could be seen this contraction continued until the flow reached the eastern side of the channel. From visual observations, it was concluded this contraction started at the beginning of the longitudinal slope.

In the vertical direction the flow was thought to remain attached to the bottom throughout the channel length, indicating no vertical flow separation occurred. However, this could not be said for certain by analysing the data due to a relatively large clearing of the ADCP with respect to the bottom.

2. ***Which of these hydrodynamic processes can be reproduced by 2DH and 3D numerical models of a laboratory experiment of a shallow jet?***

The 2DH numerical model was capable of reproducing the Coanda-like effect, the horizontal streamline contraction over the slope, and the dominant and non-dominant recirculation zone. The 2DH model was incapable of reproducing the upstream corner eddies due to the absence of wall friction.

Even though the hydrodynamic processes were reproduced in the 2DH model, the accuracy with which they were modelled is debatable. The curvature of the flow towards the east was modelled too high, resulting in an attachment point to the lower side of the wall which was located 1.2 m further upstream compared to the 3D model, which is 23% of the downstream distance to the attachment point in the 3D model. It was hypothesized this was partially caused by the absence of wall friction in the 2DH model. Consequently, the maximum error made in the non-dominant recirculation zone was 56.6% of the center-line velocity. This increase in recirculating velocities in the 2DH model was attributed to the higher curvature, the absence of wall friction, and the relatively low turbulent viscosity. The flow velocity in the non-dominant recirculation zone was overestimated by a maximum of 9.17% of the center-line velocity. The higher recirculating velocities in the non-dominant recirculation zone were concluded to be the result of an imperfect downstream Riemann boundary condition. A contraction of the horizontal streamlines over the slope was reproduced by the model. However, this contraction was shown to be a direct result of the changes in water depth. Therefore, the contraction stopped at the end of the slope. It was concluded this dependency of the horizontal contraction on the changes in water depth originates from the instantaneous adaptation of the vertical velocity profile to the new water depth in the 2DH model. It was shown the standard log-profile employed by the 2DH model results in a maximum relative error of 32.5% compared to the ADV measurements.

The 3D numerical model was capable of reproducing the Coanda-like effect, the horizontal streamline contraction throughout the DOI, and the dominant and non-dominant recirculation zone. Furthermore, the 3D numerical model was capable of reproducing the upstream corner eddies.

Using the weighted center of gravity, it was determined the curvature towards the east was reproduced correctly in the 3D model. The better curvature in the 3D model was shown to be the result of lower negative lateral velocities in the dominant recircultaion zone. The reproduced recirculating velocities in both the non-dominant and dominant recirculation zone were too high compared to the PIV measurements with a maximum error of 18.9% and 3.66% of the peak velocity in the jet respectively. In the dominant recirculation zone, it was concluded the higher recirculating velocities were partially caused by the imperfect downstream Riemann boundary condition. In the non-dominant recirculation zone, it was hypothesized the recirculating velocities were underestimated by the PIV measurements due to clumping of the tracer particles, which could not be verified in the current study. The addition of wall friction in the 3D model ensured the upstream corner eddies were reproduced. These upstream corner eddies change the shape of the dominant and non-dominant recirculation zone, which was shown to contribute to the better reproduced flow curvature in the 3D model. The outline of the horizontal streamline contraction on the longitudinal slope and further downstream were modelled correctly by the 3D model. However, the magnitude of the flow contraction was underestimated by 6% of the starting jet width. Corresponding to this, the effect of the adverse pressure gradient on the flow velocities in the

lower half of the water column was modelled with a maximum relative error of 10% compared to the ADV measurements. In the lower half of the water column, the flow velocity was underestimated by the 3D model, indicating the 3D model adapts to the adverse pressure gradient slightly slower compared to the ADV data. Downstream from the start of the slope, the vertical velocity profiles deviate from the equilibrium log-profile throughout the entire DOI, corresponding to the continuous streamline contraction throughout the DOI. This justifies the conclusion of the relation between the horizontal streamline contraction and the vertical velocity profile.

3. ***Which of these hydrodynamic processes can be reproduced by 2DH and 3D numerical models of the shallow jet at Waterdunen?***

   In the 2DH simulation at Waterdunen, it was concluded the 2DH model was capable of reproducing the Coanda-like effect in the initial 75 m from the culvert, the flow contraction over the longitudinal slope, and the dominant recirculation and non-dominant recirculation zone. Both the curvature towards the east side of the channel and the size of the dominant recirculation zone comply with the measurements. However, the flow contraction further downstream of the slope was not reproduced.

   It was concluded the asymmetric inflow into the seaside channel at Waterdunen allowed the 2DH model to reproduce the eastern concentration of the flow caused by the Coanda-like effect. However, further downstream, the jet in the 2DH model detaches from the east side of the channel and moves towards the west side of the channel or towards a symmetrical flow configuration. This behaviour was not found in the data analysis. Furthermore, the 2DH model was incapable of reproducing the continuing horizontal streamline contraction past the longitudinal slope, similar to the laboratory simulations.

   The 3D model at Waterdunen was capable of reproducing the Coanda-like effect, the streamline contraction, the dominant and non-dominant recirculation zone, and the vertical flow attachment. The curvature towards the east side of the channel and the size of the dominant recirculation zone comply with the measurements.

   Contrary to the 2DH model, the 3D model was capable of reproducing the total effect of the Coanda-like effect, where the flow remains on the east side of the channel throughout the entire DOI. Furthermore, the 3D model was capable of reproducing the continuing streamline contraction past the longitudinal slope.

   Nevertheless, neither of the 2 models was capable of accurately reproducing the measured flow velocities. Both models underestimated the flow velocities throughout the entire DOI. Therefore, compared to the sailed transects, the 2DH and 3D models contained a relative error of 18% and 18.75% respectively. However, the shape of the velocity profiles complied well with the measurements. Furthermore, the shapes of the velocity profiles for both the 2DH and 3D models were similar. Therefore, it is thought the error was the result of errors in the model input.

7.1.3. Research question

Which hydrodynamic processes can be identified in the shallow jet at Waterdunen and what are the additional benefits of using a 3D numerical model compared to a 2DH numerical model for the reproduction of these processes?

The shallow jet at Waterdunen can be characterized by an asymmetric flow pattern with a strong concentration towards the east side of the channel caused by a Coanda-like effect. As a result, the recirculation zones on either side of the jet are asymmetrical and can be separated into a dominant and non-dominant recirculation zone. Instead of the expected streamline divergence, a horizontal contraction of the streamlines was observed. This contraction starts at the beginning of the longitudinal slope and continues until the flow hits the eastern slope. Considering the vertical velocity profile, the flow was thought to remain attached to the bottom throughout the channel as no recirculating velocities at depth were found.

Simulations of a shallow jet in a laboratory experiment showed a 3D model has several additional benefits when considering simulations in symmetrical channels with symmetrical boundary conditions. First, the 3D model is capable of accurately reproducing the location and the magnitude of the high flow velocities in the jet. This is essential for the design of bed protection, as parameters such as the bed shear stress depend on the proper reproduction of the high flow velocities. Secondly, the 3D model can reproduce the recirculating flow more accurately compared to the 2DH model. Though the model results still contained relatively high errors, the results were significantly better compared to the 2DH model. Finally, the 3D model was capable of accurately reproducing the vertical velocity profile. As a result, properties such as the bed shear stress can be calculated based on the flow velocity near the bed rather than the depth-averaged velocity. This additional information compared to a 2DH model can improve the accuracy of the design of bed protections.

Simulations of the shallow jet at Waterdunen showed the differences between a 3D and a 2DH models is less impactful on a prototype scale. Due to the asymmetrical inflow into the channel, both the 2DH and 3D models were capable of reproducing the location of the high flow velocities correctly. Additional benefits of the 3D model lie in the proper reproduction of the flow curvature further downstream and the additional information regarding the vertical velocity profile. However, it cannot be said whether the vertical velocity profile was reproduced correctly. Furthermore, both the 2DH and 3D model were incapable of correctly reproducing the velocity magnitude throughout the channel. Additionally, the Waterdunen simulations showed a 3D model is more sensitive to input errors.

7.2. Recommendations

- It would be interesting to further investigate the relationship between the horizontal streamline contraction and the vertical velocity profile. It was shown in this work that the streamline contraction was more significant for a 3D model compared to a 2DH model. It could be insightful to investigate, for example, energy balances over longitudinal slopes for 2DH and 3D numerical models to analyse why the contraction is less significant in 2DH models.

- Additional simulations of shallow jets using more advanced turbulence closure models can give more insight in the effect of turbulence on the different hydrodynamic processes in shallow jets. In this work, the effect of turbulence on the flow was limited to the effect of different turbulent viscosity's calculated using a horizontal mixing-length model. However, a LES using, for example, TUDFlow3D could properly assess the influence of turbulence on shallow jet flows.

- The simulations in this model used either triangular grid element or tetrahedrons. Using this grid, a symmetrical flow configuration was only found by introducing nonphysical amounts of dissipation to the simulation. However, other numerical analyses of the Coanda-like effect such as the analysis in Dewals et al. (2008) required the introduction of asymmetries in the model input to obtain an asymmetric flow profile. Therefore, it would be interesting to assess the effect of the shape of grid elements on the reproduction of asymmetric flow fields.

- In this work the primary focus was to determine the capabilities of 2DH and 3D numerical models regarding the reproduction of the hydrodynamic processes in shallow jet flows. It would be interesting to extrapolate this data towards morphodynamics and see what the impact of the named differences in this work is on the sediment transport within shallow jets.

- This work was limited to the analysis of vertically attached flows. At the time of writing, no formula is available to determine whether a vertical boundary layer remains attached or separates over streamwise slopes. However, it is known these processes depend on the slope steepness and the horizontal non-uniformity of the flow. It would be interesting to see whether a 3D numerical model is capable of reproducing the transition between vertically attached and vertically separating flows

- This work has shown the recirculation zones influence the flow symmetry and the flow symmetry influences the recirculation zones. It would be interesting to investigate what the effect of the recirculating flow is on the flow curvature when the symmetric flow configuration becomes unstable. This way, the role played by the recirculation zones in the formation of the asymmetric flow

profile can be determined. This in turn can lead to parameterizations for 2DH model which allow them to correctly simulate the flow curvature.

Bibliography

Adrian, R. J., Durão, D., Durst, F., Heitor, M., Maeda, M., and Whitelaw, J. *Laser Techniques Applied to Fluid Mechanics: Selected Papers from the 9th International Symposium Lisbon, Portugal, July 13–16, 1998*. Springer Science & Business Media, 1998.

Afanasyev, Y. Formation of vortex dipoles. *Physics of fluids*, 18(3):037103, 2006.

Andersson, B., Andersson, R., Håkansson, L., Mortensen, M., Sudiyo, R., and Van Wachem, B. *Computational fluid dynamics for engineers*. Cambridge University Press, 2011.

Bardina, J., Huang, P., Coakley, T., Bardina, J., Huang, P., and Coakley, T. Turbulence modeling validation. In *28th Fluid dynamics conference*, page 2121, 1997.

Bradshaw, P. and Wong, F. Y. F. The reattachment and relaxation of a turbulent shear layer. *Journal of Fluid Mechanics*, 52(1):113–135, 1972. doi: 10.1017/S002211207200299X.

Broekema, Y., Labeur, R., and Uijttewaal, W. Observations and analysis of the horizontal structure of a tidal jet at deep scour holes. *Journal of Geophysical Research: Earth Surface*, 123(12):3162–3189, 2018.

Broekema, Y., Labeur, R., and Uijttewaal, W. Suppression of vertical flow separation over steep slopes in open channels by horizontal flow contraction. *Journal of Fluid Mechanics*, 885, 2020.

Canestrelli, A., Nardin, W., Edmonds, D., Fagherazzi, S., and Slingerland, R. Importance of frictional effects and jet instability on the morphodynamics of river mouth bars and levees. *Journal of Geophysical Research: Oceans*, 119(1):509–522, 2014. doi: 10.1002/2013JC009312. URL https://agupubs.onlinelibrary.wiley.com/doi/abs/10.1002/2013JC009312.

Castro, I. P. and Epik, E. Boundary-layer relaxation after a separated region. *Experimental Thermal and Fluid Science*, 13(4):338 – 348, 1996. ISSN 0894-1777. doi: https://doi.org/10.1016/S0894-1777(96)00092-1. URL http://www.sciencedirect.com/science/article/pii/S0894177796000921. Peter Bradshaw 60th Birthday Issue: Part II.

Chen, L., Asai, K., Nonomura, T., Xi, G., and Liu, T. A review of backward-facing step (bfs) flow mechanisms, heat transfer and control. *Thermal Science and Engineering Progress*, 6:194 – 216, 2018. ISSN 2451-9049. doi: https://doi.org/10.1016/j.tsep.2018.04.004. URL http://www.sciencedirect.com/science/article/pii/S2451904918300167.

Cohen, C. *Shallow-water plane and tidal jets*. PhD thesis, Citeseer, 2012.

de Wit, L. *3D CFD modelling of overflow dredging plumes*. PhD thesis, 2015. URL http://www.sciencedirect.com/science/article/pii/S0025326X14006390.

Deltares. D-flow flexible mesh technical reference manual. Technical report, 2020.

Dewals, B., Kantoush, S., Erpicum, S., Pirotton, M., and Schleiss, A. Experimental and numerical analysis of flow instabilities in rectangular shallow basins. *Environmental Fluid Mechanics*, 8(1): 31–54, 2008.

Fearn, R. M., Mullin, T., and Cliffe, K. A. Nonlinear flow phenomena in a symmetric sudden expansion. *Journal of Fluid Mechanics*, 211:595–608, 1990. doi: 10.1017/S0022112090001707.

Ghidaoui, M. S. and Kolyshkin, A. A. Linear stability analysis of lateral motions in compound open channels. *Journal of Hydraulic Engineering*, 125(8):871–880, 1999. doi: 10.1061/(ASCE)0733-9429(1999)125:8(871).

Graber, S. D. Asymmetric flow in symmetric supercritical expansions. *Journal of Hydraulic Engineering*, 132(2):207–213, 2006. doi: 10.1061/(ASCE)0733-9429(2006)132:2(207).

Ho, C.-M. and Huerre, P. Perturbed free shear layers. *Annual review of fluid mechanics*, 16(1):365–422, 1984.

Hoffmans, G. J. and Booij, R. Two-dimensional mathematical modelling of local-scour holes. *Journal of Hydraulic Research*, 31(5):615–634, 1993.

Houtekamer, J. Improving the advection discretization in d-flow flexible mesh. Master's thesis, 2017.

Jirka, G. H. and Uijttewaal, W. S. Shallow flows: a definition. *Shallow flows*, pages 3–11, 2004.

Kantoush, S. A., Bollaert, E., and Schleiss, A. J. Experimental and numerical modelling of sedimentation in a rectangular shallow basin. *International Journal of Sediment Research*, 23(3):212 – 232, 2008. ISSN 1001-6279. doi: https://doi.org/10.1016/S1001-6279(08)60020-7. URL http://www.sciencedirect.com/science/article/pii/S1001627908600207.

Kuzmin, D. Algebraic flux correction i. In *Flux-corrected transport*, pages 145–192. Springer, 2012.

Labeur, R. J. Finite element modelling of transport and non-hydrostatic flow in environmental fluid mechanics. 2009.

Ma, X. and Schröder, A. Analysis of flapping motion of reattaching shear layer behind a two-dimensional backward-facing step. *Physics of Fluids*, 29(11):115104, 2017. doi: 10.1063/1.4996622. URL https://doi.org/10.1063/1.4996622.

Nicolau del Roure, F., Socolofsky, S. A., and Chang, K.-A. Structure and evolution of tidal starting jet vortices at idealized barotropic inlets. *Journal of Geophysical Research: Oceans*, 114(C5), 2009.

Panitz, T. and Wasan, D. T. Flow attachment to solid surfaces: The coanda effect. *AIChE Journal*, 18(1):51–57, 1972. doi: 10.1002/aic.690180111. URL https://aiche.onlinelibrary.wiley.com/doi/abs/10.1002/aic.690180111.

Pietrzak, J. An introduction to oceanography for civil and offshore engineers. *Dept. of Hydraulic Engineering, Faculty Civil Engineering and Geosciences, TU Delft*, 2013.

Pope, S. B. *Turbulent flows*. IOP Publishing, 2001.

Razi, P., Tazraei, P., and Girimaji, S. Partially-averaged navier–stokes (pans) simulations of flow separation over smooth curved surfaces. *International Journal of Heat and Fluid Flow*, 66:157–171, 2017.

Schiereck, G. J. *Introduction to bed, bank and shore protection*. CRC Press, 2017.

Simpson, R. L. Aspects of turbulent boundary-layer separation. *Progress in Aerospace Sciences*, 32 (5):457–521, 1996.

Sobey, I. J. and Drazin, P. G. Bifurcations of two-dimensional channel flows. *Journal of Fluid Mechanics*, 171:263–287, 1986. doi: 10.1017/S0022112086001441.

Svasek Hydraulics. Eindrapport monitoring bodembescherming. Technical report, 2020.

Talstra, H. *Large-scale turbulence structures in shallow separating flows*. PhD thesis, 2011.

Uijttewaal, W. *Turbulence in hydraulics*. Delft University of Technology, 2018.

Üşenti, B. Scour hole formation for lateral non-uniform flow in non-cohesive sediments. Master's thesis, 2019.

van de Zande, B. Jet behaviour in longitudinal deepening shallow flows: A case study to the eastern scheldt storm surge barrier. Master's thesis, 2018.

van Prooijen, B. *Shallow mixing layers*. PhD thesis, 2004.

van Prooijen, B. C. and Uijttewaal, W. S. J. A linear approach for the evolution of coherent structures in shallow mixing layers. *Physics of Fluids*, 14(12):4105–4114, 2002. doi: 10.1063/1.1514660. URL https://doi.org/10.1063/1.1514660.

van Prooijen, B. C. and Uijttewaal, W. S. The relevance of a back-scatter model for depth-averaged flow simulation. *Flow, turbulence and combustion*, 82(1):73, 2009.

Wells, M. G. and van Heijst, G.-J. F. A model of tidal flushing of an estuary by dipole formation. *Dynamics of Atmospheres and Oceans*, 37(3):223 – 244, 2003. ISSN 0377-0265. doi: https://doi.org/10.1016/j.dynatmoce.2003.08.002. URL http://www.sciencedirect.com/science/article/pii/S0377026503000472.

Wendt, J. F. *Computational fluid dynamics: an introduction*. Springer Science & Business Media, 2008.

Zijlema, M. Computational modelling of flow and transport. *Collegedictaat CIE4340*, 2015.

A

Data analysis Waterdunen

This appendix serves to show additional information regarding the measurement campaign at Waterdunen. The set-up of the measurement campaign is explained in in appendix A.1. Afterwards, the Hampel filter and change of basis used in the data post-processing are explained in appendix A.2 and A.3 respectively. The relative discharge which was used in the data-analysis is explained in appendix A.4. Finally, the scenario-by-scenario analysis of the measurement data is given in appendix A.5 for the 2DH analysis and appendix A.6 for the 2DV analysis.

A.1. Measurement campaign

The primary objective of the measurement campaign was to ensure the scour protection is not damaged during daily- and design-loads, to test the model calculations done with the Finel2D model, and to formulate a fitting and safe discharge regime for the culvert. The campaign took place from 16-09-2019 to 20-12-2019 with a total of 13 measurements done, of which 6 are relevant for the sea-side of the culvert. An overview of the measurements done at the sea-side is shown in table A.1.

Table A.1: Overview of the measurement scenarios on the sea-side of the culvert at Waterdunen. The negative discharges indicate water is flowing from the land side to the sea-side.

#	Date	Water level sea-side [m+NAP]		Water level land side [m+NAP]		Discharge [m^3/s]
		Low water	High water	Low water	High water	
1	**17-09**	-1.55	0.09	-0.18	0.24	-18.2
2	**20-09**	-1.78	0.44	-0.06	0.49	-33.1
3	**25-09**	-1.34	0.60	-0.26	0.65	-40.2
4	**07-11**	-1.23	0.28	-0.23	0.40	-49.7
5	**04-12**	-1.54	0.38	-0.46	0.51	-53.6
6	**20-12**	-1.40	-0.38	-0.24	0.74	-68.4

During the study, multiple types of measurements were carried out. The H-ADCP measurements were stationary and consistent during all six measuring days. Additionally, sailing ADCP and valeport measurements were carried out.

Due to high air entrapment in the flow, several (H-)ADCP measurements were rendered inaccurate. Therefore from scenario 4 to 6 valeport measurements were carried out simultaneously to validate the (H-)ADCP data. The conclusion was that the ADCP and valeport measurements were similar, but the H-ADCP measurements were invalid. Furthermore, it turned out the H-ADCP measurements did not measure in the primary flow stream. Therefore the study primarily used the ADCP and valeport measurements. Up until a discharge of around 55 m^3/s the ADCP measurements were accurate. For higher discharges the valeport measurements were rendered more accurate.

A.2. Hampel filter

The data was evaluated using a Hampel filter. The Hampel filter determines the median of a window size k with the to-be-evaluated data point in the center of the window. The standard deviation of the window is expressed as the median absolute deviation (MAD), defined as the median of the difference between the data points in the window and the computed median of the window. Usage of the MAD in stead of the regular Standard Deviation (STD) follows from the definition of both values: the MAD is less sensitive to outliers compared to the STD. As the Hampel filter is an outlier detection method, the MAD is preferred. As the MAD will be used an approximation of the STD, it should be consistent with the STD. Assuming a Gaussian distribution of the data, this means a multiplication with a factor 1.4826. A certain threshold value t_0 is then set, which defines how many times the approximated STD a value can differ from the median before it is defined as an outlier. Once the value is defined as an outlier it can either be replaced or removed.

Due to the natural variability of the flow in space, the data points collected in one transect can be expected to differ significantly. An example would be a transverse transect over the recirculation zone and the primary jet flow, which changes the sign and magnitude of the flow velocities substantially. The variable parameters k and t_0 should therefore be adjusted to allow large variations of the flow to occur. To determine both values, a sensitivity analysis of the Hampel filter is performed for scenarios 4 and 5. The results are shown in figure A.1. The objective of the sensitivity analysis is to find values for the window size and threshold for which the sensitivity to either value is low. This would mean, for example, an increase in the threshold value does not result in a significant amount of extra outliers, meaning only those values which deviate the most are detected. This gives no assurance any presumably valid datapoints are detected as outliers, yet it reduces the chance to a minimum while still removing actual outliers. Based on figure A.1, the Hampel filter seems to stagnate at a window size of 9 and a threshold value of 7 times the estimated standard deviation, which are the values used in the Hampel filter for all scenarios. To ensure enough data points are available for interpolation, the data is replaced using linear interpolation over the window rather than removing the data points.

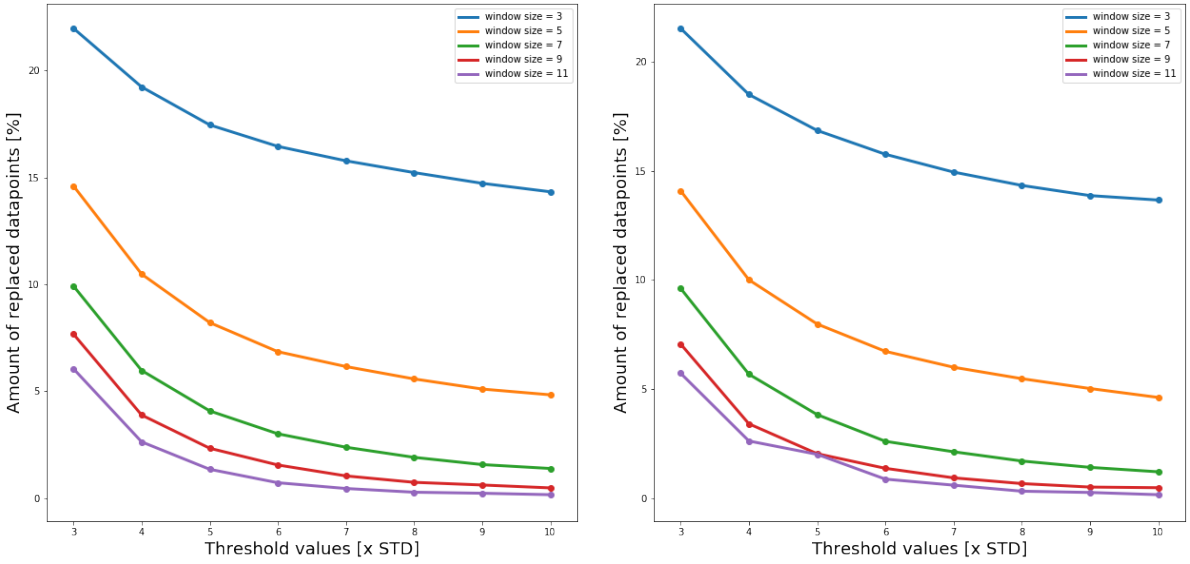

(a) Scenario 4

(b) Scenario 5

Figure A.1: Effect of different values for the window size k (different lines) and threshold value t_0 (x-axis) on the amount of erroneous data detected by the Hampel filter in (a) scenario 4 and (b) scenario 5.

A.3. Change of basis

As the data was obtained in a global (x, y, z) coordinate system, a change of basis was required in order to rewrite the coordinates and velocities. This can be done using a 2x2 transformation matrix A which

depends on the unit vectors in the new coordinate system. Both the x and y axis were rotated 25° leftward, resulting in a transformation matrix A with columns $[\cos 25°, -\sin 25°]^T$ and $[\sin 25°, \cos 25°]^T$. The origin of the new coordinate system was placed at the outflow point of the culvert and along transect 13. This rotation as practised on the boundary line coordinates combined with the local coordinate system are shown in figure A.2. The result is a transformation from (x, y, z) to (x', y', z) and from (u, v, w) to $(u_{x'}, v_{y'}, w)$. References to velocities appoint the latter coordinate system. For the purpose of readability, the figures in the main matter of this work are rotated by 90 degrees to place them horizontally. However, in this appendix, the images remain vertical to allow more images on one page.

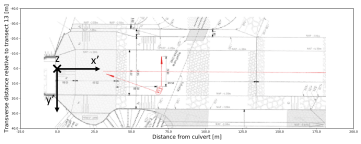

Figure A.2: Boundary lines of the canal as obtained in the global (x,y,z) coordinate system rotated towards a local (x', y', z) coordinate system.

A.4. Relative discharge

The discharge through the culvert can largely influences the observed flow patterns in the channel. It is therefore important to know which discharge corresponds to the observed flow field during the interpolation. Due to variation in the contraction coefficient μ for the inflow in the culvert, it was chosen to compute the discharge based on the volume change inside the inland lake of Waterdunen. For water levels between 0.80 m+NAP and -0.80 m+NAP the storage change in the lake is known for layers of 0.05 meters. An example (not scaled) is shown in figure A.3. Assuming this volume varies linear within each layer the change in storage at the beginning and end of each 10 minute interval can be computed to determine the average discharge during the time interval.

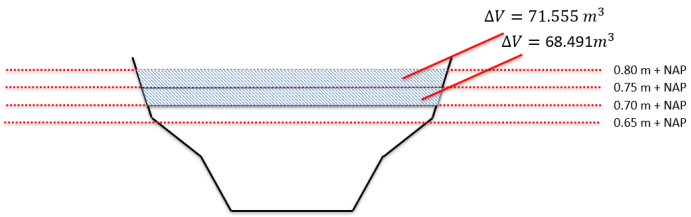

Figure A.3: Schematization of how the storage change in the inland lake of Waterdunen is determined.

For the depth-averaged 2DH analysis, the computed discharge through the culvert can be compared with the discharge through transverse cross-sections to determine the accuracy of the interpolation. The average flow velocity through each grid cell is computed. Based on the downstream water level and the grid cell width ($\Delta y' = 1$ m), the discharge through one grid cell can be determined. The total discharge can then be determined based on the summation of each grid cell in a strictly transverse line through the channel. This process is schematically shown in figure A.4 (not scaled). The interpolation is then evaluated for each cross-section by using the relative discharge, defined as the discharge computed through the cross-section divided by the discharge computed through the culvert.
It can preemptively be said that this approach is largely dependent on the coverage in the channel. If certain sections in the channel are not mapped with measurements the relative discharge is immediately affected. In the analysis it was shown that scenarios 4 and 5 contain the most accurate mapping of the channel as transverse transects are sailed, which allows for a broader spatial interpolation. In both these scenarios the relative discharge is an useful tool to determine the accuracy of the interpolation. For scenarios 1 to 3 the relative discharge is less useful due to the lower coverage.

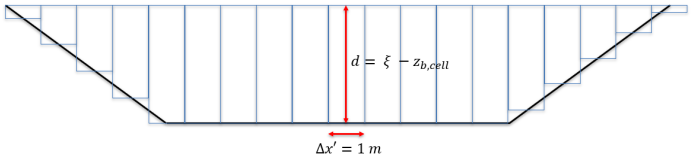

Figure A.4: Schematization of how the discharge through a transverse cross-section is estimated based on the average flow velocity through the individual grid cells and the downstream water level.

A.5. 2DH Analysis

This section explains the entire 2DH analysis which was carried out for the data at Waterdunen. Scenario 5 is discussed first, as the measurements during scenario 5 are of high quality and therefore allows for most important characteristics to be discussed. Afterwards the scenarios are discussed in descending order. For the purpose of readability, the images in this appendix are vertical rather than horizontal to fit more images on one page.

A.5.1. Scenario 5

During scenario 5 the slide was not used, meaning the flow was not compressed and could freely flow between the inland side and the seaside of the culvert. In total 47 transects were sailed with the ADCP, of which 40 were sailed with the valeport active. Based on a direct comparison with the valeport data it was chosen to discard 4 transects due to inaccurate results. The variation of the discharge through time combined with the variation of the downstream water level due to the tide is shown in figure A.5. It can be seen that the discharge slowly ramps up to a maximum value of nearly 54 m^3/s, after which it slowly decays. The initial discharge is already high compared to other scenarios. It should be kept in mind that the discharges were computed based on the assumption that the volume in Waterdunen varies linearly throughout layers, which might influence the accuracy of the computed discharges. During the measurement scenario the tide in the Western Scheldt moves from high tide to low tide, meaning the water level on the seaside of the culvert is dropping nearly linearly with time.

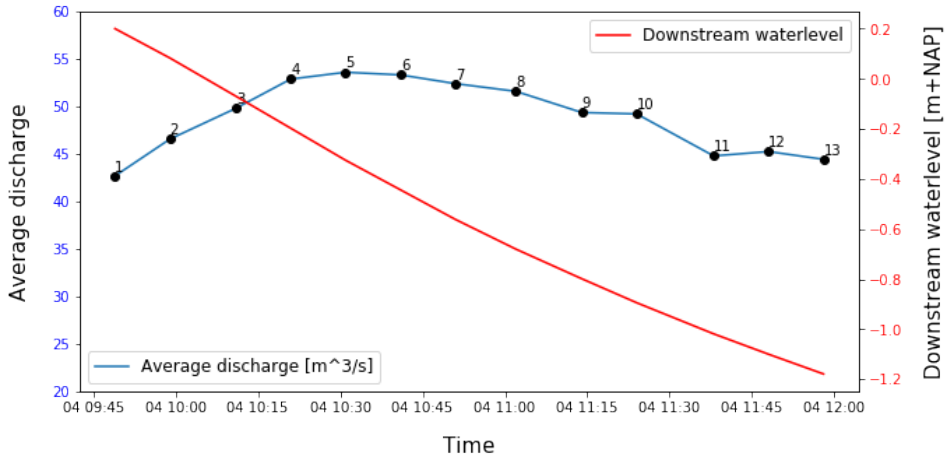

Figure A.5: Variation of discharge and downstream water level through time for measurement scenario 5. The black dots indicate the interpolated timesteps for which the values were obtained.

A.5.1.1 Chosen timesteps

During scenario 5 the highest discharges were measured. The best measurement coverage in the channel was found at the initial timesteps, after which the primary focus of the campaign lied in single point measurements and transverse transects. Figures A.6 to A.8 show the streamlines, relative discharges and absolute velocity magnitudes for three timesteps T = 2, T = 4 and T = 6. The characteristic parameters for these timesteps are summarized in table A.2.

Table A.2: Characteristic parameters for T = 2, T = 4 and T = 6 during measurement scenario 5.

Timestep	Average water depth [m]	Duration [minutes]	Water level difference [m]	Q [m^3/s]
2	4.03	7	0.4	46.6
4	3.74	10	0.63	52.9
6	3.51	10	0.79	53.3

To properly assess the differences between the timesteps, two lateral transects are inspected for each timestep. One of the transects is in the vicinity of the recirculation zone while the other is further downstream where the flow is more uniform. The transects in the recirculating area have been chosen based on the transverse measurements done during the measurements scenario and the relative discharge. The transects further downstream have been chosen solely based on relative discharge. The transects are compared based on the average flow velocity throughout the transect ($\overline{u_a}$), the maximum velocity difference over the transect (Δu) and the ratio between the two ($\frac{\overline{u_a}}{\Delta u}$). The latter serves as an indicator for shape of the transverse distribution of the streamwise velocity. These parameters are summed up in table A.3. Additional to the parameters mentioned above, the discharge and relative discharge are given.

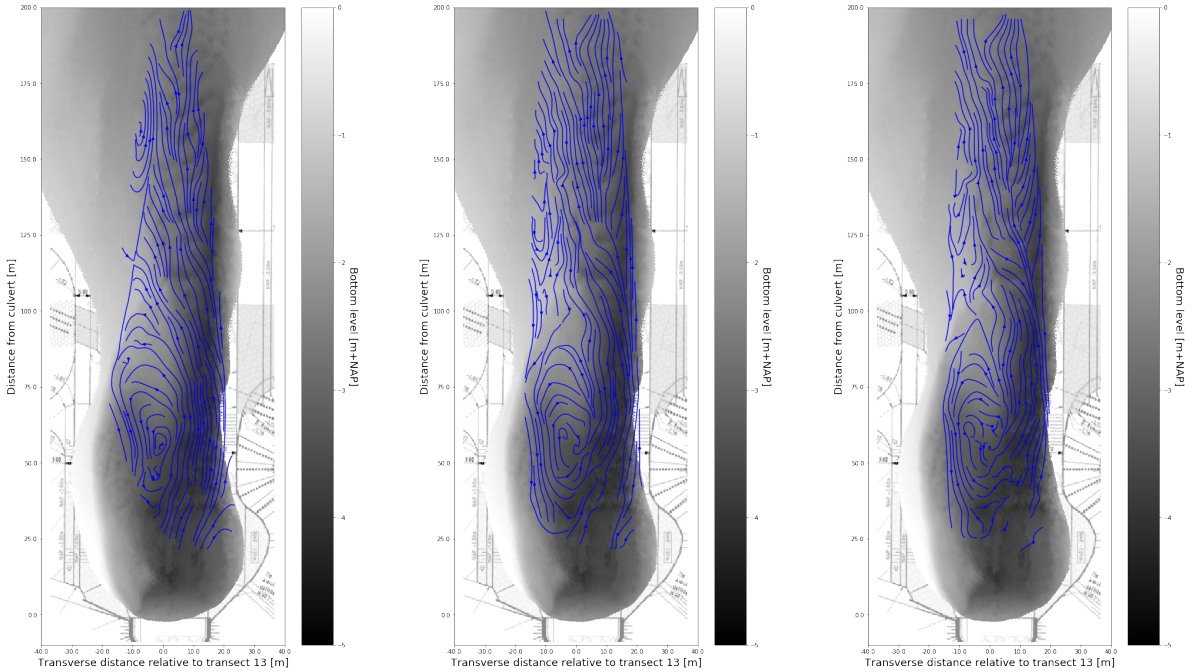

(a) T = 2. (b) T = 4. (c) T = 6.

Figure A.6: Streamplots for interpolation times T = 2, T = 4 and T = 6 during meausurement scenario 5.

A.5.1.2 Jet symmetry and strength

From figure A.6 it is clear that the flow concentrates on the eastern slope of the channel, where the highest flow velocities occur. From figures A.8a and A.8b it appears the flow velocities in the jet increase with increasing discharge and decreasing downstream water level. Additionally, by comparing figures A.8b and A.8c, it can be concluded that the flow velocities in the jet increases solely with a decrease in water level, though with a smaller amount. Comparing figure A.8a to figures A.8b and A.8c it is evident the high velocities in the jet persist over longer distances for higher discharges. At T = 2 a large portion of the kinetic energy in the jet is already removed at a distance of 100 m from the culvert, whereas high flow velocities persist in the channel further downstream at T = 4 and T = 6. Remarkably, it seems a

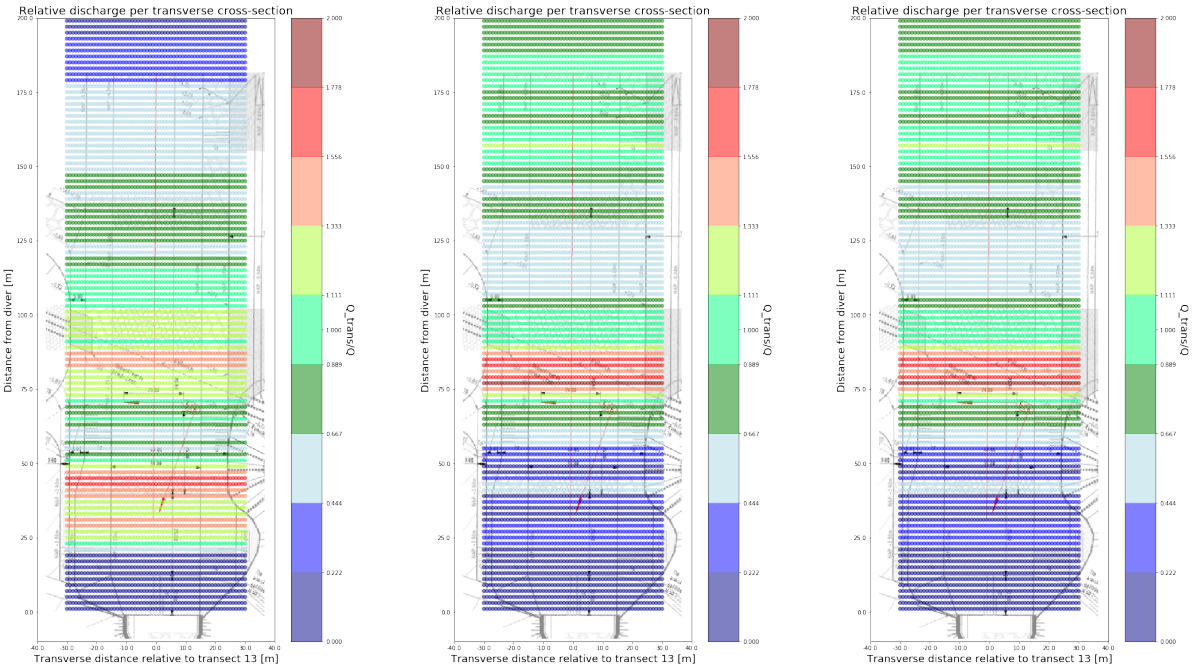

(a) T = 2. (b) T = 4. (c) T = 6.

Figure A.7: Relative discharge, defined as the Q based on the volume difference in the inland lake of Waterdunen divided by the interpolated discharge per transverse cross-section, during measurement scenario 5.

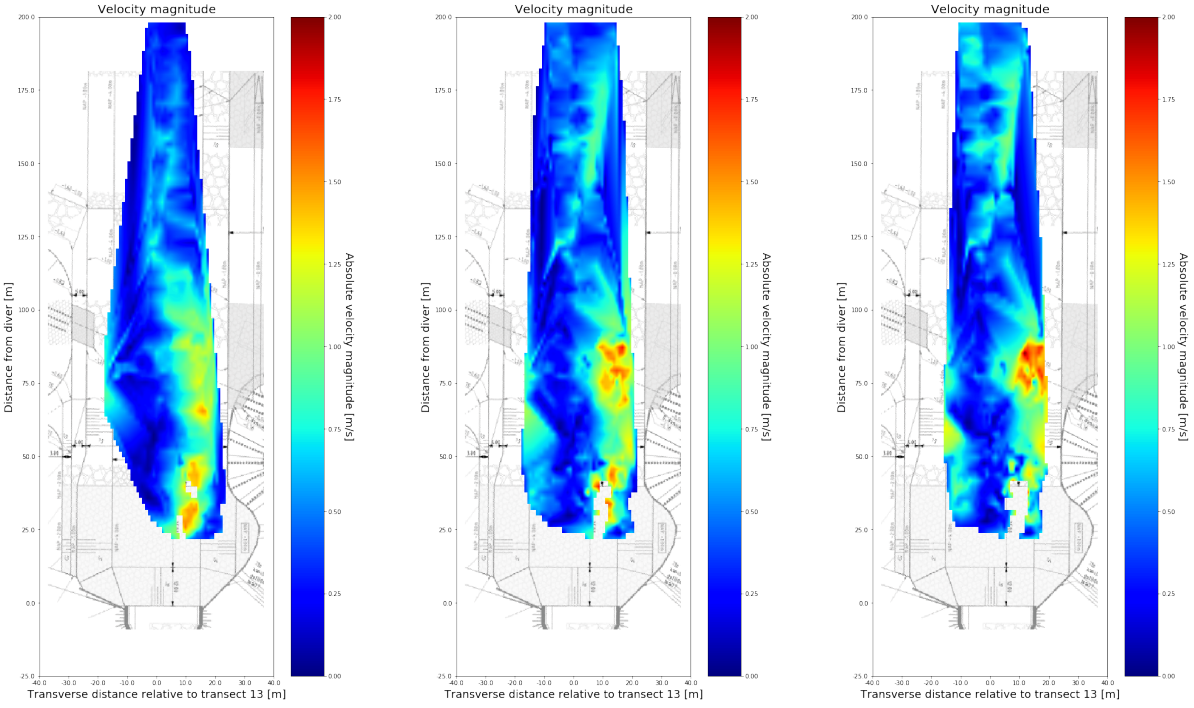

(a) T = 2. (b) T = 4. (c) T = 6.

Figure A.8: Absolute velocity magnitude for scenario 5.

velocity 'gap' is present at T = 4 and T =6, which separates the jet at the eastern side of the channel from the higher flow velocities further downstream at a distance of around 85 m from the culvert. As no significant topographic changes occur at this location, it is hypothesized this gap is the result of interpolation errors and that in reality the jet would have a more continuous shape.

Table A.3: Measurement scenario 5 velocity data over two transverse transects for T = 2, T = 4 and T = 6.

	Distance from culvert [m]	Q_{rel} **[**m^3/s**]**	u_a **[**m/s**]**	Δu **[**m/s**]**	$\frac{\Delta u}{u_a}$	**Q [**m^3/s**]**
T = 2	70	0.90	0.27	1.94	7.14	46.6
	114	0.91	0.35	1.27	3.58	
T = 4	70	1.1	0.38	2.23	5.81	52.9
	150	0.92	0.43	1.04	2.42	
T = 6	70	0.96	0.34	2.29	6.67	53.3
	150	0.94	0.48	1.03	2.14	

A.5.1.3 Streamline convergence

Figure A.6 shows the streamlines do not seem to diverge according to the classical plane jet pattern as depicted in figure 2.1. Instead, the streamlines seem to converge around 60 m from the culvert, as visible in figure A.6. Visual observations showed that at the water surface this contraction of streamlines was also visible, as shown in figure 3.5. To verify this with the data, a plot of the first ADCP data point in the water column has been made for T = 2 for scenario 5. The result is visible in figure 3.11, showing clear convergence of streamlines. Broekema et al. (2020) concluded the convergence of streamlines is a result of the topographic influence on the flow, occurring after a longitudinal slope.

A.5.1.4 Recirculating area

To investigate the growth of the recirculating area, the lateral jet profiles are fitted by a fourth degree polynomial. An example of such a fit is shown in figure A.9. Using the fitted polynomial, the location where the streamwise velocity becomes negative can be determined to serve as an indication of the width of the recirculation zone. This value is computed for all transverse cross-sections during T = 2, T = 4 and T = 6 to create three lines showing the start of the recirculating area for all three timesteps. The result is shown in figure A.10. Recall that in the visual observations, a secondary recirculation zone was observed to be present to the east of the culvert. The initial points for each line indicate negative values found in this recirculation zone, which is why the lines cross the jet at a distance of around 25 m from the culvert. Aside from a few data points, the lines are relatively equal. A general trend up to a distance of 100 m from the culvert shows the recirculation zone is at most places a little larger at T = 6 compared to T = 4 and T = 2, but only by a small amount. At around 125 m from the culvert a clear difference between the timesteps is measured, where it seems at T = 2 the recirculation zone is at its largest. However, looking at figures A.6a and A.8a most of the west side of the channel lacks data around this area for T = 2. Therefore the data in figure A.10 for T = 2 after a distance of 100 m from the culvert is deemed in accurate. It can be concluded the size of the recirculation area seems to vary little between timesteps for scenario 5. However, from figures A.8a to A.8c it can be observed the strength of the recirculating flow increases with increasing discharge. This is conform theory: a higher discharge increases the kinetic energy in the jet, allowing for more momentum transfer to the recirculation zone and therewith a stronger return current.

A.5.1.5 Topographic influence

At the beginning of each measurement campaign a topographic survey was carried out. The streamlines in figure A.6 are projected onto the depth map. For clarity, a larger copy is shown below in figure A.11. Directly after outflow past the longitudinal slope the morphology adapts to the imposed flow conditions, as is visible in the deeper water depths at the locations of the three eastern cases. This depth configuration appears to be relatively straight up to a distance of around 50 m from the culvert. A clear topographic channel formation towards both sides of the channel is evident. On the western side this topographic channel is relatively short and ill-defined, lasting for about 25 m. On the eastern side the topographic channel is well-defined and lasts up to around 90 m from the culvert. Afterwards the channel seems to narrow and keep straight just in front of the eastern slope, while an alternating sand bar pattern appears moving towards the middle.

The bottom topography confirms part of the jet diverges towards the middle of the channel around 90 m from the culvert. Furthermore, it also seems to confirm a section of the jet keeps concentrated on

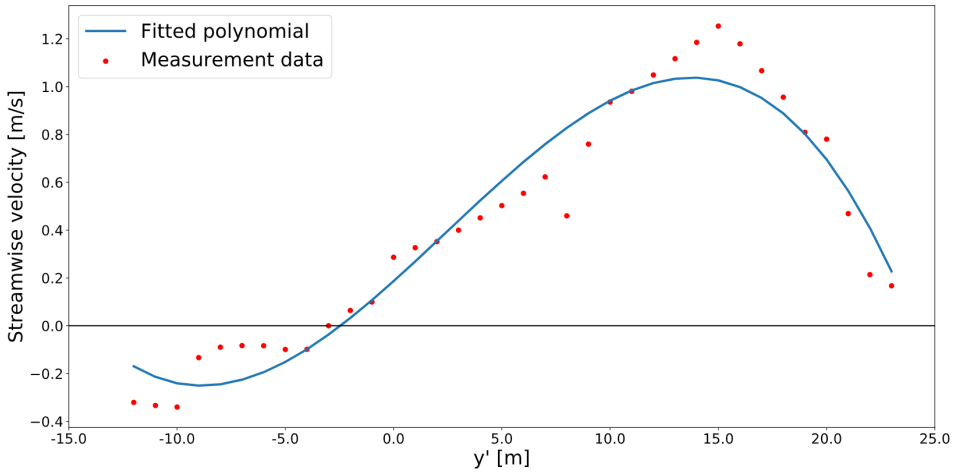

Figure A.9: Example of polynomial fit through the lateral data points for a lateral cross-section 40 m from the culvert during T = 6 in measurement scenario 5.

the eastern slope. Whether these two flows co-exist or appear for different flow configurations cannot be made clear with the current interpolation.

A.5.1.6 Conclusion

To conclude, it was seen that scenario 5 is characterized by an asymmetric jet with a strong eastern concentration. The strong concentration loosens around 80 m from the culvert, where a lot of the kinetic energy in the jet seems to have dissipated. During the scenario the width of the recirculation zone seems to remain constant, whereas the strength of the recirculating flow increases with increasing discharge. A contraction of the streamlines is observed around 50 m from the culvert. Measurements close to the east side of the culvert seem to validate the visual observation of a secondary recirculation zone, yet concise proof thereof is lacking.

A.5.2. Scenario 4

During scenario 4 the slide was used with a passing height of 1.62 meters. In total 51 transects were sailed with the ADCP, of which the last 22 transects were sailed with the valeport active. Based on a direct comparison with the valeport data it was chosen to discard 4 transects due to inaccurate results, primarily focussing on measurements close to the culvert. During the measurement scenario the tide in the Western Scheldt transitions from high to low tide, meaning the water level on the seaside of the culvert is dropping. The variation of the discharge through time combined with the variation of the downstream water level due to the tide is shown in figure A.12. It can be seen that the discharge ramps up in a progressive manner during around half the total time of the scenario. After T = 8 the discharge remains relatively constant with an average value of around 45 m^3/s apart from one peak at T = 10. It should be kept in mind that the discharges were computed based on the assumption that the volume in Waterdunen varies linearly throughout layers, which might influence the accuracy of the computed discharges. During the scenario the tide in the Western Scheldt transitions from high to low tide, meaning the water level on the seaside of the culvert is dropping nearly linearly with time.

During the analysis of the transects it was found that every first measurement per transect yielded unrealistic high values compared to measurements in the direct surrounding of the first measurement. Therefore it was chosen to discard every first measurement of each transect, as this was likely caused by an calibration error. Furthermore, as the discharges were compared it was be noticed that the discharge was severely overestimated between 25 and 75 meters in streamwise direction from the culvert for most time steps. It was therefore chosen to discard three transects sailed through the jet center line which yielded significantly higher flow velocities compared to measurements under relatively equal conditions.

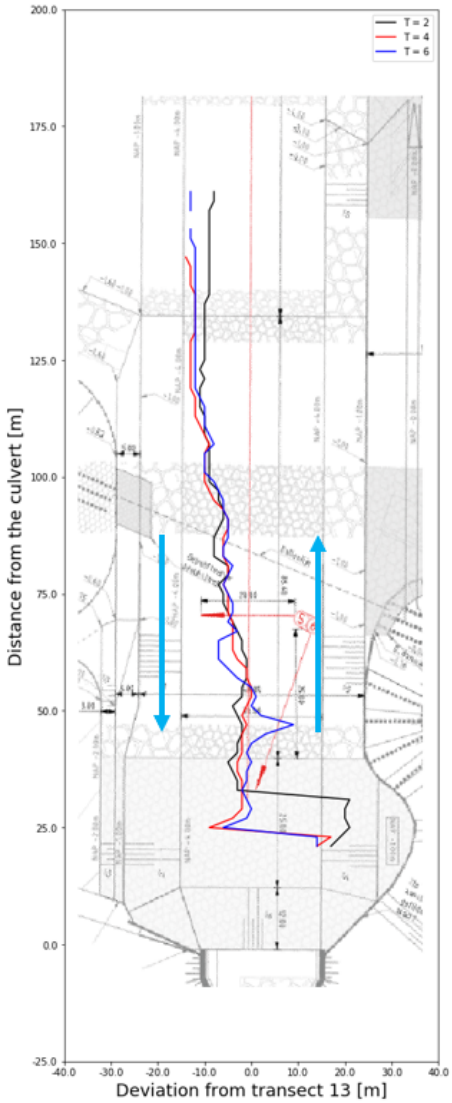

Figure A.10: Lines indicating the start of the recirculating area for timesteps T = 2 (black), T = 4 (red) and T = 6 (blue) during measurement scenario 5.

A.5.2.1 Chosen timesteps

At the beginning of scenario 4 the water level difference between the sea- and inland side of the culvert is still negative, meaning water flows from the seaside to the inland side. The reverse happens after the 6th sailed transect, or after around 12 minutes. After the reverse the discharge slowly builds up over the first 6 time intervals. In figures A.13 to A.15 the streamlines, relative discharges and absolute velocity magnitudes are shown for T = 5, T = 8 and T = 12. The characteristic parameters for these time steps are summarized in table A.4. Between time step 5 and 8 the discharge increases and the downstream water level decreases, which both theoretically increase the flow velocity in the jet. Between time step 8 and 12 only the water level decreases and the discharge remains relatively constant.

Table A.4: Characteristic parameters for T = 5, T = 8 and T = 12 during measurement scenario 4.

Timestep	Average water depth [m]	Duration [minutes]	Water level difference [m]	Q [m^3/s]
5	4.04	10	0.33	35.5
8	3.74	10	0.55	45.6
12	3.35	10	0.79	47.4

Figures A.14 and A.15 show a large section west of transect 13 is not covered during the scenario.

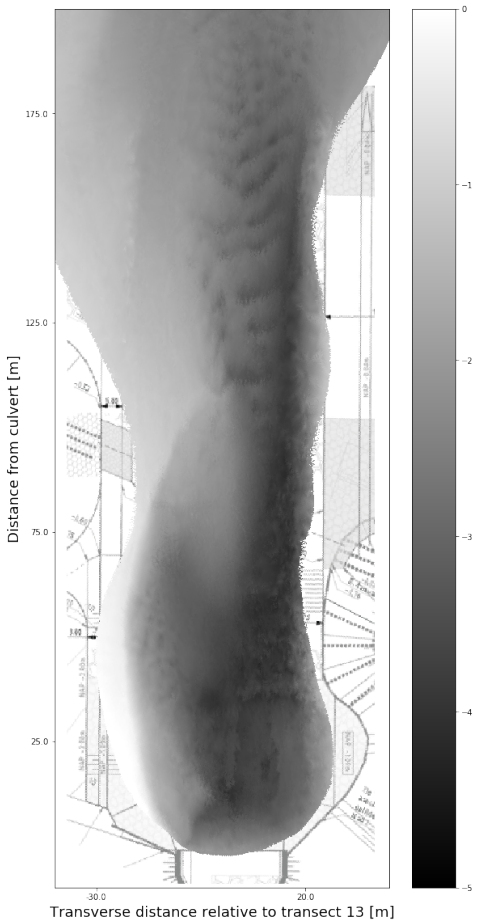

Figure A.11: Depth map as a result of the topographic survey carried out by Svasek Hydraulics at the beginning of measurement scenario 5.

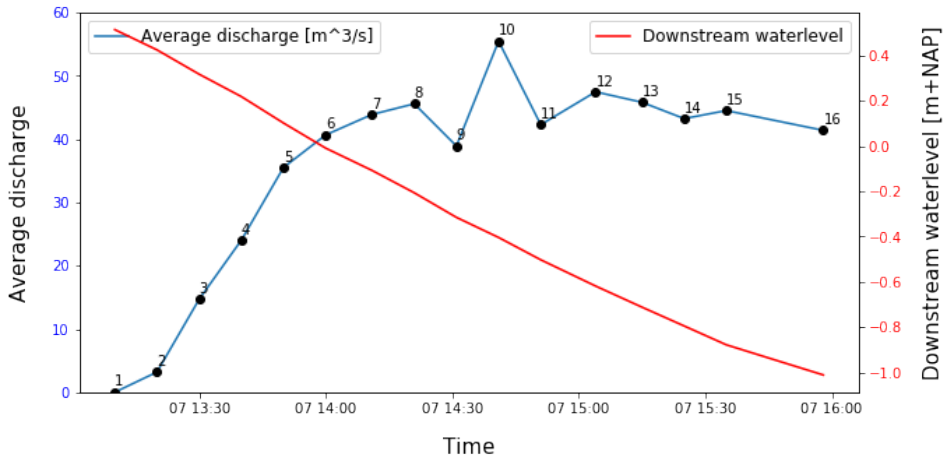

Figure A.12: Variation of discharge and downstream water level through time for measurement scenario 4. The black dots indicate the interpolated time steps for which the values were obtained.

This is well-captured in the relative discharge at T= 5 as shown in figure A.14a as most transects compute a smaller discharge except for the recirculating area, where the discharge is overestimated. However, at T = 8 and T = 12 the discharge is either overestimated or well-fit in the vast majority of the transects as shown in figures A.14b and A.14c. Both figures A.14b and A.14c show an overestimation of the discharge over the recirculation zone, which seems logical as part of the recirculation zone is not

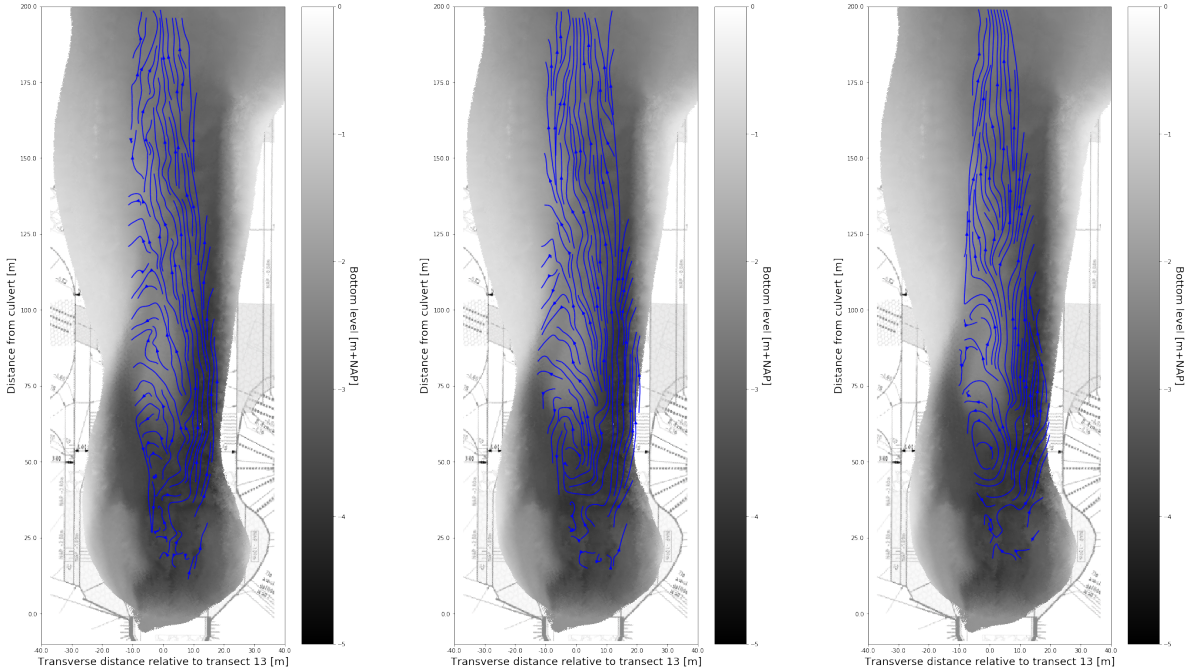

(a) T = 5. (b) T = 8. (c) T = 12.

Figure A.13: Streamplots for interpolation times T = 4, T = 8 and T = 12 during measurement scenario 4.

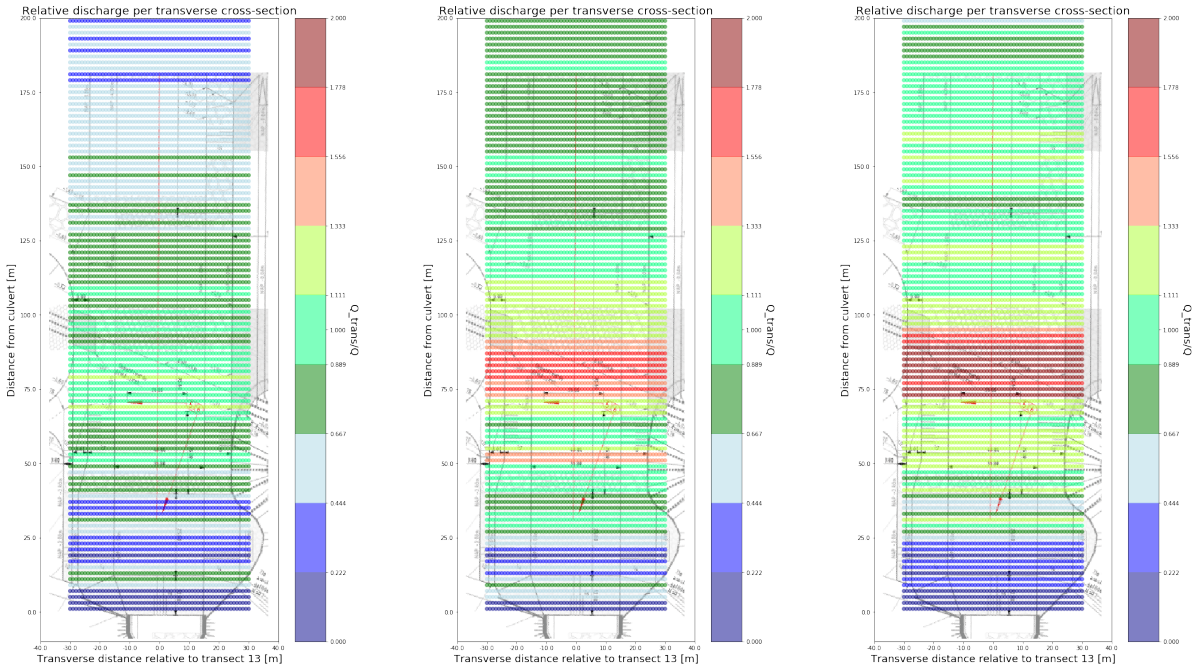

(a) T = 5. (b) T = 8. (c) T = 12

Figure A.14: Relative discharge, defined as the Q based on the volume difference in the inland lake of Waterdunen divided by the interpolated discharge per transverse cross-section, during measurement scenario 4.

mapped. Furthermore, it is remarkable the high recirculating velocities found on the west side of the channel during scenario 5 (A.8) are not visible during scenario 4. Two transects in which the relative discharges are close to 1 are further investigated per time step. The first transect lies in the recirculating area around 70 m from the culvert, while the second lies in a more uniform section around 150 m from the culvert. The result is shown in table A.5.

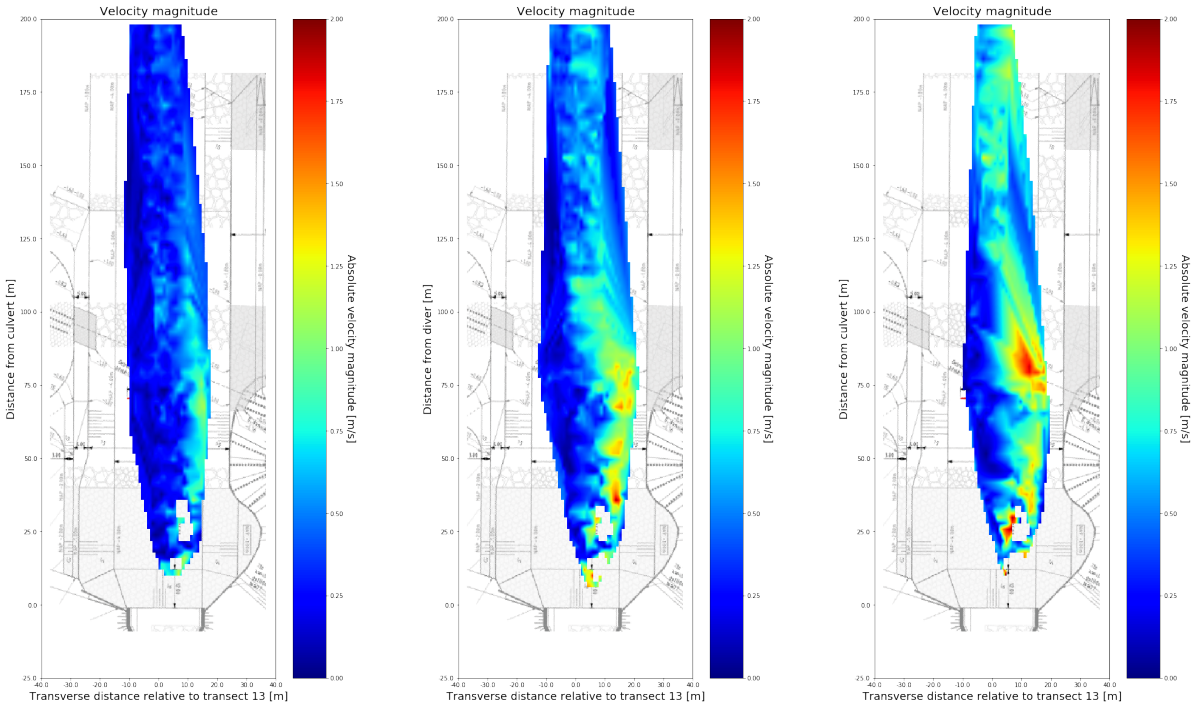

(a) T = 5. (b) T = 8. (c) T = 12.

Figure A.15: Absolute velocity magnitude for scenario 4.

Table A.5: Measurement scenario 4 velocity data over two transverse transects for T = 5, T = 8 and T = 12.

	Distance from culvert [m]	Q_{rel} $[m^3/s]$	u_a $[m/s]$	Δu $[m/s]$	$\frac{\Delta u}{u_a}$	**Q** $[m^3/s]$
T = 5	70	0.94	0.28	1.21	4.34	35.5
	108	0.93	0.32	0.90	2.84	
T = 8	64	0.97	0.37	1.58	4.28	45.5
	150	0.90	0.43	0.72	1.68	
T = 12	64	0.95	0.38	1.26	3.33	47.4
	150	1.08	0.66	0.57	0.86	

A.5.2.2 Jet symmetry and strength

From figure A.13 it is evident the jet concentrates on the eastern slope of the channel, creating an asymmetric flow pattern throughout the channel. At a location of around 80 m from the culvert the jet seems to loosen the strong eastern concentration and move towards the middle of the channel. From figure A.15 it is evident the velocity magnitude increases with time. This is confirmed by table A.5 as the mean velocity per transect tends to increase with time. The most remarkable finding is the steady decrease of $\frac{\Delta u_s}{\overline{u_s}}$ for both the recirculating area and the uniform channel section. This means an increasing Q and decreasing downstream water level reduces the jet-like behaviour of the flow. From figures A.15b and A.15c it is evident the jet spreads out when the eastern concentration is loosened around 80 m from the culvert. It is therefore only logical the jet-like profile decreases as the transverse velocity profile smoothens. For the recirculating area the decreasing $\frac{\Delta u_s}{\overline{u_s}}$ is unexpected. One would expect the velocity difference over a transect in the reciruclating area to be increasing for increasing discharge, yet only a slight increase is measured. One of the explanations lies in the absence of the strong recirculating currents as found in scenario 5 due to lack of measurements. These negative currents were shown to increase in magnitude for increasing discharge, contributing to a larger velocity difference over the recirculation zone. The relative discharges in figures A.14b and A.14c seem to confirm a part of the recirculating flow is missing, as the discharge is overestimated in a large area over the recirculation zone. Therefore no clear conclusion can be drawn based on the jet-profile parameter

in table A.5.

A.5.2.3 Streamline convergence
Looking at figure A.13 the streamlines in the jet do not seem to diverge but rather to converge when the jet hits the eastern slope, similar to scenario 5. However, the contraction of the streamlines is less visible as the upstream streamlines close to the culvert are not mapped in high quality. The low quality measurements also largely influence the surface streamline plots, which is why it has been chosen to not include the images.

A.5.2.4 Recirculating area
In the initial phases of scenario 4 the flow was still reversed, flowing from the Westescheldt to Waterdunen. Therefore, the development of the recirculation zone can be mapped by comparing the width of the zone for increasing discharges. The same approach as in scenario 5 will be used, with a polynomial fit through the transverse streamwise velocity datapoints. However, no conclusion could be drawn based on the images.

A.5.2.5 Topographic influence
The topographic map shows a similar profile in the initial 50 m from the culvert compared to scenario 5. Figure A.16 shows an enlarged figure of the topographic map as measured at the beginning of scenario 4. The depth appears to be relatively uniform over the length of the culvert up to that point, after which it splits in two topographic channels towards either lateral slope. A distinct difference lies in the western topographic channel, which is better defined in this scenario compared to scenario 5. Further downstream the eastern topographic channel again starts spreading towards the middle at a distance of around 90 m from the culvert. However, the alternating bar pattern appears to be less present, creating a more uniform channel. Additionally the length of the topographic channel is shorter compared to scenario 5.

A.5.3. Scenario 3
Scenario 3 is characterized by low field coverage, yet has the most measurements close to the culvert. Therefore, valuable information can be obtained regarding the initial jet behaviour. The slide configuration during the scenario resulted in a passing height of 0.9 m. In total 66 transects were sailed with a large priority on transect 13. Aside from sailing measurements over transect 13 some stationary measurements were carried out. No transverse transects were sailed, which is the primary cause for the low coverage. The variation of the discharge through time combined with the variation of the downstream water level due to the tide is shown in figure A.17. It can be seen that the discharge ramps up in the initial stages of the scenario, after which it remains relatively constant with an average value of around 42 m^3/s. It should be kept in mind that the discharges were computed based on the assumption that the volume in Waterdunen varies linearly throughout layers, which might influence the accuracy of the computed discharges. During the scenario the tide in the Western Scheldt transitions from high to low tide, meaning the water level on the seaside of the culvert is dropping nearly linearly with time.

A.5.3.1 Chosen timesteps
Figures A.18 to A.20 show the streamplots, relative discharges and absolute velocity magnitudes for time steps T = 4, T = 6 and T = 8. The characteristic parameters for these time steps are summarized in table A.6.

Table A.6: Characteristic parameters for T = 5, T = 8 and T = 12 during measurement scenario 3.

Timestep	Average water depth [m]	Duration [minutes]	Water level difference [m]	Q [m^3/s]
4	4.13	6	0.48	31.13
6	3.75	10	0.80	47.0
8	3.51	10	0.984	40.2

Eyeing the streamplots in figure A.18 and the corresponding relative discharges in figure A.19 it is evident the low coverage during scenario 3 has large consequences for the accuracy of the computed

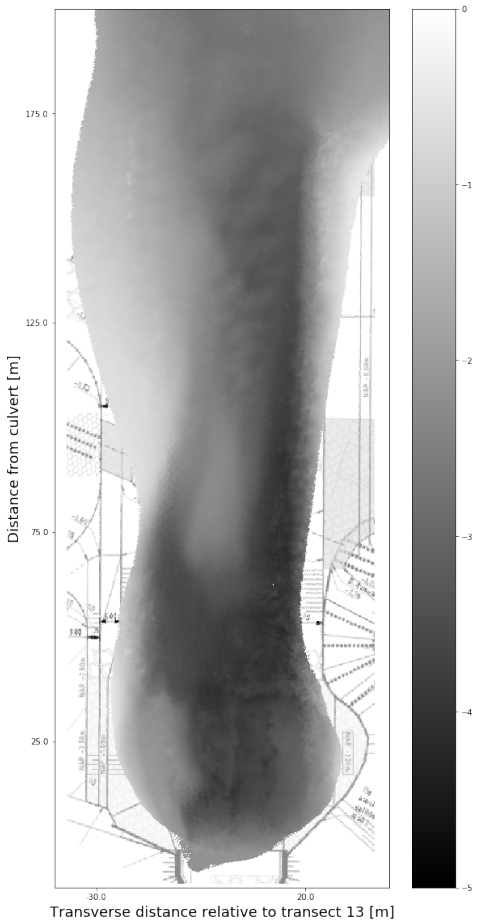

Figure A.16: Depth map as a result of the topographic survey carried out by Svasek Hydraulics at the beginning of measurement scenario 4.

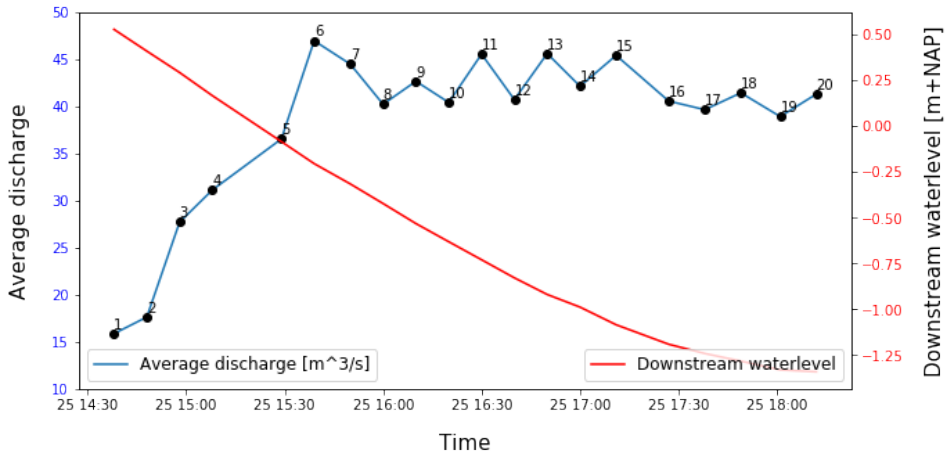

Figure A.17: Variation of discharge and downstream water level through time for measurement scenario 3. The black dots indicate the interpolated time steps for which the values were obtained.

discharges. Most of the west-side of the channel is not mapped in figure A.18. Furthermore, as explained before, some measurements on the eastern side of the channel contained oddly high velocities which were deemed inaccurate based on previous observations. However, it cannot be said whether all unrealistic velocities were removed. Both the low coverage of the recirculation zone and the unrealistic high values in the jet cause the discharge over the recirculation zone to be severely overestimated, as

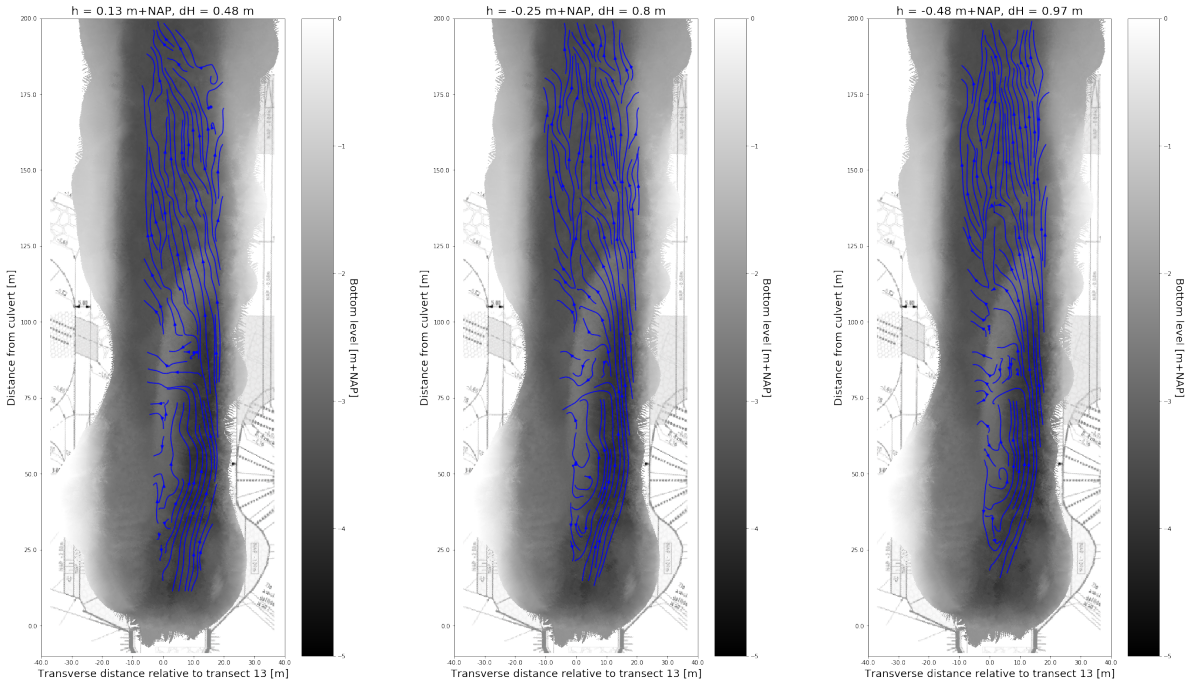

(a) T = 4. (b) T = 6. (c) T = 8.

Figure A.18: Streamplots for interpolation times T = 4, T = 6 and T = 8 during meausurement scenario 3.

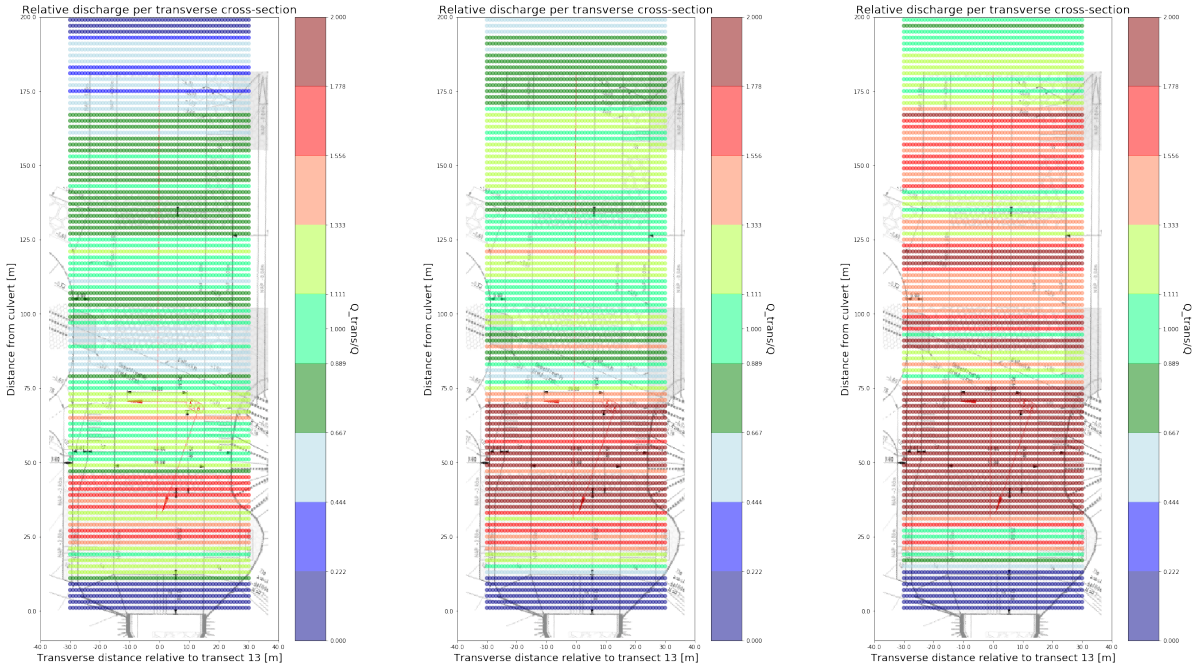

(a) T = 4. (b) T = 6. (c) T = 8.

Figure A.19: Relative discharge, defined as the Q based on the volume difference in the inland lake of Waterdunen divided by the interpolated discharge per transverse cross-section, during measurement scenario 3.

is evident from figures A.19b and A.19c.

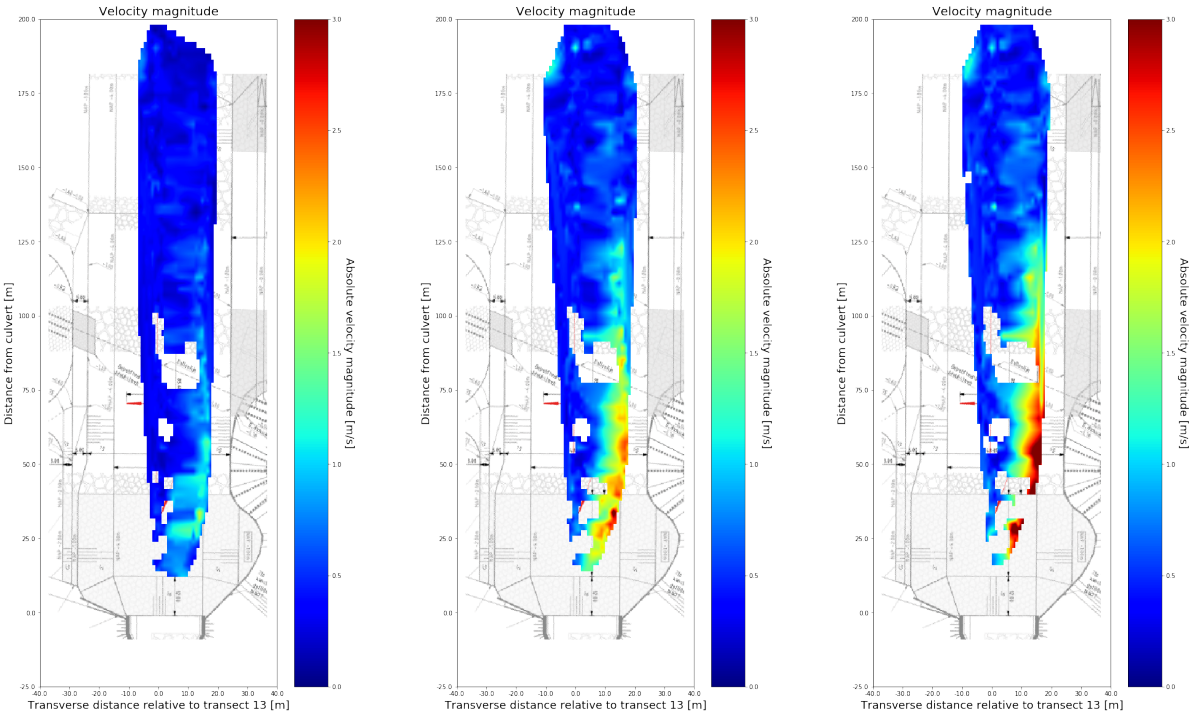

(a) T = 4. (b) T = 6. (c) T = 8.

Figure A.20: Absolute velocity magnitude for scenario 3.

A.5.3.2 Jet symmetry and strength

Scenario 3 is characterized by a strong eastern concentration of the jet. Compared to scenario 4 and 5, this asymmetric behaviour seems amplified, as the peak velocities seem to travel over the eastern slope. Furthermore, it appears the jet itself is largely asymmetric. This is made visible in a polynomial fit through the streamwise velocity for a transect in the recirculation zone for T = 6 in figure A.21. The expected, more parabolic jet shape as expected from other measurement scenarios (figure A.9) does not occur, but a rather linear profile over the transverse cross-section is obtained. As a consequence the velocity gradient close to the eastern wall is much steeper compared to the parabolic jet shape. Therefore during this scenario the influence of wall friction plays a more dominant role in the jet dissipation compared to other scenarios. Additionally, the flow does not seem to loosen the eastern concentration further downstream. The combined effect of both these phenomena cause the jet to dissipate over shorter distances compared to scenario 4 and 5, which is visible in figure A.20. Whereas in scenario 4 and 5 relatively high flow velocities are still measured around 150 m from the culvert for high discharges, figure A.20b indicates that during scenario 3 most of the jet energy is dissipated 125 m from the culvert for a dishcarge of 47 m^3/s. From the evolution of figures A.20a to A.20c it can be seen the jet velocity scales positively with both discharge decreasing downstream water level.

A.5.3.3 Recirculating area

The same approach to determine the width of the recirculating area is taken for scenario 3. Figure A.22 shows the growth of the recirculating area in time for T = 3, T = 5, T = 7 and T = 9. Remarkable is that, contrary to scenario 4 and 5, a steady growth of the recirculating area is observed for the first 50 m from the culvert. Furthermore, it seems the recirculation zone grows for an increased discharge (T = 3 to T = 7) and also for a decreasing water level (T = 9), though the author is hesitant to draw conclusions based on the apperant random shape of the four curves.

A.5.3.4 Streamline convergence

The streamlines in figure A.18 no longer show the converging behaviour of the streamlines when the jet collides with the eastern slope, which was observed during scenario 4 and 5. Additionally, the surface

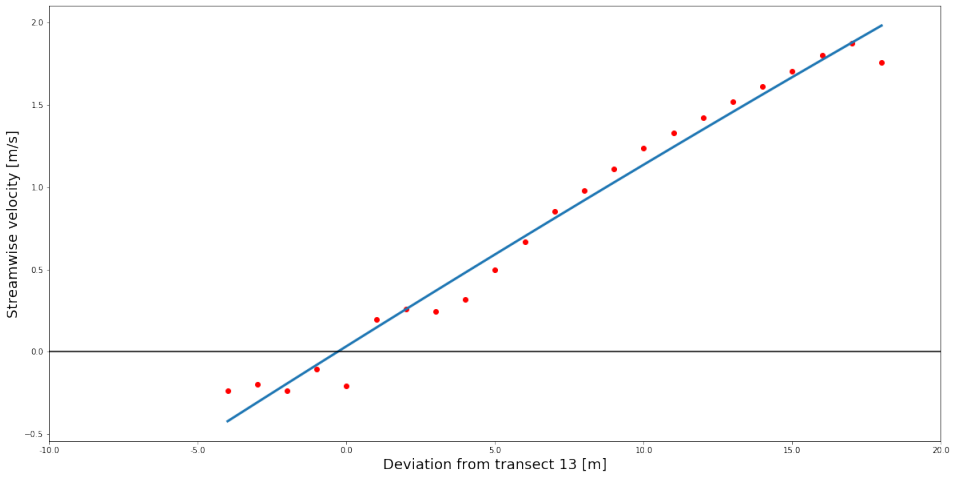

Figure A.21: Fourth degree polynomial fit through the stream wise velocity data points for transect 30 at T = 6 during measurement scenario 3.

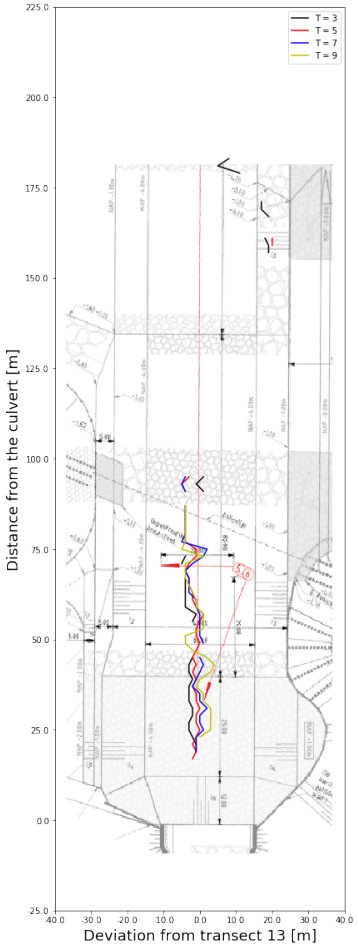

Figure A.22: Line where the streamwise flow velocities become negative which serves as a proxy for the width of the recirculation zone for T = 3 (Q = 27.7 m^3/s), T = 5 (Q = 36.5 m^3/s), T = 7 (Q = 44.5 m^3/s) and T = 9 (Q = 42.7 m^3/s).

plots tend to show a more diverging behaviour at this location, as is visible in figure A.23. Figure A.23 also shows the streamlines seem to converge closer to the jet, around 30 m from the culvert. However, this was not observed in both the depth-averaged streamplots or other surface streamplots.

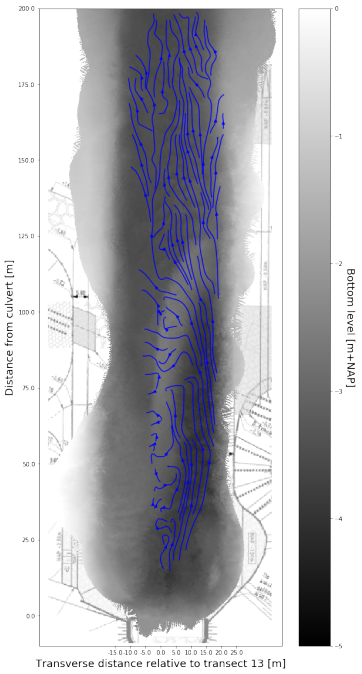

Figure A.23: Plot of the surface streamlines for T = 7 for scenario 3.

A.5.3.5 Topographic influence

Recall that between scenario 3 and 4 a flushing campaign was carried-out to erode excess sediment. Figure A.24 shows an enlarged image of the topography during scenario 3, before the campaign. The effect of the flushing campaign can be addressed by comparing figure A.24 and figure 3.12b. Figure A.24 shows a sandbar concaving to the east around 120 meters downstream from the culvert, resulting in a 'blockage' of the deeper channel. A clear deep topographic channel is found directly at outflow of the culvert, moving towards the east. This channel coincides with the sand bar at a streamwise distance of around 110 m from the culvert. The channel then narrows and eventually diminishes as the sand bar blocks it off.

A.5.4. Scenario 2

During scenario 2 the slide was used with a passing height of 0.69 metes. In total, 46 transects were sailed with the sailing ADCP. During the analysis of the transects it was found that every first measurement per transect yielded unrealistic high values compared to measurements in the direct surrounding of the first measurement. Therefore it was chosen to discard every first measurement of each transect. The variation of the discharge through time combined with the variation of the downstream water level due to the tide is shown in figure A.25. The black dots annotate the interpolated time steps. It can be seen that the discharge remains relatively constant after the third time step, with an average value of around 35 m^3/s. Throughout the measurement scenario the variation in discharge is small compared to other scenarios. It should be kept in mind that the discharges were computed based on the assumption that the volume in Waterdunen varies linearly throughout layers, which might influence the accuracy of the computed discharges.

Computing the discharge per transverse transect is difficult due to the low coverage throughout the channel. Therefore it was found the discharge is severely underestimated up to a distance of around 125 m from the culvert for most time steps. Furthermore, the measurements further downstream showed high flow velocities along transect 13 outside of the recirculation zone. As there are few transect that deviate from transect 13, these flow velocities get interpolated in space to result in an overestimation of the average flow velocity along lateral transects, which in turn results in an overestimation of the discharge. Even though this disables the analysis of absolute values, some general statements about the flow can be made. Figure A.26a shows the depth-averaged streamlines for T = 2

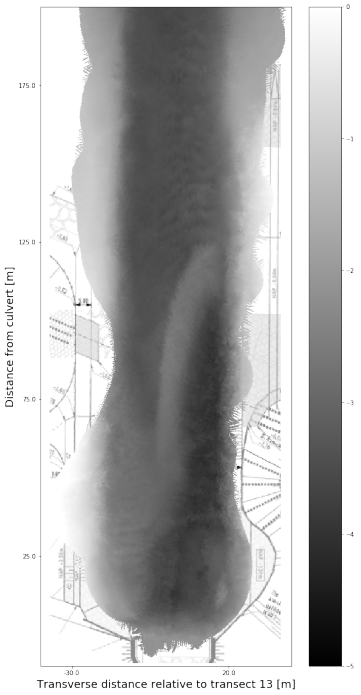

Figure A.24: Topographic map of the seaside channel at Waterdunen measured at the beginning of measurement scenario 3.

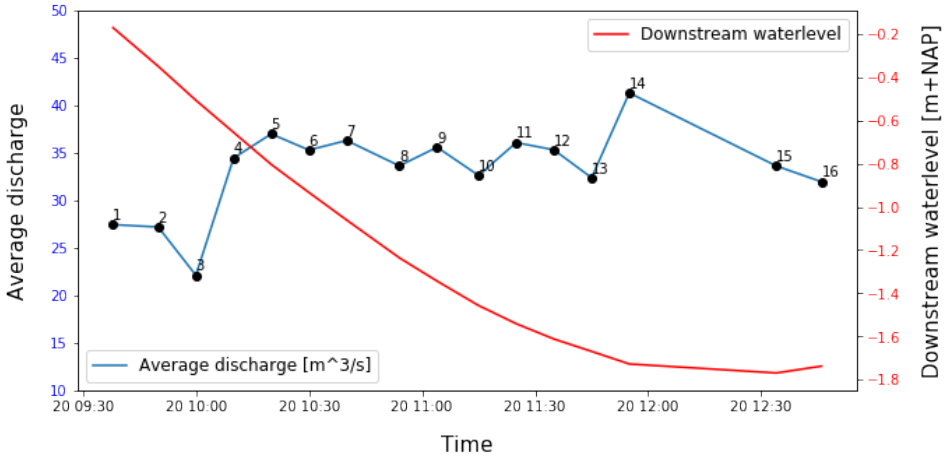

Figure A.25: Variation of discharge and downstream water level through time for measurement scenario 2. The black dots indicate the interpolated time steps for which the values were obtained.

with Q = 27.2 m^3/s. The figure nicely illustrates the jet flow and the corresponding recirculation zone, which seems to compress the jet and converge the streamlines. Furthermore, it shows the jet loosens the eastern concentration around 75 m from the culvert, contrary to the observations made during scenario 3. Recall that, as the flushing campaign was carried out between scenario 3 and 4, scenario 2 and 3 have very similar topographies. Unfortunately, this behaviour cannot be explored further as the streamlines become scrambled for subsequent time steps (figure A.26b for T = 3) and the flow velocity magnitude is largely interpolated in an incorrect manner (figure A.26c for T = 3).

A.5.5. Scenario 1

During scenario 1 the slide was used with a passing height of 0.39 metes. In total, 43 transects were sailed with the sailing ADCP. During the analysis of the transects it was found that every first measurement per transect yielded unrealistic high values compared to measurements in the direct surrounding of the first measurement. Therefore it was chosen to discard every first measurement of each transect.

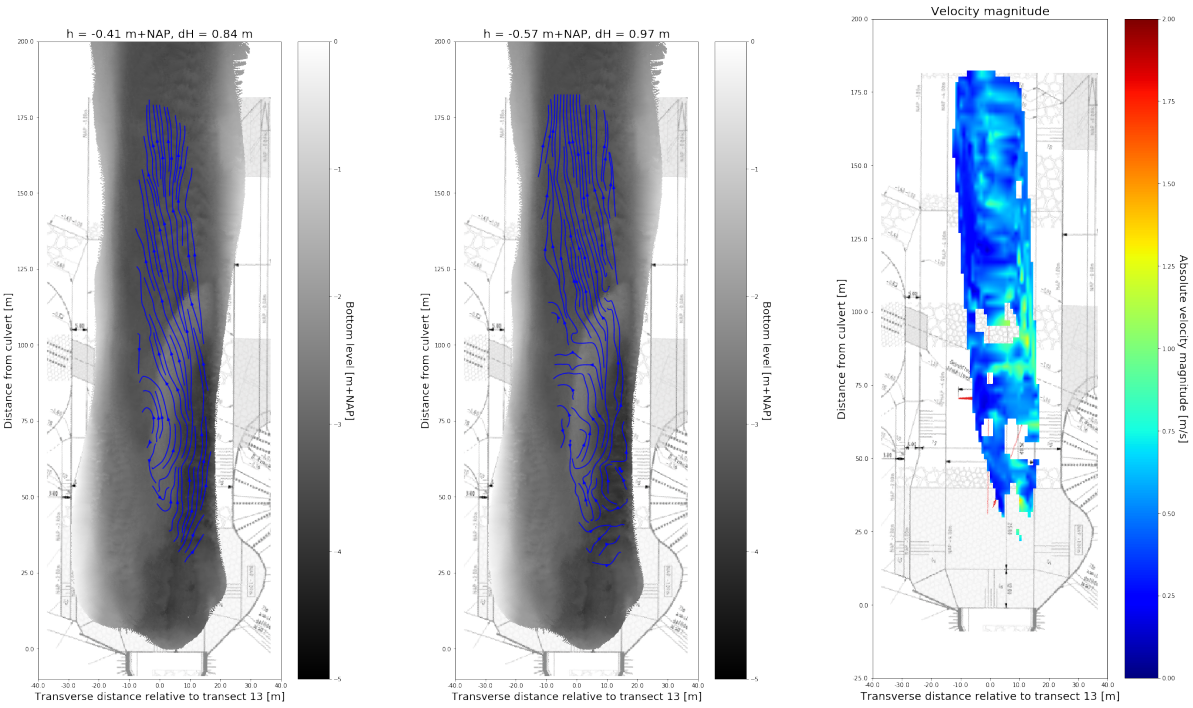

(a) Streamplot T = 2 (b) Streamplot T = 3 (c) Flow velocity magnitude T = 3

Figure A.26: Streamplots for T = 2 and T = 3 and absolute flow velocity magnitude for T = 3 during measurement scenario 2.

The variation of the discharge through time combined with the variation of the downstream water level due to the tide is shown in figure A.27. The black dots annotate the interpolated time steps. It can be seen that the discharge ramps up to a value of 20 m^3/s, after which it fluctuates around that value. The discharges measured during this scenario are small compared to other scenario due to the low passing height induced by the slides. It should be kept in mind that the discharges were computed based on the assumption that the volume in Waterdunen varies linearly throughout layers, which might influence the accuracy of the computed discharges.

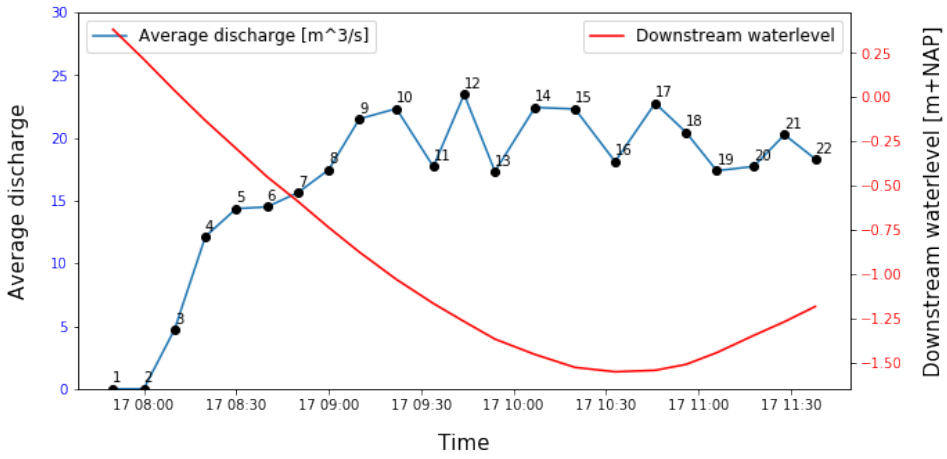

Figure A.27: Variation of discharge and downstream water level through time for measurement scenario 1. The black dots indicate the interpolated time steps for which the values were obtained.

The primary focus of scenario 1 lies on sailing measurements over transect 13. However, the vessel often deviated slightly from the sailed path, which resulted in a remarkably broad coverage of the

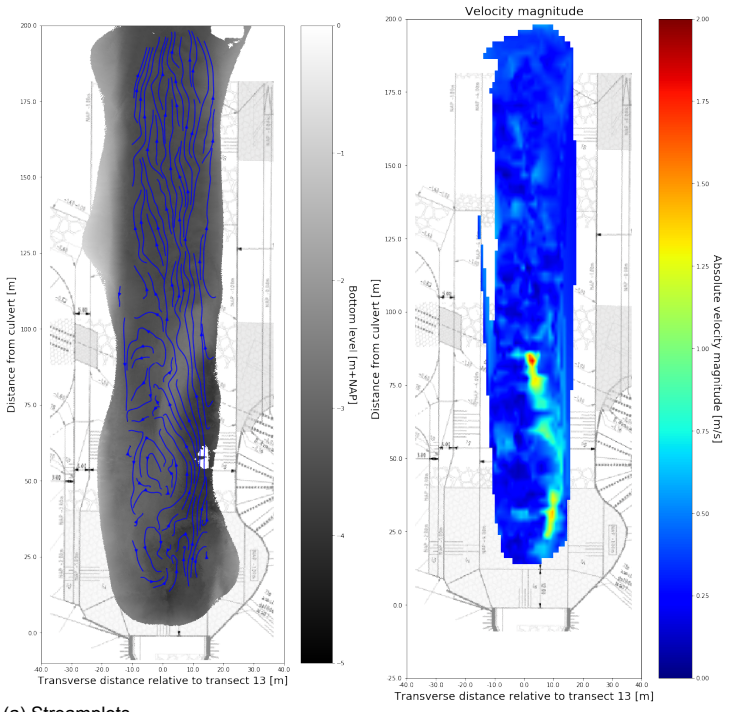

(a) Streamplots

(b) Absolute velocity magnitude

Figure A.28: Streamplot and absolute velocity magnitude for T = 12 with Q = 22.3 m^3/s during scenario 1.

channel. However, most values are interpolated. This largely affects the relative discharges, which are very inaccurate over the entire domain for most of the time steps. It was therefore chosen to solely observe the flow behaviour, rather than to look at absolute numbers. Figure A.28 shows the streamlines and absolute velocity magnitude for T = 12 during scenario 1. Due to the similar topography, the flow during scenario 1 can best be compared to the flow during scenario 2 and 3. Remarkably, it seems the jet curves to the middle of the channel at a distance of around 50 m from the culvert in figure A.28b similarly to scenario 2, whereas the jet remained concentrated on the eastern slope in figure A.20 for scenario 3. The latter is more expected based on the topography in the channel. Figure A.18 shows the jet moves over the sand bar in the middle of the channel rather than staying in the deep topographic channel on the eastern side. Furthermore, a large velocity increase is measured above the sand bar in figure A.28b, as the shallower water depths on the sand bar require the flow to accelerate. Confirmation regarding this acceleration will be sought after in the 2DV analysis. Finally, it appears the strong concentration of streamlines is also visible when the flow hits the eastern slope. This effect is also well-defined in other time steps in the scenario.

A.6. 2DV Analysis

This section explains the entire 2DV analysis which was carried out for the data at Waterdunen. Scenario 1 is discussed first, after which each subsequent scenario is investigated. The primary focus of the 2DV lies in the detection of vertical flow separation over the longitudinal slope, whereas other phenomena as observed during the 2DH analysis are also sought after. During the analysis, the sailed transects are followed and the streamwise velocity component is plotted over the vertical. Therefore the y' coordinate is not taken into account. In the background, the absolute velocity magnitude is plotted to gain a slight indication of the strength of the transverse velocity component. For a clear description of the post-processing mechanism used, the reader is referred to section 3.5.

A.6.1. Scenario 1

During the 2DH analysis it was observed the flow strongly concentrates towards the east during scenario 1. Therefore, the most valuable information regarding the vertical jet structure can be obtained in transects sailed over the eastern section of the channel. Unfortunately, scenario 1 only contained 2

transects sailed over the eastern section. A close-up of the vertical variation of the horizontal stream wise velocity is shown in figure A.29. The close-up spans the initial 75 m of the jet, after which the 2DH analysis showed the velocities already diminished significantly.

From both figure A.29a and A.29b it can be concluded the horizontal profile varies over the vertical, yet no clear separation phenomena can be observed. The latter is also caused by the relatively large portion of the water column close to the bottom which is unmapped by the ADCP. Furthermore, the two transects do not cross the sand bar at the location the flow was observed to cross the sand bar in figure A.28b, meaning the rest of the measurements are not as interesting. Note that the bump present between 50 and 75 m is a result of the projection: the vessel sailed over the transverse slope on that interval and it is not a sediment bump.

Furthermore, during the 2DH analysis it was observed the flow accelerates as it moves over the sand bar around 75 m from the culvert. Unfortunately, it appears the decrease in water depth allowed for only one measurement above the sand bar. Therefore the interpolation on the vertical grid did not contain sufficient measurements to accurately show this phenomenon occurred.

(a) Q = 17 m^3/s (b) Q = 18 m^3/s

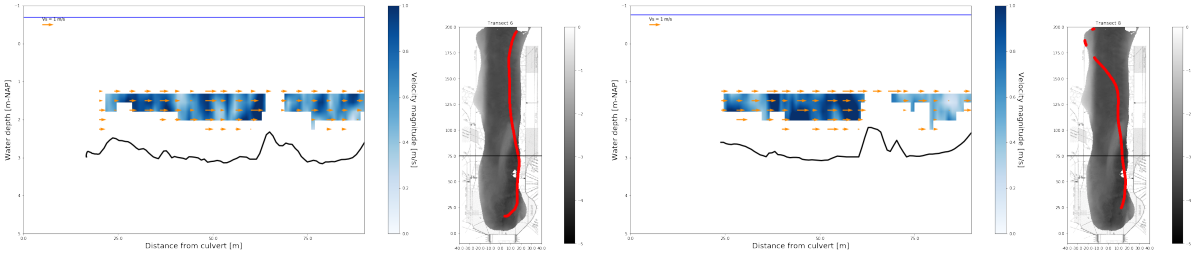

Figure A.29: Vertical velocity profile for 2 sailed transects (transect 6 and 8) during measurement scenario 1.

A.6.2. Scenario 2

Even though the data of scenario 2 was insufficient for a proper 2DH analysis, some interesting phenomena over depth can be seen. Figure A.30 shows two cut-off sections of two different transects for the initial 75 to 125 m from the culvert. In figure A.30a shows the streamwise velocity is relatively uniform over depth. This is also visible in he absolute velocity magnitude. However, it cannot be said for certain that no flow separation occurs. Figure A.30b shows a longer section which highlights the acceleration of the flow as it travels over the obstructing sand bar. This phenomenon also occurs in scenario 1 but was not observed during the 2DH analysis of scenario 2 due to the low quality of the data. Scenario 2 shows varying velocity profiles over depth close to the culvert, as shown in figure A.30. From A.30a it appears the flow velocity profile is uniform over depth in the primary jet stream, while figure A.30b shows a decreasing flow velocity over depth. Furthermore, figure A.30b shows that the primary jet stream 'hits' the eastern slope after a downstream distance of around 50 meters as also observed by the 2DH analysis.

Figure A.31 shows the vertical velocity profile over the entire length of transect 6. It is shown to highlight the acceleration of the flow observed after the flow has crossed the channel. Furthermore, it nicely shows the spreading of the jet as high flow velocities have reached the western side of the channel. Finally, it shows a high recirculating current at depth close to the culvert. Though these measurements were not obtained in the primary jet stream, these high currents at depth indicate some sort of recirculating process happens over the vertical. However, these recirculating currents were not observed during scenario 1, though they will be sought after in the other scenarios.

A.6.3. Scenario 3

Figure A.32 shows the vertical profile over the initial 75 m in streamwise distance for four transects with different discharges during scenario 3. Note that figure A.32d has a different scale color bar to indicate the absolute velocity magnitudes. It is observed that the vertical velocity profile becomes more uniform

(a) Initial 75 m from transect 2 with Q = 27 m^3/s

(b) Initial 125 m of transect 3 with Q = 25 m^3/s

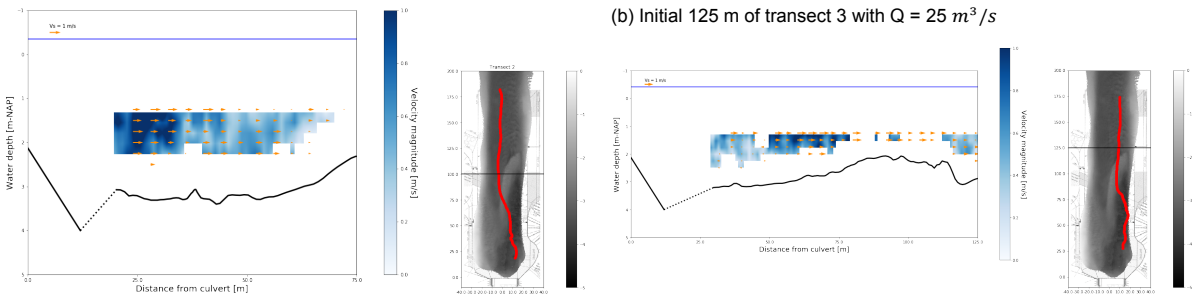

Figure A.30: Vertical velocity profile for 2 sailed transects during measurement scenario 2

(a) Q = 27 m^3/s

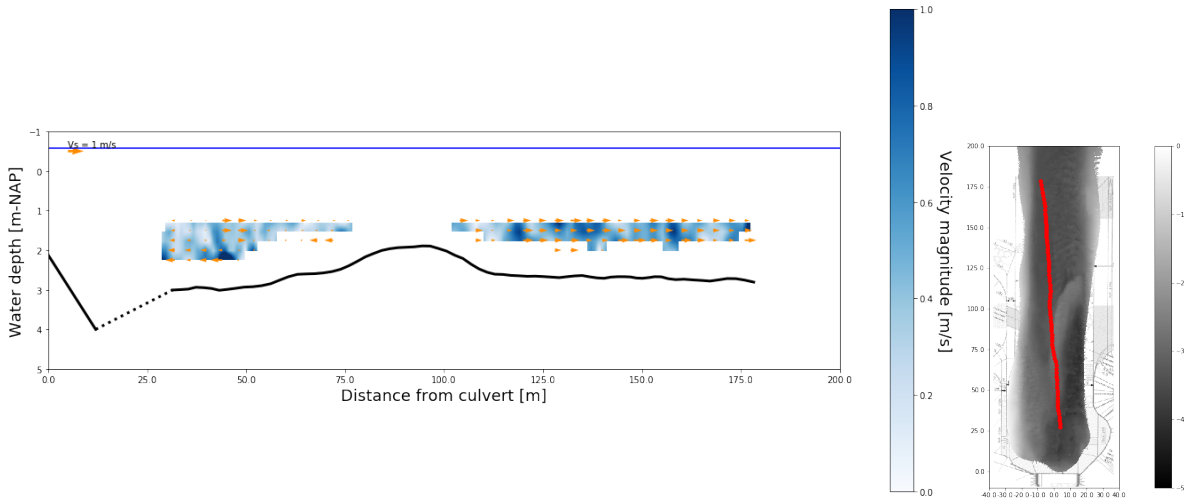

Figure A.31: Vertical velocity profile over the entire length of transect 6 of measurement scenario 2.

over depth as the discharges increase. However, even in figures A.32a and A.32b with relatively low discharges, no clear flow separation can be observed.

The horizontal analysis has shown the flow remains attached to the eastern slope until it has dissipated most of the kinetic energy. The flow therefore does not flow over the sand bar, meaning no additional acceleration is expected. Furthermore, this means the flow likely does not separate over the sand bar. To confirm this, some transects over the sand bar and transects remaining on the eastern side of the channel are investigated and shown in figure A.33. Figure A.33a shows a full transect over the sand bar, indicating relatively little discharge flows over the sand bar. Figure A.33b shows the full length of figure A.32d. Note the different scale, meaning the velocities further downstream are still high. Figure A.33b also nicely highlights the large amount of kinetic energy which is dissipated in the initial 75 m from the culvert, as was also shown in the 2DH absolute velocity magnitude plots in figure A.20. Though the flow seems to cross the sand bar around 120 m from the culvert, no flow separation is observed after the sand bar has been passed.

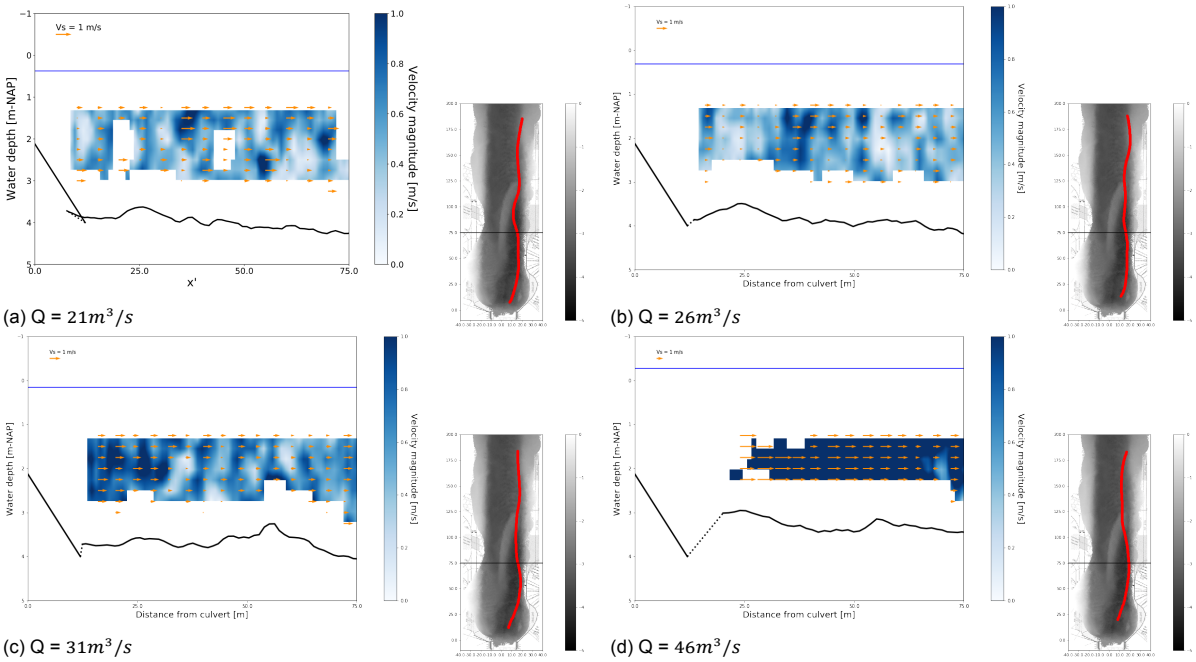

(a) Q = $21m^3/s$ (b) Q = $26m^3/s$

(c) Q = $31m^3/s$ (d) Q = $46m^3/s$

Figure A.32: Vertical velocity profiles of 4 sailed transects with increasing discharge during measurement scenario 3. The topography maps show the sailed transects, in which the horizontal black line indicates the range over which is the profile image is mapped.

A.6.4. Scenario 4

Figure A.34 shows the development of the vertical variation of the velocity for four sailed transects in the initial 75 m from the jet. In figure A.34a the flow velocity magnitude at the surface appears to be higher compared to further down into the water column. However, this pattern is variable in stream-wise direction. Figure A.34b shows that for a slightly higher discharge the flow pattern is much more uniform over depth. It is likely that the transect sailed in figure A.34a is on the outskirt of the primary flow-conveying channel and moves towards the recirculation zone. It is possible flow detachment takes place at this location, while the flow remains attached in the middle of the jet as also found by van de Zande (2018). However, convincing proof of this phenomenon is lacking. Figures A.34c and A.34d show the jet is far more uniform over depth for higher discharges. No clear flow separation can be identified. Furthermore, high recirculating velocities at depth such as observed in scenario 3 are not found.

It can be observed the water depth starts decreasing significantly around 50 m from the culvert, whereas the water depth increases once the shallow section is passed (figure A.16. During the 2DH analysis it was observed the flow remains on the eastern side of the channel for an extended duration and flows towards the middle once the water depth again decreases in the middle of the channel. It is for this reason that no accelerations or decelerations are measured when an extended transect is plotted, as visible in figure A.35a. Following a transect which remains in the deeper section of the channel, one finds an uniform depth profile along the entire jet as seen in figure A.35b. The flow magnitude seems to decrease around 120 m from the culvert, which is likely a result of the spreading of the flow which can also be observed in the velocity magnitude plots in figure A.15.

A.6.5. Scenario 5

During measurement scenario 5, three transects were sailed on the east side of transect 13 and relatively close to the culvert. As their profiles are similar, one transect is shown in figure A.36. In the initial 10 meters of measurements within the primary jet stream it can be observed the flow velocity is slightly higher near the surface, though it remains relatively constant over depth. Again, no clear recirculating velocities can be measured. Two full transects are shown in figure A.37. Figure A.37a shows the flow velocities increase over the shallower section of the channel around 75 m from the culvert. The abso-

(a) Q = 46 m^3/s

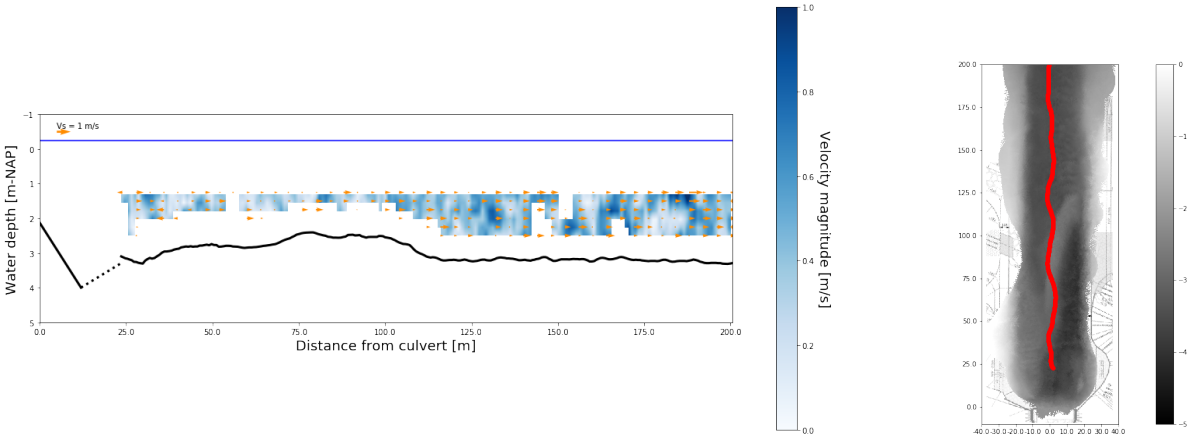

(b) Q = 45 m^3/s

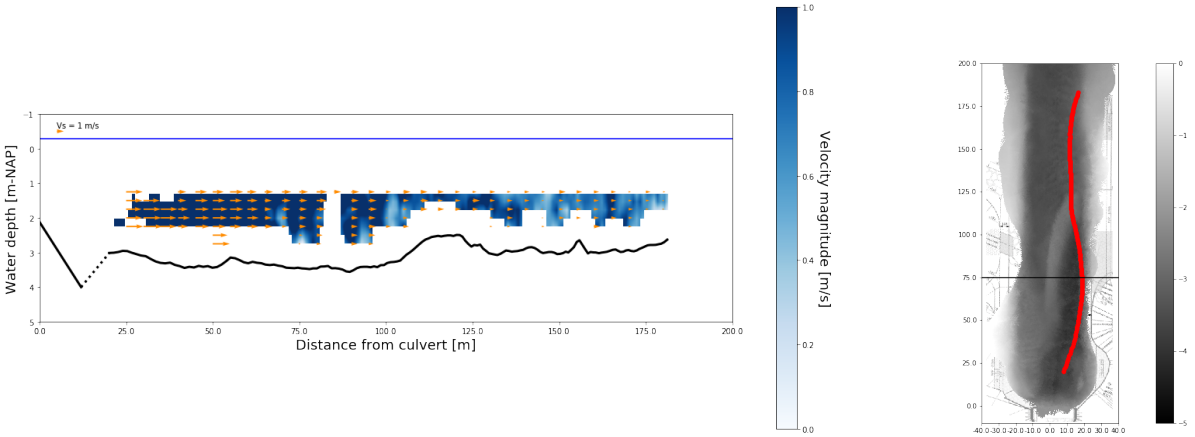

Figure A.33: Vertical velocity profile for transect 20 and 21 during measurement scenario 3

lute velocity magnitudes as in figure A.8 shows the flow starts expanding in lateral sense around this location. Figure A.37b shows the primary flow-conveying stream remains relatively undisturbed at the same location, meaning the horizontal expansion of the jet is likely caused by accelerating flow over the shallow section of the channel. Also further in the channel no clear recirculating pattern can be observed.

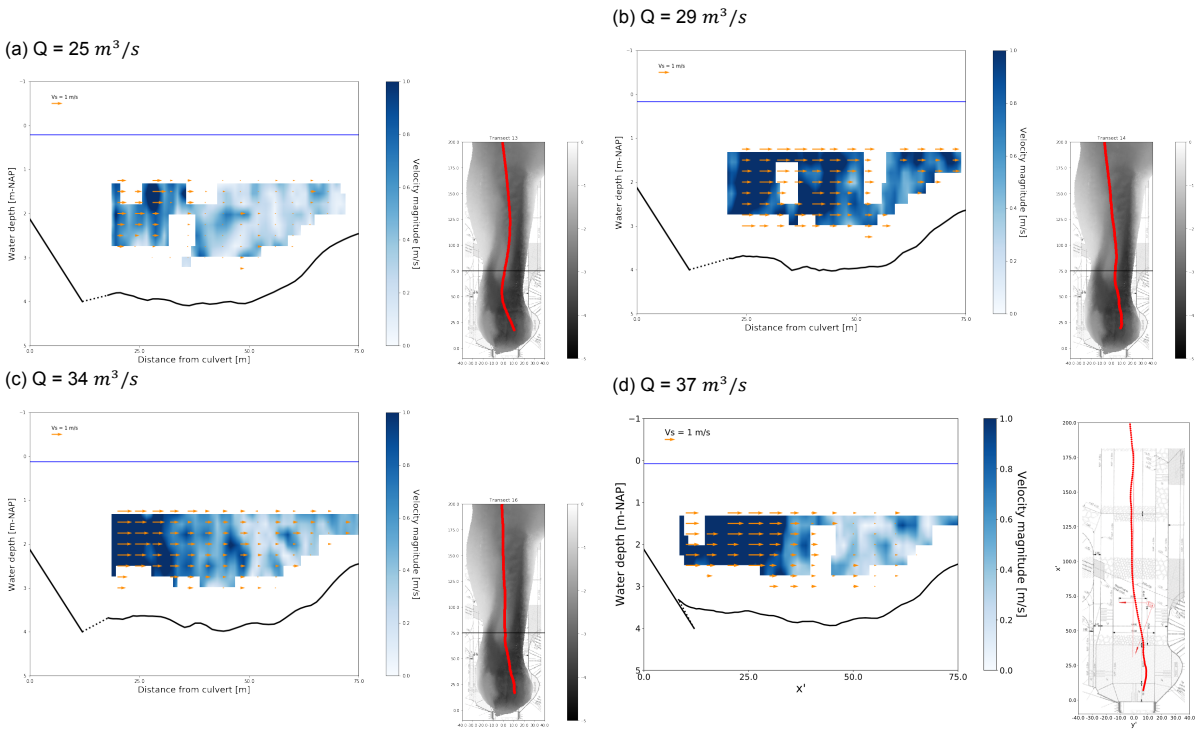

Figure A.34: Vertical velocity profiles of 4 sailed transects during measurement scenario 4. The topography maps show the sailed transects, in which the horizontal black line indicates the range over which is the profile image is mapped.

(a) Q = 29 m^3/s

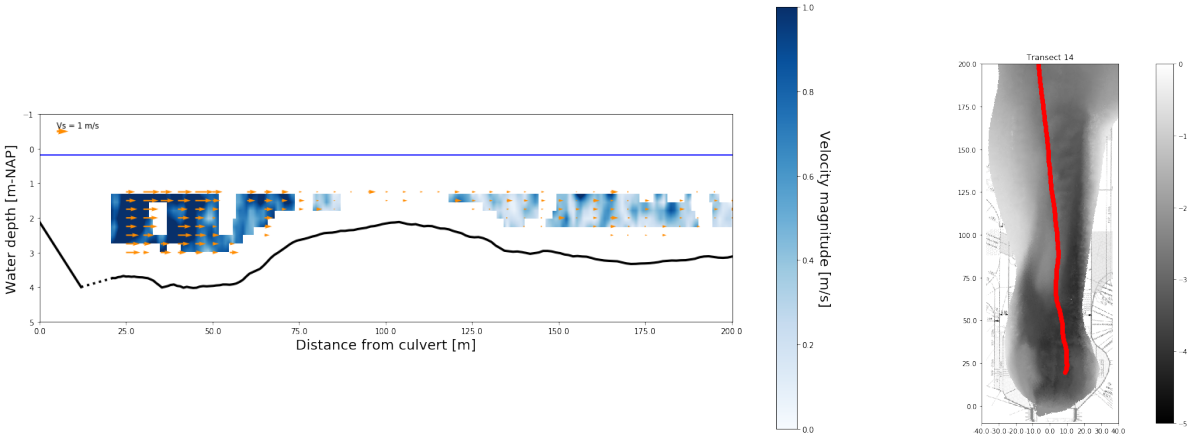

(b) Q = 42 m^3/s

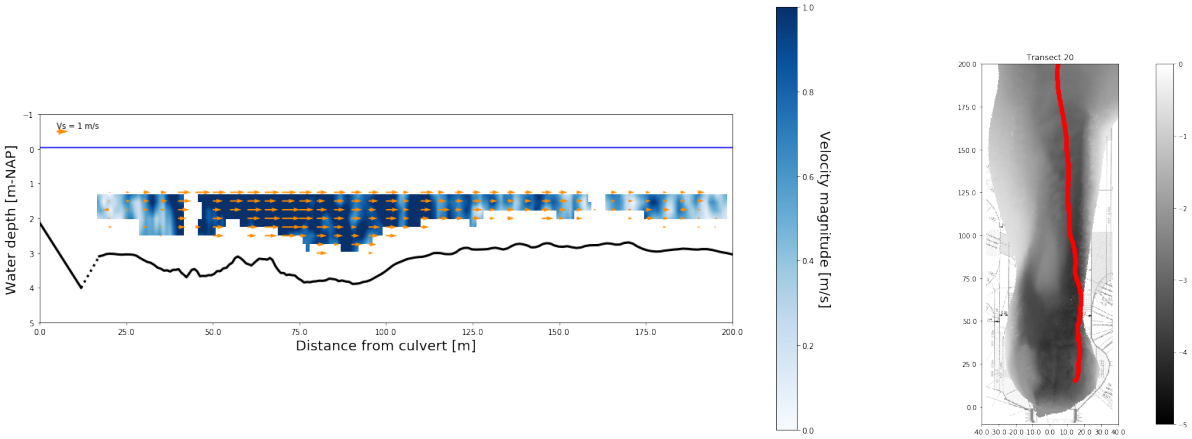

Figure A.35: Vertical velocity profile for transect 14 and transect 20 during measurement scenario 4

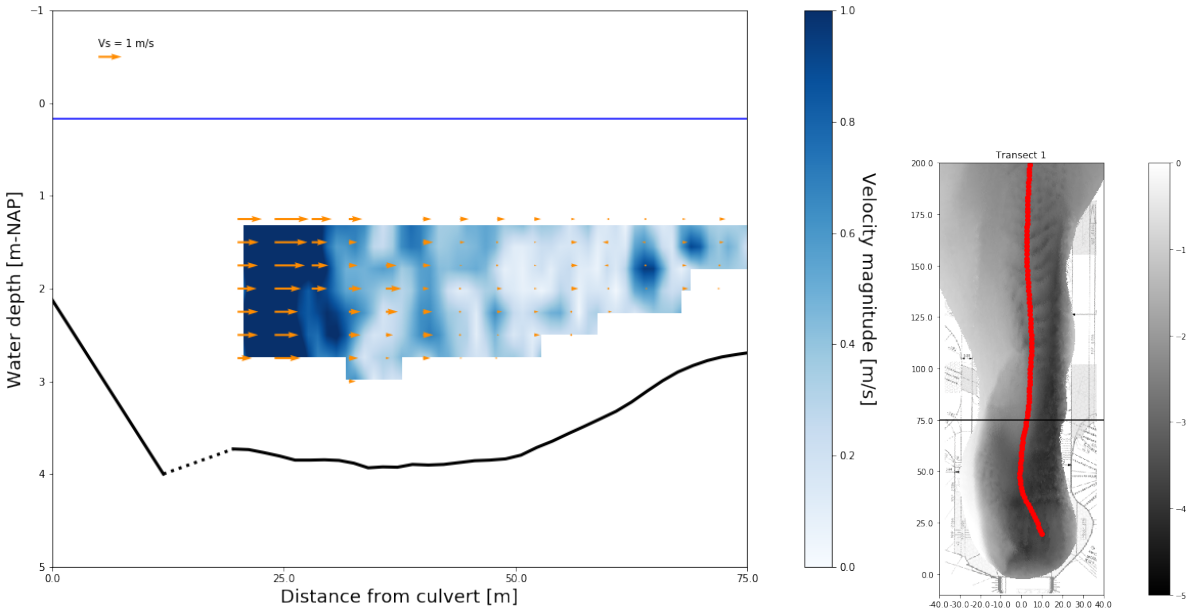

Figure A.36: Velocity profile over depth as observed during one transect in measurement scenario 5 with Q = $44m^3/s$

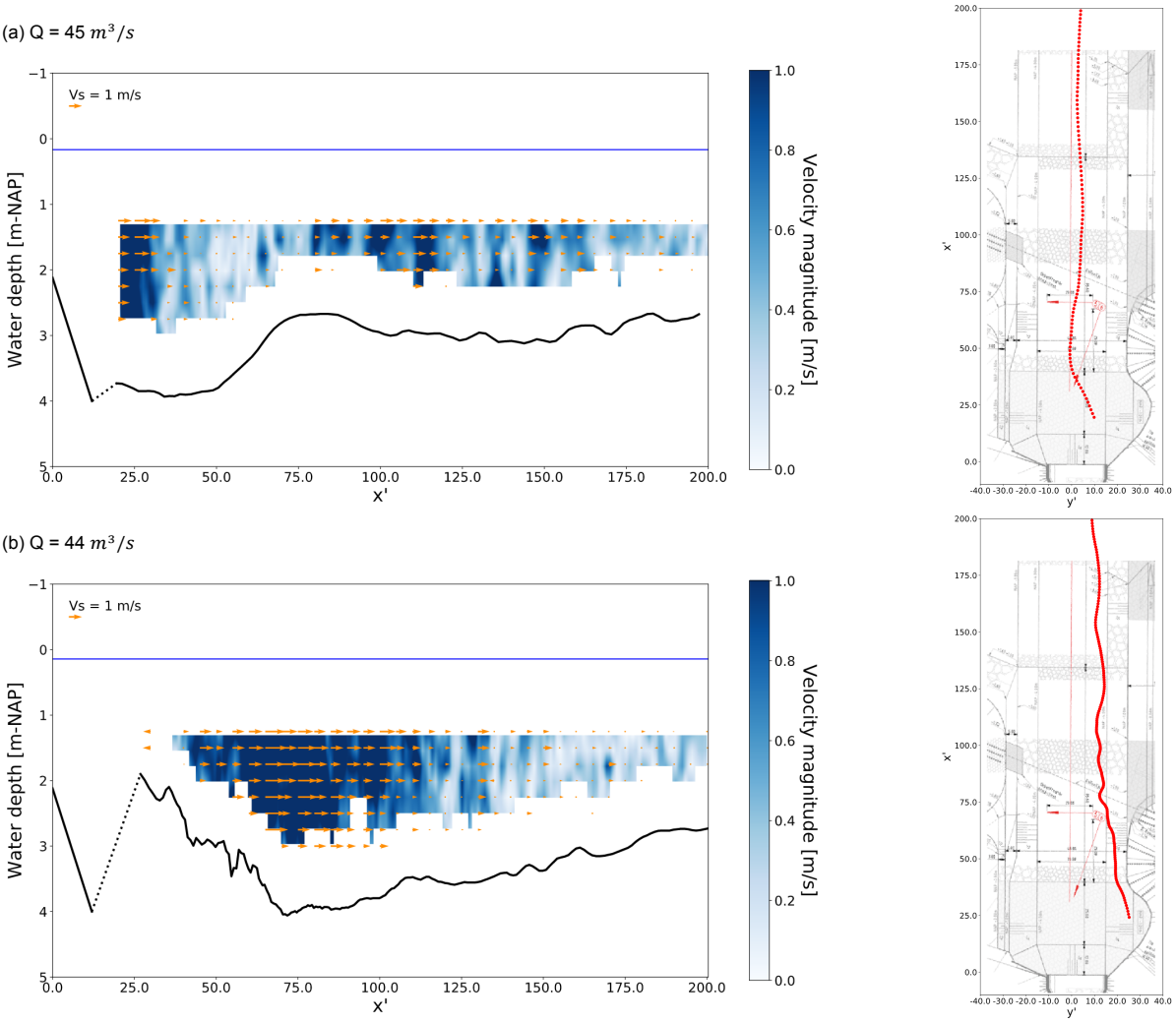

Figure A.37: Vertical velocity profile for 2 sailed transects during measurement scenario 5

B

Additional information for the model validation

This appendix serves to supply additional information regarding the model validation performed in chapter 4 in the main report. First, the chosen experiment of van Prooijen and Uijttewaal (2009) is explained in appendix B.1. Afterwards, the arguments for the choice of the model software FINEL is given in appendix B.2. Further information regarding the FINEL software is subsequently shown, with an in-depth explanation of the turbulence closure models in appendix B.3 and the definition of roughness in chapter B.4. Additional information regarding the 2DH simulation for the model validation is given in appendix B.5, whereas additional information regarding the 3D simulation for the model validation is given in appendix B.7.

B.1. Chosen experiment

This section highlights the reasoning behind the chosen experiment of van de Zande (2018) which was used for the model validation. In total 34 experiments were carried out by van de Zande (2018). Table B.1 shows the important variable parameters during the different experiments. An overview of the exact parameters for each experiment is given in van de Zande (2018).

Table B.1: Overview of the experimental variables.

Experimental variable	Symbol	Value
Downward slope	β	1:4 - 1:6
Length of bed protection	$L_{b,m}$	0 - 2 m
Width of contracting elements	D	0.5 - 1 m

B.1.1. Grid elements

The measurements containing the grid elements simulate the effect of grid turbulence near the ES-SSB. These elements disturb the incoming flow and induces wakes downstream. Coherent structures within these wakes develop further downstream, yet were shown to not amalgamate. Therefore the overall influence of the grid elements is limited. At Waterdunen two metal grates are placed at either end of the culvert to prevent debris from flowing into the culvert. Though some analogy with the grid elements holds, the dimensions of the individual bars within the grate are significantly smaller than the outflow water depth. Therefore, coherent structures generated by the grate are expected to have little effect on the outflow properties at Waterdunen, meaning the grid elements should not be included in the to-be-simulated laboratory experiment.

B.1.2. Expansion ratio

Graber (2006) has shown the importance of the expansion ratio on the stability of the symmetric flow configuration. For $Fr < 0.2$ it was shown the critical expansion ratio is approximately 1.5, the value of

which decreases with increasing Froude number. In van de Zande (2018) expansion ratios of 2 and 3 are considered. At Waterdunen the expansion ratio is approximated to vary between 2.5 and 3.5 depending on the downstream water level. To most closely resemble the field study at Waterdunen, it was chosen to simulate a laboratory experiment with an expansion ratio of 3.

B.1.3. Bed protection length

The distance between the sudden lateral expansion and the longitudinal slope is varied between experiments to simulate the effect of the bed protection. Considering figure 3.2 it can be seen the flow is subject to two subsequent lateral expansions: one directly at outflow with $ER \approx 1.8$ and one 12 m from the culvert with $ER \approx 3$. Though it can be said the geometry of the initial expansion together with the asymmetric outflow from the culvert will already force asymmetrical flow, the transverse movement of the jet is forced by the second expansion. The longitudinal slope is located directly at the start of the second expansion, around 12 m from the culvert. Therefore it was chosen to simulate the experiment without bed protection length.

B.1.4. Slope steepness

Broekema et al. (2020) has shown the slope steepness can affect the vertical flow structure in horizontal non-uniform flows. In the experiments of van de Zande (2018) the slope steepness varied from 1:6 to 1:4. At Waterdunen the slope steepness is 1:6. To most accurately represent Waterdunen, it was chosen to simulate an experiment with a slope of 1:6.

B.1.5. Conclusion

The above considerations lead to the simulation of experiment 2.4.1 in van de Zande (2018). The corresponding discharge is $Q = 30$ l/s with a downstream water level of $h = 16$ cm. The observed flow is asymmetric towards the east side of the flume and the flow was measured to remain attached to the bottom on the longitudinal slope.

B.2. Software package choice

For computational fluid dynamics a broad variety of numerical software packages are available. Each software package can differ based on the used assumptions and discretization methods. Furthermore, software must be chosen based on the availability of the software, experience of the user and available support. Therefore four different CFD software packages are discussed in this section.

B.2.1. Delft3D-FLOW

Delft3D-FLOW is the inhouse numerical model for hydrodynamics and morphodynamics of Deltares for both 2D and 3D computations. Considering the third dimension, the vertical grid is defined by either Z-layers or σ-layers. The model employs a finite volume scheme on regular grids to solve the Navier-Stokes equations under the shallow water and Boussinesq approximations. For 3D computations the vertical velocity components are derived from the continuity equation. Without going into detail regarding the discretization methods, it can already be said *a priori* that a regular grid will be difficult to employ on a complex geometry such as Waterdunen. Even though the other characteristics of Delft3D-FLOW are favourable for this research, an unstructured grid is required for an accurate representation of the system. Therefore, D-Flow Flexible Mesh might be an option, allowing for the use of an unstructured grid. The application of the flexible mesh came paired with difficulties regarding the advection discretization in the model. It was found that the advection scheme used in Delft3D can be very inaccurate for certain test cases (Houtekamer, 2017), combined with the finding that momentum is not conserved within the model (Deltares, 2020).

B.2.2. FINEL2D-Explicit

FINEL2D-Explicit is an inhouse model created by Svašek Hydraulics and was used for the initial design of the bed protection at Waterdunen. The model is a spin-off of the regular FINEL model which can only run in the 2DH mode. Therefore, many similarities with the regular FINEL model persist. The model employs the Discontinuous Galerkin method as a solution method for the depth-integrated Shallow Water Equations. One of the major approximations used in the model is the negligence of turbulent shear stresses, which makes usage of the model for turbulent jet flows doubtful.

B.2.3. TUDFlow3D

TUDFlow3D is a complex three-dimensional numerical model created in de Wit (2015). The model solves the non-hydrostatic variable density Navier Stokes equations and was originally designed to simulate the mixing of an overflow flume of a trailing suction hopper dredger. Only a 3D mode is available, where the system of flow equations is solved on an cylindrical coordinate system (r, ϕ, z). In the vertical direction the grid is required to be equidistant, while in the horizontal directions the grid distance is allowed to be variable. TUDFlow3D employs a finite volume solution method on rectangular grids which are allowed to locally refine in horizontal direction. One of the major advantages of TUDFlow3D is its complex yet efficient turbulence modelling. Due to the importance of the turbulence closure model in the simulation of the overflow flume, detailed LES computations can be simulated with three different sub-grid-scale models relatively efficiently. Additionally a mixing-length turbulence model is available. Another benefit of TUDFlow3D lies the available morphological module, which allows the effect of the jet flow on the bathymetry at Waterdunen to be investigated.

TUDFlow3D was used by Svašek Hydraulics to further understand the flow near Waterdunen after the measurement campaign. The scope of this thesis is to investigate what the minimum requirements for a numerical model are to properly reproduce jet flows. For that purpose, TUDFlow3D is already an extremely complex model using accurate LES turbulence modelling and solely computing in three dimensions. It can therefore already be stated that proper usage of TUDFlow3D will yield the most accurate results, while possible simplifications cannot be compared. From a practical point of view, a simpler model with the appropriate simplifications is preferred over a complex model due to the reduced computational costs. It is therefore valuable information to know which simplifications can safely be made in similar scenarios, which calls for a numerical model which allows for these simplifications. As TUDFlow3D does not meet the before-mentioned criterion, the model will not be further exploited during this thesis. The TUDFlow3D computations done by Svašek can/will be used as comparison with the FINEL model. Furthermore, TUDFlow3D can be employed if the morphodynamical feedback of the jet will be investigated.

B.2.4. FINEL

Contrary to FINEL2D-Explicit, the total FINEL software package allows for much more variability. FINEL is based on the work of Labeur (2009) where a combination of continuous and discontinous Galerkin is exploited to create an accurate yet fast finite element software package for the computation of flow and transport processes in rivers and coastal waters. Though the model is based on the work of Labeur (2009), Svašek Hydraulics is responsible for the model quality.

The total FINEL package can run in 1DV, 1DH, 2DV, 2DH and 3D mode, allowing for a lot of variability in the solving method. Furthermore, the horizontal grid as used in 2D computations can be extended using layers to create a 3D model. The discretization method for the advection terms is identical for both 2D and 3D computations, which means differences in the computed flow is the result of the added layers only, rather than numerical differences created by the usage of different discretization methods. This allows models of different complexities to be compared solely based on the additional complexity.

Regarding turbulence models FINEL differentiates between horizontal and vertical turbulence closure models. For the 2D modes it is obvious only the horizontal turbulence closure models are available, while for the 3D mode this means a lot of combinations between horizontal and vertical turbulence closure models are available. It should be noted that FINEL is less suitable for high resolution LES computations compared to a package such as TUDFlow3D due to the usage of the finite element methods. One of the major advantages of the finite element method lies in the flexibility of the grid to be unstructured, allowing the reconstruction of complex geometries to be available rather easily. This is an important aspect due to the observed asymmetric flow field, which is influenced by the inflow geometry.

Practially speaking, the FINEL model is a well-rounded model suitable for a broad variety of flows. The model is limited regarding high resolution LES and is unable to compute super-critical flows. For the purpose of this work, the latter serves as a restriction as the flow in Waterdunen has been shown to reach the super-critical flow regime during all measurement scenarios.

B.2.5. Conclusion

The purpose of this work is to assess which numerical properties a model should have to properly represent the hydraulic processes in jet flows over complex geometries. From the numerical models which have already been used to simulate Waterdunen, it can be concluded the FINEL2D-Explicit model does not perform well for Waterdunen. The TUDFlow3D model is more accurate and seems to capture the recirculating areas, asymmetric flow and flow magnitude in a satisfactory manner, except close to the lateral walls. A model employing the finite element method might improve the computation near solid walls due to the extra variability in grid resolution possible. Variation within numerical models is essential to determine which numerical properties are important for the respresentation of the flow. It is therefore chosen to employ the FINEL software package for the numerical models in this work, as it both uses the finite element method to accurately reproduce the geometry of the channel and it allows for plenty of variation within the model, both in the simulated dimensions within the model and the used assumptions within the model.

B.3. Turbulence closure models

The size of turbulent eddies fluctuates between the smallest Kolmogorov scale to the largest eddies in the order of half the water depth or channel width. If one were to fully solve the 3D Navier-Stokes equations, all the length scales would require to be solved, resulting in an extremely dense computational grid. This process, called Direct Numerical Simulation (DNS), is therefore computationally expensive and time-consuming. For practical applications the Navier-Stokes equations are often modified to remove parts of the turbulence, such as the smallest scales (Andersson et al., 2011). This modification often introduces new variables which need to be determined using a model. Such models are called turbulence closure models. Depending on the modification made to the Navier-Stokes equations, different turbulence closure models are required. Aside for DNS and Large Eddy Simulation (LES), most turbulent closure models depend on the Reynolds-Averaging process of the Navier-Stokes equations. Finel employs a series of turbulence models, which are further elaborated on in this section.

B.3.1. Large Eddy Simulation

Large Eddy Simulation (LES) is considered to be one of the more accurate turbulent closure models. Contrary to most other models, LES does not require any modification of the Navier-Stokes equations. As the primary difficulty in DNS arises from the computation of the small-scale turbulence, LES solely resolves the large-scale turbulent eddies, which contain a large portion of the turbulent kinetic energy. In essence, the velocity components are spatially integrated with a filter function which returns a zero value for eddies on a scale smaller than the filter function and keeps the eddies on a larger scale than the filter function (Andersson et al., 2011). The exact velocity component can then be written to be the summation of the resulting filtered flow velocity and the filtered-out flow velocity similarly to a Reynolds decomposition. However, the mean of the filtered component is often nonzero (Pope, 2001). Similar to resolving the RANS equations, the issue lies in the determination of the residual stress tensor. Resolving for this stress tensor requires a sub-grid stress model, which can essentially be evaluated in a similar fashion compared to RANS turbulent closure models, such as the determination of a sub-grid viscosity. The extra accuracy of LES is the result of the initial filtering, meaning the sub-grid viscosity has a substantial lower potential error compared to a regular turbulent viscosity approach as a large portion of the turbulent kinetic energy is simply resolved for in the approximation of the equations. The latter also induces the high computational effort required for LES. One of the major advantages of LES lies in the composition of the large-scale motion, allowing large-scale unsteadiness in the flows to be computed such as separation and vortex shedding (Pope, 2001).

A relatively simple way to resolve the residual stress tensor is by relating it to the filtered velocity component $\overline{U}$. In the method employed by Finel, the residual stress tensor is related to the filtered rate of strain tensor as defined in equation B.1. In the equation, ν_r is a coefficient of proportionality which is defined in equation B.2. In the equation, Δ is the filter width which depends on the used grid resolution and C_s is called the Smagorinsky coefficient (Pope, 2001).

This Smagorinsky model can also be employed as a mixing-length turbulence closure model. If the applied grid resolution is not sufficiently fine for a proper LES, the primary influence of turbulence within a Smagorinsky model lies in the calculated sub-grid scale turbulent viscosity, which is in definition simply a mixing-length model using the horizontal grid size.

$$\begin{aligned} \tau_{ij} &= -2\nu_r \overline{S}_{ij} \\ \overline{S}_{ij} &= \frac{1}{2}\left(\frac{\partial U_i}{\partial x_j} + \frac{\partial \overline{U}_j}{\partial x_i}\right) \end{aligned} \tag{B.1}$$

$$\begin{aligned} \nu_r &= (C_s\Delta)^2\overline{S} \\ \overline{S} &= (2\overline{S}_{ij}\overline{S}_{ij})^{1/2} \end{aligned} \tag{B.2}$$

B.3.2. Reynolds decomposed turbulence closure models

Aside from DNS and LES, most other turbulence closure models are based on the Reynolds decomposition of the Navier-Stokes equations. The Reynolds decomposition states the pressure and velocity components can be separated in a mean part and a fluctuating part. If the time-averaging period is long enough, the mean part indicates the mean flow properties and the fluctuating part the turbulent flow properties. Therefore the transformation from the Navier-Stokes equations to the RANS equations requires filling-in of the decomposed parameters and time-averaging over a certain period. The RANS equations are shown in equation B.3 (Andersson et al., 2011). U_i indicates the three velocity components (u,v,w) while x_j represents the three dimensions (x,y,z). For the definition of the other parameters the reader is referred to Andersson et al. (2011). The consequence of the Reynolds decomposition is shown in the usage of the time-averaged $\langle U_i \rangle$ compared to the total velocity component U_i, which is used in the regular Navier-Stokes equations. Additionally, a secondary term arises in the equation to address the fluctuating part of the velocity components, defined as $-\rho\langle u_i u_j \rangle$. The definition of this term, referred to as the Reynolds stress, is the baseline of the turbulence closure models described in this section. Note that u_i and u_j have 3 dimensions each, making the total Reynolds stress τ_{ij} a 3x3 stress tensor with 6 unique entries due to symmetry.'It is the determination of these stresses which lie at the basis of most turbulence closure models (Andersson et al., 2011).

$$\frac{\partial\langle U_i\rangle}{\partial t} + \langle U_i\rangle\frac{\partial\langle U_i\rangle}{\partial x_j} = -\frac{1}{\rho}\frac{\partial}{\partial x_j}\left(\langle P\rangle\delta_{ij} + \mu\left(\frac{\partial\langle U_i\rangle}{\partial x_j} + \frac{\partial\langle U_i\rangle}{\partial x_j}\right) - \rho\langle u_i u_j\rangle\right) \tag{B.3}$$

B.3.2.1 Turbulent eddy viscosity

The Boussinesq approximation simplifies the determination of the Reynolds stresses by assuming the Reynolds stress is proportional to the mean velocity gradients. It states that transport of momentum via turbulence is analogous to transport of momentum via viscosity, promoting the usage of a turbulent viscosity to prescribe the Reynolds stresses. The Boussinesq approximation implies the flow is isotropic and in equilibrium, essentially limiting its use to such flows. In some cases however, the turbulent eddy viscosity can be calibrated using measurement data to find a fitting value, yet the physical basis of this method is doubtful. Following the analogy to kinematic viscosity, the turbulent viscosity is proportional to a velocity and length scale with the appropriate unit being $\nu_t = [m^2/s]$. Determination of the turbulent viscosity can be done using a variety of equations, ranging from a direct computation of ν_t to a two-equation system that determines the velocity and length scale used to compute ν_t, though the turbulent kinetic energy is often used as a proxy for the velocity scale.

The first and easiest turbulence closure model employed in Finel describes the turbulent eddy viscosity directly as a constant throughout the computation. The value for ν_t is then defined by the user and will not be re-iterated throughout the computation. This turbulence model is named the Constant Eddy Viscosity model.

B.3.2.2 k-ϵ model

For engineering purposes, the k-ϵ is widely used as it is a proper compromise between accuracy and computational costs and therefore also a possibility within Finel. Within the k-ϵ model, two transport

equations are defined for both the transport of turbulent kinetic energy k and the transport of the energy dissipation rate ϵ. The transport for turbulent kinetic energy is shown in equation B.4.

$$\underbrace{\frac{\partial k}{\partial t}}_{(1)} + \underbrace{\langle U_j \rangle \frac{\partial k}{\partial x_j}}_{(2)} = \underbrace{-\langle u_i u_j \rangle \frac{\partial \langle U_i \rangle}{\partial x_j}}_{(3)} - \underbrace{\nu \left\langle \frac{\partial u_i}{\partial x_j} \frac{\partial u_i}{\partial x_j} \right\rangle}_{(4)} + \frac{\partial}{\partial x_j} \left(\underbrace{\nu \frac{\partial k}{\partial x_j}}_{(5)} - \underbrace{\frac{\langle u_i u_i u_j \rangle}{2}}_{(6)} - \underbrace{\frac{\langle u_j p \rangle}{\rho}}_{(7)} \right) \tag{B.4}$$

In equation B.4, terms (3), (4), (6) and (7) are unknown and require closure. Term (3) can be approximated using the Boussinesq approximation, describing $\langle u_i u_j \rangle$ in terms of the turbulent viscosity and mean flow properties. Term (4) can be solved once the energy dissipation rate ϵ is determined in the other transport equation. Terms (6) and (7) describe the turbulent transport of k. These two terms can be approximated if gradient-diffusion transport mechanism is assumed, which essentially means the turbulent kinetic energy diffuses from high concentrations to low concentrations. By that means, terms (6) and (7) can be combined and written as the multiplication between the concentration gradient of k, the turbulent viscosity and a coefficient called the Prandtl-Schmidt number denoted by σ_k. The modelled transport equation for turbulent kinetic energy is shown in equation B.5. This equation can be solved for known ϵ and ν_t.

$$\frac{\partial k}{\partial t} + \langle U_j \rangle \frac{\partial k}{\partial x_j} = \nu_t \left[\left(\frac{\partial \langle U_i \rangle}{\partial x_j} + \frac{\langle U_j \rangle}{\partial x_i} \right) \frac{\partial \langle U_i \rangle}{\partial x_j} \right] - \epsilon + \frac{\partial}{\partial x_j} \left[\left(\nu + \frac{\nu_t}{\sigma_k} \right) \frac{\partial k}{\partial x_j} \right] \tag{B.5}$$

The transport equation for the energy dissipation rate ϵ is given in equation B.6.

$$\begin{aligned} &\underbrace{\frac{\partial \epsilon}{\partial t}}_{(1)} + \underbrace{\langle U_j \rangle \frac{\partial \epsilon}{\partial x_j}}_{(2)} \\ &\quad = \underbrace{-2\nu \left(\left\langle \frac{\partial u_i}{\partial x_k} \frac{\partial u_j}{\partial x_k} \right\rangle + \left\langle \frac{\partial u_k}{\partial x_i} \frac{\partial u_k}{\partial x_j} \right\rangle \right) \frac{\partial \langle U_i \rangle}{\partial x_j}}_{(3)} - \underbrace{2\nu \left\langle u_k \frac{\partial u_i}{\partial x_j} \right\rangle \frac{\partial^2 \langle U_i \rangle}{\partial x_k \partial x_j}}_{(4)} \\ &\quad - \underbrace{2\nu \left\langle \frac{\partial u_i}{\partial x_k} \frac{\partial u_i}{\partial x_j} \frac{\partial u_k}{\partial x_j} \right\rangle}_{(5)} - \underbrace{2\nu\nu \left\langle \frac{\partial^2 u_i}{\partial x_k \partial x_j} \frac{\partial^2 u_i}{\partial x_k \partial x_j} \right\rangle}_{(6)} \\ &\quad + \frac{\partial}{\partial x_j} \left(\underbrace{\nu \frac{\partial \epsilon}{\partial x_j}}_{(7)} - \underbrace{\nu \left\langle u_j \frac{\partial u_i}{\partial x_j} \frac{\partial u_i}{\partial x_j} \right\rangle}_{(8)} - \underbrace{2 \frac{\nu}{\rho} \left\langle \frac{\partial p}{\partial x_j} \frac{\partial u_j}{\partial x_j} \right\rangle}_{(9)} \right) \end{aligned} \tag{B.6}$$

In equation B.6, terms (3), (4), (5), (6), (7) and (9) are unknown and need to be approximated. Therefore, the general equation is often simplified to equation B.7. The reader is referred to Andersson et al. (2011) for the physical interpretation of the equation. Note that equation B.7 can be solved for known constants $C_{\epsilon 1}$, $C_{\epsilon 2}$ and σ_ϵ combined with a formulation for ν_t.

$$\underbrace{\frac{\partial \epsilon}{\partial t}}_{(1)} + \underbrace{\langle U_j \rangle \frac{\partial \epsilon}{\partial x_j}}_{(2)} = \underbrace{C_{\epsilon 1} \nu_t \frac{\epsilon}{k} \left[\left(\frac{\partial \langle U_i \rangle}{\partial x_j} + \frac{\partial \langle U_j \rangle}{\partial x_i} \right) \frac{\partial \langle U_i \rangle}{\partial x_j} \right]}_{(3)} - \underbrace{C_{\epsilon 2} \frac{\epsilon^2}{k}}_{(4)} + \underbrace{\frac{\partial}{\partial x_j} \left[\left(\nu + \frac{\nu_t}{\sigma_\epsilon} \right) \frac{\partial \epsilon}{\partial x_j} \right]}_{(5)} \tag{B.7}$$

As the turbulent viscosity is explained to be a function of a length scale and a velocity scale, $\nu_t \propto k^2 \epsilon^{-1}$ as $\epsilon \propto k^{3/2} l^{-1}$ and $k \propto u^2$. This relation is often prescribed with a constant C_ν, with the complete formulation shown in equation B.8. The system of equations B.5, B.7 and B.8 contain the three unknowns k, ϵ and ν_t and is therefore a solvable system. It should be noted that the turbulent viscosity is not bounded for every value of ϵ or k. Therefore, within Finel the turbulent viscosity is bounded to a maximum with the turning point at $k^{3/2} = \epsilon l_{max}$. This system is shown in equation B.9. l_{max} is a maximum turbulent length scale, which is set as the water depth in Finel.

$$\nu_t = c_\nu \frac{k^2}{\epsilon} \tag{B.8}$$

$$\nu_t = \begin{cases} c_\nu \frac{k^2}{\epsilon} & \text{if } k^{3/2} < \epsilon l_{max} \\ \max\left(\nu, l_{max} k^{1/2}\right) & \text{if } k^{3/2} \geq \epsilon l_{max} \end{cases} \tag{B.9}$$

B.4. Roughness in FINEL

B.4.1. Bed roughness

In two-dimensional simulations bed roughness is simplified to a single roughness parameter. Within FINEL four different prescriptions are available, though internally they are all rewritten to the Nikuradse roughness height k_s. The reasoning behind this is the fact that the Nikuradse roughness height is a property of the bottom, whereas parameters such as the hydraulic roughness c_f or the Chezy coefficient C are always related to the flow. Within two-dimensional simulations the specified roughness can be coupled to the resolved depth-averaged flow velocity to recreate the bed shear stress using a simple quadratic law.

In three-dimensional simulations the near-wall treatment is more complicated due to the rapid velocity decay in the region. Besides the required vertical mesh resolution to fully capture the velocity gradient, the $k-\epsilon$ model tends to become inaccurate in the viscosity dominated wall region. To bypass this problem, FINEL forces the standard logarithmic velocity profile for uniform flow within the initial grid cell. This velocity profile is obtained by assuming uniform flow along a wall and applying Bakhmetev's definition of the mixing length. The definition is shown in equation B.10. FINEL always assumes solid walls to be hydraulically rough, meaning the roughness length z_0 can be described in terms of the Nikuradse roughness length only.

$$u(z) = \frac{u_*}{\kappa} \ln\left(\frac{z+H}{z_0}\right) \tag{B.10}$$

Where: u_* = Friction velocity [m/s]
κ = Von Kármánn constant (0.4)
z = Position in water column [m]
z_0 = Roughness length [m] = $k_s/30$
H = Water depth [m]

Compared to the quadratic relation for the bed shear stress as used in two-dimensional simulations, three-dimensional simulations allow the user to define the bed shear stress in terms of the actual velocity close to the bed. However, this shifts the problem to the determination of this velocity. The logarithmic velocity profile does not hold in the viscous sub-layer and the buffer layer. One can readily see that for $\lim_{z\to H} u(z) = -\infty$ when considering equation B.10. Furthermore, FINEL employs a co-located grid, meaning velocities are defined at the cell corners. Therefore the velocity closest to the bed is the velocity at the bottom of the final grid cell, which should be 0 due to the no-slip condition.

Both issues are resolved simultaneously by creating a fictional bed velocity $u_b > 0$ to resolve for the bed shear stress and serve as an estimate for the flow velocity close to the bed. First, the velocity near the bed u_b is expressed in terms of the friction velocity u_* in equation B.11. Note the hydraulic roughness is specified in the equation. This term will later be expressed in terms of the Nikuradse roughness height.

$$u_b = \frac{u_*}{\sqrt{c_{f,3D}}} \tag{B.11}$$

It is assumed that the flow velocity in the first grid cell above the bottom u_1 is well described by the logarithmic velocity profile. With the logarithmic formulation of u_1 and equation B.11 for u_b, one can discretize the flow velocity gradient over the vertical as shown in equation B.12.

$$\frac{\partial u}{\partial z} = \frac{u_1 - u_b}{\Delta z_b} = \frac{u_*}{\Delta z_b}\left(\frac{1}{\kappa}\ln\frac{\Delta z_b}{z_0} - \frac{1}{\sqrt{c_{f3D}}}\right) \tag{B.12}$$

Using the mixing length model of Bakhmetev, one can prescribe the turbulent eddy viscosity in the first grid cell from the bottom as in equation B.13. As the shear stress is defined as the product between ν_t and the vertical velocity gradient, one can formulate an equation for the shear stress at the bottom τ_b by multiplying equation B.13 and B.12, which should also hold for equation B.14.

$$\nu_t = l_m^2 \left| \frac{\partial u}{\partial z} \right| \approx \kappa^2 \left(\frac{1}{2} \Delta z_b \right)^2 \left(\frac{u_1 - u_b}{\Delta z_b} \right) \tag{B.13}$$

$$\tau_{x,z} = \nu_t \frac{\partial u}{\partial z} \tag{B.14}$$

Using the above manipulations and expressing u_b in terms of equation B.11 in equation B.14, one can eliminate the friction velocity u_* to formulate u_b as in equation B.15.

$$u_b = \frac{u_*}{\sqrt{C_{f3D}}} = \frac{u_*}{\kappa} \ln \left(e^{-2} \frac{\Delta z_b}{z_0} \right) \tag{B.15}$$

The resulting hydraulic roughness on the wall is therefore defined in equation B.16.

$$c_{f,3D} = \left(\frac{1}{\kappa} \ln \frac{\Delta z}{k_s/30} - \frac{2}{\kappa} \right)^{-2} \tag{B.16}$$

From equation B.16 one can see the actual hydraulic roughness of the wall within the simulation is dependent on both the user-defined roughness height and the vertical grid size of the first grid cell. The definition of the two-dimensional hydraulic roughness is similar to the three-dimensional hydraulic roughness. Rather than construction the bed shear stress from the bottom velocity, the bed shear stress is computed using the depth-averaged flow velocity, which is assumed to neatly comply with the logarithmic velocity profile. Equation B.17 shows the resulting expression for $c_{f,2D}$.

$$c_{f,2D} = \left(\frac{1}{\kappa} \ln \frac{H}{k_s/30} - \frac{1}{\kappa} \right)^{-2} \tag{B.17}$$

B.4.2. Lateral wall roughness

The treatment for lateral walls within FINEL differs largely between 2DH and 3D simulations. In 3D simulations the friction along every closed wall is simulated similar to the bed friction, as described in appendix B.4. Therefore the simulated wall roughness is not only dependent on the user-specified roughness height, but also on the lateral grid length Δy next to the solid wall. The modelled equation is shown in equation B.18. The restriction on the horizontal grid resolution next to the solid wall is therefore similar to the rectriction of the vertical resolution next to the bottom, stating $\Delta y_{w,max} = 0.001$ m.

$$c_{wall,3D} = \left(\frac{1}{\kappa} \ln \frac{\Delta y}{k_s/30} - \frac{2}{\kappa} \right)^{-2} \tag{B.18}$$

Regarding 2DH simulations the lateral walls are modelled as close boundaries with a free-slip condition. This translates to the negligence of wall friction along lateral walls.

B.5. Preliminary 2DH simulations

An initial model was set-up based on a priori estimates of the required numerics to properly reproduce the experiment of van de Zande (2018). Nevertheless, the sensitivity of the model to certain assumptions and esimations needs to be assessed. For this reason, the 2DH model was optimized by altering a variety of parameters and investigating the effect on the model results. This process has been highlighted in this appendix.

B.5.1. Reference model

A reference model was set-up based on a first-guess of the model requirements. The model settings are shown in table B.2. The domain of interest (DOI) within the numerical model was set to be equal to the available PIV measurements of van de Zande (2018), ranging between $6.16 < x < 10.96$. Nevertheless, the entire 19.2 m for the flume have been simulated. The horizontal grid resolution varied between $\Delta x = \Delta y = 0.1$ m outside of the DOI and $\Delta x = \Delta y = 0.045$ m inside the DOI. It was verified the local coarsening outside of the DOI had little effect on the accuracy of the model. The inflow boundary condition was set to be a constant discharge $Q = 0.03$ l/s, complying with the experimental setting in van de Zande (2018). The downstream boundary condition was a constant water level $h = 0.16$ m.

Table B.2: Initial model settings for the simulations of experiment 2.4.1 of van de Zande (2018) .

Run	Δx **[m]**	Δy **[m]**	Δt **[s]**	k_s **[m]**	**limiter**	θ	C_s	**Bound**
REF	0.045 - 0.1	0.045 - 0.1	0.11	0.001	adaptive	1	0.1	h

Figure B.1 shows the distribution of the absolute velocity magnitude and the streamlines for the reference model. Figure B.2 shows the laateral velocity profiles compared to the surface and depth-averaged ADV measurements and the PIV measurements for $x = 8.70$ m and $x = 9.04$ m. Note that both the depth-averaged and the surface ADV measurements are likely an underestimation of the actual depth-averaged and surface velocities as the primary focus of the ADV measurement lied at the bottom measurements. This can be observed in figure 2.14. Furthermore, the surface velocity measurements were taken at a depth of $z = 0.026$ m from the surface. From the simple overview of figure B.1 it can already be seen the curvature of the stream towards the eastern slope is significantly more steep compared to the PIV measurements in figure 2.13. This causes the non-dominant recirculation zone to contain relatively high recirculating velocities, which are not observed in the experiment. Furthermore, though the model correctly shows a contraction of the jet over the longitudinal slope, the contraction seems to stop directly at the end of the slope, while during the experiment the contraction was observed to persist more gradually further downstream. The additional 'noise' which seems to be present along either side of the jet is hypothesised to be the result of the usage of the adaptive flux limiter.

Considering the standard logarithmic velocity profile one would expect the 2DH model results to have a lower velocity magnitude compared to the surface velocities as measured in the experiment. Nevertheless, the lateral distribution of streamwise velocity should be similar, which is not the case as is evident from figure B.2. In both figure B.2a and B.2b it can be observed the simulated velocity profile is more block-shaped, whereas the PIV profile is more parabolic. This is likely the result of the lack of wall friction in FINEL, which means the velocity in the initial 8.8 m of the flume is block-shaped without velocity gradients at each confining wall. Another possible consequence of the lack of wall friction is the lack of corner eddies in the model results. It was shown in Dewals et al. (2008) that the wall friction is pivotal for the reproduction of these corner eddies as observed in both upstream corners in figure 2.13.
Considering the full length of the expanded flume as in figure B.3, it can be seen the jet remains attached to the eastern wall of the flume and remains that way when propagating through the downstream boundary condition. In reality a spillway was present at the downstream end of the flume to maintain the constant water level. This spillway is more reflective compared to a simple water level boundary and was hypothesized to create a more recirculating pattern in the flume where the jet stream moves more towards the middle. Therefore, a Riemann boundary at the downstream end of the numerical domain might be more accurate.

B.5.2. Flux limiter and downstream boundary condition

Simulating without a flux limiter would be preferred over the used flux limiter in the reference simulation due to the fist-order accuracy and the additional numerical dissipation of the used flux limiter. However, it turned out the second order flux limiter became unstable around the downstream boundary condition. Due to the short distance between the downstream boundary condition and the DOI, these instabilities advanced into the DOI and yielded inaccurate results. It was therefore chosen to induce a more reflective Riemann boundary condition downstream of the flume. The Riemann boundary condi-

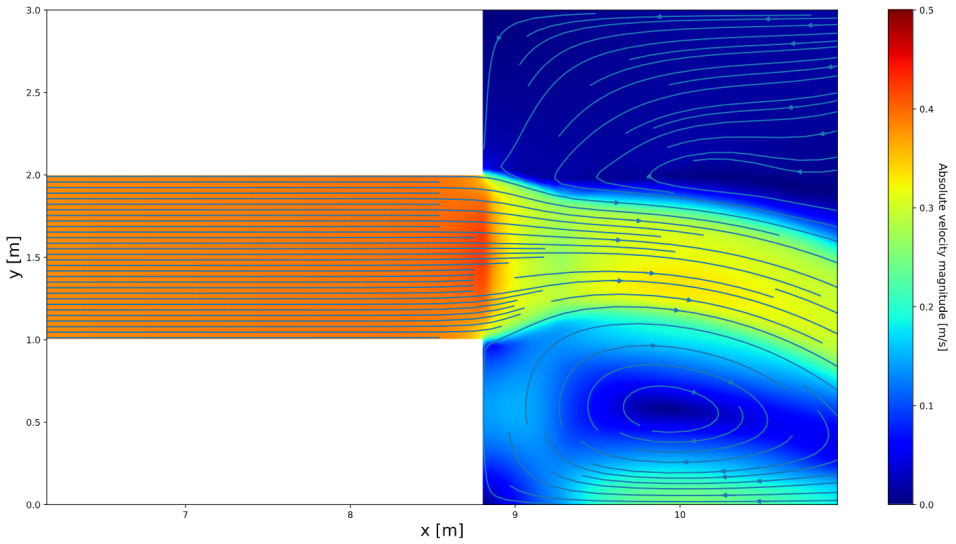

Figure B.1: Reference simulation of experiment 2.4.1 in van de Zande (2018) - absolute velocity magnitude and streamlines. The image shows the simulated flume from $x = 6.16$ m and $x = 10.96$ m similar to the PIV measurements.

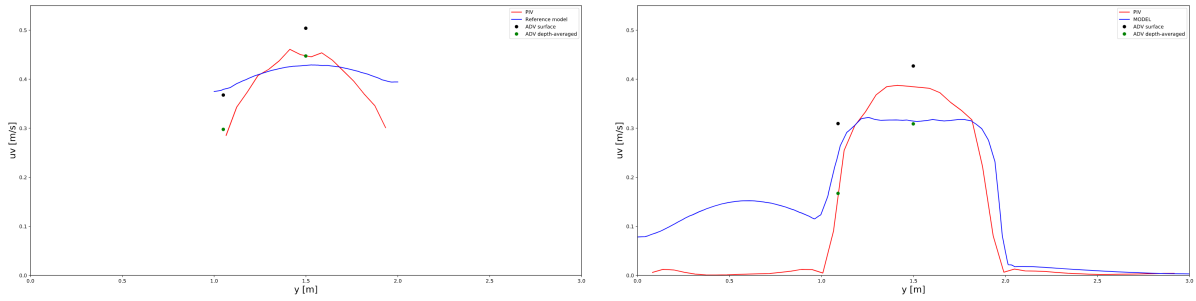

(a) x = 8.70 m.

(b) x = 9.04 m.

Figure B.2: Lateral velocity profiles for the reference simulation at $x = 8.70$ m and $x = 9.04$ m compared to the surface and depth-averaged ADV measurements and the PIV measurement of van de Zande (2018).

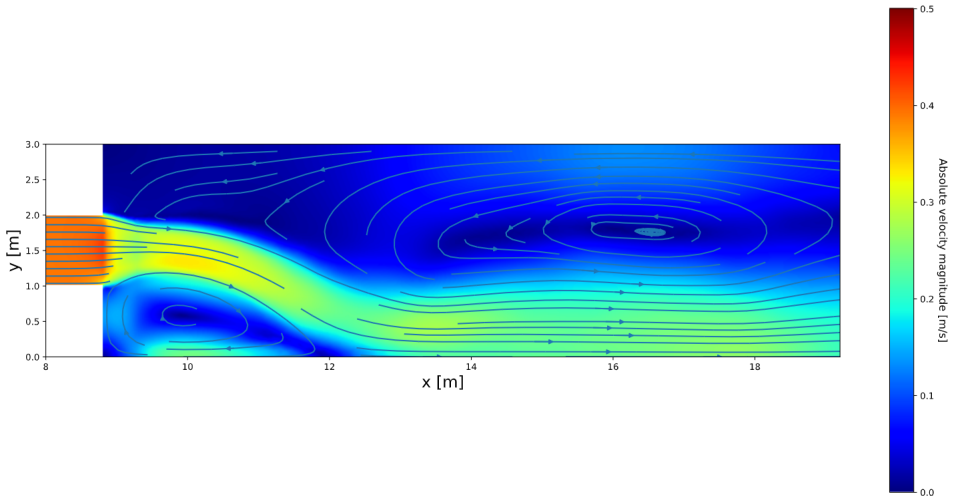

Figure B.3: Reference simulation of experiment 2.4.1 in van de Zande (2018) - absolute velocity magnitude and streamlines. The image shows the simulated flume from $x = 6.16$ m and $x = 19.2$ m to show the full length of the expanded flume.

tion was also hypothesized to better represent the spillway which was present in the experiments. The specified velocity for the Riemann invariant was set to be the estimate of the mean velocity through

the downstream cross-section, being $u = Q/(B * h) = 0.03/(3 * 0.16) = 0.0625$ m/s. The water level constraint was kept at $h = 0.16$ m.

Figure B.4 shows the full length of the expanded flume with both the different flux limiter and the Riemann boundary condition. It can be seen the movement of the jet is far more realistic compared to figure B.3. Furthermore, the transition between the jet and the recirculation zone is modelled far more accurately. Finally, it can be seen the velocity in the jet is higher due to the lower amount of numerical dissipation added to the system. Nevertheless, some unfavourable properties arise as well. The recirculating velocities increase in the non-dominant recirculating area, as well as in the dominant recirculating area. This can be seen in figure B.5, which shows the lateral velocity profile similar to figure B.2. Furthermore, it can be observed some wiggles appear around the transition between recirculating flow and jet flow. This was expected as no flux limiter was employed. As long as these wiggles do grow into instabilities, they will not impose problems. It was concluded that no flux limiter is the preferred option as long as the simulation remains stable.

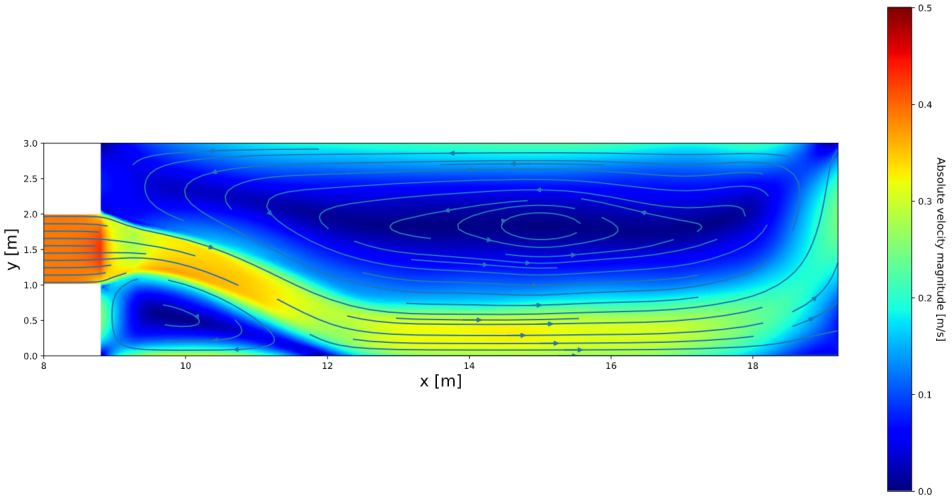

Figure B.4: Simulation with Riemann boundary and no flux limiter for experiment 2.4.1 in van de Zande (2018) - absolute velocity magnitude and streamlines. The image shows the simulated flume from $x = 6.16$ m and $x = 19.2$ m to show the full length of the expanded flume.

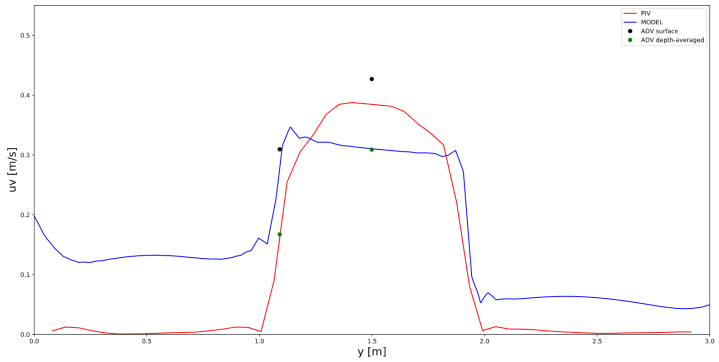

Figure B.5: Lateral velocity profiles for the simulation with the Riemann boundary and no flux limiter at $x = 9.04$ m compared to the surface and depth-averaged ADV measurements and the PIV measurement of van de Zande (2018).

B.5.3. Wall friction

It was hypothesized the negligence of wall friction in FINEL2D caused inaccuracies in the representation of the recirculating areas, the curvature of the jet stream and the upstream flow profile. Therefore, it was chosen to simulate wall friction by artificially heightening the bed friction in the grid cells adjacent to the confining walls. To ensure compatibility with a three-dimensional model, the additional roughness

was calculated as follows. In appendix B.4 it was explained the hydraulic roughness as calculated in a three-dimensional model in FINEL is calculated based on the user specified Nikuradse roughness and the vertical grid resolution as stated in equation B.16. Furthermore, it was explained in section 4.1 that the wall roughness is parameterized identical to the bed roughness but with the horizontal grid resolution rather than the vertical grid resolution. The corresponding equation is shown in equation B.19.

$$c_{wall,3D} = \left(\frac{1}{\kappa} \ln \frac{\Delta y}{k_s/30} - \frac{2}{\kappa} \right)^{-2} \tag{B.19}$$

Considering an identical horizontal grid resolution of $\Delta y = 0.045$ m inside the DOI, an equal Nikuradse roughness of $k_s = 0.001$ m and an equal Von Kármán constant of $\kappa = 0.4$, one finds the three-dimensional wall roughness equals $c_{wall,3D} = 0.0059$. At the bottom boundary the bed friction parameter extracts energy from the depth-averaged flow velocity in 2DH models, whereas it extracts energy from the velocity near the bed in 3D models. Therefore, a discontinuity must exist between the bed friction parameter in 2DH models and in 3D models with equal conditions to ensure the influence of bed friction is equal. For the wall friction parameter this is not the case as the same horizontal grid will be employed. Therefore the wall friction parameter must be equal for both a 2DH and a 3D model. This means the bed roughness must also be specified for each node. Using equation B.17, it was calculated $c_{f,2D} = 0.0038$ at $H = 0.08$ m and $c_{f,2D} = 0.0029$ at $H = 0.16$ m. The input roughness profile is shown in figure B.6.

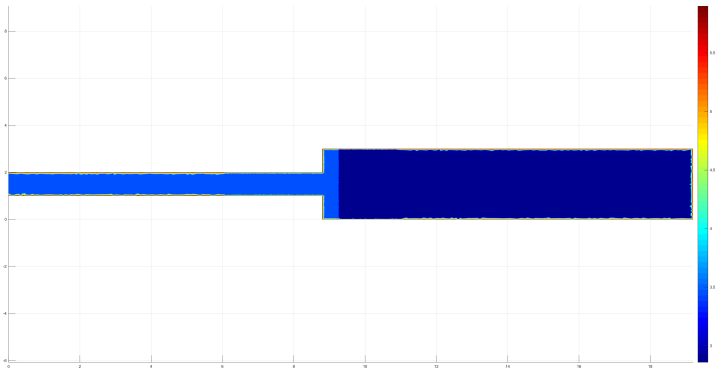

Figure B.6: Input of the roughness parameter $c_{f,2D}$ in the two-dimensional model. The discontinuities visible are the result of interpolation from the grid nodes to the grid elements. As the grid is coarser outside of the DOI, the roughness parameter will vary more over width.

B.5.4. Time-stepping

The fully implicit mode of the theta-method had been chosen for time-stepping through the simulation. As stated before, a horizontal Smagorinsky model is used in the simulations. This turbulence closure models allows for a LES-type simulation if the grid resolution is fine enough. For this purpose, θ introduces significant diffusion of the time-dependent turbulent fluctuations as resolved by the Smagorinsky LES. It was therefore chosen to analyse the effect of different values for θ. $\theta = 0.5$ implies the second-order accurate Crank-Nicolson scheme is used, which does not introduce any form of numerical dissipation into the system (Zijlema, 2015). To maintain stability, at least a small amount of numerical dissipation is desired to dissipate unstable modes. If $\theta < 0.5$ the explicit part dominates the implicit part, which is not supported by FINEL. A practical limitation lies at $\theta \geq 0.55$, with the value of $\theta = 0.55$ introducing the minimal amount of diffusion in time.

The ADV measurements were carried out a frequency of $f = 25Hz$. To match this resolution while maintaining a low simulation time, the output frequency for FINEL was set at $f = 8.3Hz$, matching the value of $\Delta t = 0.12$ s. In this way, the model output can be compared to every third ADV measurement. For both $\theta = 0.55$ and $\theta = 1$, the velocity fluctuations at the locations of the ADV measurements are compared to the fluctuations of the depth-averaged ADV measurements in figure B.9. From figure B.9 it is evident the simulated scale of the velocity fluctuations is significantly lower compared to the velocity

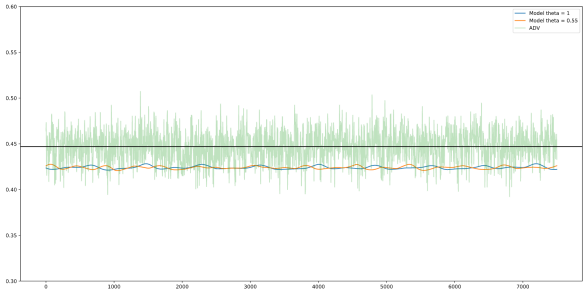

Figure B.7: x = 8.70 m

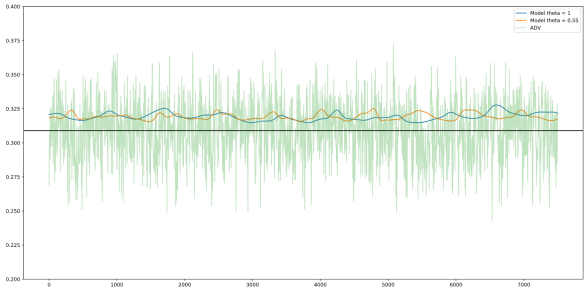

Figure B.8: x = 9.04 m

Figure B.9: Comparison between steamwise velocity fluctuations as simulated by the 2D model using $\theta = 0.55$ and $\theta = 1$ compared to the depth-averaged velocity fluctuations of the ADV measurements

fluctuations measured. Three factors are hypothesized to cause this discontinuity.

The first factor would be too much numerical dissipation added by the model. However, θ is the primary contributor to the additional dissipation.

The second factor would be the grid resolution. If the grid resolution is too low, the turbulence cannot be solved accurately by the Smagorinsky LES. Pope (2001) states that in order to adequately resolve isotropic turbulence, one requires the $k_{max}\eta > 1.5$, with $k_{max} = \pi/\Delta_{max}$ [1/m] being the maximum wave length resolved by the largest grid cell Δ_{max} and $\eta = Re^{-3/4} \cdot L$ [m] being the Kolmogorov scale (Uijttewaal, 2018). With the horizontal Reynolds number being of $2 \cdot 10^5$ considering a velocity difference of $U = 0.4$ m/s and length scale $L = 0.5$ m, one finds $\eta = 5 \cdot 10^{-5}$ followed by $k_{max} = 3 \cdot 10^4$ and $\Delta_{max} = 1 \cdot 10^{-4}$. Therefore the grid size must be approximately 450 times smaller compared to the current situation. To preserve computational effort, the required grid resolution is too high and cannot be complied.

The final factor which might influence the resolved turbulence lies in the coarser upstream grid. With Taylor's frozen turbulence hypothesis, it can be concluded the velocity profile as found in the coarse grid convects into the high-resolution grid. The turbulence of a length scale in between both grid sizes will start being resolved at the beginning of the finer grid. It might be possible the spin-up length required for this turbulence to be accurately resolved is longer than the current distance of approximately 2 meters. Therefore, two additional runs were carried out to test the influence of the coarse upstream grid on the resolved turbulence. Nevertheless, no significant differences were observed compared to the runs without the high resolution upstream grid. It can therefore be concluded the the resolved turbulence will not be accurate on instantaneous scale. Therefore the additional dissipation introduced by a value of $\theta = 1$ has little effect on the resolved turbulence and will be used to ensure stability.

B.6. Flux limiters

Flux limiters exist in numerical models to ensure monotonicity of the advection terms near steep gradients (Zijlema, 2015). The flux limiters employed in FINEL are explained in Kuzmin (2012). Without going into detail, three different options are available for the flux limiter. The first option employs a first-order upwinding approximation which is very stable but infuses a significant amount of artificial diffusion. The second option employs no flux limiter at all. This option ensures the second-order accuracy of the FEM discretization used, yet can locally produce wiggles around steep gradients. Therefore this option is less stable, especially for high-resolution numerical grids. The third option is an adaptive method which initially employs the first-order upwind method and locally disables the flux limiter where the solution is sufficiently smooth. Contrary to the iterative way as prescribed by Kuzmin (2012), within FINEL only one iteration is performed.

B.7. Preliminary 3D simulations

Though most of the model setting will be identical to the 2DH model, a sensitivity analysis is required to ensure the vertical discretization is done properly. Appendix B.4 explained the modelled roughness in FINEL is highly dependent on the vertical grid resolution close to the bottom. Furthermore, it needs to be investigated how many layers are required to accurately model the system.

B.7.1. Reference model

A reference model is set-up to state a base-line accuracy of the model. The reference model properties are highlighted in table B.3. A constant value of $\Delta z = 0.02$ m was taken, creating 4 layers in the upstream section of the flume and 8 layers in the downstream section of the flume. The streamlines and distribution of streamwise velocity are shown in figure B.10, the lateral velocity profiles in figure B.11 and the vertical velocity profiles in figure B.12.

Table B.3: Reference three-dimensional model for the simulation of experiment 2.4.1 of van de Zande (2018).

Run	Δz_0 **[m]**	Δz **[m]**	**# layers**	k_s **[m]**	**lim u**	θ	C_s	**Bound**
Final	0.02	0.02	4-8	0.001	1	1	0.1	Riemann

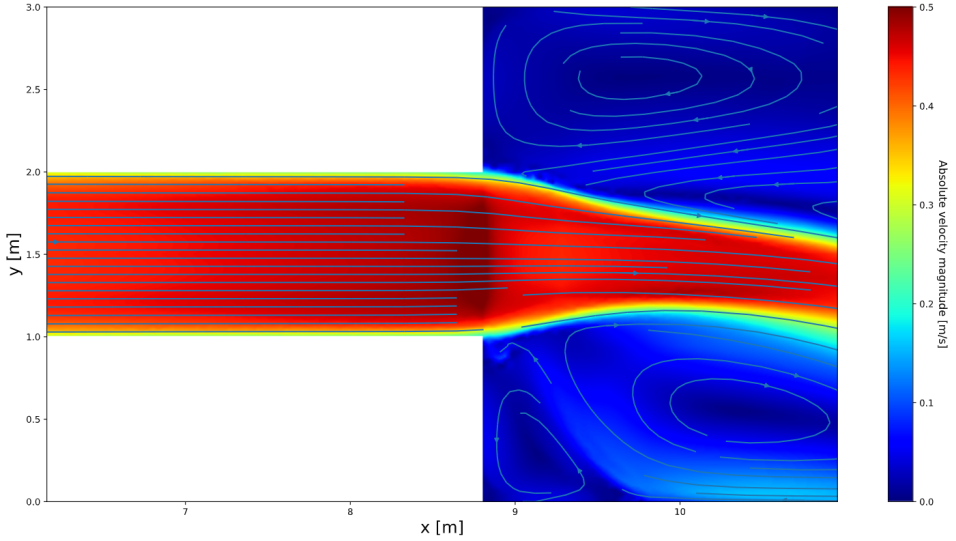

Figure B.10: 3D reference simulation of experiment 2.4.1 in van de Zande (2018) - absolute velocity magnitude and streamlines. The image shows the simulated flume from $x = 6.16$ m and $x = 10.96$ m similar to the PIV measurements.

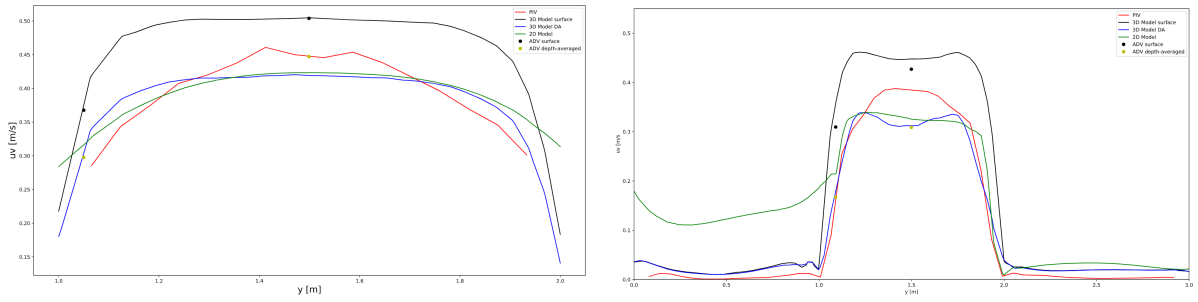

(a) x = 8.70 m.

(b) x = 9.04 m.

Figure B.11: Lateral velocity profiles for the 3D reference simulation at $x = 8.70$ m and $x = 9.04$ m compared to the surface and depth-averaged ADV measurements and the PIV measurement of van de Zande (2018).

Figure B.10 shows the curvature of the stream is already modelled significantly better compared to the 2DH simulation in figure B.1. Furthermore, the lateral velocity profiles found in figure B.11 show the

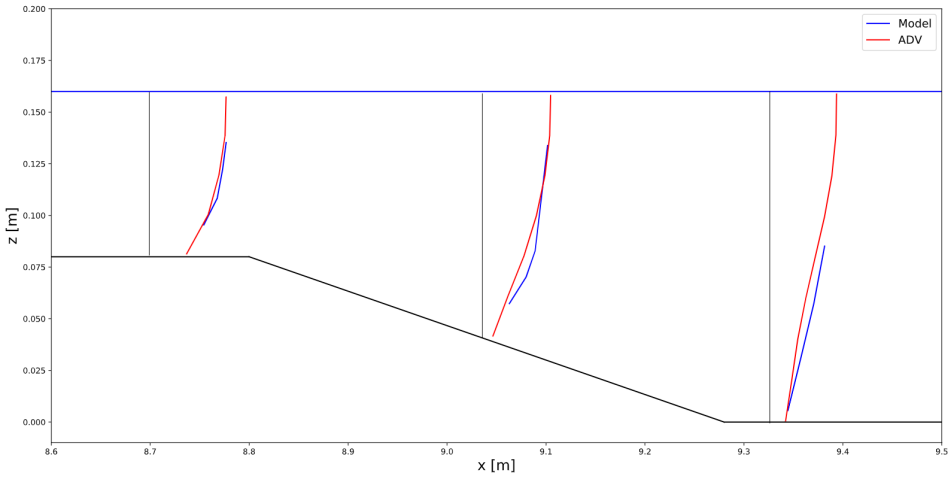

Figure B.12: Vertical velocity profiles as simulated by the 3D reference model compared to the ADV measurements of van de Zande (2018).

velocity profile just in front of the slope complies nicely with the ADV surface measurements. The additional effect from the modelled wall friction is also clearly visible when comparing the three-dimensional velocity profiles with the two-dimensional velocity profile in figure B.11a. Furthermore, figure B.11b shows the recirculation zones are modelled with only a small error towards either side of the channel. Though the surface velocity profile seems to overestimate the peak and wall velocities, this is to be expected when considering the depth at which the surface ADV measurement is taken.

The largest impact of the vertical discretization will be on the vertical velocity profiles as in figure B.12. It can be seen the upstream profile at $x = 8.70$ m nicely follows the logarithmic velocity profile and only contains a small error relative to the measured ADV profile. Moving further downstream it can be seen the vertical profiles no longer represent a logarithmic profile. Furthermore, it can be observed the model portrays more significant errors with respect to the ADV measurements, especially in the lower half of the water column. The vertical grid size close to the bed and the vertical resolution of the model both have a significant impact on the vertical velocity distribution, which is why the sensitivity of the model to both parameters will be addressed in this section.

B.7.2. Vertical discretization

The performance of each model will be evaluated using the relative error of the model. The relative error was defined as the average error made when comparing the individual ADV measurements with the modelled velocities at equal height. For this purpose, the modelled velocities needed to be interpolated to the locations of the ADV measurements. It was attempted to fit a logarithmic velocity profile of the form $u = a + b \cdot \ln cz$ through the modelled data for this purpose. Just in front of the slope at $x = 8.70m$ this method worked properly, whereas on the slope and further downstream the modelled velocity profile could not be captured accurately by a logarithmic velocity profile. It was therefore decided to simply perform a linear interpolation between data points. As this can cause errors in the approximation of the relative error, the results are investigated with caution.

B.7.2.1 Bottom grid size

The sensitivity of the model to the height of the first grid point was tested using $\Delta z = 0.02$ for the gross of the water column and $\Delta z_0 = 0.02/0.01/0.05$ at the bottom. The resulting vertical velocity profiles are shown in figure B.13 and the relative errors in figure B.14. Figure B.13 shows the impact of way the bed velocity is prescribed in FINEL3D, simulating a non-zero velocity at the bed which decreases in magnitude with decreasing Δz_0 complying with equation B.16. The model deviations at $x = 8.70$ m are relatively small, which can also be observed in figure B.14. At the two locations more downstream the velocity profile of Δz_0 starts to deviate largely from the other two simulations and the ADV data. This is translated to large relative errors in figure B.14. It was calculated the required limit for Δz_0 set

by the constraint that the grid cell should lie outside the buffer layer at $y^+ \geq 30$ roughly complies with $\Delta z_{0,min} = 0.001$ m. The current value $\Delta z_0 = 0.005$ m roughly complies with $y^+ = 120$. It was concluded the minimum limit of the grid size at the bottom lies higher than expected. In the simulations for the experiment, $\Delta z_0 \geq 0.01$ m will be used.

Between the simulations with $\Delta z_0 = 0.01$ m and $\Delta z_0 = 0.02$ m only subtle differences are visible. The general outline of the velocity profiles remains equal. It can be concluded that $\Delta z_0 = 0.01$ m yields the most accurate results, which will be used in the upcoming simulations.

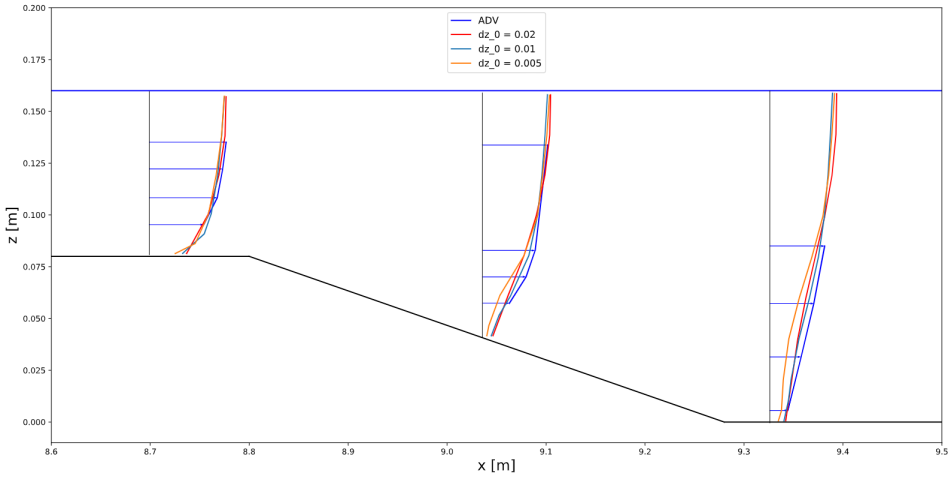

Figure B.13: Vertical velocity profiles for three different 3D simulations of experiment 2.4.1 of van de Zande (2018) with varying Δz_0 at the locations of the ADV data ($x = (8.70, 9.04, 9.34)$).

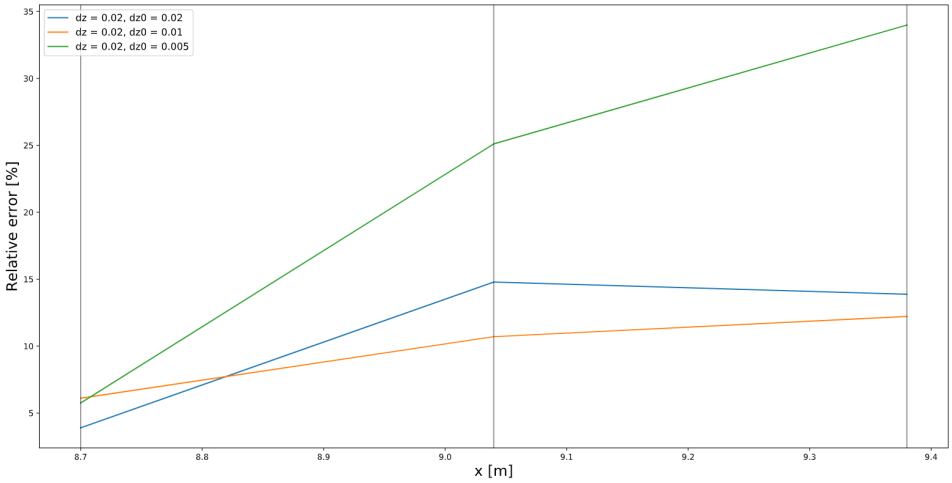

Figure B.14: Relative error for three different 3D simulations of experiment 2.4.1 of van de Zande (2018) with varying Δz_0 at the locations of the ADV data ($x = (8.70, 9.04, 9.34)$).

B.7.2.2 Vertical grid resolution

The sensitivity of the model to the amount of layers was tested using $\Delta z_0 = 0.01$ m as determined to be the most accurate in the previous subsection and $\Delta z = 0.04/0.02/0.01$ m. The resulting vertical velocity profiles are shown in figure B.15 and the relative errors in figure B.16. From figure B.15 it can be observed the differences in velocity profiles is significantly less pronounced compared to the variational Δz_0 in figure B.13. The primary impact of the usage of fewer layers lies in the simulated surface velocity, which is significantly higher for $\Delta z = 0.04$ m compared to the other two simulations. Considering figure B.16 it can be concluded the simulation with $\Delta z = 0.01$ m contains the most accurate

results. Furthermore, the figure seems to suggest the simulation with $\Delta z = 0.04$ m can be more accurate than the simulation with $\Delta z = 0.02$ m downstream of the slope. However, considering the relatively linear velocity profile measured by the ADV, it was hypothesized this was simply the result of the linear interpolation rather than a more accurate velocity simulation. The simulation with $\Delta z = 0.01$ was used in the analysis.

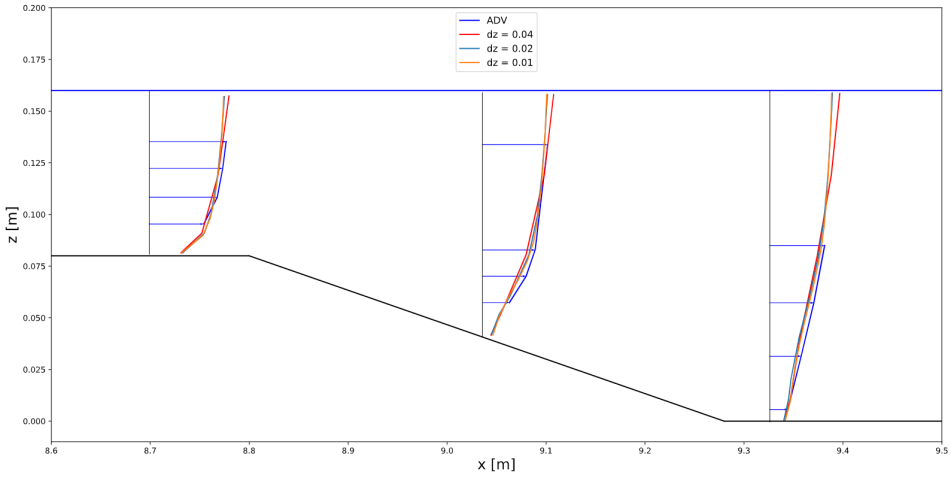

Figure B.15: Vertical velocity profiles for three different 3D simulations of experiment 2.4.1 of van de Zande (2018) with varying Δz at the locations of the ADV data ($x = (8.70, 9.04, 9.34)$).

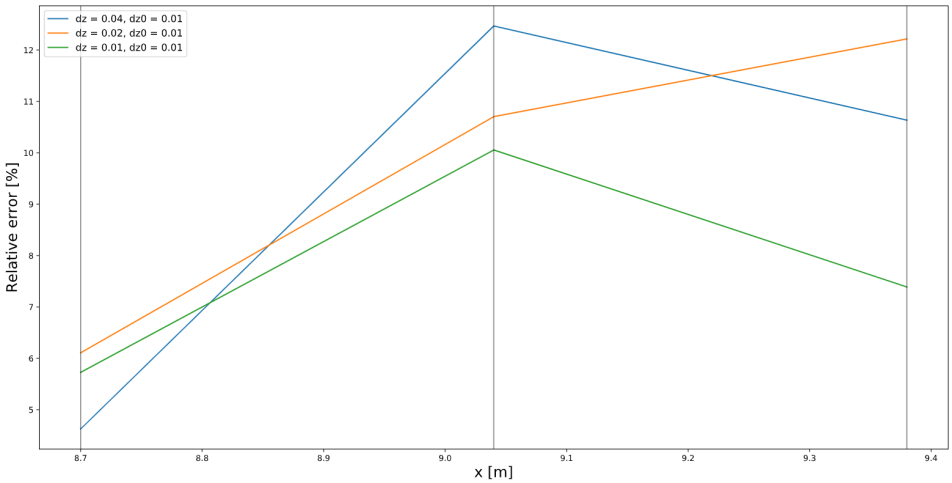

Figure B.16: Relative error for three different 3D simulations of experiment 2.4.1 of van de Zande (2018) with varying Δz at the locations of the ADV data ($x = (8.70, 9.04, 9.34)$).

C

Additional information for the Waterdunen simulations

This appendix aims to supply further information regarding the numerical simulations carried out for the field scenario at Waterdunen. Appendix C.1 explains the numerical analysis carried out by Svašek Hydraulics at Waterdunen using a FINEL2D-Explicit model and a TUDFLOW3D model. Afterwards, considerations regarding the employed turbulence closure model and outflow grid resolution are given in appendix C.2.

C.1. Svasek models

The bed protection at Waterdunen was designed based on a two-dimensional model using the software package Finel2D-Explicit. The features of this software package were explained in appendix B.2. As it was visually observed the flow moved differently compared to what was predicted by the model, the measurement campaign was launched to better understand the flow patterns at Waterdunen. Based on the measurement, a three-dimensional model was created using the software package TUDFlow3D, the features of which will be explained in the following section. The velocity magnitude and direction for two lateral cross-sections are compared with the measured velocity magnitude and direction during the campaign in figure C.1. The measurements were taken during scenario 5 with a discharge of around Q = 53 m^3/s. The first and second panel indicate the velocity and flow direction for the north cross-section respectively, whereas the third and fourth panel indicate the velocity and flow direction in the south cross-section as shown in the image to the left.

C.1.1. Finel2D-Explicit model

From figure C.1 it is obvious the Finel2D-Explicit model underestimates the velocities in both cross-sections over the entire length of both cross-sections. A clear separation point between the recirculating area and jet area can be seen in both directional plots, where over both areas the flow direction is constant. For the south cross-section this point seems to coincide with the measured transition, whereas for the north cross-section the width of the recirculating area is overestimated. In general, it can be stated the Finel2D-Explicit model shows more uniform profiles compared to both the TUDFlow3D model and the measurements.

C.1.2. TUDFlow3D

The TUDFlow3D model seems to capture the fluctuations as observed from the measurements, though the magnitude can vary with small amounts. Especially near both lateral slopes on either side of the channel the velocity magnitude seems to be underestimated by a relatively large margin. On both sides the flow seems to move towards the limit shown by the Finel2D-Explicit model, which indicates the velocity deviation might be the result of the imposed boundary conditions on the side walls. In general, the results of the TUDFlow3D model seem to capture the general outline of the flow relatively well.

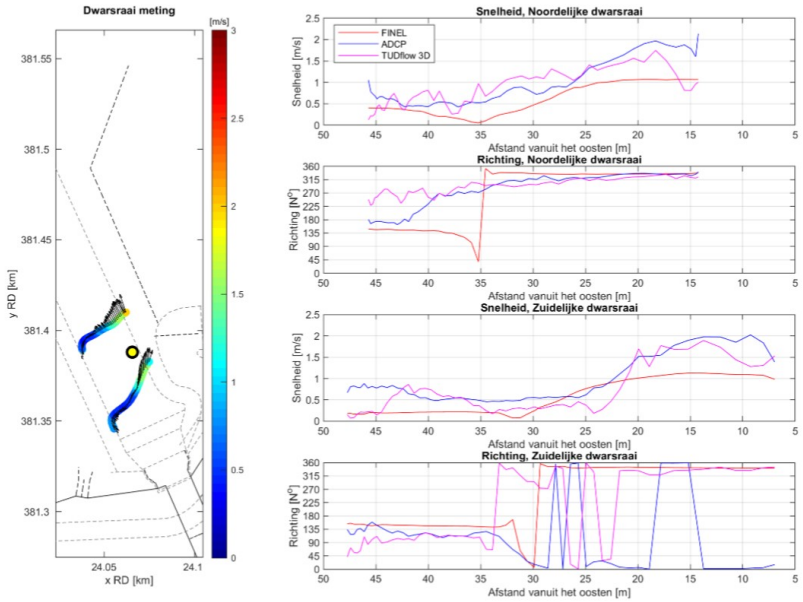

Figure C.1: Comparison of the absolute velocity magnitude and direction as computed by the TUDFlow3D and Finel2D-Explicit model and as measured during scenario 5 of the measurement campaign (Svasek Hydraulics, 2020).

C.1.3. Bottom influence

Aside from the above comparison, Svasek Hydraulics (2020) have compared simulations based on the bottom as measured in the beginning of scenario 5 to simulations on a flat 'design' bottom following solely the scour protection. The results are shown in figure C.2 for the measured topography and figure C.3.

Remarkably, it seems in the initial 75 m from the culvert both computations vary relatively little. In figures C.2a and C.3a, 25 m from the culvert, both simulations seem to show the eastern recirculation point and peak jet velocities on near-equal positions and with near-equal magnitudes. The jet width is around 1 m broader for the actual topography, whereas the magnitude of the eastern recirculation zone is overestimated for the design topography. Such subtle differences and displacements can be observed in the initial 75 m from the culvert. Further downstream the design topography simulation seems to show a strong western concentration of the flow, whereas the actual topography shows a more uniform velocity distribution over lateral cross-sections.

Considering the actual topography as visible in figure A.11 it can be observed the bottom is relatively uniform along the eastern channel section for the initial 50 m from the culvert. At that distance the middle of the channel becomes more shallow, whereas on the eastern side little topographic changes occur. The primary differences in the flow seem to occur at the location the channel expands towards the west, which is around 100 m from the culvert. With the design bottom, the shallow middle-section is not mapped. Therefore, the flow can freely move towards the west and eventually hits the western slope. Considering the actual topography, the channel remains shallow on the western side. Therefore the flow remains more central, though the flow seems to spread out similarly to the topographic channel. It is at this point the largest differences between the design and measured topography can be observed.

From both simulations it can be concluded the topographic influence in the initial 75 m from the culvert is limited. The flow does not seem to get contracted due to the presence of the shallower middle section, as the flow over a flat bottom is nearly identical. However, it can be observed slightly lower velocities thrive on the eastern slope for the flat-bottom case, which might indicate the jet spreads out less. Around 100 m from the culvert, when the flow starts to spread out, the topography influences the

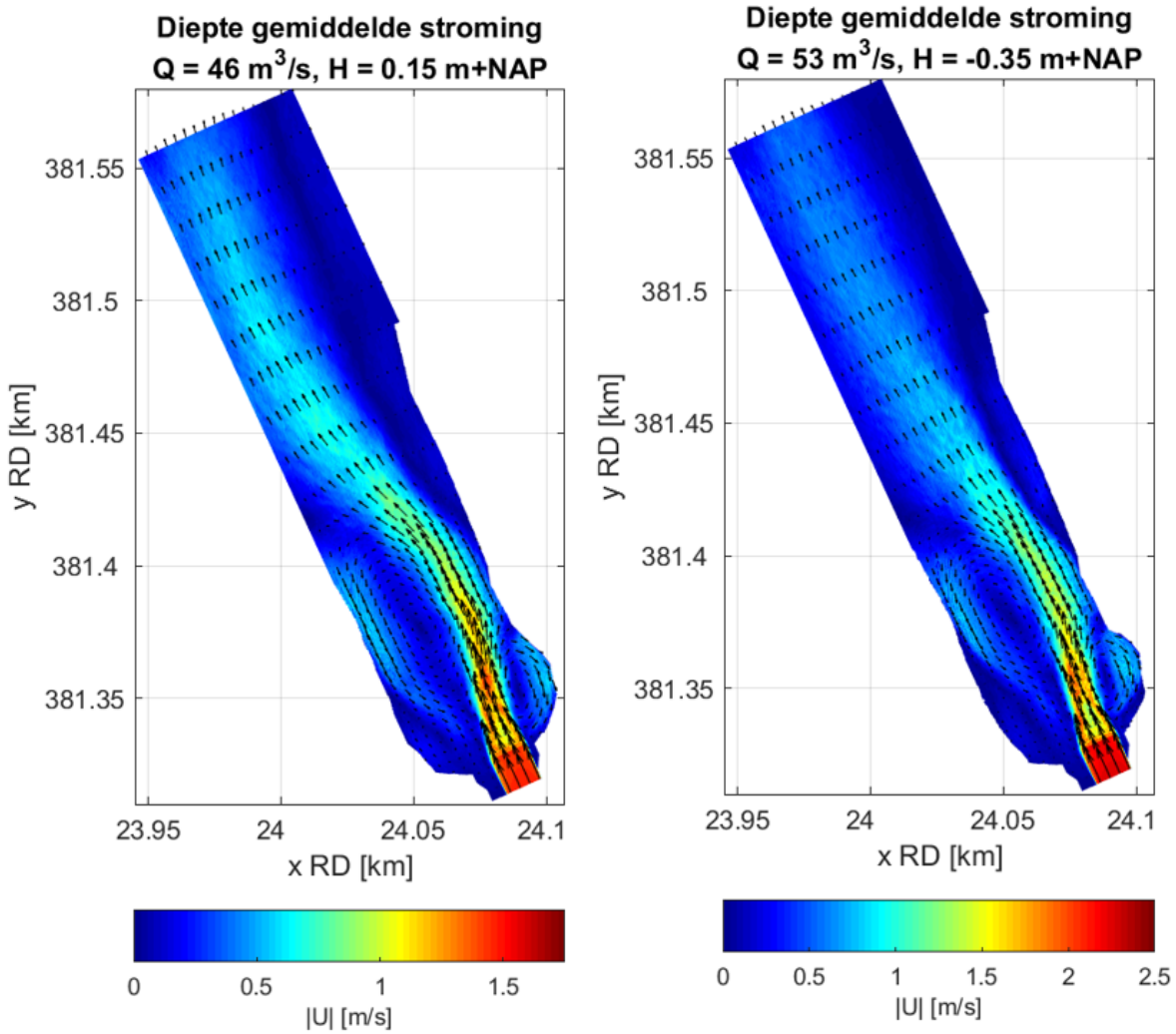

(a) Model with measured topography ($Q = 46\ m^3/s$, $H = 0.15\ m+NAP$) (b) Model with measured topography ($Q = 53\ m^3/s$, $H = -0.35\ m + NAP$)

Figure C.2: Results of the TUDFlow3D model of scenario 5 by Svasek using the topography as measured during the measurement campaign.

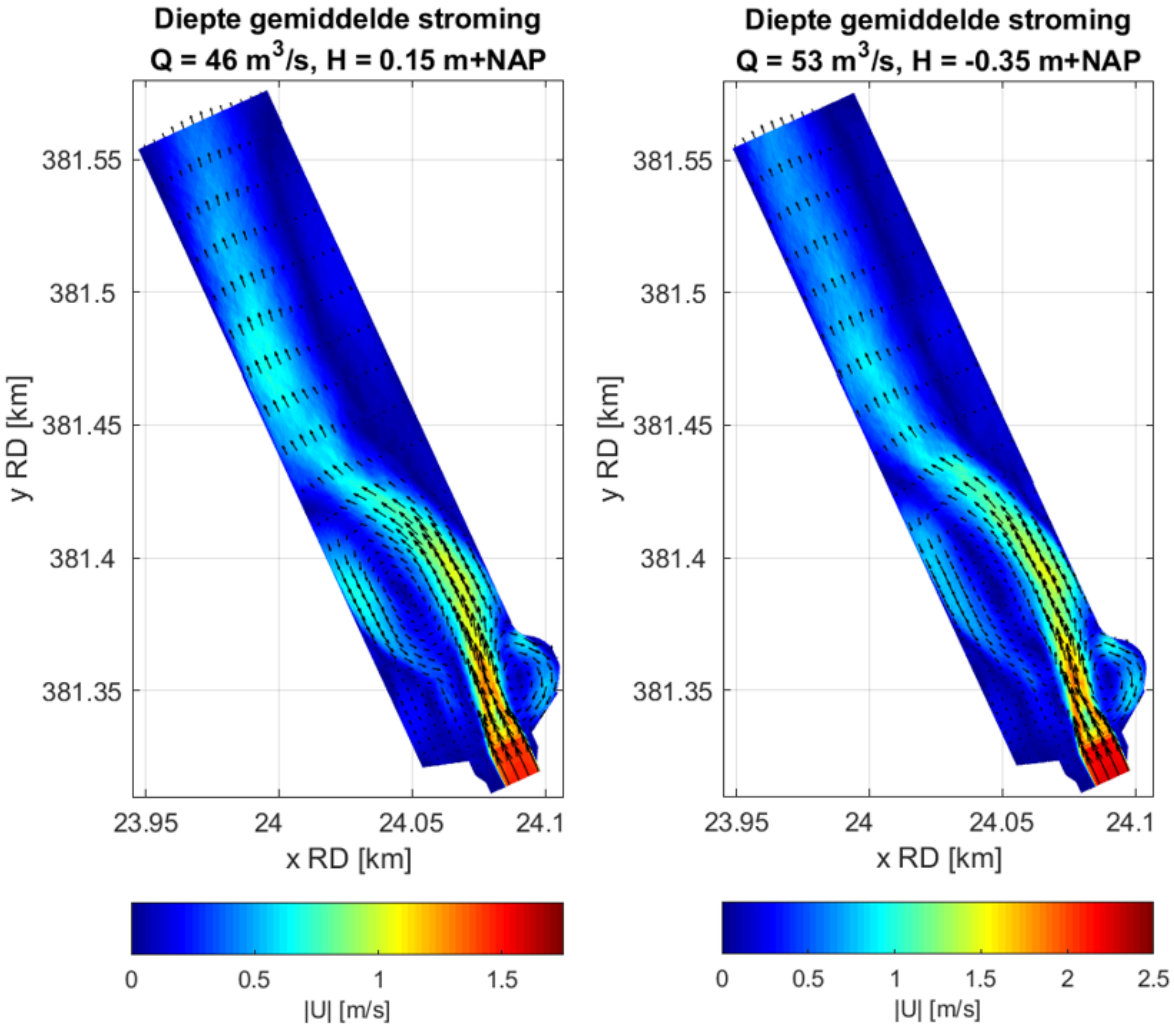

(a) Model with design topography ($Q = 46\ m^3/s$, $H = 0.15\ m + NAP$) (b) Model with design topography ($Q = 53\ m^3/s$, $H = -0.35\ m + NAP$)

Figure C.3: Results of the TUDFlow3D model of scenario 5 by Svasek using the design.

flow pattern, blocking off the movement towards the west and forcing the flow to remain in the middle-eastern section of the channel. Based on these results it is expected the topography is a result of the flow rather than a driver: the shallower middle section likely builds up due to the low flow velocities in the area. Therefore it seems the asymmetric flow pattern is important for the sedimentation-erosion pattern in the channel.

C.2. Preliminary 2DH simulations Waterdunen

The model settings have been explained in section 5.1. However, several choices were made before these model settings were set as final. The preliminary 2DH simulations supply several of the necessary arguments to validate the model settings which were used in chapter 5.

C.2.1. Turbulence closure model

Initially, a Smagorinsky model was employed to simulate the flow at Waterdunen with an identical numerical grid as explained in section 4.2. The Smagorinsky parameter C_s was again set at 0.1 to comply with Talstra (2011). It was noticed the instantaneous flow fields as reproduced using the model showed a strongly non-stationary jet flow with constant formation, growth and shredding of vortices. An example of such a simulation is shown in figure C.4. It can be observed each casing behaves as an individual jet, rather than the amalgamating behaviour that might be expected. Furthermore, the jet does not move towards the eastern slope in a clear pattern and the recirculating gyres are spread across the channel. Neither of these processes were expected. When taking the 10-minute average of the model output velocities, a more clear pattern in the flow can be observed as shown in figure C.5. Nevertheless, the flow profile is not what was expected from the data analysis at Waterdunen.

The continuous vortex shredding observed in figure C.4 might not be far off from reality. Video footage made during measurement scenario 5 also show continuous, small vortices being shred from the jet stream. Nevertheless, the video footage also shows a clear eastern concentration of the flow, which was also observed in the measurement data and was found absent in the model data. Furthermore, it was observed during the model validation that the Smagorinsky model failed to accurately reproduce instantaneous turbulent fluctuations. By comparing the instantaneous model results to instantaneous velocity measurements carried out during the measurement campaign, it was confirmed this is also the case in the Waterdunen simulations. It was hypothesized that, due to the 2DH nature of the model, large vortices created by the individual jet streams remained stable when propagating through the channel due to the absence of the energy cascade. This process has been discussed in section 2.1. This way, the vortices do not break down into smaller vortices, as can be observed between figures C.4a and C.4b.

Using this reasoning, it was decided to remove the non-stationary behaviour from the model simulations. This can be done by increasing the turbulent viscosity in the channel, which dampens the individual vortices. Increasing the turbulent viscosity can be done in Smagorinsky model by increasing the Smagorinsky coefficient C_s. However, this would achieve the same purpose as a significantly more simple mixing layer turbulence model. Instead of simply increasing C_s to yield a more accurate flow profile, it was therefore decided to use a mixing layer model as prescribed in Uijttewaal (2018). These model settings are further explained in section 5.1.

C.2.2. Outflow grid resolution

In figure C.4 it can be seen the outflow from each casing behaves as an individual jet. Furthermore, the separating walls between casings are shown to create wakes downstream of the culvert. However, these individual jet pattern were no longer visible in the mixing length simulations. It was hypothesized the current grid resolution of $\Delta = 0.7$ m was not sufficient to accurately reproduce the interactions between the outflow of each individual case as only one grid element separated each stream. The outflow resolution is pivotal for hydrodynamic processes such as the jet contraction over the longitudinal slope. It was therefore tested whether a higher grid resolution of $\Delta = 0.35$ m at outflow would reproduce the outflow from the individual casings more clearly. Figure C.6 shows the outflow from the culvert during both simulations at $t = 10:04$. It can be observed the differences between the simulated outflow are minor, indicating an additional refinement at outflow is not necessary for mixing length

(a) (b)

Figure C.4: 2DH simulation results at Waterdunen using Smagorinsky LES with $C_s = 0.1$.

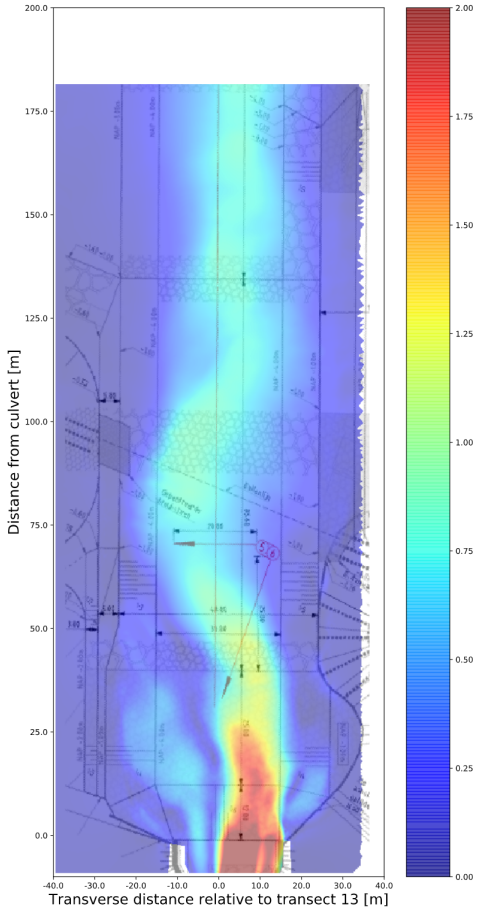

Figure C.5: 10 minute average flow profile of a 2DH Smagorinsky LES simulation at Waterdunen

simulations.

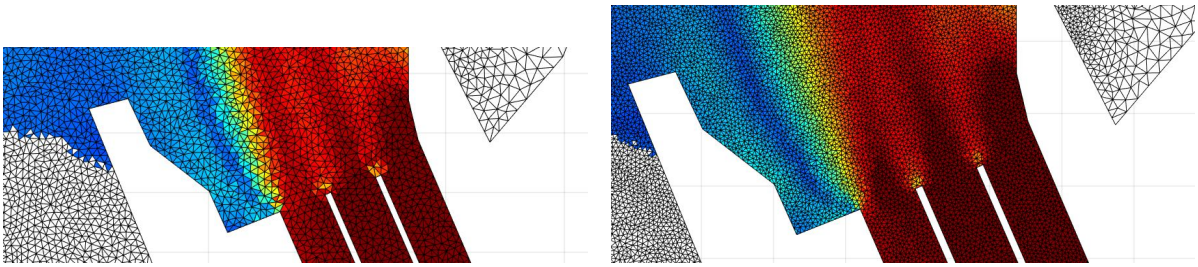

(a) $\Delta = 0.7$ m

(b) $\Delta = 0.35$ m

Figure C.6: Zoom-in of the outflow from individual casings at Waterdunen during two different mixing length simulations, of which one contained a coarse grid (A) and one contained a fine grid (B).